Topological Track Reconstruction in Liquid Scintillator and LENA as a Far-Detector in an LBNO Experiment

Dissertation

zur Erlangung des Doktorgrades

an der Fakultät Mathematik, Informatik und Naturwissenschaften

Fachbereich Physik

der Universität Hamburg

vorgelegt von

Sebastian Lorenz

aus Erlangen

Hamburg
2016

Gutachter der Dissertation:	Prof. Dr. Caren Hagner Prof. Dr. Michael Wurm
Gutachter der Disputation:	Prof. Dr. Caren Hagner Prof. Dr. Dieter Horns Prof. Dr. Günter Sigl Prof. Dr. Michael Wurm Dr. Björn Wonsak
Datum der Disputation:	11.11.2016
Vorsitzender des Prüfungsausschusses:	Prof. Dr. Dieter Horns
Vorsitzender des Promotionsausschusses:	Prof. Dr. Wolfgang Hansen
Dekan der MIN Fakultät:	Prof. Dr. Heinrich Graener

Abstract

Unsegmented *liquid scintillator* (LSc) neutrino detectors have proven to be successful instruments of neutrino physics. They usually measure terrestrial and astrophysical *low-energy* (LE) neutrinos and antineutrinos with energies up to some tens of MeV. Designs for next-generation detectors based on this technology intend to use several tens of kilotons of LSc. Two examples are the *Low Energy Neutrino Astronomy* (LENA) project with 50 kt considered in Europe and the *Jiangmen Underground Neutrino Observatory* (JUNO) with 20 kt already under construction in China. A key factor to reach the scientific goals of these projects, e.g., the determination of the neutrino *mass ordering* (MO) in the case of JUNO, will be the efficient rejection of background from radioisotopes produced by cosmogenic muons. This requires accurate reconstructions of extended muon event topologies in the LSc volume.

The first part of this work is about the implementation of a novel, iterative track reconstruction procedure for unsegmented LSc detectors and a basic evaluation of its performance with the LENA detector simulation. The ultimate goal of the new method is to reconstruct the *spatial number density distribution of optical photon emissions*. This will give access to a charged particle's differential energy loss $\mathrm{d}E/\,\mathrm{d}x$ in LSc and resolve details of an event's topology, e.g., induced particle showers. Visual comparisons of reconstruction outcomes with *Monte Carlo* (MC) truths already provide evidence for this capability. First quantitative results were extracted from the 3D reconstruction data of fully-contained muons in the kinetic energy range from 1 to 10 GeV: Despite some well understood systematic effects in the current method to find start and end point of a track, resolutions $\lesssim 25$ cm lateral to the reconstructed track were ascertained for these spots. The determined angular resolution of $\sim$1.4° at 1 GeV improves to $\sim$0.3° with rising muon energy. With the current analysis method, the relative energy resolution approximately follows the function $10\,\%/\sqrt{E/1\,\mathrm{GeV}}+2\,\%$.

The application of the new technique is not limited to cosmogenic muons. Future advancements may allow the reconstruction of the complex event topologies of GeV neutrino interactions. Beyond the (usual) LE neutrino program, this case would open up a new range of applications for unsegmented LSc detectors. The second part of this work therefore investigates the performance of LENA in a *long-baseline neutrino oscillation* (LBNO) experiment with a conventional multi-GeV neutrino beam as proposed in the *Large Apparatus for Grand Unification and Neutrino Astrophysics* (LAGUNA)-LBNO design study: A 750 kW neutrino beam aiming over a distance of $\sim$2300 km from the *Conseil Européen pour la Recherche Nucléaire* (CERN) to the *Pyhäsalmi mine* in central *Finland*. The potential to discover the *neutrino MO* and *leptonic CP-violation* was studied with the *General Long Baseline Experiment Simulator* (GLoBES) package in combination with MC techniques. Assuming ten years of runtime equally shared between neutrino and antineutrino mode, only a low sensitivity to CP-violation was found. However, in the MO study, the *inverted ordering* (IO) (*normal ordering* (NO)) hypothesis could be rejected at true NO (IO) with a *median sensitivity* of 4.6–6.7σ (4.2–5.8σ), depending on the true value of the CP-violating phase δ_{CP}.

Zusammenfassung

Unsegmentierte *Flüssigszintillator* (FSz)-Neutrinodetektoren haben sich als erfolgreiche Instrumente in der Neutrinophysik erwiesen. Üblicherweise messen diese terrestrische und astrophysikalische Niederenergieneutrinos und -antineutrinos mit Energien bis zu einigen zehn MeV. Designs für Detektoren der nächsten Generation basierend auf dieser Technologie beabsichtigen den Einsatz mehrerer zehn Kilotonnen an FSz. Zwei Beispiele sind das in Europa in Betracht gezogene *Low Energy Neutrino Astronomy* (LENA)-Projekt mit 50 kt und das sich in China im Bau befindende *Jiangmen Underground Neutrino Observatory* (JUNO) mit 20 kt. Ein Schlüsselfaktor zum Erreichen der wissenschaftlichen Ziele dieser Projekte, z.B. die Bestimmung der Neutrinomassenordnung im Fall von JUNO, wird die effiziente Unterdrückung von Untergrund durch von kosmogenen Myonen produzierte Radioisotope sein. Diese benötigt präzise Rekonstruktionen von ausgedehnten Myonereignistopologien im FSz-Volumen.

Im ersten Teil dieser Arbeit geht es um die Implementierung eines neuartigen, iterativen Spurrekonstruktionsverfahrens für unsegmentierte FSz-Detektoren und eine grundlegende Evaluierung dessen Leistungsfähigkeit mit der LENA Detektorsimulation. Das endgültige Ziel der neuen Methode ist es die *räumliche Anzahldichteverteilung von Emissionen optischer Photonen* zu rekonstruieren. Das wird den differentiellen Energieverlust $\mathrm{d}E/\,\mathrm{d}x$ eines geladenen Teilchens in FSz zugänglich machen und Details der Topologie eines Ereignisses auflösen, z.B. erzeugte Teilchenschauer. Visuelle Vergleiche von Rekonstruktionsergebnissen mit *Monte Carlo* (MC)-Wahrheiten geben bereits Hinweise auf diese Fähigkeit. Erste quantitative Resultate wurden aus den 3D Rekonstruktionsdaten von vollständig im Detektor enthaltenen Myonen im Bereich von 1 bis 10 GeV kinetischer Energie extrahiert: Trotz einiger gut verstandener systematischer Effekte in der momentanen Methode zum Auffinden von Start- und Endpunkt einer Spur wurden für diese Punkte Auflösungen von $\lesssim 25$ cm lateral zur rekonstruierten Spur festgestellt. Die bestimmte Winkelauflösung von $\sim 1.4°$ bei 1 GeV verbessert sich mit zunehmender Myonenergie auf $\sim 0.3°$. Mit der momentanen Analysemethode folgt die relative Energieauflösung in etwa der Funktion $10\,\%/\sqrt{E/1\,\mathrm{GeV}} + 2\,\%$.

Die Anwendung des neuen Verfahrens ist nicht auf kosmogene Myonen beschränkt. Zukünftige Weiterentwicklungen könnten die Rekonstruktion komplexer Ereignistopologien von GeV Neutrinointeraktionen ermöglichen. Über das (übliche) Niederenergieneutrinoprogramm hinaus würde dieser Fall neue Verwendungsmöglichkeiten für unsegmentierte FSz-Detektoren eröffnen. Der zweite Teil dieser Arbeit untersucht daher das Potential von LENA in einem Neutrinooszillationsexperiment mit langer Verbindungslinie zwischen Quelle und Detektor und mit einem konventionellen Multi-GeV-Neutrinostrahl wie in der *Large Apparatus for Grand Unification and Neutrino Astrophysics* (LAGUNA)-*Long-baseline Neutrino Oscillation* (LBNO) Designstudie vorgeschlagen: Ein 750 kW Neutrinostrahl, der über eine Distanz von ~ 2300 km vom *Conseil Européen pour la Recherche Nucléaire* (CERN) auf die *Pyhäsalmi-Mine* in *Zentralfinnland* zielt. Das Potential die *Neutrinomassenordnung* und *leptonische CP-Verletzung* zu entdecken wurde mit dem *General Long Baseline Experiment Simulator* (GLoBES)-Paket in Kombination mit MC-Techniken studiert. Unter der Annahme von gleichmäßig zwischen Neutrino- und Antineutrinomodus aufgeteilter, zehnjähriger Laufzeit wurde nur eine niedrige Sensitivität bezüglich CP-Verletzung gefunden. Allerdings konnte in der Massenordnungsstudie, abhängig vom wahren Wert der CP-verletzenden Phase δ_{CP}, die Hypothese *Invertierte Ordnung* (IO) (*Normale Ordnung* (NO)) mit einer *Mediansensitivität* von 4.6–6.7σ (4.2–5.8σ) verworfen werden, wenn die NO (IO) realisiert ist.

Contents

Introduction

"To make the impossible come true, one must try the impossible again and again."[1]
Although the will to go beyond the currently possible by repeated trying is part of the spirit of any experimental science, one sees how true the above phrase is if one looks back at the history of (experimental) neutrino physics.
In 1914, *James Chadwick* experimentally showed that the energy spectrum of radiation from β-decay is continuous [2] and thereby started a broad controversy. Since the β-decay was considered a two-body decay at that time, including the sole emission of a beta particle, *J. Chadwick's* finding constituted nothing less than a violation of the law of conservation of energy. To preserve this fundamental law, *Wolfgang Pauli* proposed in 1930 the emission of a second, neutral, spin-$^1/_2$ particle from β-decay [3]. It is supposed that he has commented his postulate of what is today known as *neutrino* (ν) and *antineutrino* ($\overline{\nu}$) in the following way [4]: *"I've done a terrible thing today, something which no theoretical physicist should ever do. I have suggested something that can never be verified experimentally."*
However, about 26 years later, the "impossible" had been tried—twice—by *Clyde L. Cowan* and *Frederick Reines* [5, 6]. They finally confirmed the existence of what was named the *Poltergeist* [7], the electron antineutrino ($\overline{\nu}_e$), in 1956.[2] In the following years, other experiments again tried the "impossible". Pioneering the *neutrino beam* technology, *Leon M. Lederman*, *Melvin Schwartz* and *Jack Steinberger* discovered the muon neutrino (ν_μ) in their experiment at *Brookhaven National Laboratory* in 1962 [9].[3] The discovery of the tau neutrino (ν_τ) was reported by the *Direct Observation of NU Tau* (DONUT) experiment in 2000 [10].
Nowadays, the three neutrino flavors, ν_e, ν_μ and ν_τ, which solely interact via the *weak force*, are part of the *Standard Model* (SM) *of elementary particle physics* [11]. Only the assumed existence of the $\overline{\nu}_\tau$ has not yet been unambiguously verified. However, the proposed *Search for Hidden Particles* (SHiP) [12] experiment could be the first to do so as part of its ν_τ / $\overline{\nu}_\tau$ program with a dedicated neutrino detector.

After the detection of neutrinos and antineutrinos was shown to be possible, experimental neutrino physics, dedicated to study the properties of the neutral leptons, their weak interactions and also their sources, became an aspiring field of science.

[1] Original, German quotation: „Damit das Mögliche entsteht, muss immer wieder das Unmögliche versucht werden." – Hermann Hesse – Brief an *Wilhelm Gundert* (September 1960) [1].
[2] *Frederick Reines* was awarded with the *Nobel Prize in Physics* "for the detection of the neutrino" [8] in 1995.
[3] *Leon. M. Lederman*, *Melvin Schwartz* and *Jack Steinberger* were awarded with the *Nobel Prize in Physics* "for the neutrino beam method and the demonstration of the doublet structure of the leptons through the discovery of the muon neutrino" [8] in 1988.

This was also due to the upcoming of new challenges—both to neutrino theory and experiment.
Towards the end of the 1960s, the famous *Homestake experiment* by *Raymond Davis Jr.* performed a first-time measurement of ν_e's from the Sun [13, 14]. It was found that the measured neutrino interaction rate was lower than the prediction from the so-called *Standard Solar Model* (SSM) [15, 16], which had been developed by *J.N. Bahcall* since 1962. Similar results for solar neutrino observations were later on reported by other experiments (see Ref. [11]), e.g., by the *Kamioka Nucleon Decay Experiment* (Kamiokande)-II [17].[4] Possible changes to the SSM, however, would have caused tensions between predictions and measurements of other observables. The solution to this *solar neutrino problem* was proposed by *Bruno Pontecorvo* in 1967 [18]: *neutrino flavor oscillations*, i.e., the quantum-mechanical phenomenon that one neutrino flavor eigenstate can transmute into another flavor eigenstate in an oscillatory way. It took until 2001/2002 before this theory became confirmed with the *Sudbury Neutrino Observatory* (SNO) [19]. By simultaneously measuring both the ν_e and the total neutrino flux, the experiment clearly showed that ν_e change their flavor to ν_μ or ν_τ along their way from the Sun to Earth [20,21]. Previously, a publication of the *Super-Kamiokande* (SK) experiment [22] had reported the finding of a variation in the atmospheric $\nu_\mu + \overline{\nu}_\mu$ flux as a function of the zenith angle [23]. This result was inconsistent with calculated expectations for the atmospheric neutrino flux and could be compellingly explained with $\nu_\mu \leftrightarrows \nu_\tau$ and $\overline{\nu}_\mu \leftrightarrows \overline{\nu}_\tau$ oscillations. The flavor change $\nu_\mu \to \nu_\tau$ in a multi-GeV neutrino beam was later directly observed by the *Oscillation Project with Emulsion-Tracking Apparatus* (OPERA) [24], whose evidence for ν_τ appearance recently reached a statistical significance of $> 5\sigma$ [25].

The occurrence of neutrino flavor oscillations shows that the neutrino is a massive particle with mass eigenstates that are different from the flavor eigenstates.[5] This is opposed to the masslessness of neutrinos assumed in the SM.
Nowadays, the precise measurement of the parameters describing the three-flavor oscillation model is among the top priorities of experimental neutrino physics. One outstanding question concerns the neutrino *mass ordering* (MO)[6] [26]: Current neutrino oscillation data can only provide absolute values on mass-squared differences and show that there is a small and a large splitting between the three neutrino mass eigenvalues. However, the ordering of these eigenvalues, i.e., the answer to the question if the mass eigenvalue separated by the large splitting is smaller (the *inverted ordering* (IO) case) or larger (the *normal ordering* (NO) case) than the two other values, is not known. Several experiments around the world want to solve this issue by precisely measuring flavor oscillations of neutrinos and antineutrinos from beams, the atmosphere or nuclear reactors. The neutrino MO has implications for the sensitivity goals of experiments searching for the *neutrinoless double-beta* ($0\nu\beta\beta$) *decay* [11] and for the determination of the *sum of neutrino masses* from cosmological observations [27].

[4] *Raymond Davis Jr.* and *Masatoshi Koshiba* (Kamiokande-II) were awarded with the *Nobel Prize in Physics* "for pioneering contributions to astrophysics, in particular for the detection of cosmic neutrinos" [8] in 2002.
[5] *Arthur B. McDonald* (SNO) and *Takaaki Kajita* (SK) were awarded with the *Nobel Prize in Physics* "for the discovery of neutrino oscillations, which shows that neutrinos have mass" [8] in 2015.
[6] Also referred to as neutrino *mass hierarchy.*

In addition to the above, the MO is also an important factor for forthcoming neutrino beam experiments aiming to precisely measure the neutrino mixing parameter δ_{CP}. The determination of this parameter, which can indicate the presence of *leptonic CP-violation* [28], is a second pressing issue of neutrino flavor oscillation physics. In an oscillation experiment, a violation of the symmetry from *charge conjugation C* and *parity transformation P* would become evident through different probabilities for the same flavor transition of neutrinos and antineutrinos. According to the three so-called *Sakharov conditions*, CP-violation in general is a necessity to explain the predominance of matter over antimatter in the universe. One possible mechanism to create such an asymmetry is *leptogenesis*, which relies specifically on leptonic CP-violation.
Apart from flavor oscillations, there are also unresolved issues in other fields of (experimental) neutrino physics. For example: *What are the absolute neutrino masses? Are there sterile neutrino states in addition to the three known flavor states? Is the neutrino its own antiparticle, i.e., is the neutrino a* Dirac *or* Majorana *fermion?*

Besides the relevance of neutrinos as elementary particles, a second aspect of interest is the use of the light neutral leptons as *messengers* for information from terrestrial and extraterrestrial phenomena. Since the weakly interacting particles can traverse large amounts of matter essentially unhindered, neutrinos act as *natural probes*. They allow to look at physics processes behind or even within objects from which information in the form of photons or charged particles is either strongly deteriorated or not available at all. One example for messenger neutrinos are the previously mentioned *solar neutrinos*. Their study already provided valuable insights into the elemental composition and energy release processes of our Sun. Similarly, *geo-neutrinos* from within Earth allow inferences on the heat budget of our planet or the abundance of radioactive elements. In addition, *supernova* (SN) neutrinos, either from a single incident or the background of former SNe, are the most promising witnesses of the death of a massive star in order to get a better understanding of one of the most violent phenomena in the Universe. The use of neutrinos as messengers lead to a *growing interdisciplinarity* between experimental neutrino physics and other fields of natural sciences.

All the named examples of messenger neutrinos cover an energy range of up to some tens of MeV. A common type of *unsegmented* neutrino detector to measure such *low-energy* (LE) neutrinos uses *liquid scintillator* (LSc) as designated target material for neutrino interactions. It detects these interactions based on the isotropic scintillation light emitted in response to outgoing charged particles, the only indicators for a neutrino interaction. Prominent instances of LSc detectors are the *Kamioka Liquid Scintillator Antineutrino Detector* (KamLAND) [29] in *Japan* with 1 kt target mass and Borexino [30] in *Italy* with ∼0.28 kt target mass. KamLAND measured neutrino flavor oscillation parameters with $\overline{\nu}_e$'s from multiple nuclear reactors. Borexino is focused on *solar neutrino spectroscopy*; its latest result in this field is the first measurement of *pp neutrinos* [31]. Additionally, both experiments successfully measured geo-neutrino signals [32, 33].
Another set of experiments, which use one or more LSc neutrino detectors with target masses of about 10–20 t, are Double Chooz [34] in *France*, Daya Bay [35] in

China and the *Reactor Experiment for Neutrino Oscillation* (RENO) [36] in *South Korea*. They survey the oscillation of reactor $\overline{\nu}_e$'s over a distance of 1–3 km in order to measure a flavor mixing parameter named θ_{13}, the smallest out of three so-called *mixing angles*.
LSc detectors feature a good energy resolution and have essentially no intrinsic energy threshold. Moreover, the designated target material can be purified to reduce *intrinsic radioactive contaminants*, whose decays are background to the search for rare LE neutrino events. Another type of background is the one caused by decays of *cosmogenic radioisotopes*. As in the case of intrinsic background, the decays of the cosmogenic radionuclides, which can be produced in the interaction of a *cosmogenic muon* traversing the detector, potentially mimic the event signature of a neutrino interaction signal. Although neutrino detectors are often placed below ground to have some shielding against cosmogenic muons, the rejection of cosmogenic background nevertheless is an important factor. A possible strategy for this task is to veto the entire detector after every muon traversal for a period of time that depends on the mean life time of the isotope to reject. However, for high muon rates (large detector and/or low muon shielding) or long-lived radionuclides (relevant half-lives range up to some minutes), this strategy can easily yield 100 % dead time of the detector. In a more efficient strategy, the veto is restricted to spatial regions of interest relative to the muon track. A prerequisite for this procedure is knowledge on the muon path inside the detector. This is a complication for LSc detectors because a muon track in the active volume can only be reconstructed based on the isotropically emitted scintillation light; something that was even considered impossible. Referring to the quotation at the beginning, the "impossible" has been tried and today there are methods to approximatively reconstruct a muon track in LSc (e.g., see Refs. [37, 38]).

The first part of this work comprises the implementation and advancement of a novel reconstruction approach[7], which enables more detailed analyses. Its goal is the reconstruction of the spatial number density distribution of optical photon emissions (mostly from scintillation). The 3D output data of the algorithm allow, amongst other things, the investigation of spatial variations in an event's energy deposition. This is fundamental to get access to a particle's differential energy loss $\mathrm{d}E/\,\mathrm{d}x$. Moreover, it enables the development of more efficient veto schemes, which focus the veto regions mainly on muon-induced particle showers, the dominant sources of cosmogenic radioisotopes.
Within the scope of this work, I have implemented the new reconstruction method as a `C++`-based software package, enhanced it in terms of speed and precision and finally applied it to a sample of simulated muon events in the energy range from 1 to 10 GeV. Moreover, I have developed a set of basic analyses for the 3D reconstruction output data and applied them to the reconstruction outcomes from the simulated muons. This represents a first evaluation of the new method's performance. The results indicate that the novel reconstruction approach is competitive with respect to other, commonly used techniques. Since the employed analyses do not yet make use of the full potential to extract useful information from the 3D reconstruction output, the performance of the new method likely improves with future development.

[7] It has been developed by *Björn S. Wonsak* [39].

Especially large-volume LSc detectors of the next generation could benefit from improved muon tracking capabilities. Two examples for such projects are *Low Energy Neutrino Astronomy* (LENA) [40] and the *Jiangmen Underground Neutrino Observatory* (JUNO)[8] [42,43]. LENA comprises 50 kt of LSc and has been considered as future neutrino observatory in *Europe*, focusing on the detection of terrestrial and astrophysical LE neutrinos and antineutrinos. The project was part of the now concluded European design studies *Large Apparatus for Grand Unification and Neutrino Astrophysics* (LAGUNA) [44,45] and its successor LAGUNA-*long-baseline neutrino oscillation* (LBNO) [46,47]. These studies also investigated the favored site for LENA, which is about 1400 m below ground in the *Pyhäsalmi mine* in *Finland*. In the context of LAGUNA-LBNO, this location was even considered as far-detector site for a European LBNO experiment with a multi-GeV neutrino beam over ∼2300 km baseline[9] from the *Conseil Européen pour la Recherche Nucléaire* (CERN)[10].
The line between "the possible" and "the impossible" would be further shifted if not only muons but also *high-energy* (HE) neutrino interactions could be reconstructed from detected scintillation photons (e.g., see Refs. [48–51]). This would open up new areas of application for LSc detectors besides the detection of LE neutrinos, e.g., measurements with GeV neutrinos from the beam of the previously mentioned LBNO experiment.

In the second part of this work I have studied the potential to discover the neutrino MO and leptonic CP-violation with the above neutrino beam setup and LENA as far-detector. Different to other evaluations, my performance estimation takes a model for the selection of *fully-contained events* into account, which I have produced in an ancillary study. This is important because the LSc technology bases on a *calorimetric energy measurement*. Although I have found a low sensitivity to CP-violation, there is a high chance to make a significant measurement of the neutrino MO. As a conclusion, a neutrino beam from CERN to *Pyhäsalmi* would bring a meaningful extension of the already broad physics program of LENA.

The JUNO project in *China* bases on a 20 kt LSc detector. Construction works for this experiment, which is expected to start data taking by 2020, began in 2015. The primary goals of JUNO are the determination of the neutrino MO and precision measurements of oscillation parameters with $\overline{\nu}_e$'s from multiple, about 52 km distant nuclear reactors. Both objectives rely on the resolution of an oscillatory fine structure in the oscillated $\overline{\nu}_e$ event spectrum. This requires a *relative visible energy resolution* of $3\,\%/\sqrt{E_{\text{vis}}/\text{MeV}}$. Since existing LSc measurement devices reach values around $7\,\%/\sqrt{E_{\text{vis}}/\text{MeV}}$ [11], JUNO is forced to advance the LSc technology beyond the current state of the art. Moreover, an overburden of only ∼700 m at the experimental site makes the large JUNO detector face a high muon event rate of $\sim 3\,\text{s}^{-1}$ [42], including not only single, through-going muons but also stopping and/or showering muons as well as muon bundles. The consequence is an expected signal to cosmogenic background ratio of about 1:1. Therefore, a sophisticated muon reconstruction algorithm with the capability of reconstructing single muon tracks as well as showering events and muon bundles is an essential ingredient to the success

[8] Another experiment similar to JUNO is RENO-50 [41] in *South Korea*.
[9] Connecting line between source and detector.
[10] European Organization for Nuclear Research

of the experiment.

This thesis is structured as follows: Chapter 1 outlines the formalism of neutrino flavor oscillations and gives an overview on neutrino interactions. Additionally, open questions on neutrinos besides flavor oscillation physics are briefly addressed. Chapter 2 details the production of LE and HE neutrinos by a selection of different natural and artificial sources. The basic function principle of LSc particle detectors is topic of Chapter 3. In Chapter 4, the use of LSc for real-time neutrino detection, including an overview of detection channels and background sources, is described. Moreover, the projects LENA and JUNO are outlined. Chapter 5 provides details on the detector simulation I employed to simulate events in LENA. Muon events from this simulation were used by me to test the novel track reconstruction approach for LSc. Its general function principle as well as my implementations and advancements are presented in Chapter 6. The outcomes from the performance evaluation are reported in Chapter 7. My study regarding the potential of LENA to discover the neutrino MO and leptonic CP-violation in an LBNO experiment with a multi-GeV neutrino beam from CERN to *Pyhäsalmi* is detailed in Chapter 8. Finally, a summary and conclusions are given at the end of this work.

Chapter 1

The Neutrino

In the SM of elementary particle physics [11], neutrinos are electrically neutral, spin-$^1/_2$ *Dirac fermions* with zero mass and no color charge. They only interact through the *charged current* (CC) and the *neutral current* (NC) of the *weak force*, which are mediated by the massive bosons $W^\pm$ ($m_W = 80.4\,\text{GeV}$ [11]) and Z^0 ($m_Z = 91.2\,\text{GeV}$ [11]), respectively. Results from e^+e^--collider experiments indicate that the number of neutrinos with masses smaller than the half mass of the Z^0 boson is 2.9840 ± 0.0082 [11]. The three neutrinos are the counterparts of the three charged leptons e, μ and τ, which define the so-called *flavor* of a neutrino (ν) and its antiparticle ($\overline{\nu}$): ν_e ($\overline{\nu}_e$), ν_μ ($\overline{\nu}_\mu$) and ν_τ ($\overline{\nu}_\tau$). A neutrino ν_ℓ being of the Lorentz invariant flavor associated with the charged lepton $\ell = e, \mu, \tau$ is produced from ℓ^- or together with ℓ^+ in a CC weak interaction. The opposite holds for the antineutrino $\overline{\nu}_\ell$. According to the chiral *V-A-theory*, only the chiral *left-handed* (LH) component of a fermion or the chiral *right-handed* (RH) component of an antifermion participates in the CC weak interaction. For massless particles, the eigenstate of chirality equals the eigenstate of *helicity*. The helicity is defined as the projection of a particle's spin on its momentum direction and has the eigenvalues $-^1/_2$ or $+^1/_2$ for a spin-$^1/_2$ fermion [52]. As a consequence, SM neutrinos (antineutrinos) are always chiral LH (RH) particles with helicity $-^1/_2$ (helicity $+^1/_2$). Although the assumed masslessness of neutrinos and antineutrinos in the SM is inadequate in the light of neutrino flavor oscillations (see Section 1.1), the above is nevertheless in good agreement with experimental findings because measurements are usually performed with ultrarelativistic neutrinos or antineutrinos.
Together with the chiral LH charged lepton field $\ell_L(x)$, where x is a space-time four-vector, the chiral LH neutrino field $\nu_{\ell L}(x)$ forms a doublet of *weak isospin* in $SU(2)_L$. The RH charged lepton field $\ell_R(x)$ transforms as a weak isospin singlet under $SU(2)_L$. Because the quark sector can be structured in a similar way, the particles taking part in weak interactions may be ordered as shown in Table 1.1. Chiral RH neutrinos and chiral LH antineutrinos are supposed not to exist in the SM. However, they are used in theoretical models to generate neutrino masses (see Refs. [11, 53] and references therein). If these *sterile states* exist, they do not interact via the weak force.

In this chapter, the major topic of neutrino flavor oscillations is treated in Section 1.1.

Table 1.1 – Particles taking part in the SM weak interaction. The chiral LH fields of quarks and the charged / neutral leptons are weak isospin doublets of $SU(2)_L$. Chiral RH quark and charged lepton fields are singlets under $SU(2)_L$ transformation.

Fermions	Doublets	Singlets
Quarks	$\begin{pmatrix} u_L \\ d_L \end{pmatrix}$, $\begin{pmatrix} c_L \\ s_L \end{pmatrix}$, $\begin{pmatrix} t_L \\ b_L \end{pmatrix}$	(u_R), (d_R), (c_R), (s_R), (t_R), (b_R)
Leptons	$\begin{pmatrix} \nu_{eL} \\ e_L^- \end{pmatrix}$, $\begin{pmatrix} \nu_{\mu L} \\ \mu_L^- \end{pmatrix}$, $\begin{pmatrix} \nu_{\tau L} \\ \tau_L^- \end{pmatrix}$	(e_R^-), (μ_R^-), (τ_R^-)

It provides the theoretical basis for the studies presented in Chapter 8. Interactions of both LE and HE neutrinos and antineutrinos are covered in Section 1.2. While the former are in general of main interest for a LSc-based neutrino detector (see Chapter 4), the latter are important for the use of such a detection device to observe neutrinos from an accelerator (see Section 2.6) or the atmosphere (see Section 2.5). Finally, open questions on neutrinos besides issues in flavor oscillation physics are subject of Section 1.3.

1.1 Neutrino flavor oscillations

First thoughts on the concept of neutrino oscillations were published by *B. Pontecorvo* in 1957-1958 [54,55]. By that time, only the existence of electron flavor neutrinos was experimentally verified. Therefore, he initially considered the oscillatory transitions $\nu_e \leftrightarrows \overline{\nu}_e$. After the discovery of the muon flavor neutrino at the *Brookhaven National Laboratory* in 1962 [9], *B. Pontecorvo* for the first time discussed oscillations between different neutrino flavors, $\nu_e \leftrightarrows \nu_\mu$, in 1967 [18]. Throughout the years, he and his collaborators formulated a theory for the neutral lepton flavor oscillation in analogy to the neutral meson oscillations observed in the quark sector [56]. Moreover, he predicted what is today known as the *solar neutrino problem* in the course of his work [18]: Starting in the 1960s, the famous *Homestake experiment* by *R. Davis Jr.* [13, 14] measured ν_e's from the Sun (see. Section 2.1). It was found that the determined interaction rate corresponds to only one third of the ν_e flux predicted by the SSM [15, 16], which had been developed by *J.N. Bahcall* since 1962. Similar findings were reported by other experiments (see Ref. [11] and references therein). Besides disfavored changes to the SSM, the oscillation of the solar ν_e's to a flavor not observable with the Homestake detector was another possible solution to the solar neutrino problem.

It took until 2001/2002 before measurements performed with SNO [19] provided evidence for the existence of a non-electron flavor component in the solar neutrino flux[1]—and thus for the flavor oscillation of solar neutrinos—independently of any SSM neutrino flux calculations. The first results of SNO [20, 21] with its Cherenkov detector containing 1 kt of ultra-pure heavy water (D_2O) were obtained by comparing the neutrino fluxes calculated from the interaction rates of the following detection

[1] Due to the energy threshold of the detector, the observed solar neutrinos were predominantly from ^{8}B decay (see Section 2.1).

channels:

$$\begin{aligned}
\nu_e + D &\rightarrow p + p + e^- \quad \text{(CC)}\,, \\
\nu_\ell + e^- &\rightarrow \nu_\ell + e^- \quad \text{(ES)}\,, \\
\nu_\ell + D &\rightarrow p + n + \nu_\ell \quad \text{(NC)}\,.
\end{aligned}$$

While the CC detection channel is only sensitive to ν_e's, interactions via the *elastic scattering* (ES) and NC channels are possible for all neutrino flavors $\ell = e, \mu, \tau$. Due to an observed deficit of CC interactions compared to ES and NC interactions, a non-electron flavor solar flux component greater than zero by 5.3σ [21] was reported. The measured flux from the ES channel was consistent with the result of a precision measurement with the SK detector [22, 57]. Its predecessor, Kamiokande-II, had already shown that ν_e's come from the direction of the Sun [17].
Nowadays, the phenomenon of neutrino flavor oscillation is a well established fact that has been observed by numerous experiments in various energy ranges and with different types of neutrino sources (see review in Ref. [11]). Due to the implication that neutrinos must be massive particles, neutrino flavor transitions actually describe physics beyond the SM. The continued research on neutrino oscillations, with the goal to precisely measure all underlying parameters and to explore all of its aspects, surely is a core activity in the neutrino physics community.

In the following, Section 1.1.1 sketches the theory of neutrino flavor oscillations in vacuum. The impact of matter on the oscillatory flavor transitions is subject of Section 1.1.2. Some information on the current status of the research field and a brief prospect on future activities are given in Section 1.1.3.

1.1.1 Oscillations in vacuum

The quantum-mechanical phenomenon of neutrino flavor oscillations in vacuum is the consequence of the facts that i) neutrinos have non-zero rest masses, ii) the corresponding mass eigenstates have slightly different eigenvalues and that iii) mixing between the neutrino flavors exists. Based on Refs. [11, 58], the theory of neutrino flavor oscillations in vacuum is shortly explained below. This is done by using a plane wave approximation[2] to describe the evolution of the massive neutrino states.

Using the formalism of local quantum field theory, which underlies the SM of particle physics, a chiral LH neutrino flavor eigenstate $|\nu_\ell\rangle$ can be described as a coherent superposition of chiral LH neutrino mass eigenstates $|\nu_j\rangle$ with energy eigenvalues E_j:

$$|\nu_\ell\rangle = \sum_j U^*_{\ell j} \, |\nu_j\rangle \,. \tag{1.1}$$

In the case of an antineutrino, $U^*_{\ell j}$ changes to $U_{\ell j}$. The *unitary mixing matrix* U must not be the unit matrix in order that neutrino oscillations can occur. In general, a unitary $n \times n$ matrix is fully characterized by $n_\theta = \frac{n(n-1)}{2}$ angles and $n_\phi = \frac{n(n+1)}{2}$ phases. Depending on the nature of the neutrino, being either a *Dirac* or a *Majorana* particle (see Section 1.3.1), the number of physically relevant phases reduces to

[2] A rigorous derivation would require the wave packet formalism or a field-theoretical approach that takes into account the production, propagation and detection of neutrinos.

$n_\phi^D = \frac{(n-1)(n-2)}{2}$ in the Dirac case and to $n_\phi^M = \frac{n(n-1)}{2}$ in the Majorana case. All of these phases can be responsible for *CP-violation in the lepton sector* (see also Section 1.1.3).
The probability $P(\ell \to \ell')$ at time T to observe the flavor eigenstate $|\nu_{\ell'}\rangle$ from the propagated initial eigenstate $|\nu(T)\rangle$, $|\nu(T=0)\rangle = |\nu_\ell\rangle$, is given by

$$P_{\ell\ell'} \equiv P(\ell \to \ell') = |\langle \nu_{\ell'} | \nu(T) \rangle|^2 = \left| \sum_j U_{\ell' j}\, D_j\, U_{\ell j}^* \right|^2 . \tag{1.2}$$

Based on relativistic quantum mechanics, the plane-wave propagation D_j of the neutrino state $|\nu_j\rangle$ with relativistic energy eigenvalue E_j is given by

$$D_j = e^{-i(E_j T - p_j L)} , \qquad p_j \equiv |\mathbf{p}_j| . \tag{1.3}$$

There it was used that $\mathbf{p}_j(\mathbf{x}_f - \mathbf{x}_0) = p_j \mathbf{k}(\mathbf{x}_f - \mathbf{x}_0) = p_j L$, where L is the distance from the neutrino creation point at $\mathbf{x}_0$ to the well-defined neutrino CC interaction point at $\mathbf{x}_f$. The three-vector $\mathbf{k}$ denotes the unit vector in momentum direction, $\mathbf{p}_j = p_j \mathbf{k}$. For the calculation of the oscillatory probability in Equation (1.2), the relevant part is the interference factor $D_j D_k^*$, which depends on the phase difference $\delta\varphi_{jk}$ [11]:

$$\begin{aligned} \delta\varphi_{jk} &= (E_j - E_k)T - (p_j - p_k)L \\ &= (E_j - E_k)\left[T - \frac{E_j + E_k}{p_j + p_k} L \right] + \frac{m_j^2 - m_k^2}{p_j + p_k} L . \end{aligned} \tag{1.4}$$

Using the *equal energy assumption*, $E_j = E_k = E$, the first term in Equation (1.4) with the unmeasurable time-dependence vanishes. With $p = (p_j + p_k)/2$ and in the *relativistic limit* $p = E$ the second term of the phase difference $\delta\varphi_{jk}$ becomes

$$\delta\varphi_{jk} \cong \frac{m_j^2 - m_k^2}{2p} L = \frac{\Delta m_{jk}^2}{2E} L , \quad \Delta m_{jk}^2 \equiv m_j^2 - m_k^2 . \tag{1.5}$$

Together with Equation (1.5), the flavor oscillation probability in Equation (1.2) for neutrinos (+) and antineutrinos (−) can be written as

$$\begin{aligned} P(\ell \to \ell') = \delta_{\ell,\ell'} &- 4 \sum_{j>k} \mathrm{Re}(U_{\ell j}^*\, U_{\ell' j}\, U_{\ell k}\, U_{\ell' k}^*) \sin^2\left(\frac{\Delta m_{jk}^2}{4E} L \right) \\ &\pm 2 \sum_{j>k} \mathrm{Im}(U_{\ell j}^*\, U_{\ell' j}\, U_{\ell k}\, U_{\ell' k}^*) \sin\left(\frac{\Delta m_{jk}^2}{2E} L \right) . \end{aligned} \tag{1.6}$$

One would obtain the same result if one makes other assumptions than the equal energy assumption to remove the time dependence from the phase difference in Equation (1.4) (see Ref. [11]). Moreover, the result coincides with the outcome of a wave packet treatment, which would not require such assumptions at all. The probability $P(\ell \to \ell)$ is usually called the *survival probability* of flavor $\ell = e, \mu, \tau$, whereas $P(\ell \to \ell')$, $\ell \neq \ell'$, is often named the *appearance probability* of flavor ℓ'. The *disappearance probability* of flavor ℓ follows as $1 - P(\ell \to \ell)$.

If only transitions between two neutrino flavors need to be considered, U can be written as a real 2×2 rotation matrix parameterized by one angle θ. In this case Equation (1.6) simplifies to

$$P(\ell \to \ell') = \sin^2(2\theta) \, \sin^2\left(\frac{\Delta m^2 L}{4E}\right) , \quad \ell \neq \ell' . \tag{1.7}$$

1.1.2 Oscillations in matter

It was first pointed out by *Lincoln Wolfenstein* [59] that the physics of neutrino flavor oscillation changes if it takes place in matter. Today, the corresponding effect is called the *Mikheyev–Smirnov–Wolfenstein* (MSW)[3] effect [60]. Its general impact is now shortly summarized based on Refs. [11, 58].

When neutrinos propagate through *normal matter*, they interact with the contained electrons, protons and neutrons. This yields an additional contribution H_{int} to the *effective Hamiltonian* $H_{\text{eff}} = H_0 + H_{\text{int}}$, whose eigenstates $|\nu_j^m\rangle$ with energies E_j^m in general differ from the eigenstates $|\nu_j\rangle$ of the free Hamiltonian H_0. It turns out that incoherent elastic and *quasi-elastic* (QEL) scattering processes have negligible impact in this case. However, *coherent elastic forward scattering* of neutrinos and antineutrinos is of importance: While the flavor-symmetric NC contributions cancel for all neutrino flavors, only ν_e's and $\overline{\nu}_e$'s can in addition scatter elastically from electrons through coupling to W^-. This difference can be translated into an effective potential $V = \pm\sqrt{2} G_F n_e(T)$ for ν_e's (+) and $\overline{\nu}_e$'s (−), where G_F is the *Fermi constant* and $n_e(T)$ is the matter's electron number density traversed by a neutrino (antineutrino) at time T. It is this term V that introduces matter effects to neutrino flavor oscillations.
In case the electron density is constant, $n_e(T) = n_e = \text{const.}$, the interaction Hamiltonian H_{int} becomes time-independent and allows easy diagonalization of H_{eff}. One finds that the flavor oscillation probability in matter $P^m(\ell \to \ell')$ has the same form as Equation (1.2) for the vacuum case:

$$P^m(\ell \to \ell') = \left| \sum_j U^m_{\ell' j} \, D^m_j \, U^{m*}_{\ell j} \right|^2 , \tag{1.8}$$

where $D^m_j = e^{-i(E^m_j T - p^m_j L)}$ is analogous to Equation (1.3). The matrix U^m connects the flavor eigenstates with the new mass eigenstates in matter $|\nu_j^m\rangle$ having energies E_j^m. In the two-flavor case, the effective quantity in matter θ^m is related to the vacuum quantity θ in the following way:

$$\sin(2\theta^m) = \frac{\sin(2\theta)}{\sqrt{\left(\cos(2\theta) - \frac{A}{\Delta m^2}\right)^2 + \sin^2(2\theta)}} , \tag{1.9}$$

with $A = 2\sqrt{2} G_F n_e p$. Using $p = E$ in the relativistic limit, the so-called *MSW resonance condition*

$$A = 2\sqrt{2} G_F n_e E = \Delta m^2 \cos(2\theta) \tag{1.10}$$

[3] Named after *Stanislav Mikheyev*, *Alexei Y. Smirnov* and *Lincoln Wolfenstein*.

maximizes $\sin(2\theta^m)$.
One example for the two-flavor MSW effect in variable electron number density, which is now briefly summarized based on Ref. [11], is the case of solar neutrinos (see Section 2.1): If the electron density in the Sun's core is much bigger than the *resonance density* n_e^{res} fulfilling Equation (1.10), a solar ν_e is almost certainly created with the heavier mass eigenstate $|\nu_2^m(t_0)\rangle$ at time t_0. On its way to the surface of the Sun, the ν_e traverses a layer of matter with $n_e = n_e^{\text{res}}$ at time t. At this point, the energy difference $E_2^m(t) - E_1^m(t)$ is minimal and the system can evolve in different ways. The first extreme option is that the neutrino continues to propagate in the state $|\nu_2^m(t)\rangle$ until it reaches the Sun's surface at time t_s. Since $n_e(t_s) = 0$, the neutrino system from there on propagates in the state $|\nu_2\rangle$. The probability to find the flavor ν_μ at the surface of the Sun follows as $\cos^2\theta$. This case is called *adiabatic transition* and is characterized by the fact that the probability of the transition $\nu_2^m(t_0) \to \nu_1^m(t_s)$, $P' \equiv P'(\nu_2^m(t_0) \to \nu_1^m(t_s))$, is essentially zero on the whole neutrino path. A condition for adiabatic flavor transitions is that $n_e(t)$ changes sufficiently slow along the neutrino trajectory. The second extreme option is that the system "jumps" from $E_2^m(t)$ to $E_1^m(t)$ in the resonance region, $P' \sim 1$, and continues to propagate in the state $|\nu_1^m(t)\rangle$. Since in that case the neutrino system reaches the Sun's surface as $|\nu_1^m(t_s)\rangle \equiv |\nu_1\rangle$, the probability to find the flavor ν_μ follows as $\sin^2\theta$. This case is called *extremely nonadiabatic*. In summary, solar $\nu_e \to \nu_\mu$ transitions are heavily affected by the jump probability P', which can have a value from 0 to $\cos^2\theta$. Experimental data for solar ^{8}B neutrinos indicate a survival probability of $\sim$30 %, the value found by experiments having studied the solar neutrino problem. This is in good agreement with expectations from three-flavor oscillations including matter effects. The fact that solar neutrinos run through the MSW resonance also fixes the sign of Δm_{21}^2, as one can infer from Equation (1.9) with $A > 0$ in the two-flavor case. Solar neutrinos with lower energy, like the *pp* neutrinos, do not run through the MSW resonance. Their flavor transitions can be described with good accuracy as vacuum oscillations. Therefore, the solar neutrino spectrum includes the *transition region* from *vacuum-dominated* oscillations (at lower energy) to *matter-dominated* oscillations (at higher energy).

The MSW effect changes flavor transition probabilities in matter by altering the flavor *mixing*. A second way to influence neutrino oscillations in matter is via the *oscillation phase*: The flavor transition probability can be enhanced if there are certain correlations between a matter density modulation along the neutrino's path and changes to the phase of the oscillation. This so-called *parametric resonance* is of interest for atmospheric neutrinos that see abrupt and strong changes of matter density as they traverse both the mantle and the core of Earth. Details on this topic, which is not further discussed here, can be found in Refs. [11, 61].

1.1.3 Current status and prospect

With three known neutrino flavors, mixing in the lepton sector is described by the unitary 3×3 *Pontecorvo–Maki–Nakagawa–Sakata* (PMNS)[4] matrix U_{PMNS} [54, 62]. The number of possible phases is one in the *Dirac* case or three if the neutrino

[4]Named after *Bruno Pontecorvo*, *Ziro Maki*, *Masami Nakagawa* and *Shoichi Sakata*.

is a *Majorana* particle (see also Section 1.3.1). A common parameterization [11] of the neutrino mixing matrix is to write U_{PMNS} as the product of three rotation matrices with three rotation angles, θ_{12}, θ_{13} and θ_{23}, and one CP-violating phase δ_{CP} associated with θ_{13}:

$$U_{\text{PMNS}} = \begin{pmatrix} 1 & 0 & 0 \\ 0 & c_{23} & s_{23} \\ 0 & -s_{23} & c_{23} \end{pmatrix} \begin{pmatrix} c_{13} & 0 & s_{13}\, e^{-i\delta_{\text{CP}}} \\ 0 & 1 & 0 \\ -s_{13}\, e^{i\delta_{\text{CP}}} & 0 & c_{13} \end{pmatrix} \begin{pmatrix} c_{12} & s_{12} & 0 \\ -s_{12} & c_{12} & 0 \\ 0 & 0 & 1 \end{pmatrix}, \quad (1.11)$$

with the denotations $s_{ij} \equiv \sin\theta_{ij}$ and $c_{ij} \equiv \cos\theta_{ij}$. A fourth matrix with the additional two unknown phases in the *Majorana* case, $V = \text{diag}(1, e^{i\alpha_1/2}, e^{i\alpha_2/2})$, would be multiplied from the right. These phases do not affect neutrino oscillation physics. However, they are important for the $0\nu\beta\beta$ *decay* [11]. In addition to the PMNS matrix, the oscillation of three neutrino flavors is also described in terms of two independent mass-squared differences, commonly chosen as Δm^2_{21} together with Δm^2_{32} or Δm^2_{31}.

The parameters θ_{12} and Δm^2_{21} can be determined by investigating the disappearance of ν_e's from the Sun or of $\overline{\nu}_e$'s from nuclear reactors (see Section 2.4). Significant contributions to the measurement of these parameters were made by SNO, SK and most notably KamLAND [29]. Precision measurements with JUNO will provide more accurate values in the future (see Section 4.3.2). Similarly, experiments searching for the oscillatory disappearance of atmospheric or accelerator-based ν_μ's and $\overline{\nu}_\mu$'s at baseline lengths of some hundreds to thousands of kilometers allow to quantify the parameters θ_{23} and Δm^2_{32} (or Δm^2_{31}). Prominent examples from this category are the atmospheric neutrino studies of SK and the experiments *Tokai-to-Kamioka* (T2K) [63] and *Main Injector Neutrino Oscillation Search* (MINOS) [64] using neutrino beams. Around 2011/2012, the LSc-based experiments Double Chooz [34], Daya Bay [35] and RENO [36], which explore reactor $\overline{\nu}_e$ disappearance at 1–3 km baseline length, measured a non-zero value for the last mixing angle θ_{13}. This was in agreement with results from the LBNO experiments T2K and MINOS, which searched for ν_e appearance in a ν_μ beam. The appearance of ν_τ in a multi-GeV ν_μ beam was discovered by OPERA [24]; the project recently reported its fifth ν_τ CC event [25]. A review of the findings of the above-mentioned and other experiments dealing with oscillation parameter measurements can be found in Ref. [11].

In addition to the unknown absolute neutrino masses (see Section 1.3.2), one outstanding issue is the unknown ordering of the neutrino masses $m_j > 0$ [26]. Current results for the mass-squared difference including the third neutrino mass state only comprise $|\Delta m^2_{32}|$ (or $|\Delta m^2_{31}|$), but not the sign of the quantity: As depicted in Figure 1.1, a NO is realized if $m_1 < m_2 < m_3$ (Δm^2_{32}, $\Delta m^2_{31} > 0$). The IO is defined by $m_3 < m_1 < m_2$ (Δm^2_{32}, $\Delta m^2_{31} < 0$). Taking into account the lack of knowledge about the neutrino MO, an analysis of combined experimental data reported in Ref. [65], i.e., a *global analysis*, yielded the best-fit parameters and uncertainties summarized in Table 1.2. Similar results can be found in Refs. [11, 66]. Due to the chosen parameterization of U_{PMNS}, the smallness of θ_{13} and the primary source of information, θ_{12} and Δm^2_{21} are commonly referred to as *solar parameters* θ_{sol} and Δm^2_{sol}. Similarly, θ_{23} and Δm^2_{32} (or Δm^2_{31}) are often named *atmospheric parameters* θ_{atm} and Δm^2_{atm} [11].

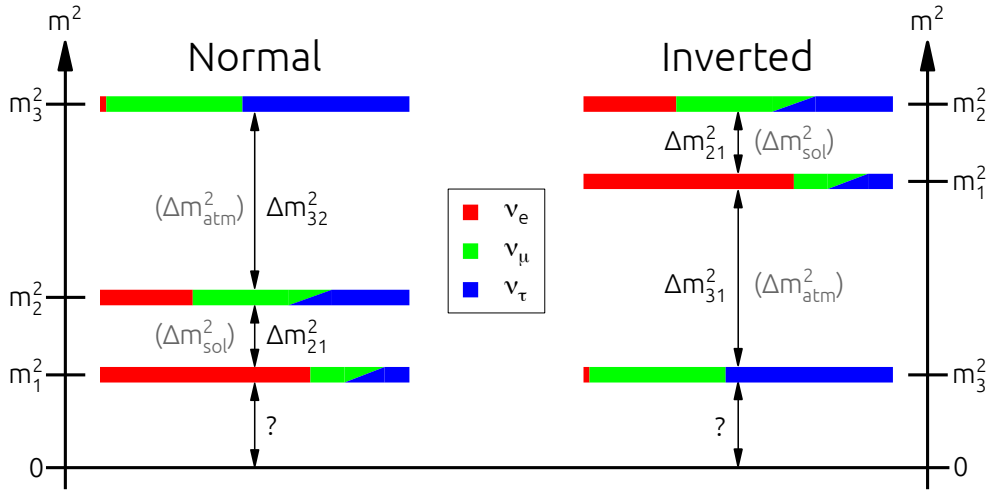

Figure 1.1 – Possible MOs for three neutrino states with masses m_1, m_2 and m_3: NO (*left*) and IO (*right*). The horizontal width of a colored bar part relative to the total bar width indicates the proportional admixture of the respective flavor to the given mass state. Each flavor content was calculated with the best-fit NO mixing angles from Table 1.2. Imprecise ν_μ and ν_τ bar widths for the mass states with m_1 and m_2 reflect the uncertainties from the fully unknown phase δ_{CP}. Notice the different definitions of $\Delta m^2_{\mathrm{atm}}$. The absolute neutrino masses are not yet known.

Table 1.2 – Best-fit parameters (bfp) with 1σ uncertainties and allowed ranges at 3σ CL from the global analysis reported in Ref. [65]. Depending on the assumed neutrino MO, $\Delta m^2_{3x} \equiv \Delta m^2_{31} > 0$ (NO; left column) or $\Delta m^2_{3x} \equiv \Delta m^2_{32} < 0$ (IO; right column).

	Normal Ordering		Inverted Ordering	
	bfp$\pm1\sigma$	3σ range	bfp$\pm1\sigma$	3σ range
$\theta_{12}/^\circ$	$33.48^{+0.78}_{-0.75}$	$31.29 \to 35.91$	$33.48^{+0.78}_{-0.74}$	$31.29 \to 35.91$
$\theta_{13}/^\circ$	$8.50^{+0.20}_{-0.21}$	$7.85 \to 9.10$	$8.51^{+0.20}_{-0.21}$	$7.87 \to 9.11$
$\theta_{23}/^\circ$	$42.3^{+3.0}_{-1.6}$	$38.2 \to 53.3$	$49.5^{+1.5}_{-2.2}$	$38.6 \to 53.3$
$\delta_{\mathrm{CP}}/^\circ$	306^{+39}_{-70}	$0 \to 360$	254^{+63}_{-62}	$0 \to 360$
$\frac{\Delta m^2_{21}}{10^{-5}\,\mathrm{eV}^2}$	$7.50^{+0.19}_{-0.17}$	$7.02 \to 8.09$	$7.50^{+0.19}_{-0.17}$	$7.02 \to 8.09$
$\frac{\Delta m^2_{3x}}{10^{-3}\,\mathrm{eV}^2}$	$+2.457^{+0.047}_{-0.047}$	$+2.317 \to +2.607$	$-2.449^{+0.048}_{-0.047}$	$-2.590 \to -2.307$

Comprehensive probing of the three flavor neutrino oscillation framework and the precise ascertainment of its parameter values are among the top priority tasks of neutrino physics for the forthcoming years. This especially includes i) identifying the θ_{23} octant[5], ii) determining the neutrino MO and iii) searching for *leptonic CP-violation* [28] through a measurement of δ_{CP}. Violation of the symmetry from *charge conjugation* C and *parity transformation* P is observable in neutrino oscillations if

[5] If θ_{23} is different from $\pi/4$, it can be $< \pi/4$ (first octant) or $> \pi/4$ (second octant) based on current precision and unknown neutrino MO. This problem is also known as θ_{23} *octant degeneracy*.

$P(\nu_\ell \to \nu_{\ell'}) \neq P(\overline{\nu}_\ell \to \overline{\nu}_{\ell'})$ with $\ell, \ell' = e, \mu, \tau$.
With increasing precision on θ_{13} from the running reactor neutrino experiments, the ν_μ disappearance studies with the LBNO beam experiments T2K and *NuMI Off-axis* ν_e *Appearance* (NOνA) [67] will improve the precision on θ_{23}. Depending on the true value of θ_{23}, a combined analysis of the T2K and NOνA data with included information from the ν_e appearance channel can resolve the θ_{23} octant degeneracy with $\sim 2\sigma$ significance for almost all combinations of MO and δ_{CP} [68]. However, the experiments can only provide limited evidence regarding the true neutrino MO and CP violation (see Refs. [69–71]). Multiple projects, which partially base on different detector technologies (*liquid argon* (LAr) *time projection chamber* (TPC), Cherenkov effect in water or ice, LSc), are proposed [41, 42, 72–79] to deal with these issues via detailed investigations of flavor oscillations of neutrinos from different sources (accelerator, atmosphere, reactor). First experimental hints on the neutrino MO are expectable in the course of the next decade (see Ref. [69]). Among the competitors in the quest to determine the neutrino MO is the medium-baseline reactor $\overline{\nu}_e$ oscillation project JUNO, which is shortly outlined in Section 4.3. The possibility to determine the neutrino MO with an LBNO beam experiment involving LENA is presented in Chapter 8. Beyond the three neutrino flavor model, there is also a direct search for additional *sterile neutrino states* with future oscillation experiments (see Section 1.3.3).

1.2 Neutrino interactions

Besides gravitation, which will be neglected in the following, the three neutrinos and three antineutrinos of the SM are subject only to the weak force through the flavor eigenstates ν_ℓ and $\overline{\nu}_\ell$ with $\ell = e, \mu, \tau$. Therefore, a neutrino interaction is either of CC or NC type. Due to the nature of the weak force, the probability of a neutrino to interact with matter is very small. For example, neutrino cross-sections are $\sim 10^{-40}$–$10^{-44}\,\mathrm{cm}^{-2}$ at an energy of $E_\nu \sim 10\,\mathrm{MeV}$ (e.g., see Ref. [80]), depending on the neutrino flavor, the interaction process and the interaction target.
Given an energy- and time-dependent flux $\phi_{kl}(E_\nu, t, R, \boldsymbol{\theta})$ of neutrino type k at the detector with distance R from source l, which is oscillated with the parameter set $\boldsymbol{\theta} = \{\theta_{12}, \theta_{13}, \theta_{23}, \delta_{\mathrm{CP}}, \Delta m^2_{\mathrm{sol}}, \Delta m^2_{\mathrm{atm}}\}$, the differential event rate for interaction process m can be predicted with

$$\frac{\mathrm{d}^2 N_{klm}}{\mathrm{d}E_\nu\,\mathrm{d}t} = \phi_{kl}(E_\nu, t, R, \boldsymbol{\theta})\,\sigma_{km}(E_\nu)\,N_{T,km}\,. \tag{1.12}$$

$\sigma_{km}(E_\nu)$ names the energy-dependent cross-section for neutrino type k and process m. The number of available interaction targets for this neutrino type and interaction process is denoted by $N_{T,km}$. A prediction for the total number of neutrino interactions in the detector follows from Equation (1.12) by integrating over E_ν and the time t for the six neutrinos and antineutrinos (k), all relevant neutrino sources (l) and all interaction processes (m).
Different types of natural and man-made neutrino sources with their characteristic fluxes $\phi_{kl}(E_\nu, t)$ will be discussed in Chapter 2. The number of available targets depends on the mass of the employed neutrino detection device and its material composition. For example, in a LSc-based neutrino detector (see Chapter 4), the

designated target mass mainly contains electrons as well as hydrogen and carbon nuclei.

Based on Refs. [11, 81] and from an experimental perspective, this section deals with neutrino interactions, the physics defining $\sigma_{km}(E_\nu)$. Theoretical background information on this subject can be found in the review in Ref. [81]. Section 1.2.1 focuses on the *LE domain*, which is arbitrarily defined to be $E_\nu \leq 100\,\text{MeV}$. This is the main area of operations of LSc neutrino detectors. Interactions from the *HE domain* with $E_\nu > 100\,\text{MeV}$ are treated in Section 1.2.2. They are relevant for the LBNO beam experiment with GeV neutrinos described in Chapter 8. In the following, a neutrino interaction is considered to be in the laboratory frame of reference where the target particle is essentially at rest.

1.2.1 Low-energy domain

Relevant neutrino interactions with $E_\nu \leq 100\,\text{MeV}$ are *elastic scattering on electron or proton*, the *inverse beta decay* (IBD) and *neutrino–nucleus interactions*.

Elastic neutrino scattering on electron or proton The elastic scattering of ν_ℓ or $\overline{\nu}_\ell$ on an electron,

$$\nu_\ell + e^- \to \nu_\ell + e^- \qquad \text{or} \qquad \overline{\nu}_\ell + e^- \to \overline{\nu}_\ell + e^-\,, \tag{1.13}$$

can occur for all flavors $\ell = e$, μ, τ via a NC interaction. Both ν_e and $\overline{\nu}_e$ have an additional CC channel. In the case of ν_e, this CC channel is a form of *(quasi-)elastic neutrino–lepton scattering*,

$$\nu_\ell + e^- \to \ell^- + \nu_e\,. \tag{1.14}$$

This interaction cannot occur for ν_μ and ν_τ in the LE domain because E_ν is too small to produce the corresponding charged lepton partners. Both ν_ℓ and $\overline{\nu}_\ell$ can also scatter elastically off a proton [82]:

$$\nu_\ell + p \to \nu_\ell + p \qquad \text{or} \qquad \overline{\nu}_\ell + p \to \overline{\nu}_\ell + p\,. \tag{1.15}$$

Cross-sections for all these processes are summarized in Table 1.3.

Inverse beta decay The IBD reaction is

$$\overline{\nu}_e + p \to e^+ + n\,. \tag{1.16}$$

It requires $E_\nu \geq 1.806\,\text{MeV}$. The reaction's cross-section can be approximated by $\sigma_{\text{IBD}}(E_\nu) = 9.61 \times 10^{-44}\,(E_\nu - 1.29\,\text{MeV})\,\sqrt{(E_\nu - 1.29\,\text{MeV})^2 - 0.26\,\text{MeV}^2}\,\text{cm}^2\,\text{MeV}^{-2}$ [84, 85]. In LSc-based detectors, the IBD reaction is efficiently tagged via a technique described in Section 4.1.1.

Table 1.3 – Energy-dependent cross-sections for elastic neutrino scattering on electron (reaction (1.13)) and proton (reaction (1.15)). The energy E_ν is in MeV. The index x stands for e, μ, τ, whereas y only refers to μ, τ. Data extracted from Refs. [82, 83].

Reaction	Current	Cross-section $[10^{-44}\,\mathrm{cm}^2]$
$\nu_e + e^- \to \nu_e + e^-$	CC + NC	$0.95\,E_\nu$
$\overline{\nu}_e + e^- \to \overline{\nu}_e + e^-$	CC + NC	$0.42\,E_\nu$
$\nu_y + e^- \to \nu_y + e^-$	NC	$0.16\,E_\nu$
$\overline{\nu}_y + e^- \to \overline{\nu}_y + e^-$	NC	$0.13\,E_\nu$
$\nu_x + p \to \nu_x + p$	NC	$2.03\,E_\nu^2$
$\overline{\nu}_x + p \to \overline{\nu}_x + p$	NC	$2.03\,E_\nu^2$

Neutrino–nucleus interaction *Neutrino capture* is the inelastic CC interaction between ν_e or $\overline{\nu}_e$ and a nucleus: The nucleus A with Z protons and N neutrons is transformed according to

$$\nu_e + A_N^Z \to e^- + A_{N-1}^{Z+1} \qquad \text{or} \qquad \overline{\nu}_e + A_N^Z \to e^+ + A_{N+1}^{Z-1}\,. \tag{1.17}$$

If the emerging nucleus decays shortly after creation with a characteristic energy release, the decay signature in combination with the prompt signal from the emitted e^- / e^+ can be used to tag the neutrino interaction.
Incoherent (inelastic) NC neutrino–nucleus scattering,

$$\nu_\ell + A_N^Z \to \nu_\ell + A_N^{Z*} \qquad \text{or} \qquad \overline{\nu}_\ell + A_N^Z \to \overline{\nu}_\ell + A_N^{Z*}\,, \tag{1.18}$$

leaves behind the nucleus in an excited state A^*. If the nuclear disexcitation occurs via a characteristic, easily detectable particle emission, the original neutrino interaction can in principle be tagged. This is different to the case of *coherent (elastic) NC neutrino–nucleus scattering*,

$$\nu_\ell + A_N^Z \to \nu_\ell + A_N^Z \qquad \text{or} \qquad \overline{\nu}_\ell + A_N^Z \to \overline{\nu}_\ell + A_N^Z\,, \tag{1.19}$$

where the (anti-)neutrino of flavor $\ell = e$, μ, τ scatters from the nucleus as a whole and only leaves the low-energetic nuclear recoil for detection. Due to the hard experimental challenges to detect this recoil, this process has not yet been observed. Examples for neutrino capture and inelastic scattering on carbon are described in Appendix A.

1.2.2 High-energy domain

In the HE domain with $E_\nu > 100\,\mathrm{MeV}$, the probability rises that a neutrino or antineutrino transfers momentum to the smaller constituents of matter, i.e., the nucleon of a nucleus or a quark in a nucleon. Without claim to completeness, the following list includes interactions of a HE neutrino ν_ℓ or antineutrino $\overline{\nu}_\ell$, $\ell = e$, μ, τ, with a nucleon N or an entire nucleus A. Together with the sub-dominant (quasi-)elastic neutrino–lepton scattering in (1.14) they are of interest in research with HE neutrinos

from the atmosphere (see Section 2.5) or accelerators (see Section 2.6).

(Quasi-)Elastic scattering:	$\nu_\ell\,(\overline{\nu}_\ell) + N \to \ell^-\,(\ell^+) + N'\,,\ N \neq N'$	(CC)
	$\nu_\ell\,(\overline{\nu}_\ell) + N \to \nu_\ell\,(\overline{\nu}_\ell) + N$	(NC)
Resonant single pion production:	$\nu_\ell\,(\overline{\nu}_\ell) + N \to \ell^-\,(\ell^+) + N + \pi^+(\pi^-)$	(CC)
	$\nu_\ell\,(\overline{\nu}_\ell) + N \to \ell^-\,(\ell^+) + N' + \pi^0\,,\ N \neq N'$	(CC)
	$\nu_\ell\,(\overline{\nu}_\ell) + N \to \nu_\ell\,(\overline{\nu}_\ell) + N + \pi^0$	(NC)
	$\nu_\ell\,(\overline{\nu}_\ell) + N \to \nu_\ell\,(\overline{\nu}_\ell) + N' + \pi^\pm\,,\ N' \neq N$	(NC)
Coherent single pion production:	$\nu_\ell\,(\overline{\nu}_\ell) + A \to \ell^-\,(\ell^+) + A + \pi^+(\pi^-)$	(CC)
	$\nu_\ell\,(\overline{\nu}_\ell) + A \to \nu_\ell\,(\overline{\nu}_\ell) + A + \pi^0$	(NC)
Deep-inelastic scattering:	$\nu_\ell\,(\overline{\nu}_\ell) + N \to \ell^-\,(\ell^+) + \text{hadrons}$	(CC)
	$\nu_\ell\,(\overline{\nu}_\ell) + N \to \nu_\ell\,(\overline{\nu}_\ell) + \text{hadrons}$	(NC)

Particles in parentheses substitute the preceding particle in the corresponding antineutrino interaction. A comparison between existing measurements and predictions for the ν_μ and $\overline{\nu}_\mu$ CC cross-sections is shown in Figure 1.2 for an *isoscalar*[6] target. As one can see, the $\overline{\nu}_\mu$ cross-section is roughly one half of the ν_μ cross-section. This results from the chiral structure of the weak interaction and the inner structure of the matter (not antimatter) target on quark-level. NC cross-sections (not shown) are roughly $^1/_2$ to $^1/_3$ of the CC cross-sections.
Some of the above processes have a threshold on E_ν. For example, in a QEL CC interaction E_ν must be sufficient to produce the charged lepton complement $\ell^\mp$ of ν_ℓ ($\overline{\nu}_\ell$), especially $\mu^\mp$ ($m_\mu = 105.6\,\text{MeV}$ [11]) and $\tau^\mp$ ($m_\tau = 1776.8\,\text{MeV}$ [11]). In addition, for resonant pion production E_ν must enable the creation of an intermediate resonance state for the struck nucleon, e.g., the baryonic resonance $\Delta(1232)$ ($m_{\Delta(1232)} \sim 1232\,\text{MeV}$ [11]).

Precise knowledge of the neutrino cross-section normalizations and shapes for the individual interaction processes is important to minimize systematic uncertainties on predicted signal and background event distributions in neutrino flavor oscillation searches. A particular source of considerable incertitude comes from the fact that the above mentioned processes not only occur on free nucleons but also inside nuclear targets. *Intranuclear scattering* of the outgoing particles, especially of nucleons and mesons, changes the final state observable from outside of the nucleus, i.e., total energies, angular distributions and hadronic multiplicities. Neglecting such nuclear effects potentially biases the reconstruction of neutrino properties and can finally lead to false inference on oscillation parameters. For example, a resonant CC event where the outgoing pion is absorbed in the nucleus probability becomes misidentified as a QEL CC event with lower neutrino energy.

[6] An isoscalar nucleus has the same number of protons and neutrons.

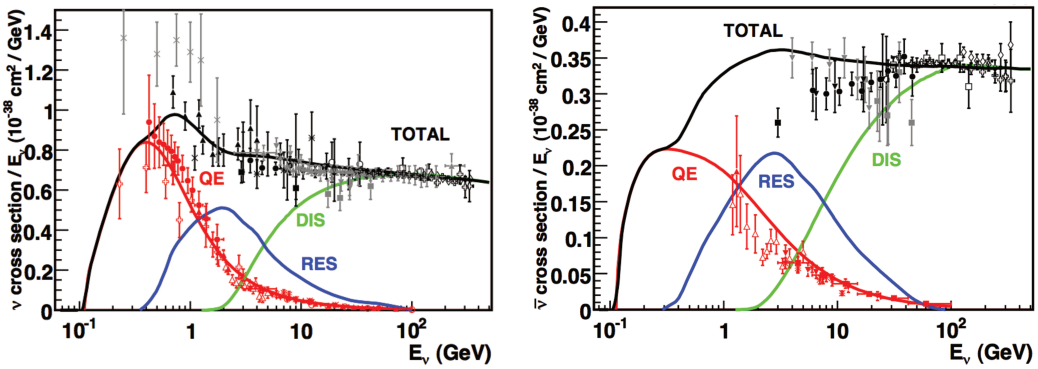

Figure 1.2 – Measurements [81] and predictions [86] for the per nucleon ν_μ **(left)** and $\overline{\nu}_\mu$ **(right)** CC cross-sections (isoscalar target) divided by neutrino energy E_ν as a function of E_ν. The different processes contributing to the total cross-section (*black*) are quasi-elastic scattering (QE; *red*), resonance production (RES; *blue*) and deep-inelastic scattering (DIS; *green*). In the intermediate energy range, the uncertainties in the cross-sections reflected by the error bars are typically 10–40 %, depending on the channel. Figures from Ref. [87].

In order to cancel systematic effects from neutrino flux and cross-section uncertainties, oscillation experiments can measure the (almost unoscillated) event rates close to the source with a *near-detector* and may use it as reference for the measurements at the *far-detector* site. However, due to the flavor oscillations, the neutrino flux composition at the far site is different with respect to the near site. Since this is also true for the probabilities of some interaction processes, precise cross-section information is still needed to accurately predict signal and background event populations at the far site. One intuitive example is the appearance of ν_τ's ($\overline{\nu}_\tau$'s) in the original ν_μ ($\overline{\nu}_\mu$) beam along the way to the far-detector of an LBNO experiment. Their CC interactions are background to the $\nu_\mu \to \nu_e$ oscillation search (see also Section 8.2.1). Since usually no ν_τ or $\overline{\nu}_\tau$ CC interactions are detected in the near-detector, the systematic uncertainties on the corresponding far-detector event rates are in the end again dominated by the precision of model predictions based on sparse experimental data. However, the physics case of the proposed SHiP experiment [12] amongst other things includes the separate measurements of these interaction vertices. With a total of 723–1151 ν_τ and $\overline{\nu}_\tau$ CC events, the expected statistics would by far exceed the current world data of 12.5 events[7]. This also includes that SHiP would be the first to unambiguously observe interactions of $\overline{\nu}_\tau$.

With the imminent entrance into an era of precision measurements of neutrino flavor oscillation parameters, the interest in supportive neutrino cross-section evaluations with dedicated scattering experiments grows. This is especially true with a view on maximizing the sensitivity of (proposed) oscillation experiments to determine the CP-violating phase δ_{CP} with GeV neutrinos from accelerators [63, 67, 72–75].
The *Main Injector Experiment for ν-A* (MINERνA) [89] at *Fermi National Accelerator Laboratory* (FNAL) is dedicated to the study of GeV ν_μ, $\overline{\nu}_\mu$, ν_e and $\overline{\nu}_e$ interactions on a variety of nuclei (H, He, C, O, Fe, Pb) in the *Neutrinos at the*

[7] The OPERA experiment detected 5 ν_τ interactions [25]. DONUT found 7.5 $\nu_\tau + \overline{\nu}_\tau$ events after background subtraction [88], but the actual types, ν_τ or $\overline{\nu}_\tau$, could not be identified.

Main Injector (NuMI) beam. First results of MINERνA [90–93] clearly demand for the consideration of *final state interactions* (intranuclear scattering) in an extended nuclear environment. Moreover, the data show tensions with current neutrino interaction models underlying state-of-the-art *Monte Carlo* (MC) *neutrino event generators* like `GENIE` [94, 95] (for a review on MC neutrino event generators see Ref. [11]). For flavor oscillation studies, the latter represent the essential bridge from neutrino interaction theory to the interpretation and prediction of today's and future experimental outcomes. The new insights into neutrino interactions from experiments like MINERνA will eventually stimulate progress in neutrino and nuclear theory and finally improve existing MC event generator frameworks.

1.3 Open Questions

In the following, some information is given regarding open questions on other important topics of neutrino physics aside from flavor oscillations. This includes the question if the neutrino is its own antiparticle in Section 1.3.1, the issue with the not yet known neutrino mass in Section 1.3.2 and the unsettled discussion about unitarity of the current 3×3 neutrino mixing matrix in Section 1.3.3.

1.3.1 Dirac or Majorana particle

Contrary to the charged leptons of the SM of particle physics, which are always *Dirac fermions*, a neutrino could alternatively be a *Majorana fermion*. In the latter case, the neutral lepton would be its own antiparticle. One way to probe the nature of the neutrino is the search for the $0\nu\beta\beta$ *decay* [11]: Due to the prerequisites for this process, which violates lepton number conservation, its observation would reveal the neutrino as Majorana particle. Assuming the exchange of a light Majorana neutrino is the cause to $0\nu\beta\beta$ decay, one key parameter for its rate is the *effective Majorana ν_e mass* $m_{ee} \equiv \left|\sum_i U_{ei}^2\, m(\nu_i)\right|$ [96, 97], where U is the neutrino mixing matrix including the Majorana phases (see Section 1.1.3). As shown in Figure 1.3 for the mentioned assumption, plotting allowed values of m_{ee} as a function of the lightest neutrino mass m_{lightest} results for $m_{\text{lightest}} \lesssim 0.01\,\text{eV}$ in two completely separated regions depending on the neutrino MO: For IO, the 3σ allowed band is roughly $0.01\,\text{eV} < m_{ee} < 0.05\,\text{eV}$, taking into account uncertainties on the neutrino oscillation parameters. If the NO is realized, values for m_{ee} from about 0.01 eV down to zero (not shown) are allowed.

Several experiments have been looking for the $0\nu\beta\beta$ decay with different candidate isotopes and detector technologies (see review in Ref. [96]). Apart from a claimed signal for ^{76}Ge [98, 99], which has recently been challenged by the *Germanium Detector Array* (GERDA) experiment [100], all projects could only set lower limits for the $0\nu\beta\beta$ half-life of their respective isotopes and upper limits for m_{ee}. Current lower sensitivity bounds achievable for the latter are well above 0.1 eV and estimates for the m_{ee} sensitivity of planned experiments are above 0.05 eV [97]. Therefore, an external determination of the neutrino MO defines sensitivity goals for future $0\nu\beta\beta$ projects and certainly impacts their strategy to reach them. Additionally, more precise values for the solar oscillation parameters would help to reduce uncertainty on

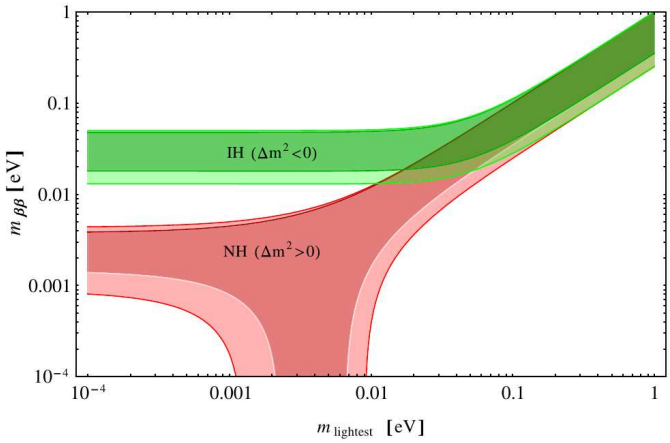

Figure 1.3 – Predictions on the effective Majorana ν_e mass m_{ee} as a function of the lightest neutrino mass m_{lightest}. It is assumed that the exchange of a light Majorana neutrino is the cause to $0\nu\beta\beta$ decay. The colored bands illustrate the predictions in case the NO (*red*) or the IO (*green*) is realized in Nature. Uncertainties on the oscillation parameters are taken into account, resulting in the shaded 3σ regions. Reprinted figure with permission from Ref. [97]. Copyright 2016 by the *American Physical Society*.

the sensitivity requirements, i.e., decrease the sizes of the above-mentioned regions. It has to be taken into account, however, that the situation changes if one considers models for $0\nu\beta\beta$ decay that are different from the exchange of a single light Majorana neutrino.

1.3.2 Neutrino mass

Besides the unknown neutrino MO, a definite value for the lightest neutrino mass has not yet been determined. From cosmological[8] observations, a somewhat model and analysis-dependent result for the *sum of neutrino masses* is $\sum_i m(\nu_i) < 0.23\,\text{eV}$ at 95 % CL from the *Planck* space observatory [27]. A combination of *Planck* data and information from the flux power spectrum of the *Lyman-α* forest in quasar absorption spectra gives an even tighter limit of $\sum_i m(\nu_i) < 0.12\,\text{eV}$ at 95 % CL [101].
Experiments searching for $0\nu\beta\beta$ decay are sensitive to the *effective Majorana* ν_e *mass* m_{ee} (see Section 1.3.1), but their precision on m_{ee} is currently limited due to systematic uncertainties, e.g., from nuclear physics.
In the *Mainz* [102] and *Troitsk* [103] experiments, the end point of the electron energy spectrum from β^- decays of tritium was precisely measured. Upper limits $m(\nu_e) < 2.3\,\text{eV}$ and $< 2.1\,\text{eV}$ at 95 % CL were obtained for the *average* ν_e *mass* $m(\nu_e) \equiv \sqrt{\sum_i |U_{ei}|^2\, m(\nu_i)^2}$, respectively. The forthcoming *Karlsruhe Tritium Neutrino Experiment* (KATRIN) [104] aims to be sensitive to $m(\nu_e) \sim 0.2\,\text{eV}$ at 90 % CL with the same technique.

[8] Neutrino masses for example play a role in large-scale structure formation, e.g., of galaxy clusters.

1.3.3 Sterile neutrinos / unitarity of PMNS matrix

As reviewed in Ref. [105], anomalous results from ν_μ / $\overline{\nu}_\mu$ disappearance and ν_e / $\overline{\nu}_e$ appearance searches with accelerator-based short-baseline neutrino oscillation experiments are currently in tension with the three neutrino mixing model: The experiments observed oscillations with $\Delta m^2 \sim 1\,\mathrm{eV}^2$ that could be accounted for by assuming the existence of additional *sterile neutrino states*, which do not couple to $W^\pm$ and Z^0 bosons.
A second evidence for the possible existence of sterile neutrinos comes from calibration measurements of the *Soviet–American Gallium Experiment* (SAGE) and the *Gallium Experiment* (GALLEX) (see Refs. [11, 106] and references therein), which originally measured solar neutrinos. Both experiments used intense ^{51}Cr and/or ^{37}Ar sources to calibrate the gallium-based detectors. They found a deficit in the measured fluxes compared to the expectations, which is now named *Gallium Anomaly* and has a statistical significance of about 3σ [106].
Lastly, a recent re-evaluation of the $\overline{\nu}_e$ reference spectra for nuclear reactors [107,108] yielded a $\simeq 3\,\%$ increase in the total flux prediction compared to results from former measurements (see also review in Ref. [85]). As a consequence, the mean ratio of observed to predicted events decreased for earlier reactor neutrino experiments with distances $\leq 100\,\mathrm{m}$ to the core. This effect with 2.9σ significance got the name *Reactor Antineutrino Anomaly* [85, 109] and further fired the controversy about neutrino oscillations into sterile states. Nowadays, multiple experiments are in preparation to explore the outstanding anomalies and to challenge the assumed unitarity of the 3×3 U_{PMNS} mixing matrix. For example, the *Short distance neutrino oscillations with* Borexino (SOX) project [110] wants to use radioactive sources to probe neutrino oscillations with $\Delta m^2 \sim 1\,\mathrm{eV}^2$ at short distances. Moreover, JUNO will precisely measure the solar mixing parameters and thus helps to test the three neutrino oscillation paradigm at the percent level (see Section 4.3.2).

Chapter 2

Neutrino Sources

After the postulation of the neutrino by *W. Pauli* in 1930 and the stepwise discovery of its different flavors since 1956 [6], the light neutral lepton got into the focus of intense research. The characterization of the neutrino's properties as an elementary particle and the creation of a comprehensive description of its exhibited flavor mixing behavior (see Chapter 1) is an ongoing endeavor. Both issues need the application of well-understood and powerful neutrino sources to obtain significant results from dedicated measurements in a reasonable amount of time. Probing neutrino physics at different energy scales is essential to establish a strong theoretical framework and thus requires access to a wide spectrum of sources in terms of neutrino energy. Fluxes from natural neutrino sources already satisfy this requirement: A large flux of cosmic relic neutrinos, which covers the lowest energy range from µeV to meV, is predicted by cosmological models but has not yet been measured [111]. Successful neutrino detections range from some keV with solar neutrinos, e.g., in Borexino, up to PeV observed in the neutrino telescope IceCube [112, 113]. Contrary to natural sources, artificial neutrino and antineutrino sources, like nuclear reactors or accelerators, are controllable and very localized. Although such sources may still include some systematic uncertainties on the total flux, its composition or the energy spectrum, they are nevertheless very helpful for detailed and systematic investigations of neutrino flavor oscillations.
Besides the use of natural neutrino sources to learn about neutrino (mixing) properties, a detailed study of their emitted neutrino energy spectra and flavors enables a deeper understanding of the sources' physical states and evolutions. Since a neutrino easily permeates large amounts of matter essentially unhindered as a result of its weak interaction, it can provide unique and complimentary information from deep inside neutrino emitting phenomena. This is especially important when information from the commonly used electromagnetic spectrum is insufficient or not available for a deeper understanding of the physical processes. Prominent examples treated in this chapter are the Sun, Earth or a core-collapse SN. It is this messenger particle aspect of neutrinos that creates a growing interdisciplinarity in neutrino-based research projects and in consequence makes future neutrino observatories a matter of interest for science communities beyond fundamental particle physics.

In the following parts of this chapter, natural and man-made neutrino sources will be described that are particularly important for the LSc-based next-generation neutrino observatories LENA (Section 4.2) and JUNO (Section 4.3). Section 2.1 deals with neutrinos from the Sun and their contribution to make us understand the energy release in our home star. Astrophysical core-collapse SN neutrinos, either from a single instance in our galaxy or from the diffuse flux originating past stellar collapses, are subject of Section 2.2. Geo-neutrinos are products of natural radioactivity within Earth and are described in Section 2.3. Reactor antineutrinos as products of artificially induced nuclear fission processes are subject of Section 2.4. As mentioned in Section 1.1.3, nuclear reactors have already been used as antineutrino sources in LE oscillation experiments and will also be employed for measurements with JUNO. Section 2.5 is about neutrino and antineutrino production in the atmosphere. The created neutrinos are accompanied by cosmogenic muons, which can induce serious background to rare neutrino event searches with underground detectors (see Section 4.1.2). Finally, artificial generation of neutrinos and antineutrinos with particle accelerators is topic of Section 2.6. The focus is on the conventional neutrino beam concept, which underlies the LBNO experiment with LENA discussed in Chapter 8.

2.1 Sun

The Sun emits a total power of $\sim 3.846 \times 10^{26}\,\mathrm{W}$ [114] as electromagnetic radiation. On Earth, which has an average distance of $149.6 \times 10^{6}\,\mathrm{km}$ [114], this results in a mean energy flux of $\sim 1.3\,\mathrm{kW\,m^{-2}}$, a value commonly known as *solar constant*. The source of the emitted energy is a sequence of nuclear fusion processes taking place in the $\sim 1.6 \times 10^{2}\,\mathrm{g\,cm^{-3}}$ dense and $\sim 1.5 \times 10^{7}\,\mathrm{K}$ [114] hot center of the star, which effectively combines protons to helium nuclei. As a product of the nuclear transformations, ν_e's are created at several stages of the fusion process chain. Contrary to photons, which require at least 10^5 years [115] to diffuse out of the Sun, the rarely interacting neutrinos leave the star immediately. They produce a permanent flux of $\sim 6.5 \times 10^{10}\,\mathrm{cm^{-2}\,s^{-1}}$ [83] at Earth and make the Sun the closest extraterrestrial neutrino source. Solar neutrinos are subject to the MSW effect and played an important role in the confirmation of neurino flavor oscillations and the determination of underlying parameters (see Section 1.1.2 and Section 1.1.3).

The main sequence of fusion reactions forms the so-called *pp* chain, which is depicted with its *branching ratios* (BRs) in Figure 2.1a. It accounts for $\simeq 98.5\,\%$ of the solar energy release and is named after the chain's initial step fusing two protons to a deuteron [83, 116, 118]. The net overall reaction in terms of energy is

$$2e^- + 4p \rightarrow {}^4\mathrm{He} + 2\nu_e + 26.7\,\mathrm{MeV}\,. \tag{2.1}$$

Two ν_e's are created along any path of the chain. Several experiments together have measured the neutrino fluxes from all the different stages of the *pp* chain. Most recently, the Borexino experiment—dedicated to solar neutrino spectroscopy—measured the flux of *pp* neutrinos from the dominant initial reaction of the *pp* chain to be $(6.6 \pm 0.7) \times 10^{10}\,\mathrm{cm^{-2}\,s^{-1}}$ [31]. That is in agreement with current predictions (see Table 2.1).

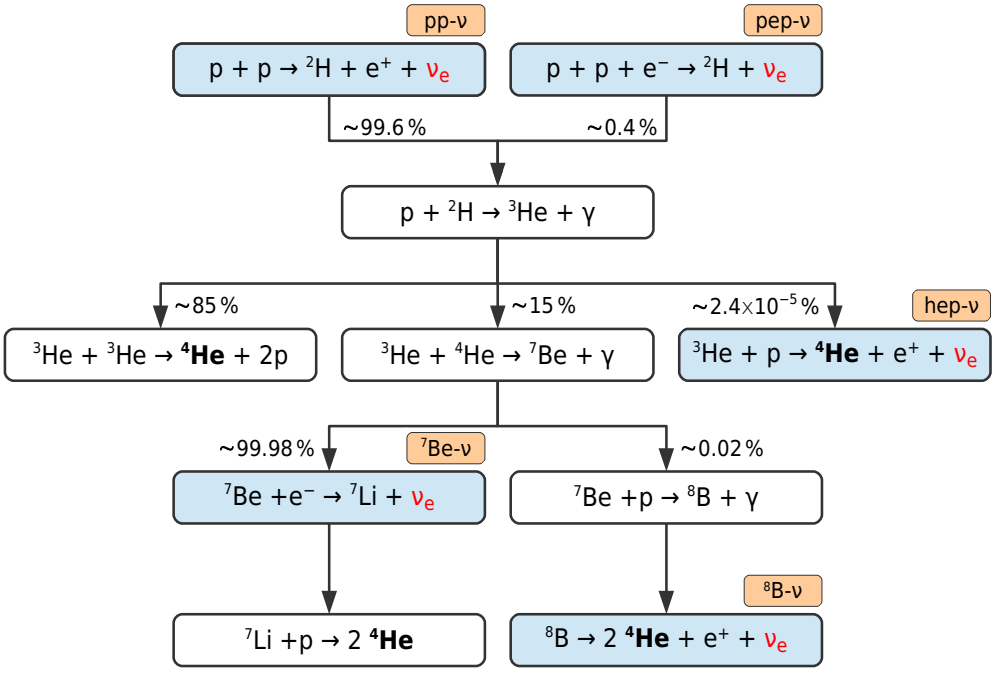

(a) The *pp* chain.

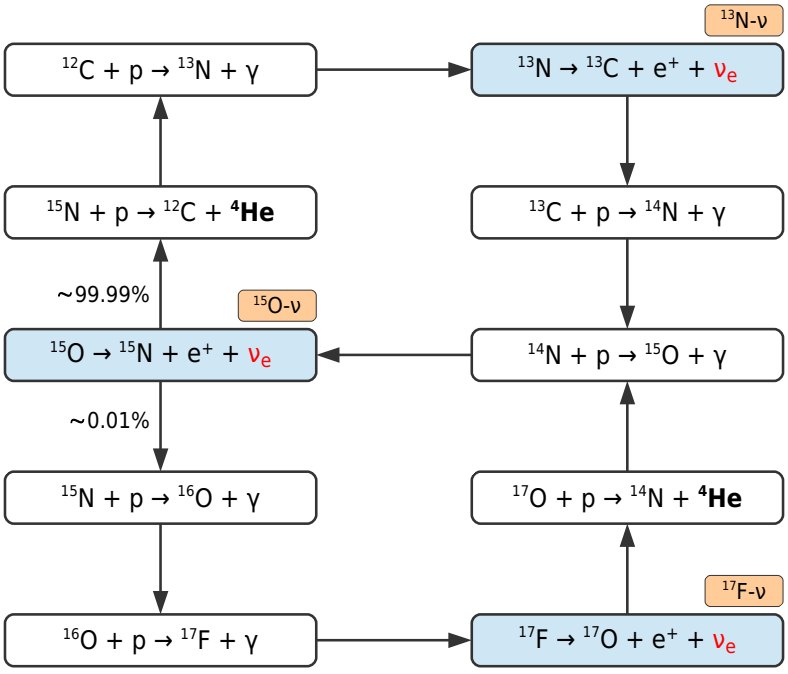

(b) The *CNO*-I (*upper part*) and *CNO*-II (*lower part*) cycles.

Figure 2.1 – Fusion reactions in the Sun effectively combining four protons to one helium nucleus. **Figure (a)**: The *pp* chain with its four branches accounting for $\simeq 98.5\,\%$ [116] of the solar energy release. The BRs are from Ref. [83]. **Figure (b)**: The *CNO* sub-cycles I and II contributing $\simeq 1.5\,\%$ [116] to the Sun's total energy release. The BRs are from Ref. [117].

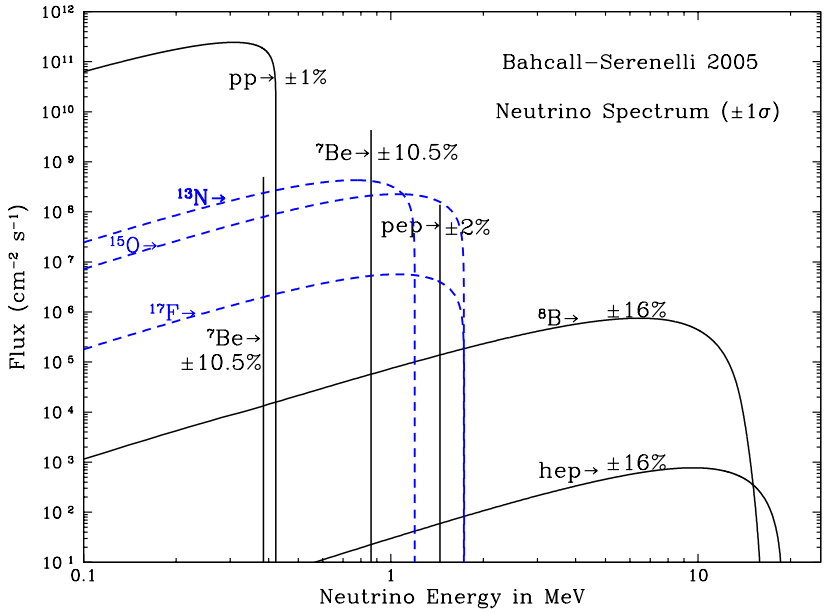

Figure 2.2 – Energy spectra for the solar neutrinos from the *pp* chain (solid black) and the *CNO* cycle (dashed blue) as predicted by the SSM *BS05(OP)* from *J. Bahcall* and *A. Serenelli* in 2005 [16]. The *pep* and ^{7}Be neutrinos are emitted at fixed energies (*sharp lines*), as one can infer from Figure 2.1a. For the ν_e fluxes of the *pp* chain, the 1σ relative uncertainties on the predictions are stated. Figure from Ref. [121].

A second sequence of fusion reactions constitutes the *CNO* cycle [83, 118] partially shown in Figure 2.1b. It contributes $\simeq 1.5\,\%$ [116] to the total energy release of the Sun and has higher contributions in heavier stars. In this cycle, protons are fused to ^{4}He nuclei in reactions using carbon, nitrogen and oxygen as catalysts. So far, only a limit of $<7.7 \times 10^8\,\mathrm{cm^{-2}\,s^{-1}}$ (95 % C.L.) [119] on the combined flux of neutrinos from the *CNO* cycle was set by Borexino. The intensity of the *CNO* cycle is sensitive to the temperature in the center of the Sun, which in the star's current state is too low for a larger *CNO* contribution to the total energy release. Moreover, the *metallicity* Z, i.e., the mass fraction of elements heavier than helium, is of importance to drive the catalytic reactions. For our Sun, a metal-rich (Population I) star, approximations of the metallicity and the mass fractions of hydrogen and helium in the present-day *photosphere* are 1 %, 74 % and 25 %, respectively [120]. The metallicity is an important parameter for a mathematical treatment of the Sun—the so-called SSM. This model allows to predict observables of the star, for example the fluxes of the ν_e's from the *pp* chain and the *CNO* cycle, and thereby enables a test of validity for not directly measurable parameters like Z. Figure 2.2 shows the neutrino flux spectra predictions based on the *BS05(OP)* SSM by *J. Bahcall* and *A. Serenelli* [16].

A re-determination of the solar chemical composition by *M. Asplund*, *N. Grevesse*, *A. J. Sauval* and *P. Scott* (*AGSS09*) [120], which based on the evaluation of the Sun's spectral absorption lines, resulted in a lower metallicity compared to a former determination by *N. Grevesse* and *A. J. Sauval* (*GS98*) [122]. Although the *AGSS09*

Table 2.1 – Fluxes for solar neutrinos from the *pp* chain and the *CNO* cycle as predicted by SSMs assuming high (*GS98*) or low (*AGSS09*) solar metallicity. Relative uncertainties on the model predictions are given in parentheses. In the last column, the relative differences in the single flux predictions are stated. Neutrino fluxes are given in units of 10^{10} (*pp*), 10^{9} (^{7}Be), 10^{8} (*pep*, ^{13}N, ^{15}O), 10^{6} (^{8}B, ^{17}F), 10^{3} (*hep*) $\mathrm{cm}^{-2}\,\mathrm{s}^{-1}$. For the *CNO* flux, the ^{13}N, ^{15}O and ^{17}F neutrino fluxes were added. Data cited from [30, 124].

Source	Energy	Neutrino Flux [see caption]		
	[MeV]	*GS98*	*AGSS09*	Difference
pp	≤ 0.420	5.98 (0.6 %)	6.03 (0.6 %)	0.8 %
pep	1.440	1.44 (1.2 %)	1.47 (1.2 %)	2.0 %
hep	≤ 18.8	8.04 (30 %)	8.31 (30 %)	3.2 %
^{7}Be I	0.384	0.53 (7 %)	0.48 (7 %)	10 %
^{7}Be II	0.862	4.47 (7 %)	4.08 (7 %)	10 %
^{8}B	≤ 15.0	5.58 (14 %)	4.59 (14 %)	22 %
^{13}N	≤ 1.199	2.96 (14 %)	2.17 (14 %)	36 %
^{15}O	≤ 1.732	2.23 (15 %)	1.56 (15 %)	43 %
^{17}F	≤ 1.740	5.52 (17 %)	3.40 (16 %)	62 %
CNO	≤ 1.740	5.24 (21 %)	3.76 (21 %)	39 %

composition exhibits a high degree of internal consistency, a corresponding SSM yields results for the sound speed in the solar interior that are in conflict with helioseismology data. This is contrary to a SSM with the *GS98* high-metallicity composition [123, 124].
As one can see from Table 2.1, the fluxes of ν_e's from the decays of ^{13}N, ^{15}O and ^{17}F in the *CNO* cycle and of ^{7}Be and ^{8}B in the *pp* chain are sensitive to the metallicity of the Sun. Consequently, their precise measurement could solve this *solar metallicity problem*. However, existing observations of solar neutrinos from various experiments did not yield a conclusive solution. A precise determination of especially the neutrino fluxes from the *CNO* cycle therefore is of utmost importance to settle the outstanding issue.

2.2 Core-collapse supernova

A SN—the tremendous explosion at the end of a massive star—is one of the most violent and spectacular events in the Universe. Its observable light phenomenon can outshine the host galaxy for weeks or even months. *Core-collapse SNe* [125–127] include all spectral types (II, Ib, Ic, etc.) except type Ia, which is associated to a *thermonuclear SN*, and emit $\sim 10^{58}$ [128] neutrinos and antineutrinos on a timescale of some tens of seconds. By using these neutrinos as messenger particles, neutrino astronomy enables probing of core-collapse physics and its aftermath beyond the capabilities of optical observations. Therefore, a goal of future large-volume neutrino observatories (e.g., of LENA in Section 4.2) is the flavor-, energy- and time-resolved high-statistics measurement of neutrinos from a galactic core-collapse SN. The sequence of such an incident is briefly described in Section 2.2.1. Together with

gravitational wave data[1], a numerous detection of core-collapse SN neutrinos [80] is, for example, important to test the current core-collapse SN paradigm, to understand the properties of SN progenitors and remnants, and to learn about nucleosynthesis in SN explosions.
The oscillation of SN neutrinos on their way through the stellar layers is subject to the MSW matter effect and thus potentially contains information on the neutrino MO. Moreover, the phenomenon of *collective neutrino oscillations* is predicted as a result of neutrino self-coupling and the matter potential created in a SN from the high neutrino density itself. Information on those subjects can be found in Ref. [130] and references therein.
Unfortunately, the rate of core-collapse SNe in our galaxy is only 1–3 per century (see Table 1 in Ref. [130]). Therefore, such an observation may only be possible once in a (detector-)lifetime. The predicted *diffuse supernova neutrino background* (DSNB) described in Section 2.2.2, however, is supposed to provide a constant but low flux of neutrinos from past core-collapse SNe. Its measurement is another goal of future experiments in neutrino astrophysics.

2.2.1 Galactic core-collapse supernova

Currently, the ideas on the physical processes taking place inside a dying massive star to create a SN explosion are to a large extent driven by theoretical investigations with computationally intensive simulations [125, 127, 131]. From initial computations in one dimension over 2D simulations the research field now strives for a numerical SN modeling in all three dimensions. Besides a precise description of the initial conditions inside the progenitor start, this task further requires input ranging from (magneto-)hydrodynamics of stellar plasma over neutrino and nuclear physics to relativistic gravity. The observables predicted by the simulations, optical and neutrino "light curves" and energy spectra, gravitational waves, remnant masses etc., could be compared to actual measurements. Unfortunately, the increasing number of successful SN explosion simulations is still limited, especially in 3D, and their predictions among different research groups have not yet fully converged [131]. Moreover, available data concerning core-collapse SN neutrino bursts solely comprise the incident of *SN 1987A* [132] observed on 23 February 1987 in the $\sim$50 kpc ($1\,\mathrm{pc} = 3.096 \times 10^{13}\,\mathrm{km}$) distant *Large Magellanic Cloud*. By that time, two independent water Cherenkov detectors observed together about 20 neutrino events in a time window of $\sim$10 s.

In the following, the "SM" for a stellar core-collapse as a source of astrophysical neutrinos and antineutrinos is briefly described based on reviews in Refs. [125–127]. When a massive star with $\gtrsim 8M_\odot$ ($1M_\odot \sim 1.99 \times 10^{30}\,\mathrm{kg}$ [114]) reaches the end of its hydrostatic burning, a central Fe-core with 3000 km diameter, $\sim 10^{10}$ K temperature and several $10^9\,\mathrm{g\,cm^{-3}}$ mass density is surrounded by shells with the remains of previous fusion phases (Si, O, Ne, C, He, H). Since the binding energy per nucleon is at its maximum and no more energy can be released in fusion or fission of Fe, the core's structural support against the self-gravitation of the star is solely provided by the *electron degeneracy pressure*. Once the growing Fe-core mass reaches

[1] The *Laser Interferometer Gravitational-Wave Observatory* (LIGO) in the *United States of America* recently reported the first detection of gravitational waves [129].

the *Chandrasekhar limit* of $1.44 M_\odot$, the internal pressure no longer suffices to maintain the equilibrium of forces. The inner core starts to collapse with free fall velocity and will form a *proto-neutron star* of 30 km radius after ∼0.2 s: Endoergic photodisintegration of Fe-group nuclei produces free nucleons and α particles in the heating core. Together with the decrease of the electron density through *electron capture* (EC) on free protons, these processes soften the pressure increase from the matter infall and thus further accelerate the collapse. When the core density exceeds $\sim 10^{12}\,\mathrm{kg\,cm^{-3}}$, ν_e's from *neutronization* ($e^- + p \to n + \nu_e$) are essentially trapped, i.e, their timescale for diffusion out of the core becomes lager than the freefall timescale of the outer gas. The homogeneously and subsonically compacting core reaches nuclear matter density ($\sim 2.7 \times 10^{14}\,\mathrm{kg\,cm^{-3}}$) around 0.11 s after the start of the collapse. As a result, it decelerates, stops and finally rebounds into the succeeding layers of supersonically infalling matter. A shock wave forms and propagates down the matter density gradient. Several SN simulations showed that this *prompt mechanism* is insufficient to cause an explosive ejection of the star's outer layers. Instead, the shock stalls at a radius between 100 and 200 km due to thermal energy losses: Dissociations of heavy nuclei from the infalling outer Fe-core produce free nucleons and α particles. This changed matter composition in the after shock region favors rapid neutronization during ∼10 ms and produces what is called the *prompt ν_e burst* (left panels of Figure 2.3).

After the core bounce, the nascent proto-neutron star in the center further accretes infalling stellar matter at a rate of some $0.1 M_\odot$ per second. Depending on the progenitor mass M, the compact remnant at a later stage either becomes a neutron star with ∼10 km radius or, for $M \gtrsim 25 M_\odot$, a black hole. During the *matter accretion phase*, the proto-neutron star cools primarily through the emission of ν_e's (middle panels of Figure 2.3). Their scatterings in the dense matter thermalize them to stellar medium temperature before they diffuse out through the *neutrinosphere* at ∼50 km, which is the transition between the neutrino opaque and free-streaming regions. Between the neutrinosphere and the stalled shock, emissions of ν_e's and $\overline{\nu}_e$'s (from positron captures on neutrons) cool the stellar matter. At the same time, CC (re-)captures on free nucleons of the ν_e's and $\overline{\nu}_e$'s from below and above the neutrinosphere heat the after shock region. If this heating exceeds the net cooling effect, a region of low density but high temperature, a *hot bubble*, forms between the stalled shock and the surface of the neutron star. On a timescale of a few 100 ms, the neutrino-driven heating expands the layer, revives the shock and eventually leads to an explosive ejection of the star's envelope—the final explosion. In summary, the neutrinos from the cooling of the proto-neutron star are decisive to make the SN explode.
About 99 % of the nascent neutron star's total loss in gravitational binding energy is carried away by neutrinos and antineutrinos, roughly 3×10^{53} erg ($1\,\mathrm{erg} \sim 10^{-7}$ J). Only 1 %, 1–2×10^{51} erg, convert into kinetic energy of the SN ejecta.
In the *cooling phase* after the explosion, the neutron star remnant loses energy through emission of all neutrino and antineutrino flavors on a timescale of ∼10 s (right panels of Figure 2.3). Muon and tau flavors are produced as neutrino-antineutrino pairs in thermal processes, e.g., electron-positron annihilation and nucleon-nucleon bremsstrahlung (for a list of important neutrino reactions in SNe see Fig. 3 of Ref. [127]). Due to missing CC capture processes on free nucleons, the ν_μ, $\overline{\nu}_\mu$, ν_τ and

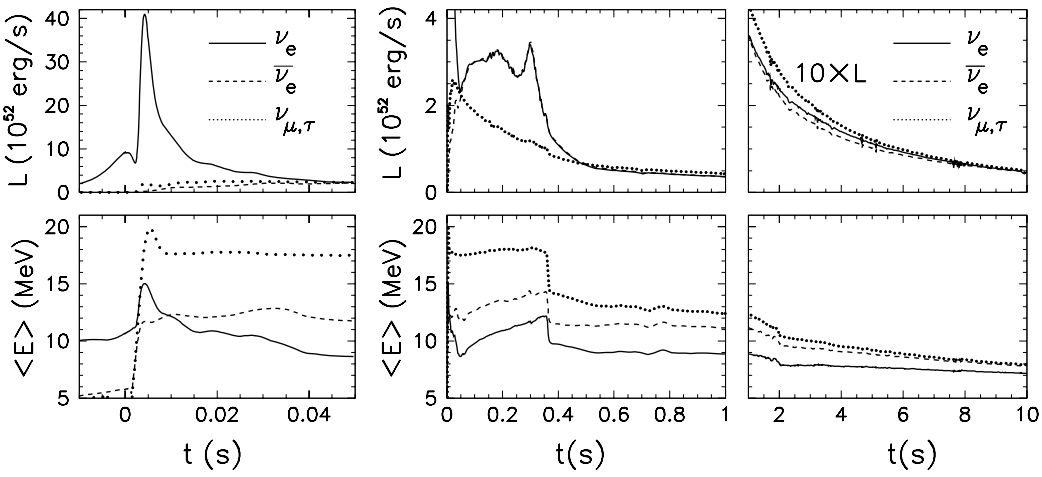

Figure 2.3 – Neutrino luminosities **(top)** and energy spectra **(bottom)** for a core-collapse SN with $10.8 M_{\odot}$ progenitor star as obtained by numerical simulations described in Ref. [133]. The neutrino-driven explosion of the Fe-core progenitor was triggered artificially through implementation of enhanced neutrino energy deposition in the spherically symmetric simulations. All quantities shown for the different SN phases, prompt neutrino burst **(left)**, accretion **(middle)** and cooling **(right)**, are in the laboratory frame of a distant observer. Figure reprinted from publication [40] with permission from *Elsevier*.

$\overline{\nu}_{\tau}$ energy spectra are less affected by thermalization to lower energies than those of ν_e and $\overline{\nu}_e$.

Numerical simulations indicate that the described *delayed neutrino-driven explosion mechanism* can yield SN explosions in spherical symmetry only for light progenitors with a O-Ne-Mg core. For larger progenitors with a Fe core, an asymmetric configuration due to large-scale convection in the core was found to be important to make a dying star explode [127]. A signature from this convection is expected to be visible in the time evolution of a high-statistic neutrino signal. In addition, the sudden drop of neutrino luminosity in such a *neutrino light curve*, together with data from a gravitational wave burst, would suggest the formation of a black hole. More basic information retrievable from a strong neutrino burst signal in one or more (future) detectors include estimates for the direction and the distance to the core-collapse explosion [130]. It further indicates the occurrence of a core-collapse SN at all, what is important because the light phenomenon of a SN may be obscured, e.g., by interstellar dust. Since the increased photon flux from a SN explosion requires some time to diffuse through the compacted stellar layers, the major part of the weakly interacting neutrinos may pass through the star's matter and probably reaches Earth before the visual appearance. In the case of SN 1987A, the neutrinos arrived about 2–3 hours before the light [132]. This circumstance lead to the establishment of the *SuperNova Early Warning System* (SNEWS) [134, 135] in which multiple neutrino detectors participate today. An alert from SNEWS allows to prepare for an observation of the light signal from a SN's early phase.

2.2.2 Diffuse supernova neutrino background

The DSNB is the accumulated, not yet measured flux of neutrinos from past core-collapse SNe in the visible Universe. Its intensity is expected to be on the order of $10^2\,\mathrm{cm}^{-2}\,\mathrm{s}^{-1}$ and thus much lower than the flux of solar neutrinos. The following bases on the general review in Ref. [136] and the explanations in the context of LENA in Ref. [40].
A parametric description of the isotropic DSNB flux spectrum $\frac{\mathrm{d}\phi}{\mathrm{d}E_\nu}(E_\nu)$ at the neutrino transparent Earth is commonly formulated with the line-of-sight integral

$$\frac{\mathrm{d}\phi}{\mathrm{d}E_\nu}(E_\nu) = \frac{c_0}{H_0}\int_0^\infty [\varphi[E_\nu(z+1)]]\,\frac{R_{\mathrm{SN}}(z)}{\sqrt{\Omega_m(1+z)^3+\Omega_\Lambda}}\,\mathrm{d}z\,, \tag{2.2}$$

where c_0 is the speed of light in vacuum, H_0 denotes the *Hubble constant*, Ω_m is the *pressureless matter density of the Universe* and Ω_Λ names the *dark energy density*. The two main ingredients are the average core-collapse SN neutrino emission spectrum $\varphi(E_\nu)$ and the core-collapse SN rate $R_{\mathrm{SN}}(z)$ at a distance expressed in terms of the redshift z. For $z = 0$, the predicted SN rate density is about $(1.25 \pm 0.25) \times 10^{-4}\,\mathrm{Mpc}^{-3}\,\mathrm{a}^{-1}$ and is in general correlated with the star formation rate. Moreover, the average neutrino energy spectrum $\varphi(E_\nu)$ emitted in a SN also becomes a function of z in Equation (2.2), $\varphi[E_\nu(z+1)]$. This is due to the expansion of the Universe, which shifts the energies observable at Earth to lower values for neutrinos from farther distances.

The favorable way to measure the DSNB with LSc neutrino detectors, like those discussed in Section 4.2 and Section 4.3, is the detection of $\overline{\nu}_e$'s through the IBD channel (see Section 1.2.1). For a calculation of the DSNB $\overline{\nu}_e$ flux or the IBD event rate spectrum, it is often assumed that a SN's total energy release in ν's and $\overline{\nu}$'s is equally distributed between the six different neutrinos and antineutrinos, meaning that the $\overline{\nu}_e$'s carry $E_{\mathrm{tot},\overline{\nu}_e} = 5 \times 10^{52}\,\mathrm{erg}$. This takes flavor conversion effects into account. Moreover, it is assumed that $\varphi_{\overline{\nu}_e}(E_{\overline{\nu}_e})$ after oscillation in the SN has the shape of a *Fermi-Dirac* [136] or *Maxwell-Boltzmann* [40] thermal spectrum. Predictions on DSNB $\overline{\nu}_e$ flux spectra with a Fermi-Dirac emission model are shown on the left of Figure 2.4 for different temperature parameters. The mean $\overline{\nu}_e$ energy $\langle E_{\overline{\nu}_e}\rangle$ of the spectrum is commonly set to be in the range from 12 MeV to 21 MeV, with large theoretical uncertainty. Therefore, constraints on $E_{\mathrm{tot},\overline{\nu}_e}$ and $\langle E_{\overline{\nu}_e}\rangle$ from DSNB measurements allow to rule out or to improve existing SN models. Moreover, experimental data on the DSNB can clarify if the SN 1987A was a typical core-collapse SN.
Currently, the best upper limits on the DSNB $\overline{\nu}_e$ flux are from the SK experiment: For $E_{\overline{\nu}_e} > 17.3\,\mathrm{MeV}$, the upper limit at 90 % CL is $3.1\,\mathrm{cm}^{-2}\,\mathrm{s}^{-1}$ [137] from 2853 live days, covering SK phases I to III. This is about a factor of two to four above current predictions [137]. In phase IV, the $E_{\overline{\nu}_e}$ threshold was pushed down to 13.3 MeV [138]. Differential upper limits at 90 % CL from 960 days of data are shown on the right of Figure 2.4 together with the outcomes of phases I to III and results from 2343 live days of KamLAND [139].

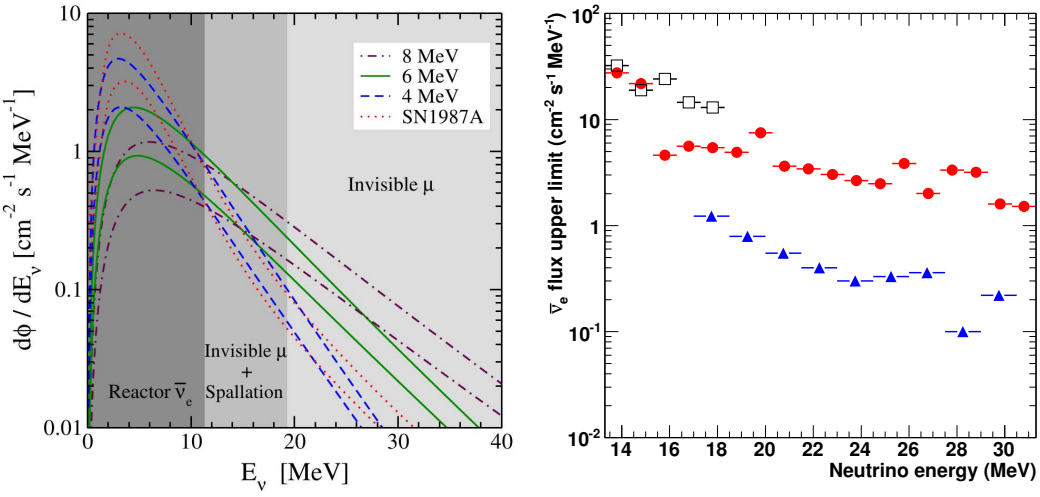

Figure 2.4 – **Left:** Predicted DSNB $\overline{\nu}_e$ flux spectra assuming an effective time-integrated spectrum $\varphi_{\overline{\nu}_e}(E_{\overline{\nu}_e})$ after mixing of *Fermi-Dirac* form with 4, 6 and 8 MeV for the temperature parameter T (outside of the star; $\langle E_{\overline{\nu}_e} \rangle = 3.15T$). The result for a reconstructed spectrum from SN 1987A is also shown. Uncertainties in astrophysics inputs are represented by the widths of the bands. The grey shaded energy ranges indicate where the stated backgrounds are present. Reprinted figure with permission from Ref. [128]. Copyright 2016 by the *American Physical Society*. **Right:** Model-independent, differential upper limits at 90 % CL on the DSNB $\overline{\nu}_e$ flux from SK phases I to III [137] (*blue triangles*), SK phase IV [138] (*red circles*) and KamLAND [139] (*open squares*). Figure reprinted from publication [138] with permission from *Elsevier*.

2.3 Earth

Antineutrinos from Earth—so-called geo-neutrinos—are produced in β^--decays of naturally occurring radioactive elements distributed in Earth [140]. The main contributions to the total geo-neutrino flux of some $10^6\,\mathrm{cm}^{-2}\,\mathrm{s}^{-1}$ at Earth's surface are from decays of radioisotopes in to the ^{238}U and ^{232}Th chains and from ^{40}K:

$$^{238}\mathrm{U} \rightarrow {}^{206}\mathrm{Pb} + 8\alpha + 8e^- + 6\overline{\nu}_e + 51.7\,\mathrm{MeV}\,, \tag{2.3}$$

$$^{232}\mathrm{Th} \rightarrow {}^{208}\mathrm{Pb} + 6\alpha + 4e^- + 4\overline{\nu}_e + 42.7\,\mathrm{MeV}\,, \tag{2.4}$$

$$^{40}\mathrm{K} \rightarrow {}^{40}\mathrm{Ca} + e^- + \overline{\nu}_e + 1.31\,\mathrm{MeV}\,. \tag{2.5}$$

The energy spectra of the $\overline{\nu}_e$'s emitted in the reactions (2.3) to (2.5) are shown in Figure 2.5.

Observations of geo-neutrinos can provide valuable input to solve outstanding questions in Earth sciences, which cannot be answered by conventional methods, e.g., seismic measurements and study of geological samples from Earth's crust and mantle: Current estimates for the Earth's total surface heat flow are (46 ± 3) TW [141] and (47 ± 2) TW [142]. The precise distribution between primordial heat left over from planet formation through mass accretion and radiogenic heat from radioactive decays is not known though. Current compositional models for the planet (see review in Ref. [140]) differ by a factor of three for the amount of U in Earth. One extreme case for the U abundance in the Earth's core is considered in Ref. [143] where a

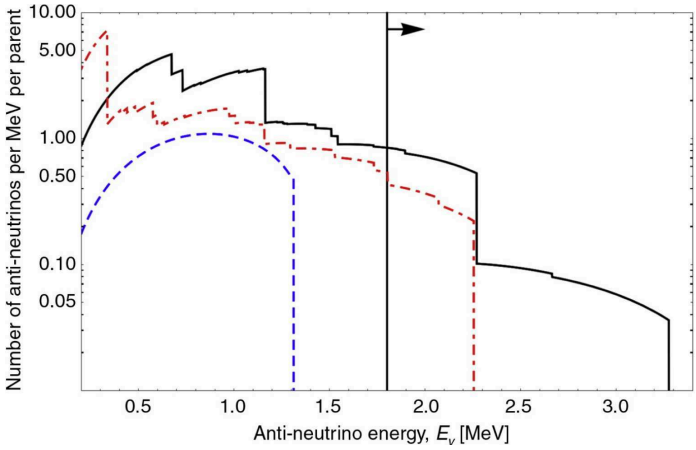

Figure 2.5 – Energy spectra of $\overline{\nu}_e$'s from Earth. The spectra correspond to the geo-neutrinos released in the ^{238}U decay chain (net reaction (2.3); *solid black*), the ^{232}Th decay chain (net reaction (2.4); *dashed-dotted red*) and in ^{40}K decay (reaction (2.5); *dashed blue*). They are normalized to 6, 4 and 1 antineutrinos, respectively. A black line at 1.8 MeV indicates the energy threshold for the IBD detection reaction (see Section 1.2.1). Figure reprinted from publication [140] with permission from *Elsevier*.

central U-driven *geo-reactor* is suggested to be the dominant source of planetary heat production.
In general, distinctive features of the different compositional models, which allow to test them, are the predicted abundances of U and Th and their distribution among inner and outer core, lower and upper mantle and the crust of Earth. So far, samples only from the crust and the upper mantle[2] could be studied. The U/Th mass ratio of *silicate Earth* (crust plus mantle) can also be compared to that of meteorites and thus sheds light on the history of the Solar System and Earth formation.

Given the limited range of conventional methods to probe the elemental composition of Earth, antineutrinos are ideal messenger particles to provide information on the abundances of radioactive elements below the upper mantle. However, a detection device for the $\overline{\nu}_e$'s from Earth primarily probes the *local abundances* of radioisotopes, which are expected to vary already between the *continental crust* and the *oceanic crust*. Therefore, combined results from multiple measurements across the planet are required to determine the total surface heat flux and to disentangle the geo-neutrino flux contributions from Earth's different layers.
Up to now, results on the measurements of geo-neutrinos were only reported by the LSc detectors KamLAND in Japan [32, 144] and by Borexino in Italy [33, 145, 146]. In both cases, the LE $\overline{\nu}_e$'s were detected through the IBD detection channel (see Section 1.2.1). Note that $\overline{\nu}_e$'s from ^{40}K decay are below the IBD energy threshold of ∼1.8 MeV (see Figure 2.5). The latest values for the determined geo-neutrino fluxes

[2]Samples from this region get to the surface by tectonic activity but may be altered in composition during the transportation.

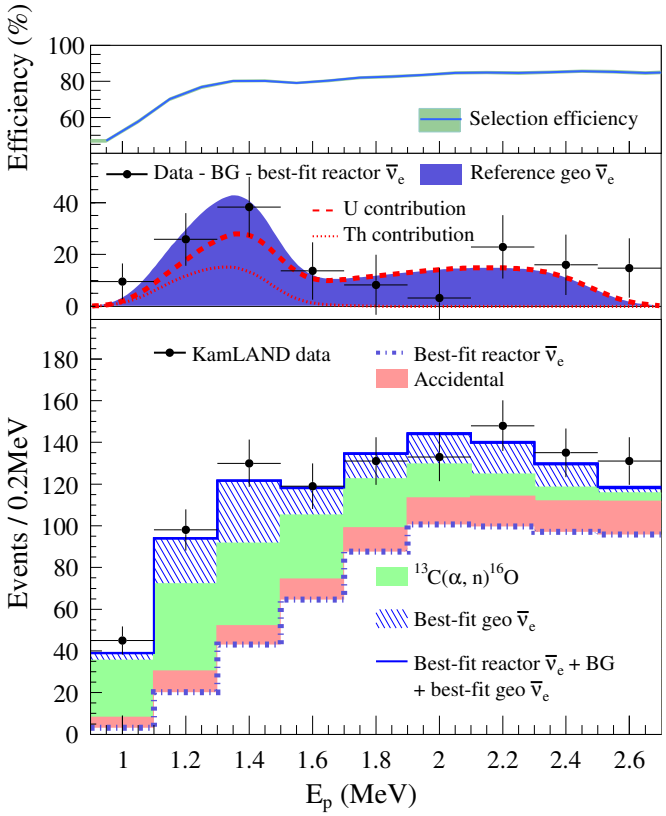

Figure 2.6 – **Bottom:** Energy spectrum of the prompt events from the IBD detection reaction for $\overline{\nu}_e$'s in the geo-neutrino energy window of KamLAND. **Middle:** Spectrum of observed geo-neutrinos after subtraction of reactor neutrinos and other backgrounds compared to a geological reference model (for details see Ref. [32]). **Top:** Selection efficiency for prompt events from IBD as a function of energy. Reprinted figure with permission from Ref. [32]. Copyright 2016 by the *American Physical Society*.

from U and Th assuming a *chondritic*[3] U/Th mass ratio of 3.9 are [32, 33]

$$\phi_{\mathrm{KL}}^{\mathrm{U+Th}}(\overline{\nu}_e) = (3.4 \pm 0.8) \times 10^6\,\mathrm{cm}^{-2}\,\mathrm{s}^{-1}\,,$$

$$\phi_{\mathrm{BX}}^{\mathrm{U}}(\overline{\nu}_e) = (2.7 \pm 0.7) \times 10^6\,\mathrm{cm}^{-2}\,\mathrm{s}^{-1}\,,$$

$$\phi_{\mathrm{BX}}^{\mathrm{Th}}(\overline{\nu}_e) = (2.3 \pm 0.6) \times 10^6\,\mathrm{cm}^{-2}\,\mathrm{s}^{-1}\,.$$

The 2013 KamLAND results regarding geo-neutrinos are shown in Figure 2.6. Both the results of KamLAND and Borexino are in fairly good agreement with the expectations from geological models. Although the precision of the statistically limited measurements is currently insufficient to discriminate between different geological models, no positive evidence for the existence of a georeactor with >4.5 TW power in Earth's core has been found at 95 % CL [140]. Further implications from the geo-neutrino measurements of KamLAND and Borexino are summarized in the review in Ref. [140].

[3] "Chondrites are primitive, undifferentiated meteorites (i.e., a chaotic assemblage of rock and metal) that are a collection of the earliest formed material in the solar system." [140].

As a conclusion, existing $\overline{\nu}_e$ detectors based on LSc proved to be successful new tools for geo-sciences, which already yielded important results. Nevertheless, more geo-neutrino measurements with larger detection devices are required at different locations on Earth in order to resolve outstanding issues, like the determination of the U/Th mass ratio or the geo-neutrino flux contribution from Earth's mantle.
As one can see in the lower panel of Figure 2.6, a major background source to the detection of $\overline{\nu}_e$'s from Earth are $\overline{\nu}_e$'s from nuclear reactors. This type of antineutrino source is treated next.

2.4 Nuclear reactor

Reactor antineutrinos are $\overline{\nu}_e$'s which, similar to geo-neutrinos, originate from the β^--decays of unstable radioisotopes produced by nuclear spallations in nuclear fission reactors. Together with the average energy release of about 200 MeV per fission, about six $\overline{\nu}_e$'s are produced along the β-decay chains of neutron-rich fission products from ^{235}U, ^{238}U, ^{239}Pu and ^{241}Pu. One expects a mean rate of isotropically emitted $\overline{\nu}_e$'s of $\sim 2 \times 10^{20}\,\mathrm{s}^{-1}$ per GW thermal reactor power [85].
A nuclear fission reactor constituted the neutrino source used in the first experimental confirmation of the existence of $\overline{\nu}_e$'s [5, 6]. Moreover, as mentioned in Section 1.1.3, nuclear reactor complexes have been used as intense and controllable $\overline{\nu}_e$ sources for oscillation experiments to determine the neutrino mixing angle θ_{13} through $\overline{\nu}_e$ disappearance [85, 147]. These experiments with LSc detectors, i.e., Double Chooz, Daya Bay and RENO, use the IBD reaction (see Section 1.2.1) to observe the spectrum of $\overline{\nu}_e$ interactions at a distance of 1–2 km from the nuclear power cores. Contrary to geo-neutrinos, the production points of reactor antineutrinos are known with a precision on the order of a few meters[4]. This has to be compared to the oscillation length of the reactor $\overline{\nu}_e$, which is about 3 km at $\sim$3 MeV, the average antineutrino energy from nuclear fission reactors. Given a detection device with sufficient energy resolution, the small source size compared to the oscillation length allows to measure the full energy-dependent phase information of the reactor antineutrino oscillation, which is more than just an averaged $\overline{\nu}_e$ disappearance effect. As it will be described in Section 4.3.2, this is particularly important in the case of the future JUNO and RENO-50 projects. They aim to investigate an oscillatory fine structure in the measured reactor $\overline{\nu}_e$ event spectrum in order to determine the neutrino MO.
If in a reactor antineutrino oscillation experiment the (almost) unoscillated $\overline{\nu}_e$ flux close to one or more reactor cores is not measured with a dedicated near-detector for reference, the antineutrino flux at the (far-)detector must be predicted based on model assumptions: For a detector at distance R to a nuclear reactor with thermal power P_{th}, the energy-dependent $\overline{\nu}_e$ flux $\phi_\nu(E_\nu)$ can be calculated as [85, 148]

$$\phi_\nu(E_\nu) = \frac{1}{4\pi R^2}\,\frac{P_{th}}{\langle E_f \rangle}\,n_\nu(E_\nu)\,P_{ee}(E_\nu, R)\,, \tag{2.6}$$

where $P_{ee}(E_\nu, R)$ is the $\overline{\nu}_e$ survival probability and $n_\nu(E_\nu)$ is the number of $\overline{\nu}_e$'s produced per fission. The latter is usually determined as the weighted sum over the

[4] It must be noted that in general one cannot determine on an event-by-event basis from which of multiple possible reactor cores an interacting $\overline{\nu}_e$ originates.

values $n_{\nu,k}(E_\nu)$ from the four model-dependent $\overline{\nu}_e$ spectra per fission of the main fissile isotopes,

$$n_\nu(E_\nu) = \sum_k f_k \, n_{\nu,k}(E_\nu) \,, \quad k = {}^{235}\mathrm{U}, {}^{238}\mathrm{U}, {}^{239}\mathrm{Pu}, {}^{241}\mathrm{Pu} \,, \quad \sum_k f_k = 1 \,. \tag{2.7}$$

The factors f_k describe the relative reactor fuel composition with the fissile isotopes that account for 99.5 % [85] of the fissions. Since the relative fuel composition in the nuclear reactor changes over time, e.g., due to depletion of U and enrichment of Pu, the factors f_k and thus also the total reactor $\overline{\nu}_e$ spectrum are time-dependent. The quotient $P_{th}/\langle E_f \rangle$ in Equation (2.6), where $\langle E_f \rangle$ is the mean energy release per fission, yields the mean rate of nuclear fissions in the reactor core. As in Equation (2.7), $\langle E_f \rangle$ is calculated as the weighted sum over the four main fissile isotopes,

$$\langle E_f \rangle = \sum_k f_k \, \epsilon_k \,, \quad k = {}^{235}\mathrm{U}, {}^{238}\mathrm{U}, {}^{239}\mathrm{Pu}, {}^{241}\mathrm{Pu} \,, \quad \sum_k f_k = 1 \,. \tag{2.8}$$

The parameters ϵ_k are the energy releases per fission of the individual isotopes.
Assuming a constant, average $\overline{\nu}_e$ flux $\phi_\nu(E_\nu)$ from the reactor, i.e., a constant, average nuclear fuel composition, a model for the IBD event spectrum $\mathrm{d}N/\,\mathrm{d}E_\nu$ follows from Equation (1.12) by integrating over the measurement time T,

$$\frac{\mathrm{d}N}{\mathrm{d}E_\nu} = \phi_\nu(E_\nu) \, \sigma_{\mathrm{IBD}}(E_\nu) \, N_p \, T \,. \tag{2.9}$$

The parameter N_p is the number of free protons available for the IBD reaction.
Reactor $\overline{\nu}_e$ spectra for the main fissile isotopes after a recent re-evaluation are shown in Figure 2.7 together with the IBD cross-section and the shape of the final event spectrum. A comparison of these new spectra with experimental data from $\overline{\nu}_e$ flux measurements close to reactor cores revealed a deficit of observed events, the *Reactor Antineutrino Anomaly* already mentioned in Section 1.3.3. However, as stated in Ref. [149], the anomaly may be the result of underestimated systematic errors on the reference spectra.
A comparison of the new reference spectra with measurements from the reactor $\overline{\nu}_e$ oscillation experiments Daya Bay, Double Chooz and RENO yielded an excess of observed events in the 4–6 MeV region [150–152]. This peculiarity of the event spectrum, which correlates with the total thermal power of the reactors, is currently unexplained.

2.5 Atmosphere

Atmospheric neutrinos and antineutrinos originate from weak decays of short-lived particles created by *cosmic ray* activity in the upper atmosphere. Additionally, the cosmic ray interactions lead to the production of muons, which can reach down to sea level and even several km below ground. These *cosmogenic muons*[5] introduce serious background to experiments searching for rare LE neutrino interactions as discussed in Section 4.1.2.
In Section 2.5.1, the cosmic ray spectrum observed at Earth is shortly addressed. The production of the atmospheric neutrinos and muons is described subsequently in Section 2.5.2.

[5] Also named "cosmic muons".

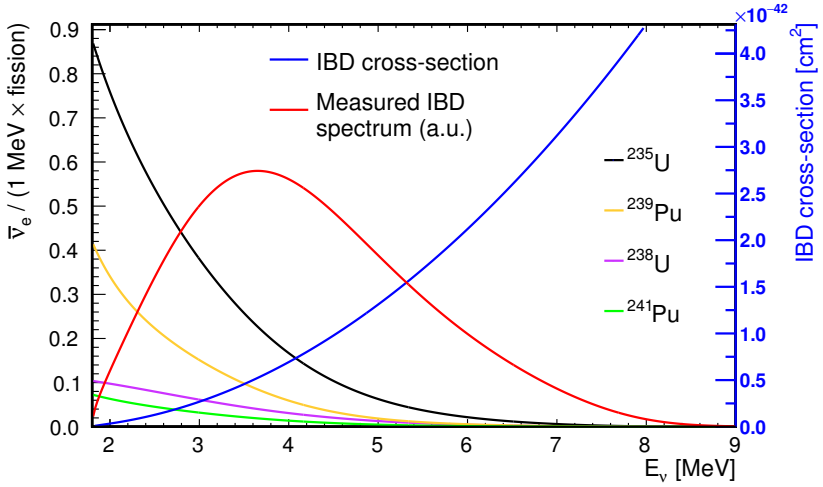

Figure 2.7 – Reactor $\overline{\nu}_e$ spectra for ^{235}U (*black*), ^{239}Pu (*orange*), ^{238}U (*violet*) and ^{241}Pu (*green*) [107, 108] above the IBD threshold of 1.806 MeV. As in Equation (2.7), the spectra were weighted according to their relative contributions in a commercial reactor: $f_{^{235}\mathrm{U}} = 0.58$, $f_{^{239}\mathrm{Pu}} = 0.30$, $f_{^{238}\mathrm{U}} = 0.07$ and $f_{^{241}\mathrm{Pu}} = 0.05$ [153]. The IBD cross-section (*blue*) from Section 1.2.1 together with the shape of the finally measured event spectrum (*red*) in *arbitrary units* (a.u.) is also shown.

2.5.1 Cosmic rays

Earth is continuously exposed to a flux of extraterrestrial HE particles. They originate from solar flares and astrophysical sources outside of the Solar System and are commonly named *cosmic rays* [11]. The component of charged particles consists of protons, helium, heavier nuclei and a small attribution of electrons. In fact, ∼79 % of the primary nucleons are protons and ∼70 % of the rest are bound in helium nuclei. For energies from several GeV to somewhat above 100 TeV, the intensity of primary nucleons $I_N(E)$ can be approximated by

$$I_N(E) \approx 1.8 \times 10^{-4} (E/1\,\mathrm{GeV})^{-\alpha} \frac{\mathrm{nucleons}}{\mathrm{m}^2\,\mathrm{s}\,\mathrm{sr}\,\mathrm{GeV}}\,, \tag{2.10}$$

where E is the energy per nucleon (including rest mass energy) and $\alpha = 2.7$ denotes the differential spectral index of the cosmic-ray flux.
When the *primary cosmic rays* propagate through space and interact with the interstellar medium, the flux composition changes: heavier nuclei not produced in stars, positrons and antiprotons are created.[6] Due to the high energies of cosmic rays, cascades of particle creation, annihilation and decay processes can be initiated once they penetrate Earth's atmosphere and interact with atomic nuclei. Depending on the energy of the incident particle, these extensive *air showers* of *secondary cosmic rays* can reach down to the sea level. Figure 2.8 shows the "all-particle" energy spectrum of cosmic rays impinging Earth as it is determined from multiple measurements. It suggests that astrophysical acceleration mechanisms can produce cosmic rays with energies up to some 10^{20} eV [11].

[6] These particles are sometimes already referred to as "secondary cosmic rays".

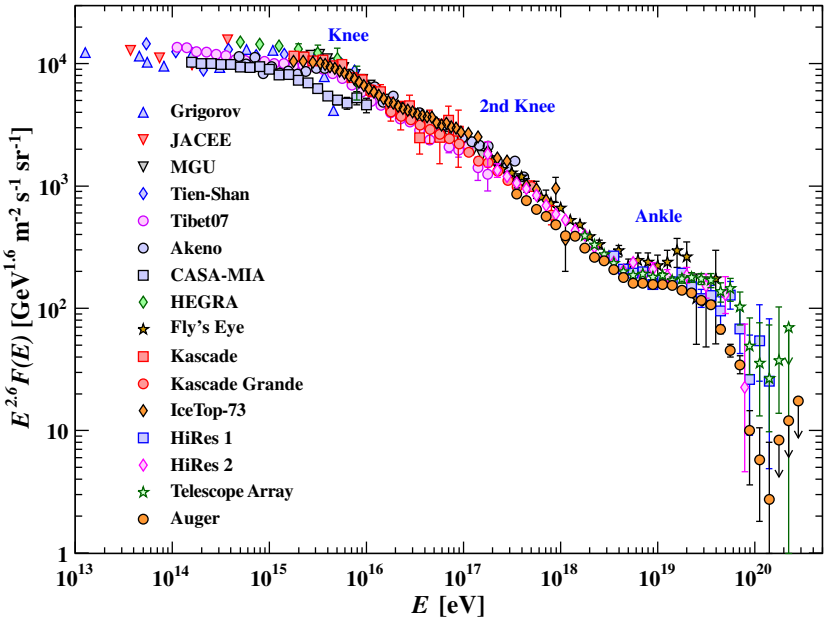

Figure 2.8 – The "all-particle" cosmic ray spectrum as a function of E (energy-per-nucleus). It was obtained from air shower measurements of multiple experiments. In order to make features of the spectrum ("Knee", "2nd Knee", "Ankle") more visible, it has been multiplied by $E^{2.6}$. Figure reprinted with permission from Ref. [11].

2.5.2 Atmospheric neutrinos and cosmogenic muons

At an altitude of $\sim 15\,\mathrm{km}$ [11] in the atmosphere, muons and neutrinos / antineutrinos are produced as secondary particles in cosmic ray interactions. They mainly originate from the following decays of pions and kaons with given BRs [11],

$$\pi^+ \to \mu^+ + \nu_\mu\,, \qquad \pi^- \to \mu^- + \overline{\nu}_\mu\,, \qquad \mathrm{BR} : \sim 99.99\,\%\,, \tag{2.11}$$

$$\pi^+ \to e^+ + \nu_e\,, \qquad \pi^- \to e^- + \overline{\nu}_e\,, \qquad \mathrm{BR} : \sim 0.01\,\%\,, \tag{2.12}$$

$$K^+ \to \mu^+ + \nu_\mu\,, \qquad K^- \to \mu^- + \overline{\nu}_\mu\,, \qquad \mathrm{BR} : \sim 64\,\%\,, \tag{2.13}$$

$$K^+ \to \pi^0 + e^+ + \nu_e\,, \qquad K^- \to \pi^0 + e^- + \overline{\nu}_e\,, \qquad \mathrm{BR} : \sim 5.1\,\%\,, \tag{2.14}$$

$$K^+ \to \pi^0 + \mu^+ + \nu_\mu\,, \qquad K^- \to \pi^0 + \mu^- + \overline{\nu}_\mu\,, \qquad \mathrm{BR} : \sim 3.4\,\%\,, \tag{2.15}$$

$$K^0_L \to \pi^+ + e^- + \overline{\nu}_e\,, \qquad K^0_L \to \pi^- + e^+ + \nu_e\,, \qquad \mathrm{BR} : \sim 41\,\%\,, \tag{2.16}$$

$$K^0_L \to \pi^+ + \mu^- + \overline{\nu}_\mu\,, \qquad K^0_L \to \pi^- + \mu^+ + \nu_\mu\,, \qquad \mathrm{BR} : \sim 27\,\%\,. \tag{2.17}$$

Moreover, atmospheric neutrinos also emerge from the decays of cosmogenic muons:

$$\mu^+ \to e^+ + \nu_e + \overline{\nu}_\mu\,, \quad \mu^- \to e^- + \overline{\nu}_e + \nu_\mu\,, \quad \mathrm{BR} : \sim 100\,\%\,. \tag{2.18}$$

The "conventional" production modes for atmospheric neutrinos and antineutrinos above are dominant up to $\sim 100\,\mathrm{TeV}$. At higher energies, the *prompt neutrino flux* from the decay of mesons with charm quark content is expected to dominate. With its hard energy spectrum, the prompt neutrino flux is background to the search for HE cosmic neutrinos. However, it has not yet been conclusively observed with

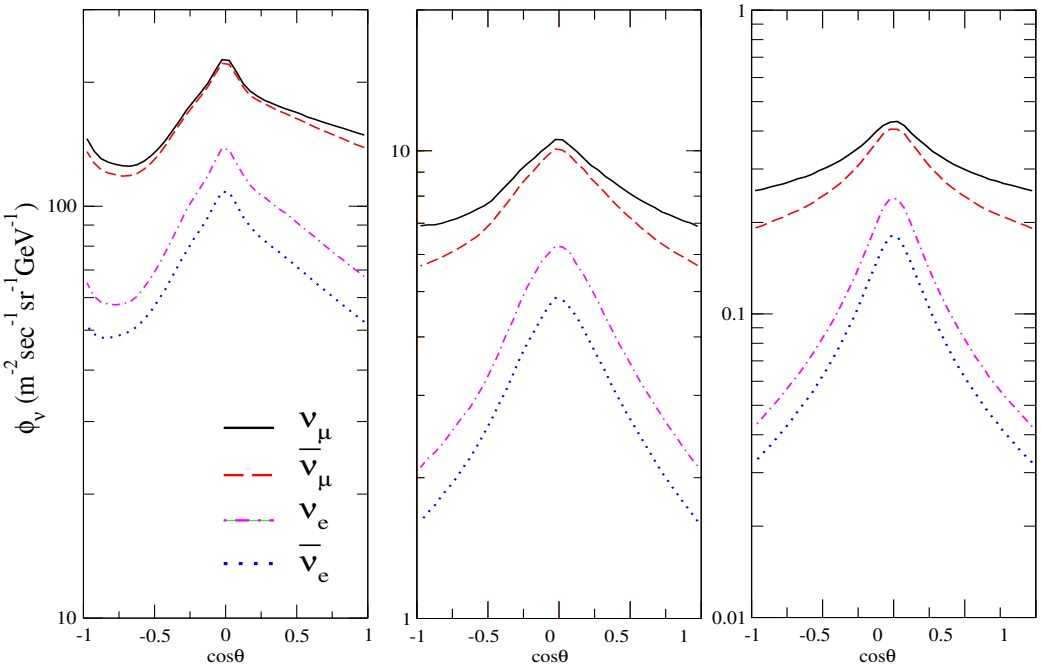

Figure 2.9 – Zenith angle dependence of the atmospheric ν_μ, $\overline{\nu}_\mu$, ν_e and $\overline{\nu}_e$ fluxes at $E_\nu = 1\,\text{GeV}$ **(left)**, $3.2\,\text{GeV}$ **(middle)** and $10\,\text{GeV}$ **(right)** as calculated in Ref. [154] for Pyhäsalmi in Finland. Results are averaged over all azimuth angles. The zenith direction $\cos\theta = 1$ corresponds to vertically downward going neutrinos and $\cos\theta = -1$ corresponds to vertically upward going neutrinos. Figures adapted with permission from Ref. [154].

neutrino telescopes like IceCube [112].
The actual atmospheric neutrino and cosmogenic muon flux spectra are geo-physical properties varying in space and time: Amongst other things, they depend on the continuously changing air density profile of the atmosphere, the local geo-magnetic field and the flux spectra of the incoming cosmic rays. In addition to these inputs, model-based predictions for local atmospheric neutrino and muon fluxes (e.g., see Ref. [154] and references therein) also require proper descriptions of the hadronic interactions in the air showers; especially the resulting kaon and pion multiplicities are of importance. As an example, calculations for the zenith angle dependence of the atmospheric ν_μ, $\overline{\nu}_\mu$, ν_e and $\overline{\nu}_e$ fluxes at Pyhäsalmi in Finland, a preferred site for the LENA detector (see Section 4.2.1), are shown in Figure 2.9 for different energies.

Due to the low neutrino interaction cross-sections, the continuous flux of atmospheric neutrinos permeates Earth from all sides almost unattenuated. However, for a given point on Earth, neutrino oscillations with matter effects (see Section 1.1.2) change the flux composition as a function of neutrino energy and zenith angle θ_{zen}. This is due to the fact that the traversed amount of matter and its density profile along the neutrino trajectory depend on θ_{zen}. Besides the influence from the MSW resonance, flavor transitions of atmospheric neutrinos traversing Earth through the core can also be affected by the *parametric resonance* (see Refs. [11, 61]).

In the past, a study of atmospheric neutrinos by SK provided first evidence for their flavor oscillation [23]. Future experiments aim to use neutrinos from the atmosphere for the determination of the neutrino MO [77, 78]. Preliminary studies [79] further suggest that these neutrinos can also provide information on the CP-violating phase δ_{CP}. It has also been pointed out that *neutrino oscillation tomography* and *neutrino absorption tomography* of Earth's interior could be performed with atmospheric neutrinos [155]. These methods to deduce the planet's electron and nucleon density distributions would be complementary and "more direct" than standard methods of geo-physics, e.g., seismic tomography by sound speed measurements.

2.6 Particle accelerator

Neutrinos and antineutrinos created with a particle accelerator originate from stimulated weak decays of artificially produced unstable particles, e.g., mesons. Contrary to the similar but uncontrolled neutrino production processes taking place in the atmosphere (see Section 2.5), the generation of a neutrino flux with an accelerator occurs in a more manageable fashion. Macroscopic control over the neutrino production environment for example allows to influence the direction, intensity and spectrum of the man-made neutrino emission from the accelerator. Therefore, this type of neutrino source is a common tool to create *neutrino beams* with energies up to some tens of GeV for oscillation experiments and cross-section measurements.
This section describes the conventional scheme for the production of a ν_μ / $\overline{\nu}_\mu$ beam. It will be assumed in Chapter 8 where the potential of LENA in an LBNO experiment with a neutrino beam is evaluated. Other concepts for accelerator-based neutrino production, like a *cyclotron-based decay-at-rest neutrino source* [156, 157], a *beta-beam* [158, 159] or a *neutrino factory* [159, 160], are not discussed here.

The original concept for an accelerator-based neutrino source is the *conventional* ν_μ / $\overline{\nu}_\mu$ *beam*. It was proposed around 1960 and first realized in the experiment proving the existence of the second neutrino flavor [9]. A review describing technical aspects of this type of machine, including historical background, can be found in Ref. [161]. Based on the illustration of the technical concept of a conventional neutrino beam in Figure 2.10, the primary components of such a neutrino source and their application to produce the final beam of ν_μ's or $\overline{\nu}_\mu$'s from accelerated protons are now described.

The first stage of the machine accelerates bunches of protons up to the intended energy and frequently brings some bunches to collision with a stationary target. Both the average number of protons filled to a bunch and the frequency of proton bunches striking the designated target affect the intensity of the final neutrino beam. The energy of a proton influences the count, types and momenta of the secondary particles produced in the interaction with the nuclear target material. These variables have an impact on the final neutrino energy spectrum. Today's proton accelerators for conventional ν_μ / $\overline{\nu}_\mu$ beams reach proton beam powers of up to some hundreds of kilowatt [11]. However, concepts for future projects with so-called *conventional neutrino superbeams* aim for proton beam powers at some MW [72, 73, 75]. An alternative measure for the power of a given accelerator-based neutrino beam is the number of *protons on target* (POT) per time unit at a given energy. This

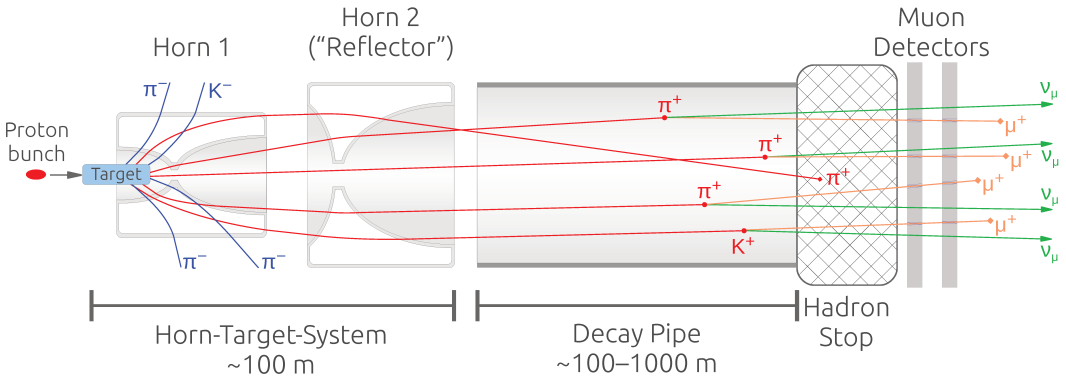

Figure 2.10 – Illustration of the concept to produce a conventional ν_μ / $\overline{\nu}_\mu$ neutrino beam. The shown generic setup is not necessarily complete with respect to existing beam line realizations. Moreover, the elements are not to scale and their count and positioning can vary. For details see text.

quantity is related to the number of neutrinos produced per time unit with the given machine.

Due to the rapidly impinging particle bunches, the target material must be capable to withstand high power densities and mechanical stress resulting from the alternating phases of heating and cooling. Common choices are graphite, Be or Al [11, 161]. Secondary particles from the proton interactions with the target material, mainly pions and kaons, can leave the interaction region in all directions but have a relativistic boost in the momentum direction of the incoming proton. Since the trajectories of the electrically neutral neutrinos cannot be changed with electromagnetic fields after their creation, a maximization of the neutrino flux in beam direction requires an early focusing of the charged secondaries produced in the target. This is done with a magnetic lens system consisting of one or more so-called *horns*: A pulsed electric current in the specially shaped structure creates a funnel-like magnetic field inside the horn. This field alters the momentum direction of through-going charged mesons towards the destined neutrino beam axis. Additional focusing horns further downstream redirect under- or over-focused mesons and thus further improve the directionality and intensity of the meson beam. The shapes of the horns and their relative positioning with respect to each other and with respect to the target critically affect the spectrum of secondary momenta focused by the magnetic lens system. Since the momentum spectrum of the focused secondaries translates to the later neutrino energy spectrum, a fixed optimization or even in-situ variation of the underlying parameters allows to tune the neutrino energy distribution for the experimental needs.

A neutrino beam focused with a horn-based system often exhibits a wide spectrum of neutrino energies and is commonly referred to as *wide band beam* (WBB) . With some technical modifications, the range of secondary momenta selected for focusing in or after the first horn can be narrowed to obtain a *narrow band beam* (NBB) . A similar effect—a narrower neutrino energy spectrum at the cost of flux intensity—can be achieved by placing the neutrino detector a few degrees off the axis of a WBB. This concept of an *off-axis beam* was realized in the T2K and NOνA experiments,

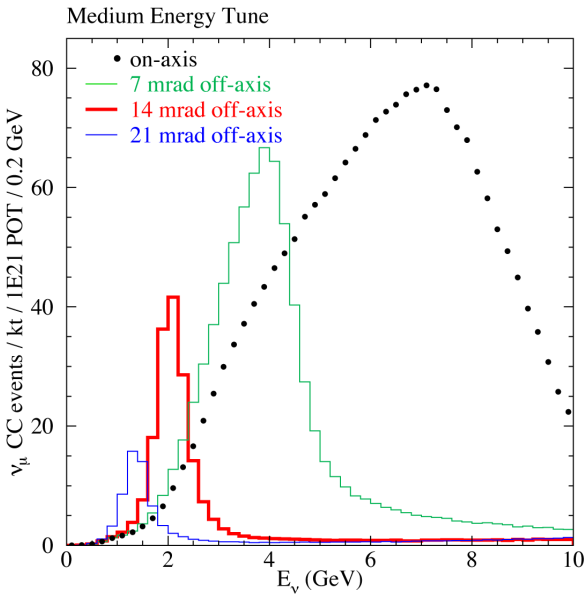

Figure 2.11 – Unoscillated ν_μ CC event rate spectra predicted for NOνA at different off-axis angles to the NuMI beam with medium energy configuration. The beam starts at the ∼800 km distant FNAL. Figure from Ref. [162].

where the detectors were placed ∼2.5° [63] and ∼0.8° [67] away from the centers of their neutrino beams, respectively. As an example, Figure 2.11 shows unoscillated ν_μ CC event rate spectra predicted for the NOνA experiment at different off-axis angles relative to its neutrino beam. For further details on horn-based focusing see Ref. [161].

Downstream of the target–horn-system, which spans ∼100 m in length, a *decay pipe* defines a dedicated volume where the focused mesons decay in flight and create neutrinos and antineutrinos according to the decays (2.11) to (2.17). With increasing energy of the accelerated protons, the energy of the single mesons may increase as well and can reach several tens of GeV. Since the momentum of the decaying meson determines the relativistic boost for the produced neutrino, lower meson energies lead to a less focused neutrino beam. To minimize defocussing of the final neutrino beam from meson scattering on air molecules, the decay pipe is often evacuated or filled with a light gas like helium. Due to relativistic effects, the decay pipe's length (typical values are on the order of several hundreds of meters) sets an upper limit on a meson's kinetic energy in order to have a high probability for a decay in flight. However, the decay pipe must not be too long in order to prevent numerous decays of muons (see (2.18)), which are also produced by in-flight decays of mesons and lead to contamination with ν_e and $\overline{\nu}_e$. The pipe's extent thus influences the final neutrino (antineutrino) energy spectrum and flux composition. Nondecayed mesons and protons passing through the target without interaction become absorbed in a *hadron stop* at the downstream end of the decay pipe. It is often comprised of blocks of high-density materials like Fe or Pb. Neutrinos from the decays of stopped meson are of low energy and can be neglected. Muons can pass through the hadron stop. Their profile allows to monitor the neutrino beam alignment with

Table 2.2 – Overview on proton synchrotrons used to produce conventional ν_μ / $\overline{\nu}_\mu$ beams: the *Super Proton Synchrotron* (SPS) at the CERN, the *Main Ring* at the *Japan Proton Accelerator Research Complex* (J-PARC) and the *Booster* and the *Main Injector* at the FNAL. Values in parentheses are design values for ongoing or planned machine upgrades. The SPS-driven CNGS neutrino beam from CERN stopped operation in 2012. The average on-axis neutrino energy of the NuMI beam in medium energy configuration from FNAL was estimated from the corresponding ν_μ CC event spectrum shown in Figure 2.11 (take cross-section into account). Remaining data cited from Ref. [11].

Facility	SPS (CERN)	Main Ring (J-PARC)	Booster (FNAL)	Main Injector (FNAL)
Date	2006–2012	2009	2002	2013
Proton kinetic energy [GeV]	400	30 (50)	8	120
POT per cycle [10^{12}]	48	123 (330)	4.5	(49)
Cycle time [s]	6	2.48 (3.5)	0.5	(1.333)
Beam power [kW]	510	240 (750)	12	(700)
Target	Graphite	Graphite	Be	Graphite
Beam type Focusing	WBB 2 horns	off-axis 3 horns	WBB 1 horn	WBB; off-axis 2 horns
Mean neutrino energy [GeV]	17	0.6	1	$\sim 6^a$ 2^b
Experiments	ICARUS OPERA	T2K	MiniBooNE MicroBooNE SciBooNE	NOνA^b MINERνA^a MINOS+^{a}

[a] on-axis
[b] off-axis

dedicated instrumentation. An overview on existing accelerator-based facilities for the production of conventional ν_μ / $\overline{\nu}_\mu$ beams is given in Table 2.2.

The primary beam flux component, ν_μ or $\overline{\nu}_\mu$, can be selected with the horns by adjusting their magnetic field directions via the polarity used to create the underlying electric currents. In the *positive horn focusing* (PHF) mode, positively charged particles are focused in beam direction whereas negatively charged particles become defocused. Since the decays of π^+ and K^+ create μ^+, the primary neutrino flux component is made of the associated ν_μ's. Correspondingly, the primary flux component is $\overline{\nu}_\mu$ if negatively charged particles are focused in the *negative horn focusing* (NHF) mode. However, the yield of $\overline{\nu}_\mu$'s produced in NHF running is lower than the yield of ν_μ created in PHF mode for an equal number of POT. This is because the in any case positive charge of the impinging protons translates to a production ratio of positively charged mesons to negatively charged mesons greater than one.

A conventional ν_μ WBB flux produced in PHF mode is never pure but can contain up to $\sim$10 % [161, 163] contamination of $\overline{\nu}_\mu$ from the decays of negatively charged mesons. The opposite holds for the NHF case. Moreover, the decays of $\mu^\pm$ (see (2.18)) and K_L^0 (see (2.16)) introduce ν_e and $\overline{\nu}_e$ flux contaminations at $\lesssim 1\,\%$. Again, ν_e contamination dominates over $\overline{\nu}_e$ in PHF mode while the opposite is true for NHF running.

In general, predictions on the absolute neutrino flux and the spectra of the primary and contamination components for a given proton energy and beam line setup is difficult and prone to large uncertainties. As shortly discussed in Ref. [161] together with other sources of uncertainties, especially unknowns regarding hadron production in the target can lead to uncertainties in the neutrino flux of about 20–30 %. The lack of precise knowledge on the neutrino beam intensity and flux composition translates to systematic uncertainties for experiments relying on this information, e.g., experiments studying neutrino oscillations. For beam-based experiments searching for leptonic CP-violation [63, 67, 72–75], the impact of systematic uncertainties on their sensitivities depends on the actual experimental setup [164]. Nevertheless, in order to maximize an experiment's performance, control over systematic uncertainties is important. Measuring the (almost) unoscillated neutrino flux spectra close to the production zone with a dedicated near-detector helps to reduce related uncertainties. For example, this is done by MINOS, T2K and NOνA.

Chapter 3

Function Principle of Liquid Scintillator Particle Detectors

The application of scintillating material for the detection of charged particle radiation is among the standard techniques of nuclear and particle physics [165]. Its properties not only allow to detect the presence of charged particles but also enable a *calorimetric measurement* of their total energy deposition in the scintillator. In liquid form, huge amounts of the substance can be handled with reasonable effort to construct one part of a particle detection apparatus—or even its core component. Moreover, large amounts of LSc can be purified more easily than corresponding masses of solid material, especially after the initial deployment.
In neutrino physics, LSc is employed to detect the charged particle products of neutrino interactions (see Chapter 4). The focus in this application is on LE neutrinos with energies up to some tens of MeV from different kinds of sources (see Chapter 2). Together with neutrino detectors based on water or ice (e.g., SK and IceCube), which utilize the *Cherenkov effect* to detect charged particles, or LAr, the LSc-based neutrino detectors often belong to the class of *unsegmented* detection devices.[1] An apparatus of this type has its entire neutrino target material homogeneously distributed in a single volume that is monitored by multiple readout-sensors as a whole. In the following, the focus is exclusively on unsegmented LSc detectors. This chapter describes the basic function principle of a LSc-based charged particle detector. The overviewed theory, which—summarized in abstract terms—includes the production, propagation and detection of information, is fundamental to the charged particle track reconstruction algorithm presented in Chapter 6.

Section 3.1 details the production of scintillation and Cherenkov light in organic LSc in response to a charged particle traversal. After that, Section 3.2 deals with the propagation of the created light through the detector medium. Some technical aspects of the light detection and the subsequent processing of the measured signal are covered in Section 3.3. Finally, the energy resolution of a LSc detector is subject of Section 3.4.

[1] In a *segmented* (LSc) detector the target material is distributed among cells with their own readout-devices. Examples of this type are the near- and far-detectors of the NOνA experiment [67].

3.1 Light production in a liquid scintillator detector

Particle detectors on the basis of a scintillating material use the substance's property of *luminescence*, i.e., the behavior to convert excitation energy other than heat to ultraviolet or visible light with a characteristic spectrum. For example, the energy to excite the material can come from mechanical stress, chemical reactions or impacting radiation. Depending on the scale of the time τ between excitation and light emission, the luminescence process is named *fluorescence* if $\tau \sim 10^{-9} - 10^{-8}\,\mathrm{s}$ or *phosphorescence* if $\tau \gtrsim 10^{-4}\,\mathrm{s}$ [166]. Scintillators are available in gaseous, liquid and solid states. One distinguishes organic scintillators, which consist of hydrocarbon molecules with aromatic rings, and inorganic scintillators. They differ in the process of how excitation energy is converted to emitted light. Examples for organic LSc solvents are *linear alkylbenzene* (LAB, $C_{18}H_{30}$)[2], *phenyl-o-xylylethane* (PXE, $C_{16}H_{18}$) and *1,2,4-trimethylbenzene* (pseudocumene, C_9H_{12}).
Two important aspects of the application of scintillating material in a charged particle detector are the dependence of the scintillation light output on the amount of deposited energy as well as the temporal correlation between the energy deposition from a particle and the emission of the scintillation light. While the former point affects the inference on the particle energy from the number of detected scintillation photons, the latter is decisive for the spatial localization of the particle based on the time structure of the detected light.
When a charged particle traverses LSc, light is not only produced from scintillation but also via the *Cherenkov effect*. The following parts of this section detail the production and some properties of scintillation light in Section 3.1.1 and of Cherenkov radiation in Section 3.1.2.

3.1.1 Scintillation light

When a charged particle passes through a scintillator, it transfers energy to the electrons of the atoms constituting the luminescent matter. In the case of a moderately relativistic charged particle heavier than an electron and an absorber material of intermediate atomic number Z, the mean electronic energy loss per unit length $\langle -\,\mathrm{d}E/\,\mathrm{d}x\rangle$ is well-described by the *Bethe-equation* discussed in Ref. [11]. For values of $0.1 \lesssim \beta\gamma \lesssim 1000$, where γ is the *Lorentz factor* and β is the particle's speed as fraction of the speed of light in vacuum c_0, the equation describes the mean rate of energy loss with an accuracy of a few percent. For electrons and particles outside of a certain energy range, additional (radiative) corrections, like the *Bloch-correction*, must be applied.
In an organic scintillator, which is assumed through the rest of this work, the energy transfer to the atomic shells leads to excited electronic states in the scintillator molecules. Subsequent transitions of electrons to lower energy levels create scintillation photons that are emitted isotropically with an energy spectrum characteristic for the scintillator. In order to shift the emitted wavelengths to a regime where the scintillator is more transparent, one or more organic *wavelength-shifter solutes* (e.g., *2,5-diphenyloxazole* (PPO, $C_{15}H_{11}NO$) or *1,4-Bis(2-methylstyryl)benzene* (bis-MSB, $C_{24}H_{22}$)) are commonly added to the basic scintillator solvent. Details concerning

[2] A general formula for LAB is $C_6H_5C_nH_{2n+1}$, with n typically being 10–16.

wavelength-shifting and the scintillation process from state transitions of electrons in an organic scintillator molecule are given in Appendix B.

Scintillation light yield The luminescence per unit length $\mathrm{d}\mathscr{L}/\,\mathrm{d}x$ of a scintillator depends on the *differential energy loss* $\mathrm{d}E/\,\mathrm{d}x$ of the traversing charged particle. About 3 % of the deposited energy are released as optical photons [11]. However, the response of an organic scintillator to an energy deposition is not linear. As pointed out in Refs. [11, 166], *quenching effects* like high ionization densities along a particle track, e.g., from a proton or α-particle, reduce the luminescence light yield compared to a value $\mathscr{L}_0$ expected at low specific ionization densities. Typically, $\mathscr{L}_0$ is one photon per 100 eV of deposited energy for organic scintillators [11]. A commonly used semi-empirical model for the light yield, which respects quenching effects, is described by *Birks' formula* [11],

$$\frac{\mathrm{d}\mathscr{L}}{\mathrm{d}x} = \mathscr{L}_0 \frac{\frac{\mathrm{d}E}{\mathrm{d}x}}{1 + kB\,\frac{\mathrm{d}E}{\mathrm{d}x}}\,. \tag{3.1}$$

It depends on the *Birks' constant* kB. This constant is material-dependent and must be deduced from measurements. As an example, the value of $kB = 0.011\,\mathrm{cm\,MeV^{-1}}$ is used for Borexino's pseudocumene-based LSc solution [30].

Scintillation pulse shape The radiative decay of an excited electron state in a molecule of the scintillator compound is a statistical process. Since the decay rate of the excited states is proportional to their populations, this process can be mathematically described by an exponential decay function. An overall description of the temporal evolution of the scintillation light emission—the *luminescence pulse shape* of the scintillator—must take into account decays of different excited states and slower decay components (see also Appendix B). Assuming a negligible rise time of the pulse, a good approximation of the pulse shape is a weighted sum of exponential decay functions [166]. Therefore, the *probability density function* (p.d.f.) $\Phi_{\mathrm{em}}(t)$ for the photon emission time t with n decay components can be written as

$$\Phi_{\mathrm{em}}(t; \boldsymbol{\tau}, \boldsymbol{\omega}) = \sum_{i=1}^{n} \frac{\omega_i}{\tau_i} e^{-\frac{t-t_0}{\tau_i}}\,, \quad t \geq t_0\,, \quad \sum_{i=1}^{n} \omega_i = 1\,. \tag{3.2}$$

The parameter t_0 is the point in time of the excitation and $\boldsymbol{\tau} = \{\tau_1, \ldots, \tau_n\}$ and $\boldsymbol{\omega} = \{\omega_1, \ldots, \omega_n\}$ are the mean lifetimes and weights of the different components, respectively. Because energy depositions of different charged particles in LSc lead to different populations of the various electron states, the combination of $\boldsymbol{\tau}$ and $\boldsymbol{\omega}$, and thus the shape of $\Phi_{\mathrm{em}}(t; \boldsymbol{\tau}, \boldsymbol{\omega})$, is particle-dependent. This feature is exploited to discriminate scintillation signals from different particles, e.g., from protons, α-particles and electrons / positrons, for the purpose of background reduction [167].

3.1.2 Cherenkov radiation

Cherenkov radiation is emitted as a *coherent response* of a dielectric medium with refractive index $n > 1$ to the passage of a charged particle at speed greater than

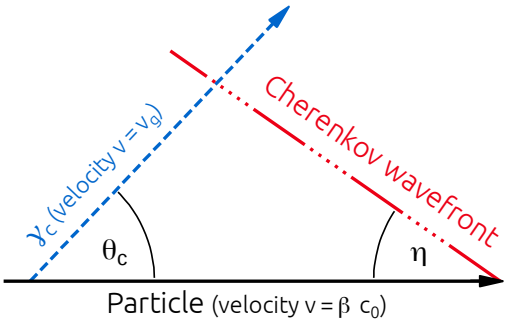

Figure 3.1 – A Cherenkov photon γ_c (*blue*) is emitted under the characteristic angle θ_c with respect to the momentum direction of the charged particle (*black*) moving with speed $v = \beta c_0$. The photon propagates with the group velocity $v = v_g$ through the dispersive medium. Constructive interference of the Cherenkov light waves forms a light cone (*red*) with vertex at the moving charge and opening half-angle η.

the *local phase velocity* of light in that medium [168]: The through-going particle polarizes the matter around its track. This polarization leads to a distortion of the local electric field that dissipates through the emission of electromagnetic waves. As a result of the transfer of the polarization energy, the particle loses energy along its path. However, the Cherenkov process is only a negligible contribution to the total energy loss of a charged particle in matter: In condensed materials, the energy loss of a charged particle due to the Cherenkov effect is $-(\mathrm{d}E/\,\mathrm{d}x)_c \simeq 10^{-3}\,\mathrm{MeV\,cm^2\,g^{-1}}$ [165]. This is about two to three orders of magnitude smaller than the energy loss from ionization.

Cherenkov angle Cherenkov photons have the characteristic property that they are emitted under a defined *Cherenkov angle* θ_c with respect to the particle's momentum direction:

$$\cos\theta_c = \frac{1}{\beta n(\epsilon)}\,. \tag{3.3}$$

The medium's refractive index $n(\epsilon)$ depends on the energy ϵ associated with the photon wave package. With β being the particle's speed as a fraction of the speed of light in vacuum, Equation (3.3) implies a medium-dependent threshold velocity $\beta_t = 1/n(\epsilon)$ that must be exceeded to produce Cherenkov photons with energy ϵ. A list of threshold velocities in four common materials for large-scale neutrino detection is given in Table 3.1, together with the respective (kinetic) energy thresholds for different particles. The disexcitation of the polarization from the charged particle passage is slower compared to the speed $v = \beta c_0$ of the particle. Therefore, as one can see in Figure 3.1, the emitted Cherenkov light waves, which propagate with the *group velocity* v_g (see Section 3.2.1), interfere constructively and create a cone with opening half-angle η and vertex at the moving particle. The existence of a group velocity for the Cherenkov photons implies a dispersive medium, $\mathrm{d}n(\epsilon)/\,\mathrm{d}\epsilon \neq 0$. In this case $\theta_c + \eta \neq 90°$ holds [11].

Cherenkov light yield The number of Cherenkov photons N emitted per unit path length $\mathrm{d}x$ and per unit photon energy interval $\mathrm{d}\epsilon$ for a particle with charge ze,

Table 3.1 – List of threshold velocities β_t for the Cherenkov effect in ice (−7 °C) [169], water (25 °C) [170], LAB ($C_{18}H_{30}$) [40] as an example for LSc, and LAr [171] together with resulting (kinetic) energy thresholds for different particles. All refractive indices are at 430 nm wavelength. The energy threshold for the γ-ray was determined such that a maximum momentum transfer from *Compton scattering* accelerates the recoil electron to the threshold velocity.

	Material			
	Ice	Water	LAB (LSc)	LAr
Ref. index n	1.32	1.34	1.49	1.23
Thr. velocity β_t	0.758	0.746	0.671	0.813
Particle	(Kinetic) Energy Threshold [MeV]			
$e^{\pm}$	0.272	0.257	0.178	0.367
$\mu^{\pm}$	56.2	53.1	36.9	75.8
$\pi^{\pm}$	74.3	70.2	48.8	100.3
$K^{\pm}$	262.6	248.0	172.3	354.2
p	499.1	471.3	327.4	673.2
γ (Compton)	0.432	0.415	0.320	0.540

where e is the elementary charge, follows from the *Frank-Tamm-formula* [11]:

$$\begin{aligned} \frac{\mathrm{d}^2 N}{\mathrm{d}\epsilon\,\mathrm{d}x} &= \frac{\alpha z^2}{\hbar c}\sin^2\theta_c(\epsilon) = \frac{\alpha z^2}{\hbar c}\left(1 - \frac{1}{\beta^2 n^2(\epsilon)}\right) \\ &\approx 370\,\sin^2\theta_c(\epsilon)\,\mathrm{eV}^{-1}\,\mathrm{cm}^{-1} \quad (z=1)\,, \end{aligned} \tag{3.4}$$

where α is the fine structure constant. Compared to scintillation light, Cherenkov photons contribute only a few percent to the total light yield in LSc.
In general, Cherenkov radiation is emitted with a continuous energy spectrum. However, as one can see from Equation (3.4), a positive, non-zero number of photons is emitted only if $\beta n(\epsilon) > 1$ holds. Therefore, Cherenkov light is emitted in spectral bands [165, 168].

3.2 Light propagation in a liquid scintillator detector

All scintillation and Cherenkov photons carry information on the total deposited energy and the time structure of the original event in the LSc detector. In order to resolve this structure—with the aim to localize the event in space and time—the transport of the timing information by the photons through the detector medium must be considered. The photon speed in a medium is topic of Section 3.2.1. Possible effects that make a photon disappear or change its flight direction are subject of Section 3.2.2. Such changes to the photon properties alter the available information on the photon's origin and creation time.

3.2.1 Photon speed

Using the approximative assumption of a non-dissipative medium with refractive index $n > 1$ and normal dispersion, i.e., $\mathrm{d}n/\mathrm{d}\epsilon' > 0$, the speed v of a photon with

energy ϵ, which is described as a wave package, is given by the *group velocity*[3] v_g [168]:

$$v \equiv v_g = \frac{c_0}{n(\epsilon) + \epsilon \, \frac{\mathrm{d}n}{\mathrm{d}\epsilon'}|_\epsilon} \, . \tag{3.5}$$

This allows to determine a photon's *time of flight* (TOF) between two spatial points.

3.2.2 Light attenuation

In addition to the transportation speed of the information carried by a photon, effects deteriorating the information's quality must be considered when inference on its origin shall be made.

Absorption, scattering and reflection While scintillation and Cherenkov photons propagate through the detector medium, they are subject to absorption and scattering effects. The relevant microscopic processes include *Rayleigh scattering* on the bound electrons of the scintillator solvent, *Mie scattering* from impurities in the liquid and absorption of the light by molecules [172]. Scattering and absorption with subsequent re-emission effectively change a photon's momentum direction. As the trajectory of a photon cannot be reconstructed, a reliable determination of the original event location in general requires timing information from unscattered photons. However, scattered and unscattered photons cannot be distinguished and so the above-mentioned effects introduce a deterioration of the available information to localize the underlying event. The same holds in the case of diffuse and specular photon reflections at surfaces surrounding the LSc volume. Absorption and subsequent conversion of the photon energy to an undetectable form, e.g., heat, in addition degrade information on the deposited energy.
Ignoring reflection, the p.d.f. for a photon to be scattered or absorbed as a function of distance $x = |\mathbf{x} - \mathbf{x}_0|$ from the source at $\mathbf{x}_0$ can be written in terms of an *attenuation length* L as [172]

$$\Phi_{\mathrm{att}}(x; L) = \frac{1}{L} e^{-\frac{x}{L}} \, . \tag{3.6}$$

Attenuation length The attenuation length L can be broken down into contributions from the individual microscopic processes, which are again parameterized in terms of characteristic lengths l_α :

$$\frac{1}{L} = \frac{1}{l_{\mathrm{A}}} + \frac{1}{l_{\mathrm{S}}}; \quad \frac{1}{l_{\mathrm{S}}} = \frac{1}{l_{\mathrm{are}}} + \frac{1}{l_{\mathrm{ray}}} + \frac{1}{l_{\mathrm{mie}}}. \tag{3.7}$$

The individual characteristic lengths are the absorption length (l_{A}), the scattering length (l_{S}), the absorption/re-emission length (l_{are}), the Rayleigh scattering length

[3] It is assumed that the wave package's spectrum of the wave number k is not too broad or that the wave propagates in a medium with only weak dependence of the wave number on the frequency ω. This allows to expand $\omega(k)$ as $\omega(k) = \frac{\mathrm{d}\omega}{\mathrm{d}k}|_0 (k - k_0) + \dots$ and to identify the group velocity as $v_g = \frac{\mathrm{d}\omega}{\mathrm{d}k}|_0$ [168]. The angular frequency ω is finally replaced according to the quantum mechanical relation $\omega = \epsilon/\hbar$ to obtain Equation (3.5).

(l_{ray}) and the Mie scattering length (l_{mie}).
It has to be taken into account that the scattering includes contributions from both isotropic processes (absorption with re-emission) and anisotropic processes (Rayleigh scattering). Therefore, the scattering length l_{S} can also be expressed in terms of isotropic (l_{iso}) and anisotropic (l_{ani}) scattering lengths,

$$\frac{1}{l_{\mathrm{S}}} = \frac{1}{l_{\mathrm{iso}}} + \frac{1}{l_{\mathrm{ani}}} \,. \tag{3.8}$$

Moreover, the characteristic lengths, and thus the attenuation length, depend on the photon energy ϵ: $l_\alpha = l_\alpha(\epsilon)$ and $L = L(\epsilon)$. They are characteristic for each scintillator material.

Due to the influence of photon scattering and absorption on the event time and event energy resolution capabilities of a LSc detector, the careful choice of a suitable scintillator mixture is a critical item at the design phase of an experiment using this technology. The absorption of scintillation light effectively puts an economic limit on the dimensions of the detector. Above that limit, the advantage of adding more target mass to increase the observed event rate is diminished by unjustifiable losses of statistics quality due to deteriorated light information quantity and quality. In order to push the economic limit beyond current bounds imposed by achievable attenuation lengths of $\sim 20\,\mathrm{m}$ (reported for a LAB sample in Ref. [43]), the idea to solve organic LSc in water is investigated [173]. Although the total light yield of such a water-based LSc is smaller compared to a pure organic mixture, the higher transparency of water ($\sim 100\,\mathrm{m}$ attenuation length) increases the photon absorption and scattering lengths. Therefore, water-based LSc enables much larger detector dimensions.

3.3 Light detection in a liquid scintillator detector

The collection of the scintillation and Cherenkov photons and their conversion into a measurable signal with subsequent digitization mark the final steps to obtain a storable and analyzable set of information on the physical event in a LSc detector. They are commonly realized by the installation of photosensors with an attached chain of electronic devices to process the analog sensor signal and to convert it to digital format.
A type of photosensor that is often employed in experiments with neutrino detectors using LSc or the Cherenkov effect is the *photomultiplier tube* (PMT) [165, 174]. It is explained in Section 3.3.1. As shortly described in Section 3.3.2, a *light concentrator* can be mounted onto the PMT to increase its effective light collection area. Some basic information on read-out electronics and processing of the signals from the PMTs is given in Section 3.3.3.

3.3.1 Photomultiplier tube

In general, the basic concept of a PMT allows for different technical designs (e.g., see Ref. [174]). One example is depicted in Figure 3.2. It consists of three main components: A *transmission photocathode* behind an input window converts an incident

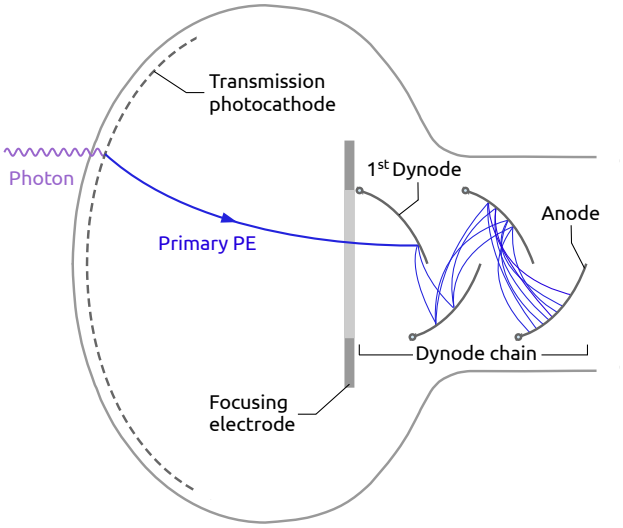

Figure 3.2 – Schematic of a PMT with transmission photocathode and linear-focused dynode structure.

photon to an electron via the photoelectric effect. The transmitted *photoelectron* (PE) is focused and accelerated into a chain of electrodes under high-voltage, so-called *dynodes*. In the chain, the number of freed electrons becomes repeatedly multiplied by knocking-out more electrons from the successive dynodes and accelerating them in an electric field. Depending on the number of dynodes and the potential difference between the dynode stages, the cascade of secondary emission processes leads to an amplification of the initial PE by a factor typically between 10^3 and 10^8. The electron avalanche is finally collected at the *anode* and sent to an external electronic circuit as measurable current. All components are contained in an evacuated housing to minimize the disturbance of the electron trajectories from scattering on gas molecules.

Quantum efficiency of the photocathode The *quantum efficiency* (QE) of the PMT photocathode $\eta_{\mathrm{PMT}}(\epsilon, \mathbf{x})$, i.e., the number of output PEs N_{e} per incident photons $N_\gamma(\epsilon, \mathbf{x})$, describes the probability that an incident photon is actually converted to an electron at point $\mathbf{x}$ on the cathode:

$$\eta_{\mathrm{PMT}}(\epsilon, \mathbf{x}) = \frac{N_{\mathrm{e}}}{N_\gamma(\epsilon, \mathbf{x})} \,. \tag{3.9}$$

This PMT property depends on the photoelectric work function of the cathode's material composition and on the energy ϵ of the incident photon. The energy-dependence of a PMT's QE should match the wavelength-shifted emission spectrum of the LSc for maximum efficiency of the scintillation photon detection. Examples for common photocathode materials are presented in Ref. [174] along with the wavelength-dependence of their QE.

Transit time through the PMT Since the passage of a growing electron bunch from the cathode through the dynode chain to the anode is a random process, the

corresponding *transit time* T with respect to a bunch's reference point, i.e., its center of charge, is a random variable. It can be expressed in terms of an average transit time $\overline{T}$ and a fluctuation δT, $T = \overline{T} \pm \delta T$. The usually asymmetric statistical distribution of δT, $\Phi_{\delta T}$, is commonly characterized by the *transit time spread* (TTS) ΔT. Both $\overline{T}$ and $\Phi_{\delta T}$ depend on the geometry and the size of the PMT, i.e., the typical parameters $\overline{T}$ and ΔT in general increase with growing dimension of the device.
Tasks like event localization and charged particle track reconstruction rely on the information contained in the photon detection times at single PMTs. While the average signal transit time through a PMT can be easily taken into account as a constant contribution to the measured photon detection time, the random fluctuation δT affects the time resolution and thus the performance of the above-mentioned tasks.

Spurious signal pulses Besides the signal pulse from an amplified PE, some phenomena can create spurious pulses at the anode. They deteriorate the time and energy resolution of the PMT.
Dark current originates from collected electrons that emerged via thermionic emission at the cathode or the dynodes, field emission, leakage current or radioactivity in the PMT material. The rate of these spurious pulses increases with higher supply voltage and temperature of the electrodes [165, 174].
A *pre-pulse* appears if a photon produces a PE not at the cathode but at the first dynode or the focusing electrode (see (1) in Figure 3.3). This PE creates an earlier pulse with lower amplitude than a PE from the cathode would do (see also Ref. [175]). If the pulse amplitude is not analyzed, the pre-pulse leads to the false assignment of a too early photon arrival time. Moreover, if multiple photons arrive at the PMT simultaneously, the pre-pulse preceding the main-pulse with a strong temporal correlation is likely misidentified as a separate photon hit.
After-pulses occur some time after the main signal pulse. As indicated by (3) in Figure 3.3, ES of an electron at the first dynode can produce a pulse with a short delay in the range from several nanoseconds up to several tens of nanoseconds. An after-pulse with a delay at the order of some hundreds of nanoseconds up to a few microseconds may arise from a positively charged ion that is created in an interaction of an accelerated electron with residual gas in the PMT. As shown by (2) of Figure 3.3, the ion is attracted towards the photocathode where its impact knocks out electrons. Some of these freed electrons are then accelerated into the dynode chain, become amplified and finally produce a delayed current pulse [174].

3.3.2 Light concentrator

A cheap possibility to enhance the light collection of a single PMT is the installation of a *light concentrator*, e.g., a *Winston cone*, at its front face. As schematically depicted in Figure 3.4, it has the shape of an off-axis parabola of revolution and a reflective inner surface.
Photons coming through the larger entrance aperture of the concentrator can get directly to the smaller exit aperture towards the opening window of the PMT or with reflections at the inner surface. With this type of construction, for example used

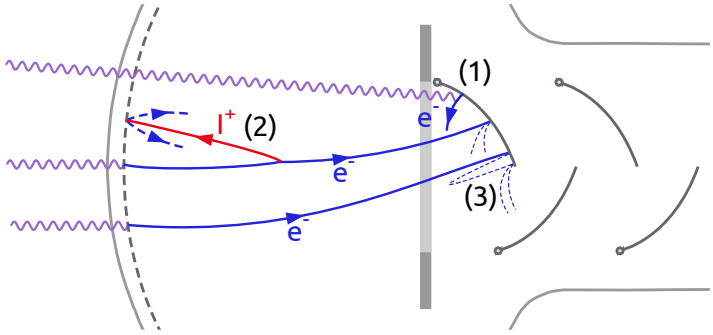

Figure 3.3 – Origins of spurious signal pulses in a large PMT. A pre-pulse (1) may be the result of a PE production behind the photocathode, e.g., at the first dynode. An after-pulse can occur due to (2) the creation of a positively charged ion I^+ that knocks out additional electrons at the photocathode or due to (3) ES of a PE at a dynode. The different PMT components are named in Figure 3.2.

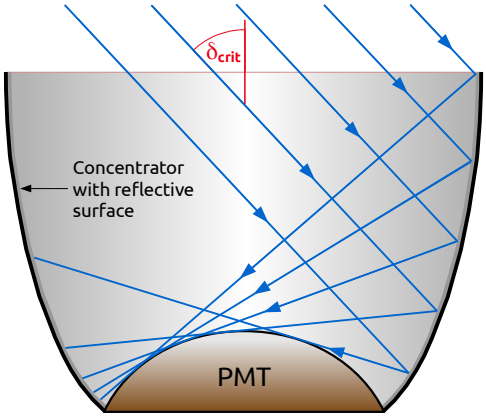

Figure 3.4 – Schematic of a light concentrator with critical angle δ_{crit}.

in Borexino [176], the effective light collection area for a single PMT is increased. This allows to reduce the overall number of photosensors required to obtain the same optical coverage. However, the light guide decreases the angular acceptance of each PMT: A photon coming through the entrance aperture with an incident angle above a certain critical angle δ_{crit} has a high probability of being reflected back through the entrance.

3.3.3 Read-out electronics

The first step in processing the PMT singal is to convert the current pulse from the PMT anode to a corresponding analog voltage signal. This can be done by measuring a voltage drop at a load resistor. A threshold for the voltage drop amplitude allows to discriminate noise, e.g., dark current, from true photon signals. However, it must be chosen carefully in order to balance the accepted noise level against the probability of rejecting amplified PEs from light signals. This is difficult, for example, in the case of single-photon detection.

The layout of the *data acquisition system* (DAQ) is crucial for an experiment's performance. Concerning processing and storage of PMT signals in digital format for later analysis, two basic approaches can be distinguished: In the *charge integration* mode, the integral over the signal pulse is digitized. This quantity is related to the total amount of collected charge. If the photon rate at the PMTs is sufficiently low, the obtained value is proportional to the total number of detected PEs. However, if multiple photon hits at one PMT overlap in time, the PMT's response to the pileup of PE pulses is not necessarily a simple superposition of single PE pulses. This is due to electronic effects (e.g., drain of electrostatic charge) which require a short period of time for a PMT to return to its normal standby state after a photon hit. Hence a high rate of photon hits might introduce an error to the integrated charged and finally to the energy determination. Moreover, the charge integration mode does not resolve the full time structure of photon hits. Therefore, a thorough track reconstruction, which relies on the information contained in the photon hit time distributions at the PMTs, is complicated.
With a view on a detailed topological reconstruction of an event in LSc, *pulse shape sampling* is a more preferable mode of operation for the DAQ. In this case, the temporal evolution of a PMT's signal pulse amplitude is digitized with an *analog-to-digital converter* (ADC). The device's properties determine the precision of the signal amplitude sampling:

- The number of available ADC-bits together with the processable dynamic range of the signal define the achievable precision of an amplitude sample point.
- The sampling rate, e.g., one sample (S) per 1–2 ns (corresponds to 1–0.5 GS/s), determines the resolution of the signal's time behavior.

Given that the photon hits at a PMT are sufficiently separated in time, the individual photon hit times can in principle be extracted from the pulse shape. However, similar to charge integration, disentangling the pileup of PE pulses is difficult. A sophisticated approach to obtain an estimate for the number of PEs and their arrival time distribution in a multi-PE pulse is, for example, described in Ref. [177]. Compared to the charge integration mode, pulse shape sampling imposes higher demands on the electronics and produces more data to store.

3.4 Energy resolution of a liquid scintillator detector

In a LSc detector, not all of an event's *total energy* E is necessarily converted to a detectable form. Some amount of *invisible energy* E_{inv} may escape from the detection device (e.g., as a neutrino) or is converted to an undetectable form (e.g., in nuclear reactions). The remaining part of the *deposited energy* is the *visible energy* E_{vis} for which $E_{\text{vis}} < E$ often holds. An estimator $\hat{E}_{\text{vis}}$ for this quantity can be constructed from the total number of observed PEs, N_{PE}. Therefore, the energy determination with a LSc detector bases on a *calorimetric measurement*. Given some knowledge on the energy dissipation processes, an estimate for the invisible energy $\hat{E}_{\text{inv}}$ can be used to construct an estimator $\hat{E}_{\text{rec}}$ for the *reconstructed energy*, $\hat{E}_{\text{rec}} = \hat{E}_{\text{vis}} + \hat{E}_{\text{inv}}$ (e.g., see IBD signal in Section 4.1.1). By construction, this reconstructed energy estimate is an approximation for the total energy E. In order to translate N_{PE} to

$\hat{E}_{\mathrm{vis}}$ and finally to $\hat{E}_{\mathrm{rec}}$, the measurement device must be calibrated[4] (e.g., to account for the positional dependence of $N_{\mathrm{PE}}(E_{\mathrm{vis}})$). This also allows to assess the visible energy resolution $\sigma_{\hat{E}_{\mathrm{vis}}}$ of the measurement device.

A generic model for the *relative visible energy resolution* at E_{vis} of a LSc detector is given by [179]

$$\frac{\sigma_{\hat{E}_{\mathrm{vis}}}}{E_{\mathrm{vis}}} = \sqrt{\frac{A^2}{E_{\mathrm{vis}}/\mathrm{MeV}} + B^2 + \frac{C^2}{E_{\mathrm{vis}}^2/\mathrm{MeV}^2}}\,. \tag{3.10}$$

The model parameters A, B and C follow from the evaluations of the calibration measurements or MC simulations. The term with parameter A on the right-hand side of Equation (3.10) takes into account the statistical uncertainty on the random number of detected PE. From *Poisson statistics* it follows that the standard deviation $\sigma_{N_{\mathrm{PE}}}$ of N_{PE} is given by $\sqrt{N_{\mathrm{PE}}}$. If one further assumes that $N_{\mathrm{PE}} \propto E_{\mathrm{vis}}$ and $\sigma_{N_{\mathrm{PE}}} \propto \sigma_{\hat{E}_{\mathrm{vis,stat}}}$, the relative visible energy resolution due to statistical fluctuations can be defined as

$$\frac{\sigma_{\hat{E}_{\mathrm{vis,stat}}}}{E_{\mathrm{vis}}} = \frac{A}{\sqrt{E_{\mathrm{vis}}/\mathrm{MeV}}}\,. \tag{3.11}$$

For existing LSc-based neutrino detectors, the parameter A is $\lesssim 7\,\%$ [11, 148].
The remaining part of Equation (3.10) takes into account systematic uncertainties:

$$\frac{\sigma_{\hat{E}_{\mathrm{vis,sys}}}}{E_{\mathrm{vis}}} = \sqrt{B^2 + \frac{C^2}{E_{\mathrm{vis}}^2/\mathrm{MeV}^2}}\,. \tag{3.12}$$

Detector non-uniformity and energy leakage are covered by the term including parameter B. The contribution containing parameter C takes into account systematic uncertainties due to background and noise. Both parameters are $\sim$1 % [179]. Obviously, one obtains Equation (3.10) by adding the right-hand sides of Equation (3.11) and Equation (3.12) in quadrature.
Another important aspect is the *energy scale*, i.e., the effective translation of E_{vis} to $\hat{E}_{\mathrm{vis}}$. It is determined by calibration and includes the correction of deviations from the ideal case $\hat{E}_{\mathrm{vis}} = E_{\mathrm{vis}}$. However, the calibration measurements determine the energy scale only with finite precision due to random electronic noise, background events, etc. Resulting uncertainties contribute to the systematic term (3.12) of the relative visible energy resolution. Neglecting complex non-linearities, a simple way to parameterize the residual deviation of the energy scale from the perfect case $\hat{E}_{\mathrm{vis}} = E_{\mathrm{vis}}$ is [180]

$$\hat{E}_{\mathrm{vis}} = (1 + v)\, E_{\mathrm{vis}} + w\,. \tag{3.13}$$

Typical values for $|v|$ and $|w|$ are at the level of 1 % and 0.01 MeV, respectively [180]. They reflect the possible precision for the energy scale determination.

[4] For example, a detailed description of the calibration of BOREXINO can be found in Ref. [178].

Chapter 4

Liquid Scintillator Neutrino Detectors

A use of LSc in a neutrino detector was first reported in 1953 [5].[1] The experiment by *C.L. Cowan* and *F. Reines* resulted in hints on the existence of what is today known as $\overline{\nu}_e$. Its more famous follow-up experiment, which also used LSc, gave the final confirmation of the results in 1956 [6]. This marked the hour of birth of experimental neutrino physics.
Nowadays, the LSc technology is a successful standard tool for the detection of LE ν_e and especially $\overline{\nu}_e$ from terrestrial and astrophysical sources in the energy range from some hundreds of keV up to some tens of MeV. LSc neutrino detectors are perfectly suited to perform spectral measurements at this energy range due to their *good energy resolution* and the *absence of an intrinsic energy threshold*. This is complemented by a big variety of methods to reduce background from sources like intrinsic radioactivity or cosmogenic radioisotopes. As mentioned in Chapter 1 and Chapter 2, past and present experiments using up to some hundred tons of LSc as designated neutrino target already contributed valuable measurements to different research fields. Examples are the detailed observation of solar and geo-neutrinos by KamLAND and Borexino, the measurement of Δm^2_{21} and constraints on θ_{12} from KamLAND and the discovery of a non-zero value for θ_{13} by Daya Bay, Double Chooz and RENO. In order to resolve outstanding issues, like the confirmation of the DSNB or the determination of the neutrino MO, new experiments with several tens of kilotons of LSc are considered (LENA, RENO-50) or even prepared (JUNO).

General aspects of the real-time detection of LE neutrinos and antineutrinos with LSc are subject of Section 4.1, including an overview of important detection channels and background sources. The LENA project, which focuses on the detection of LE neutrinos and antineutrinos from astrophysical sources, is outlined in Section 4.2. It provides the context for the studies presented later in this work. Finally, JUNO and its goal to determine the neutrino MO are the main point of Section 4.3. The expected start of its data taking at the beginning of the next decade and its demand

[1] Reactor $\overline{\nu}_e$ were detected through IBD reactions on protons of the LSc [181, 182]. The *delayed coincidence technique* explained in Section 4.1.1 was applied.

for efficient cosmogenic background rejection make JUNO a likely application context for the reconstruction method explained in Chapter 6.

4.1 Real-time detection of low-energy neutrinos and antineutrinos with a liquid scintillator detector

Contrary to radiochemical neutrino experiments, e.g., with the Homestake detector [13, 14], the *real-time neutrino detection* allows to assign a precise time-stamp to every single event observed with the measuring apparatus. This concept is employed in essentially all modern LSc detectors. It allows *coincidence analyses* in space and time for an effective counting of neutrino interactions while simultaneously reducing the impact of background events. Two important LE neutrino and antineutrino detection channels for LSc are subject of Section 4.1.1. Different types of background for the detection of neutrinos and antineutrinos with energies up to some tens of MeV are discussed in Section 4.1.2, focusing on the effects from cosmogenic muons.

4.1.1 Detection channels

In the following, two major detection channels for LE neutrinos and antineutrinos in LSc are described: ES on an electron or proton and the *delayed coincidence technique* to tag IBD interactions of $\overline{\nu}_e$'s. Additionally, Appendix A provides information on the detection of neutrinos and antineutrinos through interactions with the carbon in the organic LSc.

Elastic scattering on an electron or proton An important detection channel for a neutrino ν_ℓ, especially from the Sun (see Section 2.1), or antineutrino $\overline{\nu}_\ell$ of flavor $\ell = e$, μ, τ from the LE domain up 100 MeV (see Section 1.2.1) is the ES on an electron, represented by reaction (1.13). This elastic process has no threshold for the (anti-)neutrino energy E_ν. However, it transfers only a fraction of E_ν to the electron, which subsequently produces a scintillation signal in the LSc detector with a visible energy $E_{\text{vis}} < E_\nu$. Even in the case of mono-energetic (anti-)neutrinos, the electron recoil spectrum is continuous and features a Compton-like edge. For E_ν being of several MeV, the struck electron is mostly scattered in forward direction. Due to the electron's short track, as a result of ionization losses and scattering, this remains invisible to a LSc detector.
Similar to ES on an electron, a neutrino or antineutrino can also scatter elastically off a proton (see reaction (1.15)). As a consequence of the larger proton mass and the quenching of the scintillation light signal, the recoil proton produces a much smaller signal than a recoil electron from a scattered ν_ℓ or $\overline{\nu}_\ell$ with the same E_ν. Nevertheless, this channel is particularly useful for the detection of (anti-)neutrinos from a core-collapse SN (see Section 2.2, Refs. [82, 183]).

Inverse beta decay / delayed coincidence One key aspect of the LSc technology is the real-time detection of a $\overline{\nu}_e$ through a *delayed coincidence technique* for the IBD reaction $\overline{\nu}_e + p \rightarrow n + e^+$ (see Section 1.2.1):

The created positron annihilates on a time scale of nanoseconds and releases a prompt visible energy of $E_{\text{promt}} = E_{\bar{\nu}_e} - 0.784\,\text{MeV}$. The neutron with some tens of keV of kinetic energy thermalizes and becomes captured by a hydrogen or carbon nucleus. A capture on hydrogen after $\sim 250\,\mu\text{s}$ emits a γ-ray with the 2.2 MeV binding energy of the created deuteron. If the thermal neutron is captured on carbon, γ-rays with 4.9 MeV total energy are released. Due to the relative capture cross sections and the elemental composition of the organic LSc, about 99 % of the thermal neutron captures are expected to occur on hydrogen [184].
In order to enhance the neutron capture signature, LSc can be doped with a *neutron-absorber* like gadolinium. Existing reactor $\overline{\nu}_e$ oscillation experiments with LSc detectors, like Double Chooz, Daya Bay and RENO, have a gadolinium mass fraction of $\sim 0.1\,\%$ dissolved in their neutrino target [185–187]. If a neutron is captured by this element, a total energy of $\sim$8 MeV is released through a sequence of on average three γ-ray emissions. This is well above any expected background from natural radioactivity. Moreover, due to the higher neutron capture cross section of gadolinium compared to hydrogen and carbon, the mean capture time for the thermalized neutron reduces to $\sim 30\,\mu\text{s}$ at a gadolinium mass fraction of 0.1 % [188]. This helps to diminish *accidental background* (see Section 4.1.2).
In general, the temporal and spatial correlation of the prompt signal from the positron and the delayed signal from the neutron capture allows a strong suppression of backgrounds by requiring this delayed coincidence signature to be detected.
The directional information of the $\overline{\nu}_e$ entering an IBD interaction cannot be obtained on event-by-event basis because the position resolution of a LSc detector is usually insufficient. However, a study of the average displacement ($\sim 2\,\text{cm}$) between the neutron capture point and the position of the stopping and annihilating positron, which is assumed to coincidence with the $\overline{\nu}_e$ interaction point, allows to deduce a direction to the $\overline{\nu}_e$-source on a statistical basis [189].

4.1.2 Backgrounds

The LE neutrino and antineutrino sources commonly studied with a LSc detector (see Chapter 2) emit the neutral leptons as products of nuclear processes. Since the weakly interacting particles can only be detected by observing the event signature of their interaction products (see Section 4.1.1), a neutrino interaction signal can in principle be mimicked if the same signature emerges from a process other than a neutrino interaction. In the LE domain, examples for such processes are *natural* or *induced radioactivity*, or the interaction of a γ-ray. The resulting challenge in measuring the low rate of LE neutrino and antineutrino interactions is to identify their signal in the face of competing, omnipresent background with much higher rate. Four classes of background for the detection of LE neutrinos are shortly described in the following: *neutrino background*, *accidental background*, *intrinsic background* and *cosmogenic background*. The focus will be on the latter since it poses a strong motivation to develop new particle tracking methods for LSc-based detectors (see Chapter 6).

Neutrino background It is impossible to shield any kind of neutrino experiment from neutrinos and antineutrinos of a particular flavor or from a specific source.

Moreover, the incident direction of a LE neutrino / antineutrino cannot be determined on event-by-event basis with a LSc detector. As a consequence, any signal-like event that is created by a neutrino or antineutrino from a source other than the one under investigation is background to the actual measurement. An illustrative example is the detection of $\overline{\nu}_e$'s from Earth (see Section 2.3) in the presence of a $\overline{\nu}_e$ flux from nuclear reactors (see Section 2.4).

Accidental background Accidental background occurs in coincidence analyses due to a random association of uncorrelated sub-events. For example, this can be the accidental linking of a prompt positron-like signal with the delayed signal characteristic for a neutron capture; together they can fulfill the selection criteria for the IBD signal event class.
A method [188] to handle this type of background bases on the measurement of single rates for prompt-like and delayed-like signals. With these rates one can calculate the probability that two signals randomly fulfill the IBD selection criteria in time and space. This allows to consider a corresponding rate for the accidental background in the final analysis. Since the single rates of prompt-like and delayed-like signals can change over time, e.g., due to changes in the levels of radioactivity producing these types of signals, the accidental background rate must be continuously re-evaluated.

Intrinsic background Intrinsic background originates from radionuclides that are embedded in the construction parts of the measurement device or contaminate their surfaces. This also includes the detector's primary component, the organic LSc, which contains a natural abundance of unstable ^{14}C. A later contamination with radioisotopes can be introduced via dust particles of micron or sub-micron size during the construction, filling or a LSc purification phase. Moreover, radioactive gas, e.g., ^{222}Rn, can diffuse into the detector.
Information on prominent intrinsic contaminants being dangerous to LSc-based neutrino detectors can be found in Ref. [30], based on experience with BOREXINO. A brief summary of these contaminants with a note on their origins is given in Table 4.1. The list is not complete with respect to all elements from the ^{232}Th and ^{238}U chains. Assuming secular equilibrium, the concentration of contaminants from these chains can be measured by searching for two fast decay sequences that offer a delayed coincidence tag [30]: $^{212}\mathrm{Bi} \rightarrow {}^{212}\mathrm{Po} + e^- + \overline{\nu}_e$ succeeded by $^{212}\mathrm{Po} \rightarrow {}^{208}\mathrm{Pb} + \alpha$ for the ^{232}Th chain and $^{214}\mathrm{Bi} \rightarrow {}^{214}\mathrm{Po} + e^- + \overline{\nu}_e$ followed by $^{214}\mathrm{Po} \rightarrow {}^{210}\mathrm{Pb} + \alpha$ in the case of the ^{238}U chain. As a side-effect, emissions of α-particles from isotopes of the ^{232}Th and ^{238}U chains can induce (α, n)-reactions on the ^{13}C in the LSc, $^{13}\mathrm{C}(\alpha, n)^{16}\mathrm{O}$. The capture of the neutron in combination with a prompt signal from its scattering on protons, a disexcitation γ-ray from ^{16}O or the slowing-down α-particle can be misidentified as an IBD event signature [190].

A reduction of intrinsic background begins with a careful selection of materials with low radioactivity for the different detector components. During construction, a settling of dust, especially inside the detector, must be avoided. Flushing and filling of pipes, storage tanks and the detector vessel with ultra-pure water or nitrogen with low ^{39}Ar and ^{85}Kr content removes surface contaminations and prevents contact

Table 4.1 – List of prominent, radioactive, non-cosmogenic contaminants in LSc. The list is sorted first by increasing mass number and second by increasing atomic number. It does not show all relevant isotopes from the ^{232}Th and ^{238}U chains. Half-lives, primary decay modes (in some cases with BRs rounded to nearest percent) and line or endpoint energies (rounded to nearest keV) are presented. The stated energy values correspond to transitions between the ground states of the parent and daughter nuclei and may be distributed between multiple decay steps, e.g., EC with subsequent γ-ray emission. In case the listed decay mode includes the emission of a γ-ray, its energy is listed as a separate contribution to the total energy release. Data cited from Ref. [191]. Information on origins of contaminants from Ref. [30].

Isotope	Half-life	Decay mode	E_{max} [keV]	Origin
^{14}C	5700 a	β^-	156	organic LSc
^{39}Ar	269 a	β^-	565	air
^{40}K	1.3 Ga	β^- (89 %) EC γ (11 %)	1311 44 + 1461	dust, PMT (glass), wavelength shifter
^{85}Kr	10.8 a	β^-	687	air
^{208}Tl	3.1 min	β^-	4999	PMT (glass), ^{232}Th chain
^{210}Pb	22.2 a	β^-	64	dust, ^{238}U chain
^{210}Bi	5.0 d	β^-	1162	dust, ^{238}U chain
^{210}Po	138.4 d	α	5407	dust, ^{238}U chain
^{212}Bi	60.6 min	β^- (64 %) α (36 %)	2252 6207	^{232}Th chain
^{212}Po	0.3 µs	α	8954	^{232}Th chain
^{214}Pb	26.8 min	β^-	1019	^{238}U chain
^{214}Bi	19.9 min	β^-	3270	PMT (glass), ^{238}U chain
^{214}Po	164.3 µs	α	7833	^{238}U chain
^{222}Rn	3.8 d	α	5590	air, ^{238}U chain

with radioactive dust particles from the air. A purification of the LSc reduces the concentration of isotopes from the ^{232}Th and ^{238}U chains. For example, Borexino achieved residual contaminations of $<0.8 \times 10^{-19}$ g/g for ^{238}U and $<1.2 \times 10^{-18}$ g/g for ^{232}Th [192]. At the data analysis stage, a *fiducial volume* (FV) inside the designated neutrino target volume can be defined to remove events close to the detector walls. This is the region where background events usually dominate as a result of radioactivity in the construction parts or diffusion of contaminants into the LSc volume. Moreover, *pulse shape discrimination* allows to differentiate between α-particles and electrons (see Section 3.1.1 and Ref. [167]). This helps to distinguish radioactive decays and recoil electron signals originating the ES of a neutrino.

Cosmogenic background Cosmic ray activity in the atmosphere induces background to LE neutrino and antineutrino detection: As described in Section 2.5, the interactions of cosmic HE particles with atoms and molecules in the upper atmosphere lead to the production of muons with several GeV of energy. Primarily created in the decays of charged pions according to reaction (2.11), the muons reach down to ground level both as parts of local air showers and in a steady, uncorrelated flux. A passage of such a muon through or close by a LSc neutrino detector can produce two types of background—*fast neutrons* and *cosmogenic radionuclides*.

After the muons were produced in up to 15 km altitude, they lose $\sim 2\,\mathrm{GeV}$ to ionization on their way to the ground. At ground level, the average muon energy is $\sim 4\,\mathrm{GeV}$. For energies below 1 GeV, the energy spectrum is flat. It then steepens gradually, thereby reflecting the primary spectrum in the range from 10 GeV to 100 GeV. With further increasing energy of the parent pions above a critical energy $\epsilon_\pi = 115\,\mathrm{GeV}$ the muon spectrum steepens more as the pions interact more often before they decay. The HE tails ($E_\mu \gg 1\,\mathrm{TeV}$) of the atmospheric muon spectrum is one power steeper than the primary spectrum. At sea level, the integrated vertical muon flux is $I_\mu \sim 6 \times 10^5\,\mathrm{m^{-2}\,h^{-1}}$ for muons above $1\,\mathrm{GeV}/c$. The distribution of the incident angle θ at the ground is $\propto \cos^2\theta$ for $E_\mu \sim 3\,\mathrm{GeV}$. It approaches a $\sec\theta$ distribution for $E_\mu \gg \epsilon_\pi$ and $\theta < 70°$ [11].
Once a muon crosses over from the atmosphere into more dense material, its energy loss per covered distance increases. HE muons lose their energy through ionization and radiative processes like bremsstrahlung, e^-e^+-pair-production and photonuclear interactions. For E_μ below a *critical energy* ϵ ($\sim 500\,\mathrm{GeV}$ in "standard rock[2]"), the energy loss from ionization with $\sim 2\,\mathrm{MeV\,g^{-1}\,cm^2}$ dominates and can be described by the *Bethe-equation* [11]. As a consequence, the muon energy spectrum below ground naturally depends on the actual depth. With increasing depth, the average muon energy asymptotically approaches the critical energy ϵ: On the one hand, the linear energy loss below ϵ leads to an absorption of muons with lower energy at more shallow depths. Therefore, the average muon energy in the domain well below ϵ rises as a function of depth while the total muon flux decreases. For muons with $E_\mu > \epsilon$, on the other hand, the increased energy loss due to the additional radiative processes leads to a fast depopulation of the muon spectrum's HE tail.
The angular distribution of atmospheric muons at a given point below ground depends on the directional variance of the muon track lengths in the dense[3] material and thus on the surface structure. For example, it differs for a flat and a mountainous surface topology. Generally, muons originating the atmosphere come down from the upper hemisphere with a preferred direction towards the lower hemisphere. In addition to atmospheric muons, CC interactions of atmospheric ν_μ's and $\overline{\nu}_\mu$'s, which permeate Earth from all directions, create muons anywhere inside the detector and its vicinity. These muons pass by or go through the detection device from all directions.
In the most cases, the traversal of a muon through a LSc detector can be easily discriminated from a LE neutrino interaction. This is due to the larger energy deposition that results from the long track length in combination with an energy loss of $\sim 2\,\mathrm{MeV\,cm^{-1}}$ in LSc. If the muon creates an extended electromagnetic or

[2]Standard rock is parameterized by the atomic mass number $A = 22$, the atomic number $Z = 11$ and a mass density of $\rho = 2.65\,\mathrm{g\,cm^{-3}}$ [11].
[3]More dense than the atmosphere.

hadronic shower inside the detector, this signature is even enhanced. An important side effect from a muon passage through or close by the detector is the possible production of fast neutrons and radioisotopes. They constitute a severe background to rare LE neutrino event search and are discussed next.

Muons can knock out *fast neutrons* with considerable amounts of kinetic energy from atomic nuclei. Different from a *thermal neutron* with less kinetic energy and, consequently, a higher probability to be captured, a fast neutron easily penetrates several meters of material. Therefore, it can possibly reach the central LSc volume even from outside the detector. A fast neutron's thermalization to sub-MeV energies through scatterings produces recoil protons. The heavily quenched scintillation light signal from such a proton can be misidentified as the result of elastic neutrino–electron scattering. If, in addition, the γ-ray emission from the neutron capture is observed, the prompt proton recoil signal in combination with the delayed neutron capture mimics an IBD event signature.
Both KamLAND and Borexino measured the spallation neutron yield per muon in LSc. The value obtained by Borexino is $(3.10 \pm 0.11) \times 10^{-4}\, n/(\mu \cdot (\mathrm{g/cm^2}))$ [184]. It is consistent with a previously determined yield of $(2.8 \pm 0.3) \times 10^{-4}\, n/(\mu \cdot (\mathrm{g/cm^2}))$ from KamLAND [193]. Moreover, Borexino investigated the lateral distance profile of neutron capture vertices relative to the reconstructed parent muon tracks. An average lateral distance of $(81.5 \pm 2.7)\,\mathrm{cm}$ was reported in Ref. [184].

When a muon traverses or stops in the LSc volume, it can also produce radioactive isotopes due to inelastic *photonuclear interactions* with the carbon nuclei of the target material. A summary of prominent unstable isotopes created from such muon interactions is given in Table 4.2. Almost all of these isotopes decay via emission of a β-particle. Based on the emitted scintillation light, such a decay signature may be misidentified as a prompt IBD signal or as a recoil electron from an elastic neutrino–electron scattering event. The latter poses a severe background to solar neutrino measurements. This is especially true for the long-lived isotope ^{11}C.
Neutron-rich radioisotopes like ^{8}He and ^{9}Li have chances that their β^--decay is accompanied by the emission of a delayed[4] neutron. The probabilities are $(16 \pm 1)\,\%$ [194] and $(50.8 \pm 0.9)\,\%$ [194], respectively. When the neutron is captured, the resulting γ-ray emission together with the preceding decay electron signal in the right energy range mimics an entire IBD delayed coincidence signature. As a consequence, these βn-emitters are especially dangerous background to $\overline{\nu}_e$ measurements. The yields of different cosmogenic radioisotopes from muon-induced spallations in LSc were also measured by KamLAND [193] and Borexino [184]. For instance, the found ^{8}He and ^{9}Li yields are $Y_{\mathrm{KM}}(^{8}\mathrm{He}) = (0.7 \pm 0.4) \times 10^{-7}/(\mu \cdot (\mathrm{g/cm^2}))$ and $Y_{\mathrm{KM}}(^{9}\mathrm{Li}) = (2.2 \pm 0.2) \times 10^{-7}/(\mu \cdot (\mathrm{g/cm^2}))$ from KamLAND and $Y_{\mathrm{BX}}(^{8}\mathrm{He}) < 1.5 \times 10^{-7}/(\mu \cdot (\mathrm{g/cm^2}))$ at 3σ CL and $Y_{\mathrm{BX}}(^{9}\mathrm{Li}) = (2.9 \pm 0.3) \times 10^{-7}/(\mu \cdot (\mathrm{g/cm^2}))$ from Borexino. Their results allowed to cross-check background model predictions for the production rates of the unstable nuclei.

Respecting potential constraints from the experiment's scientific goals, e.g., a required distance to a particular neutrino source, cosmogenic background can be minimized by selecting a detector site well shielded from cosmogenic muons. One example are

[4]The emission is still fast compared to the response of a LSc detector.

Table 4.2 – Summary of prominent radionuclides produced in muon-induced spallation processes. The list is sorted by increasing isotope half-life. It further contains the important decay mode and the amount of energy released in the decay. The stated energy values correspond to transitions between the ground states of the parent and daughter nuclei and may be distributed between multiple decay steps, e.g., β^--decay with subsequent neutron emission. In case the listed decay mode includes the emission of a γ-ray, its energy is listed as a separate contribution to the total energy release. Data cited from Refs. [191, 194].

Isotope	Half-life	Decay mode	$E_{\max}$ [MeV]
^{12}N	11.0 ms	β^+	17.34
^{13}B	17.3 ms	$\beta^-\gamma$	9.75 + 3.68
^{12}B	20.2 ms	β^-	13.37
^{8}He	119.1 ms	$\beta^- n$	10.65
^{9}C	126.5 ms	β^+	16.49
^{9}Li	178.3 ms	$\beta^- n$	13.61
^{8}B	770.0 ms	$\beta^+\alpha$	17.98
^{6}He	806.7 ms	β^-	3.51
^{8}Li	839.9 ms	$\beta^-\alpha$	16.00
^{11}Be	13.8 s	β^-	11.51
^{10}C	19.3 s	$\beta^+\gamma$	2.93 + 0.72
^{11}C	20.4 min	β^+	1.98
^{7}Be	53.2 d	EC γ	0.38 + 0.48

the currently world largest underground laboratories *Laboratori Nazionali del Gran Sasso* (LNGS) in Italy. All of the local experiments, including Borexino, OPERA and GERDA, are shielded by about 1400 m of rock from the *Gran Sasso d'Italia* mountain. This corresponds to an effective depth of about 3800 m *water-equivalent* (w.e.)[5] and reduces the cosmogenic muon flux from $\sim 166.7\,\mathrm{m^{-2}\,s^{-1}}$ [11] at Earth's surface to the value of $(3.41 \pm 0.01) \times 10^{-4}\,\mathrm{m^{-2}\,s^{-1}}$ measured by Borexino [195].
At the analysis stage, the simplest strategy to reduce cosmogenic background is to reject all observed events for some period of time after a muon entered the detector or if signals in an *outer veto region* were registered. The latter is important to reject fake signals from fast neutrons that were created by unseen muons in the matter surrounding the detector's veto volume. A significant drawback of the simple *full veto strategy* is the strong reduction of the detector's effective measurement time: After a muon traversal, the time span to veto a potential decay of a particular radionuclide depends on the certainty one wants to have that the created isotope decayed. The required time to reach that certainty depends on the isotope's half-live $\tau_{1/2}$. For long-lived isotopes, like ^{11}C with $\tau_{1/2} = 20.4\,\mathrm{min}$, or a high muon rate, which depends on the muon flux and the size of the detector, the dead-time induced from vetoing the entire detector easily reaches 100 %. Therefore, only short veto time spans to reduce background from short-lived isotopes are acceptable.
A much more efficient veto strategy not only applies in time but also in space relative to the muon track. One example for such a selective method is the *three-fold*

[5]Depth of water required to reduce the cosmic muon flux to the same level.

coincidence veto technique explained in Ref. [30] in the context of BOREXINO. By using this method to reduce cosmogenic ^{11}C background, $> 89.4\,\%$ of the ^{11}C decays are rejected while maintaining a residual exposure of $48.5\,\%$ [30].
One approach to veto the βn-emitting isotopes ^{8}He and ^{9}Li is described for DOUBLE CHOOZ in Ref. [196]: For each combination of a prompt event and a preceding muon, a ^{9}Li likelihood $\mathcal{L}_{\mathrm{Li}}$ is determined. Amongst other things it bases on the distance between the event's reconstructed vertex position and the reconstructed muon track. If a prompt event satisfies a certain $\mathcal{L}_{\mathrm{Li}}$ cut condition, this event is rejected as ^{9}Li or ^{8}He candidate. About $55\,\%$ of the cosmogenic background estimate is rejected in DOUBLE CHOOZ with this method.

As indicated by the examples above, the reduction of cosmogenic background heavily relies on an accurate identification of a muon entry into the detector and a precise reconstruction of its trajectory through the LSc volume. However, not only single muons going straight through the target region but also those stopping or creating secondary electromagnetic showers inside must be reliably handled. A further complication arises from muon bundles, i.e., multiple, parallel muon tracks crossing the detector at the same time. They are difficult to reconstruct based on the simultaneous emission of isotropic scintillation light along their flight paths. Especially projects with LSc detectors of unprecedented size, like LENA and JUNO (see Sections 4.2 and 4.3, respectively), inevitably depend on an efficient reduction of muon-induced background in order to reach their scientific goals in a reasonable time. This circumstance poses a strong motivation to develop new methods for charged particle track reconstruction in LSc, such as the algorithm presented in Chapter 6.

4.2 The LENA Project

The answering of important questions from astrophysics and cosmology demands for the utilization of the messenger character of neutrinos in order to study extraterrestrial neutrino-emitting phenomena (see Chapter 2). In the near future, the contributions from existing experiments will cease to stimulate significant progress on various open issues. As a consequence, a new large-volume neutrino observatory of the next generation is required: Located in an underground laboratory, such a multi-purpose device has to make significant high-precision measurements with large samples of detected signal events and low background.
Moreover, the search for physics beyond the SM and the completion of the description of fundamental neutrino properties are among the top priorities of particle physics. This includes the test of *Grand Unified Theories* (GUTs) for the unification of the strong and the electroweak force, e.g., by searching for proton decay, and a precise determination of all parameters relevant to describe neutrino flavor oscillations (see Section 1.1).
The LENA project constitutes one option for a next-generation neutrino observatory in Europe. Employing the successful LSc technology at a new mass scale of 50 kt, the LENA detector would be well suited for the measurement of terrestrial and astrophysical LE neutrinos and antineutrinos. At the same time, the huge LSc mass allows to search for proton decay signatures that are difficult to access by experiments using the water Cherenkov technique. After the development of first

ideas on LENA, the project became part of two European design studies [197]: LAGUNA and the successor LAGUNA-LBNO. Some information on these studies can be found in Appendix C. The LENA project benefited from the European surveys especially in terms of comprehensive laboratory site investigations and the work towards a complete technical design of the detector. Both topics are subject of Section 4.2.1. The physics potential of LENA with its 50 kt of LSc is summarized in Section 4.2.2.

4.2.1 Detector design

In general, the design of the unsegmented 50 kt LSc detector LENA is founded on valuable experience from existing experiments that either successfully use the same technology, like BOREXINO and KamLAND, or are of comparable size, like SK. For a maximum performance of the experiment in terms of cosmogenic background reduction, the detector must be placed underground. Two favorable sites for the massive LSc detector, which were investigated by LAGUNA and will be covered further below, are the *Pyhäsalmi mine* in *Finland* and the *Laboratoire Souterrain de Modane* (LSM) in *France*. With a focus on building LENA at Pyhäsalmi, advanced plans for the excavation of the required cavern and the construction and filling of the detector were developed in the context of LAGUNA / LAGUNA-LBNO. They essentially document that, from the technical point of view, an upscaling of the LSc technology to unprecedented size is feasible. The following presents details on the current status of the LENA design [40, 198].

Preferred underground laboratory sites Currently, no existing underground laboratory could house a detector of the size of LENA. This would make excavation works inevitable. From the seven possible detector sites investigated by LAGUNA (see Table C.1), only the Pyhäsalmi mine and the LSM at Fréjus have an envisaged depth of ≥ 4000 m w.e. This is the preferred minimum value for the operation of LENA concerning shielding against cosmogenic muons.
The Pyhäsalmi mine in Finland, whose bottom level is ~ 1450 m below ground, currently is the deepest metal mine in Europe [40, 199]. It already houses the *Centre for Underground Physics in Pyhäsalmi* that is distributed across different mine levels. Since the mine is planned to be operational at least until 2018, the existing infrastructure, e.g., transportation connections via rail and road, could very well be used to facilitate the excavation and subsequent construction works. Parameters describing the background conditions at the bottom level of the mine can be found in Table 4.3.
The LSM is an underground laboratory located adjacent to the *Fréjus road tunnel* that connects *Modane (F)* and *Bardonecchia (I)* through the French-Italian Alps. With a rock overburden of ~ 4800 m w.e. from the *Col du Fréjus*, this place provides the best shielding against cosmogenic muons among all the sites investigated by LAGUNA [200]. Moreover, the existing road connection would enable an immediate extension of the laboratory and haulage of construction parts for a large-volume detector. However, the background level from reactor $\overline{\nu}_e$'s at the LSM is higher compared to the Pyhäsalmi site. This is due to the proximity and higher density

Table 4.3 – Current background conditions $\sim 1450\,\mathrm{m}$ below ground ($\sim 4000\,\mathrm{m\,w.e.}$ overburden) in the Pyhäsalmi mine and at the LSM with $\sim 4800\,\mathrm{m\,w.e.}$ overburden from the Fréjus mountain. The nearest nuclear power plant to the Pyhäsalmi site is 350 km away. Two more are planned for the next decades. The nuclear power plant closest to the LSM is about 130 km away. Data cited from Ref. [40].

Background source	Pyhäsalmi	Fréjus (LSM)
Radioactivity from radon	$20\,\mathrm{Bq/m^3}$	$15\,\mathrm{Bq/m^3}$
Residual muon flux	$1.1 \times 10^{-4}/(\mathrm{m^2\,s})$	$5 \times 10^{-5}/(\mathrm{m^2\,s})$
Expected reactor $\overline{\nu}_e$ flux	$1.9 \times 10^{5}/(\mathrm{cm^2\,s})$	$1.6 \times 10^{6}/(\mathrm{cm^2\,s})$

of nuclear power plants in France. A summary of the background conditions at the LSM is given in Table 4.3.

Layout of detector components As shown by the current LENA design for the Pyhäsalmi site in Figure 4.1, the central component of the detector is the cylindrical neutrino target volume. It has a height of 96 m and a radius of 14 m, containing a total mass of about 50 kt LSc in a volume of $\sim 5.9 \times 10^4\,\mathrm{m^3}$. A 2 m thick volume around the designated neutrino target region functions as buffer towards the detector tank's inner surface. Inside this buffer volume, a scaffolding structure to hold the *optical modules* (OMs) is anchored at the tank wall. The OMs are placed in such a way that their entrance apertures are situated at the boundary to the target volume. Free space inside the buffer region is filled with LSc and acts as shielding against radiation and contaminants emanating from the tank walls. An opaque foil is spanned along the scaffolding's side. It acts as an optical separation of the neutrino target volume from the buffer region where natural radioactivity from the near-by detector components produces large amounts of scintillation light. Only the OMs can look into the designated target region.
A cylindrical concrete tank in upright orientation with an inner radius of 16 m, an inner height of 100 m and a wall thickness in the range from 30 cm to 60 cm encloses all inner volumes. The thickness varies due to 30 cm wide cylindrical cavities within the concrete. They allow to do installations, e.g, for cooling, or the guiding of cables. In order to ensure material compatibility, a thin stainless-steel liner is mounted at the tank's inner surface between concrete and LSc. Outside of the tank, an excavated volume with a radial width of ≥ 2 m between the egg-shaped cavern walls and the tank's lateral area is filled with water. It is equipped with about 2000 PMTs and functions as a water Cherenkov veto against muons coming from the side. Moreover, the water-filled volume reduces background from incoming fast neutrons that were produced by muon interactions in the surrounding rock. Due to the higher mass density of water compared to LSc, an inward-facing pressure stresses the tank wall. It turned out that the concrete construction is perfectly suited to withstand the corresponding forces. The outside lateral area of the concrete tank is coated with a spray-on plastic liner to prevent inward-leaking of water.
A muon veto system on top of the detector tracks down-going muons. The electronics required to run the detector's DAQ is placed further above in an electronics hall with about 15 m dome height.

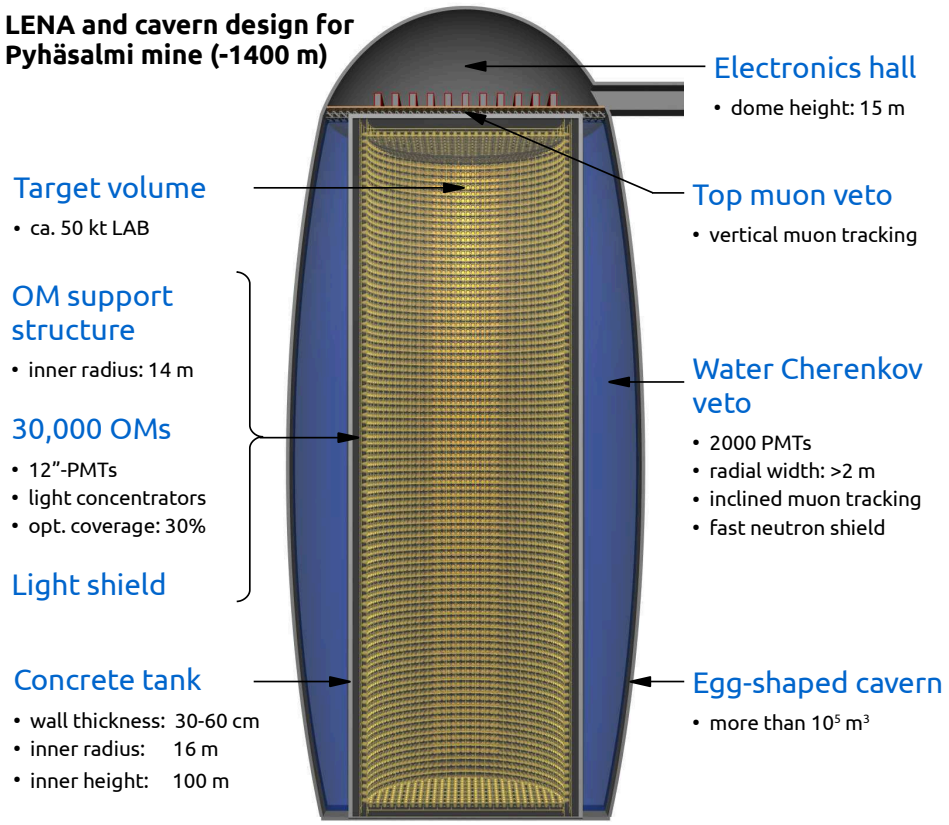

Figure 4.1 – Upright projection of the 50 kt LSc detector LENA. The shape of the cavern is adapted to the conditions at the Pyhäsalmi site and provides better resistance against inbound pressure from the surrounding rock. Figure adapted from Ref. [198].

Liquid scintillator mixture In LENA with its unsurpassed dimensions, scintillation light would need to cover distances $> 15\,\mathrm{m}$ before it is detected. This demands for a large attenuation length ($\sim$20 m) and a high scintillation light yield ($\sim$10,000 photons per MeV) of the LSc mixture to perform high-precision LE neutrino measurements, especially in terms of an accurate reconstruction of the event positions and energies. Moreover, aspects like the number of free target protons, high radiopurity and good pulse shape characteristics for background rejection need to be considered. For applications relying on the timing of the scintillation light emission, like charged particle tracking, fast fluorescence times are preferable.
Initially, LAB and PXE were considered as LSc solvent for LENA. LAB is advantageous regarding the attenuation length and the number of free protons. PXE, on the other hand, exhibits faster scintillation light emission. Nevertheless, LAB—without the loading of a neutron-absorber like gadolinium—became the preferred option, especially due to wide experience from its application in other experiments. The intended admixtures of 3 g/l PPO and 20 mg/l bis-MSB as wavelength-shifter solutes would result in a peak emission of scintillation light at 430 nm with a fast decay component of $\sim$ 4.4 ns.

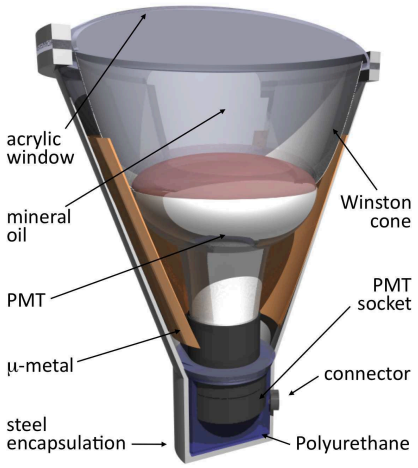

Figure 4.2 – Schematic of LENA OM with PMT and light concentrator. The μ-metal provides shielding against external magnetic fields, e.g., from Earth. This prevents a bending of electron trajectories in the PMT. Figure from Ref. [198].

Optical modules The baseline design for the light detection system of LENA comprises the arrangement of about 30,000 OMs in 4×4 arrays on the scaffolding inside the detector. An illustration of such an OM is shown in Figure 4.2. Each of the OMs consists of a 12″ PMT as photosensor (see Section 3.3.1) with >20 % peak QE and ∼3 ns TTS at *full width at half maximum* (FWHM) as design specifications. In order to increase an OM's effective light collection area by a factor of about 1.5, a light concentrator is attached to each PMT (see Section 3.3.2). The entire module is placed inside a steel encapsulation because the OM must resist at least[6] the LSc's hydrostatic pressure close to 10 bar at the bottom of the tank. Light enters the encapsulation at the front-side of the OM through an acrylic window. In order to absorb γ-rays from radioactivity in the PMT glass, which could produce scintillation light right in front of the OM, free space inside the OM is filled with non-scintillating mineral oil.
The destined overall light collection efficiency inside LENA is ∼6 %. It is the product of 30 % coverage of the detector's inner surface with photosensitive area and 20 % photon detection efficiency of a single OM. The latter is dominated by the QE of the PMT cathode and probably represents a conservative estimate in the view of modern PMTs.

4.2.2 Physics potential

The following provides a short overview over the estimated performance of the LENA detector, focusing on major points of its research program and some outstanding questions from the science fields described in Chapter 2. A detailed description of the detector's physics potential can be found in Ref. [40].

[6] If one OM implodes, a shock wave propagates through the LSc. In order to prevent the destruction of further OMs in a disastrous chain reaction, the encapsulation of an OM must be resistant to large pressure fluctuations.

Solar neutrinos Due to a fiducial LSc mass of $\geq 30\,\mathrm{kt}$ and a low energy threshold, LENA could measure SSM neutrino fluxes with great precision. The statistics of $\sim 10^4$ ^{7}Be-neutrino events per day offers the opportunity to search for time variations in the solar neutrino flux, thereby testing the long-term stability of fusion processes in the Sun. A measurement of *pep* and *CNO* neutrinos is possible roughly between 1–2 MeV. The latter provide important information on the solar metallicity, especially if the different flux contributions can be disentangled. However, such a measurement faces a strong background from cosmogenic ^{11}C: The *CNO*/*pep* neutrino signal to ^{11}C background ratio is about 1 : 8. Compared to Borexino, the ^{8}B-neutrino event rate will increase by two orders of magnitude. This allows to probe the solar neutrino survival probability P_{ee} in the 1–5 MeV range, the *transition region* between vacuum and matter dominated oscillations. For decreasing energy, the MSW effect predicts an upturn of P_{ee} (see also Section 1.1.2). LENA could detect the predicted upturn with 5σ significance after five years of measurement [201]. An unexpected shape of the upturn would indicate the effect of new physics.

Supernova neutrinos In case of a galactic core-collapse SN with a distance of 10 kpc, LENA would detect $\gtrsim 10^4$ events during $\sim$10 s. They are distributed among the different detection channels (see Section 4.1.1 and Appendix A), which enable separate measurements of ν_e and $\overline{\nu}_e$ fluxes via CC interactions and the determination of the total flux through various NC channels. The detailed time- and flavor-resolved neutrino and antineutrino spectra in combination with LENA's superior energy resolution and low energy threshold allow for a comprehensive test of SN theory. Besides probing features like the model-independent prompt ν_e-burst, this includes the search for signatures of collective and matter-driven neutrino flavor oscillations, potentially revealing the true neutrino MO. A detector like LENA would surely become part of SNEWS and provides an estimate for the distance to a galactic core-collapse SN even if the visual appearance is obscured.
A measurement of the still undetected DSNB with LENA is possible only in the energy range from 9.5 to 25 MeV. This is due to indistinguishable background from reactor and atmospheric $\overline{\nu}_e$'s as well as NC interactions of neutrinos and antineutrinos from the atmosphere. Pulse shape discrimination can reduce the dominant NC background significantly at the cost of 60 % of the signal. Assuming that the background rate is known to 5 % accuracy, the remaining $\sim$ 20 to $\sim$ 40 signal events after ten years of measurement, depending on the mean SN neutrino energy, would confirm the DSNB's existence with 3σ significance. The observation of no signal would improve the existing upper limit on the DSNB flux by a factor of eight and would further rule out all current standard DSNB models at >90 % CL [202].

Geo-neutrinos LENA has the potential to measure the total $\overline{\nu}_e$ flux from Earth at the Pyhäsalmi (Fréjus) site with a precision of 1 % (2 %) after ten years. This already takes into account future Finnish reactors. The flux contributions from ^{238}U and ^{232}Th and the U/Th ratio could be determined on the same time scale with the precisions of 2 %, 4 % and 6 % (4 %, 7 % and 11 %), respectively.

Proton decay The golden channel for proton decay search in a LSc detector is $p \to K^+ + \overline{\nu}$. It is also the favored decay mode of most *Supersymmetry* models. The current lower limit for the partial lifetime with respect to this decay mode is from SK with $\tau > 5.9 \times 10^{33}$ a at 90 % CL [203]. In LSc, the proton decay to a charged kaon exhibits a characteristic signature: A prompt scintillation signal originates from the K^+. After a mean lifetime of ∼12.3 ns [11], its decay, which is usually at rest, produces a delayed mono-energetic signal through $K^+ \to \mu^+ + \nu_\mu$ (BR: ∼64 % [11]) or $K^+ \to \pi^+ + \pi^0$ (BR: ∼21 % [11]) quickly followed by $\pi^+ \to \mu^+ + \nu_\mu$. Using a sophisticated pulse shape analysis, this allows a background-free measurement for ten years. If no event was observed in LENA during this time, a new limit of $\tau > 4 \times 10^{34}$ a would be set at 90 % CL.

A study regarding the sensitivity of LENA to the neutrino MO and leptonic CP-violation in an LBNO experiment with GeV-neutrinos from a WBB is presented in Chapter 8.

4.3 The JUNO Project

The JUNO project in China [42, 43] is among the competitors in the quest for the determination of the neutrino MO. Employing a 20 kt LSc detector, the experiment primarily aims to resolve the neutrino MO via a measurement of reactor $\overline{\nu}_e$ disappearance over a baseline of ∼52 km. In the course of this, several parameters of the three-flavor neutrino oscillation model will be determined with sub-percent level precision.
The experiment was proposed in 2008 under the name Daya Bay II. However, after the preferred detector site was moved from a place near the *Daya Bay* nuclear power plant to *Jiangmen city* in the *Guangdong* province in 2012, the project was renamed to JUNO in 2013. Following the experiment's approval by the *Chinese Academy of Sciences* in February 2013, an international collaboration was formally established in July 2014. The start of data taking is expected by 2020.

Section 4.3.1 gives a short description of the current JUNO detector design and some information on the underground laboratory site. The experiment's expected performance is summarized in Section 4.3.2. Although the multi-purpose neutrino observatory has a broad scientific program, including measurements of solar, SN and geo-neutrinos as well as the DSNB, the section solely focuses on the neutrino MO and oscillation parameter measurements.

4.3.1 Detector design

Based on Refs. [42, 43], this section covers the current JUNO detector design. After giving basic information on the experimental site, the layout of the components of the LSc detector is described. The preferred LSc mixture and the light detection system are discussed at the end.

Underground laboratory site The JUNO experiment will be located at *Jinji town*, 43 km to the southwest of the county-level city *Kaiping* and within ∼200 km

Table 4.4 – Background conditions at the JUNO underground laboratory surrounded by granite rock and with ∼700 m vertical overburden. The residual flux of muons with an average energy of 215 GeV was estimated by simulation. Data cited from Ref. [42].

Background source	Value
Radioactivity from rock	1305 Bq/kg
Residual muon flux	$3 \times 10^{-3}/(\mathrm{m}^2\,\mathrm{s})$
Muon rate in detector	$\sim 3\,\mathrm{s}^{-1}$
Expected geo-neutrino events	1.5/d

distance to cities like *Hong Kong* and *Macau* in the east. Ten reactor cores from the *Yangjiang* (6) and *Taishan* (4) nuclear power plants provide the $\overline{\nu}_e$ flux to perform the flavor oscillation studies. Their combined thermal power is 35.8 GW. However, it is likely that only a thermal power of 26.6 GW will be initially available when the experiment starts around 2020. With a tolerance of a few hundred meters imposed by the measurement principle, the laboratory site had to be chosen such that the ten baselines to the distributed reactor cores have essentially equal length: Detailed investigations ensured that all baseline lengths deviate by less then 500 m from the average value of 52.48 km for the current site. The 215 km distant *Daya Bay* nuclear power plant will still be responsible for 2.8 % of the reactor $\overline{\nu}_e$ events in the detector. To reduce cosmogenic background, the JUNO laboratory, whose construction started at the beginning of 2015, will be situated ∼460 m below ground level under a hill of 268 m height. This corresponds to a shielding of ∼ 2000 m w.e. The background conditions in the underground cavern are summarized in Table 4.4.

Layout of detector components As described in Section 4.3.2, JUNO requires a relative visible energy resolution of $3\,\%/\sqrt{E_{\mathrm{vis}}/\mathrm{MeV}}$ to achieve its primary objective, the determination of the neutrino MO.[7] Therefore, the goal to maximize the detector's PE yield in order to minimize the statistical uncertainty on the PE count essentially dictated the design of the 20 kt LSc detector. Its current state is depicted in Figure 4.3. The *central detector* is of spherical shape to obtain a PE yield as uniform as possible throughout the designated neutrino target. It is partitioned in concentric layers with different purposes: The innermost spherical volume with ∼35.4 m in diameter is the designated neutrino target filled with ∼20 kt of LSc. It is contained in an acrylic sphere with ∼12 cm shell thickness. The acrylic vessel is hold in place by a surrounding stainless-steel support structure with a diameter of ∼40 m. Depending on the realization of this element, e.g., as a double or single layer stainless-steel truss, the structure can facilitate the direct mounting of the ∼17,000 inward-facing 20″ *central detector* PMTs. To shield the neutrino target from radiation emitted from the PMTs or the support structure, the acrylic vessel is surrounded by ultra-pure water. This effectively creates a *buffer volume* around the LSc volume. The entire central detector is submerged in a cylindrical pool filled with ∼20 kt of ultra-pure water. It is equipped with PMTs and thus not only acts as shielding against external radiation but also serves as *water Cherenkov muon veto*. The water pool is optically

[7] This mainly accounts for the PE statistics, i.e., Equation (3.11). With reference to Equation (3.10), this requirement is approximately equivalent to $\sqrt{A^2 + (1.6 \times B)^2 + (C/1.6)^2} \leq 3\,\%$ [42].

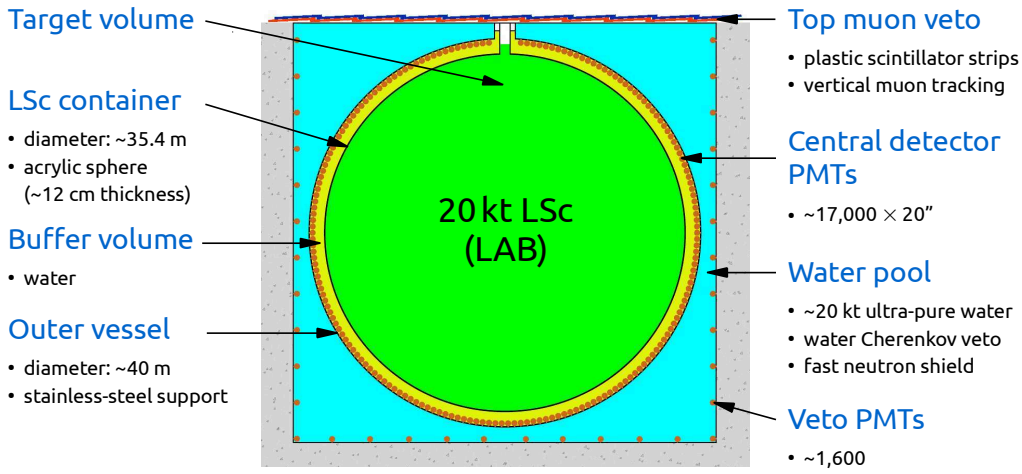

Figure 4.3 – Current schematic design of JUNO. The numbers of PMTs in the central detector and the water pool are still under study; so is the size of the PMTs for the water Cherenkov veto. Figure adapted from Ref. [42].

decoupled from the central detector such that no photons can pass over into the respective other system. A *muon tracker* made of plastic scintillator strips from the target tracker of the OPERA experiment will cover more than 25 % of the pool's surface and accurately measures downward-going muons.

Liquid scintillator mixture In order to reach the design goal concerning JUNO's energy resolution, a high-purity LSc with high light yield (∼10,000 photons per MeV) and an attenuation length $\geq 20\,\mathrm{m}$ at 430 nm is mandatory. This includes an absorption length of about 60 m, which requires special attention due to its negative effect on the PE yield. The intended scintillator mixture for JUNO will have a similar receipt as the LSc of the Daya Bay experiment. LAB will serve as basic solvent. Admixtures of 3 g/l PPO and 3.5 mg/l bis-MSB will then shift the wavelength of the emitted light to a range more convenient for the propagation through the liquid and later detection with the PMTs. Although the JUNO experiment will focus on the detection of reactor $\overline{\nu}_e$ via the IBD channel, its LSc will not be doped with a neutron-absorber like gadolinium. This hampers the detection of a strong IBD event signature, but provides better optical properties for the LSc.

Optical modules The PMT-based light detection system of the central detector is a critical part concerning the experiment's goal for the energy resolution. A photocathode coverage of $\geq 75\,\%$ is necessary to reach the required value of ∼1200 PEs per MeV. This is ensured by ∼17,000 20″ PMTs, depending on the design of the implosion prevention. No light concentrators will be mounted onto the photosensors. Furthermore, the design specifications of a JUNO PMT demand a peak photon detection efficiency of $\geq 35\,\%$ and an average value of $\geq 30\,\%$ for the broad scintillation light spectrum. This assumes a photocathode's peak QE of $\geq 38\,\%$ at ∼420 nm wavelength and a photon collection efficiency of $\geq 93\,\%$ as an average over the entire photocathode. The light detectors will operate in photon

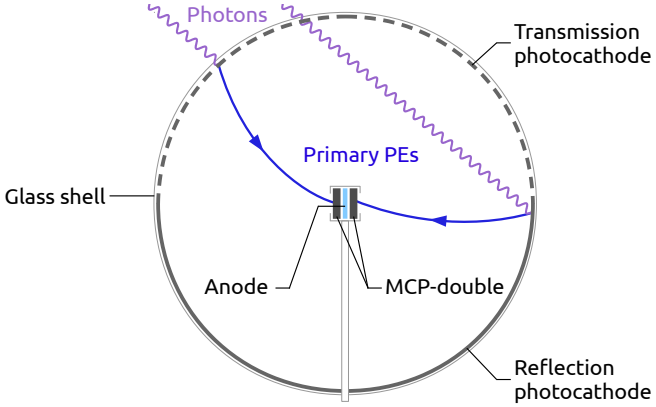

Figure 4.4 – Sketch of the MCP-PMT design for JUNO. A photon entering the photosensor can be converted to a PE either at a *transmission* or *reflection photocathode*. The PE is accelerated into a micro-channel of the central plate where it knocks out secondary electrons from the channel's inner surface. An electron avalanche builds up and finally produces a measurable current.

counting mode. For the determination of photon detection times a PMT's TTS is an important parameter. The current design value for the transit time p.d.f. is 5 ns (FWHM). Since it is difficult to achieve the design goals with a commercial high-QE PMT, a new PMT has been developed and is currently tested. Different to the dynode-based PE multiplication scheme presented in Section 3.3.1, the new PMT, which is depicted in Figure 4.4, has two different photocathodes and uses *micro-channel plates* (MCPs) to amplify the PE current.

4.3.2 Physics potential

The research program [42] of the 20 kt LSc detector JUNO is very similar to the one of the 50 kt detector LENA described in Section 4.2. Performance differences between the experiments result from the unequal target masses and shielding against cosmogenic muons in favor of LENA, and from the superior energy resolution of JUNO. Moreover, the focus of the latter experiment is the determination of the neutrino MO with reactor $\overline{\nu}_e$'s, implying a higher background rate for other studies, e.g., of geo-neutrinos. The following deals with JUNO's approach to resolve the neutrino MO and the precision measurement of oscillation parameters.

The method of JUNO (and also of RENO-50 [41]) to discover the ordering of the neutrino mass spectrum relies on a precise measurement of reactor $\overline{\nu}_e$ oscillations at a baseline length L of several tens of kilometers (see, e.g., Refs. [148, 153, 179, 180, 204–207]). In general, the $\overline{\nu}_e$ survival probability P_{ee} at energy E_ν in MeV can be written as [153]

$$
\begin{aligned}
P_{ee} &= 1 - P_{21} - P_{31} - P_{32}\,, \\
P_{21} &= \cos^4(\theta_{13})\sin^2(2\theta_{12})\sin^2(\Delta_{21})\,, \\
P_{31} &= \cos^2(\theta_{12})\sin^2(2\theta_{13})\sin^2(\Delta_{31})\,, \\
P_{32} &= \sin^2(\theta_{12})\sin^2(2\theta_{13})\sin^2(\Delta_{32})\,,
\end{aligned}
\tag{4.1}
$$

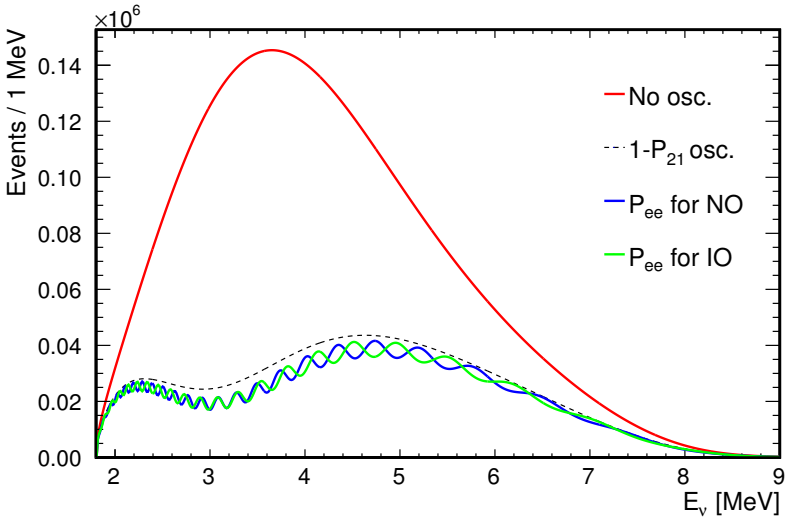

Figure 4.5 – IBD event spectra for JUNO after 1800 effective measurement days at a distance of ∼52 km to nuclear reactors with a total thermal power of 36 GW. The spectra are without oscillation (*red*), with oscillation only from the $1 - P_{21}$ term (*black dashed*), with full oscillation for NO (*blue*) and with full oscillation for IO (*green*). The NO mixing angles and Δm^2_{21} from Table 1.2 were used together with $|\Delta m^2_{32}| = 2.42 \times 10^{-3}\,\text{eV}^2$ to calculate the oscillations. Taking the IBD cross-section from Section 1.2.1 and assuming 1.5×10^{33} free protons in 20 kt LSc, the normalizations were determined according to Equation (2.6) and Equation (2.9). The assumed energy releases ϵ_k per fission of the main fissile isotopes are $\epsilon_{^{235}\text{U}} = 202.36\,\text{MeV}$, $\epsilon_{^{238}\text{U}} = 205.99\,\text{MeV}$, $\epsilon_{^{239}\text{Pu}} = 211.12\,\text{MeV}$ and $\epsilon_{^{241}\text{Pu}} = 214.26\,\text{MeV}$ [208]. All spectra are in terms of the true $\overline{\nu}_e$ energy E_ν. They neither include an energy resolution of the detector nor efficiencies.

where $\Delta_{ij} = 1.27\,\Delta m^2_{ij}\,L/E_\nu$ with Δm^2_{ij} in eV^2. The expression describes flavor oscillations in vacuum and is independent of θ_{23} and δ_{CP}. In fact, this enables a MO determination that is complementary to the approaches exploiting large matter effects in ν_μ / $\overline{\nu}_\mu$ disappearance and ν_e / $\overline{\nu}_e$ appearance searches with atmospheric and beam neutrinos (see also Chapter 8).

For JUNO, with $L \sim 52\,\text{km}$, flavor oscillations in vacuum are a good approximation. The corresponding IBD event spectrum from the reactor $\overline{\nu}_e$'s is shown in Figure 4.5. Due to the small value of $\sin^2(2\theta_{13})$, the contributions from P_{31} and P_{32} are suppressed. Using the NO mixing angles from Table 1.2, the relative amplitudes of the three terms in Equation (4.1) are about 31.1 : 2.3 : 1. However, the terms P_{31} and P_{32} contain information on the neutrino MO. Their interference leads to a phase difference between the two MO-dependent oscillation fine structures in E_ν space. With the relation $\Delta m^2_{31} = \Delta m^2_{32} + \Delta m^2_{21}$, the second leading term P_{31} has a frequency Δ_{31} that is either higher for the NO, $|\Delta m^2_{31}| = |\Delta m^2_{32}| + |\Delta m^2_{21}|$, or lower for the IO, $|\Delta m^2_{31}| = |\Delta m^2_{32}| - |\Delta m^2_{21}|$, when compared to the frequency Δ_{32}.

Using the observed IBD event spectrum, precise determinations of $|\Delta m^2_{31}|$ and $|\Delta m^2_{32}|$ from the interference of P_{31} and P_{32} in principle allow to resolve the neutrino MO. However, this is challenging since it requires a relative visible energy resolution of at least $|\Delta m^2_{21}| \,/\, |\Delta m^2_{32}| \sim 3\,\%$ at 1 MeV [207]—the design goal for JUNO. Assuming this value and a measurement time of six years at a total of 36 GW thermal reactor

Table 4.5 – Relative 1σ uncertainties on $\sin^2\theta_{12}$, Δm^2_{21} and $|\Delta m^2_{ee}|$ from a global analysis [65] and after six years of measurement with JUNO [42]. The current precision on $|\Delta m^2_{ee}|$ was calculated with Gaussian error propagation using NO (IO) parameters.

Parameter	$\sin^2\theta_{12}$	Δm^2_{21}	$\lvert\Delta m^2_{ee}\rvert$
Current	4.1 %	2.4 %	1.9 % (2.0 %)
After JUNO	0.67 %	0.59 %	0.44 %

power, JUNO's *median sensitivity* (see Section 8.3.3) to the neutrino MO is at the level of $\sim 3\sigma$ based on $\sim 10^5$ IBD signal events [42, 207]. This does not take into account external information on the atmospheric mass-squared difference. Moreover, the result assumes 1 % energy scale uncertainty. A comprehensive calibration of the JUNO detector is necessary to achieve this value. However, residual energy nonlinearity can lead to a distortion of the visible oscillation fine structure, potentially destroying information on the neutrino MO. Although numerical simulations showed that residual nonlinearity leads only to a small deterioration of the MO sensitivity, thanks to a *self-calibration effect* [207], it still is an important factor. The uncertainty on the shape of the reactor $\overline{\nu}_e$ flux is another critical aspect, especially in the light of still unexplained features like the bump in the 4–6 MeV region (see Section 2.4). A value of 1 % is assumed in JUNO sensitivity studies [42].
External information on the *effective mass-squared difference* $|\Delta m^2_{\mu\mu}|$ [207], which is a linear combination of Δm^2_{21}, Δm^2_{31} and Δm^2_{32}, can improve the power of JUNO. Assuming that that $|\Delta m^2_{\mu\mu}|$ is provided with a relative precision of 1.5 % (1 %), e.g., by combining ν_μ / $\overline{\nu}_\mu$ disappearance data from T2K and NOνA [209], JUNO's median sensitivity to the MO increases to a CL of 3.7σ (4.4σ) for a six years measurement [42]. Both results for the expected performance of JUNO were obtained with a standard least-squares analysis of the measured event spectrum. Alternatively, a *Fourier transform* [205] or separate *Fourier sine / cosine transforms* [153, 180] of the event spectrum can be used to extract information on the MO. Because the feature enabling to discriminate NO and IO is contained in frequency space, the frequency spectra from the Fourier transforms exhibit characteristics that allow to identify the realized MO.

The large number of events in JUNO also allows to measure $\sin^2\theta_{12}$, Δm^2_{21} and the effective mass-squared difference $|\Delta m^2_{ee}| = |\cos^2\theta_{12}\Delta m^2_{31} + \sin^2\theta_{12}\Delta m^2_{32}|$ with unprecedented precision. Current uncertainties on these parameters and their projected values after the JUNO measurement are summarized in Table 4.5.

A major background for the JUNO experiment are βn-decays of ^{8}He and ^{9}Li from cosmogenic muons (see Section 4.1.2): 84 events from this background type are expected every day in addition to 83 IBD signal events from reactor $\overline{\nu}_e$. One intends to reduce the background rate to 1.6 events per day at the cost of 27.7 % of the signal rate. This heavily relies on a veto strategy for the cosmogenic muons (see Ref. [42] for details). An important part of the strategy is a precise and efficient reconstruction of the tracks from non-showering, showering and stopping muons as well as from muon bundles. The track reconstruction algorithm presented in Chapter 6 aims for taking on this task.

Chapter 5

The LENA Detector Simulation

The detector simulation for LENA is a `C/C++` program based on the `GEANT4` toolkit[1] [210, 211]. For persistent storage of the output it also relies on the `ROOT` framework[2] [212]. The development of the simulation started at the *Chair for Experimental Physics and Astroparticle Physics (E15)—Technische Universität München*—around 2005 and first concentrated on aspects related to LE neutrino detection and proton decay [213]. Since then, the software has been continuously improved [214, 215]. Moreover, the possibilities to use the simulation for topics from the HE domain, e.g., studies on multi-GeV neutrinos and (cosmogenic) muons, were vastly extended [50].

In the context of this work, the LENA simulation was mainly used to provide the MC-events for the application of the reconstruction algorithm that is presented in Chapter 6. The following details relevant aspects of the program's configuration. Section 5.1 describes the parameterization of the LENA detector geometry. The optical model implemented in the simulation is treated in Section 5.2. Lastly, Section 5.3 contains information on how light detection with OMs and electronics is simulated. It has to be noted that some parts of the simulation were optimized for speed by approximating some (physics-)processes. Therefore, it does not capture every detail of a LSc detector. However, the optimizations were necessary in order to keep the required time to simulate large event samples at a reasonable level. This is especially true for events where many optical photons must be tracked through the detector, e.g., in the case of muons depositing several GeV of energy in the LSc. Despite the speed optimizations, the LENA detector simulation is considered a good starting point to test the novel track reconstruction approach from Chapter 6.

[1] `GEANT4`—an abbreviation for *geometry and tracking*—"is a toolkit for simulation of the passage of particles through matter" [210] based on MC methods. Version 4.9.6 Patch 02 was used.
[2] `ROOT` is framework for large scale data analysis programmed in object-oriented `C/C++`.

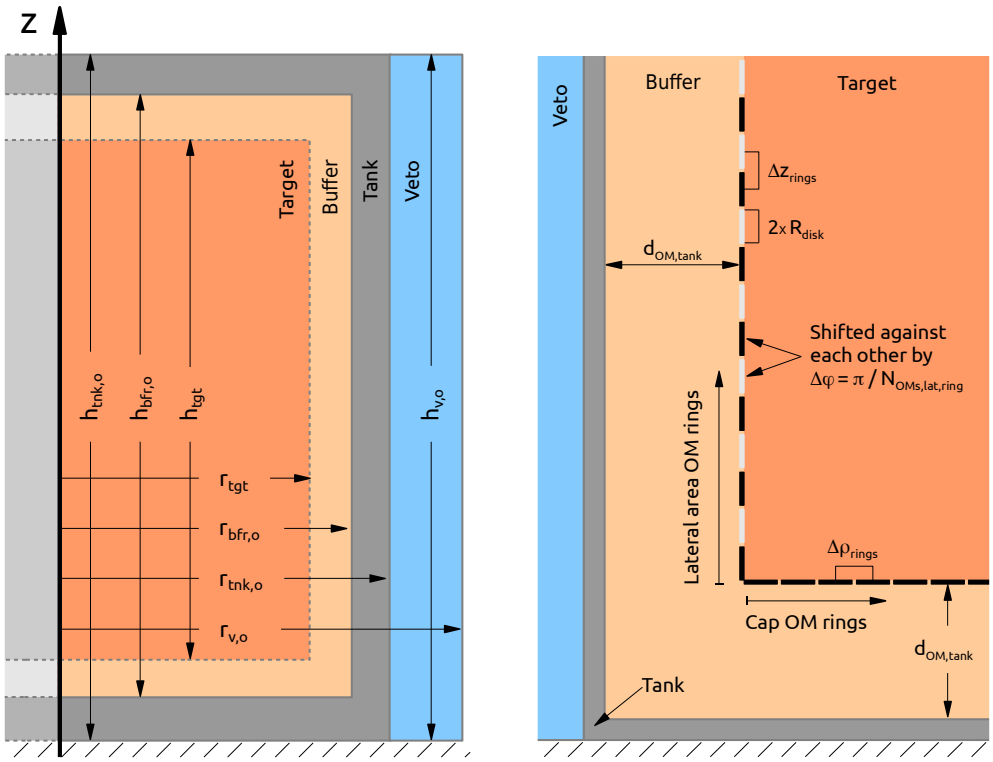

Figure 5.1 – **Left:** Schematic upright projection of the simulated LENA detector geometry with the definitions of describing parameters. The actually set parameter values are summarized in Table 5.1. The geometry in the simulation consists of four concentric, cylindrical volumes: From inside to outside they are the designated neutrino target volume (*dark orange*), the buffer volume (*light orange*), the detector tank (*gray*) and the water Cherenkov veto (*blue*). **Right:** Simulated placement of OMs in rings at the lateral area and the caps of the cylindrical detector. OMs are represented by flat, circular disks that indicate the OMs' entrance apertures and are located at the boundary between target and buffer volume. Two different OM colors at the lateral area depict that the angular positions of disks on two neighboring rings are shifted against each other by $\Delta\varphi = \pi/N_{\mathrm{OMs,lat,ring}}$. The values of the defined parameters are summarized in Table 5.1 and Table 5.2. The figures are not to scale!

5.1 Detector geometry

The description of the simulated LENA geometry is split in two parts: Dimensions and placement of the simulated detector volumes are detailed in Section 5.1.1. The distribution of OMs in the detector is subject of Section 5.1.2.

5.1.1 Volume dimensions and placement

Generally, the design strategy for LENA is a layered structure of concentric, cylindrical volumes in upright orientation. Based on Section 4.2.1, a schematic view on the simulated detector geometry and relevant parameter definitions is shown on the left of Figure 5.1. The corresponding parameter values are listed in Table 5.1.

Table 5.1 – Parameters describing the simulated LENA detector geometry. The left side of Figure 5.1 depicts their meaning. A concrete tank thickness of 30 cm was set. This differs from the design value of 60 cm for reasons explained in Ref. [215].

Parameter Description	Parameter	Value
Target radius	r_{tgt}	14.0 m
Buffer outside radius	$r_{\mathrm{bfr,o}}$	16.0 m
Tank outside radius	$r_{\mathrm{tnk,o}}$	16.3 m
Veto outside radius	$r_{\mathrm{v,o}}$	18.3 m
Target height	h_{tgt}	96.0 m
Buffer outside height	$h_{\mathrm{bfr,o}}$	100.0 m
Tank outside height	$h_{\mathrm{tnk,o}}$	100.6 m
Veto outside height	$h_{\mathrm{v,o}}$	100.6 m

The central cylinder volume with radius r_{tgt} and height h_{tgt} defines the designated neutrino target and is filled with the scintillating liquid LAB. Parameters describing the properties of the scintillator are treated in Section 5.2. The center of the innermost volume defines the origin of the detector coordinate system whose z-axis coincides with the symmetry axis of the cylinder. A hollow cylindrical volume with outside radius $r_{\mathrm{bfr,o}}$ and outside height $h_{\mathrm{bfr,o}}$ is placed between the neutrino target and the containing concrete tank. This "buffer volume" is destined for the setup of the OM support structure and filled with LSc. An optically opaque foil at the same distance to the tank wall as the entrance apertures of the OMs is intended to separate the buffer from the target region. The foil prevents scintillation light leakage from the buffer into the target. It also has to absorb impacting photons to avoid reflections back into the target volume. Neither the support structure nor the foil are implemented as objects in the simulation. Instead, the entire buffer is assumed to be filled with LSc. In order to simulate the effect of the opaque foil, the light yield $\mathscr{L}_0'$ of the LSc in the buffer is set to zero and photons are not reflected from the tank's inner walls. A coating of the inner tank walls to separate the contained LSc from the unclean concrete, for example with thin stainless-steel plates, is also not included in the simulation. The outermost layer is a hollow, open cylinder with outside radius $r_{\mathrm{v,o}}$ and outside height $h_{\mathrm{v,o}}$. Filled with pure water, this volume represents the water Cherenkov veto and shield against external radiation.

5.1.2 Optical module distribution

In LENA, OMs consist of a PMT with light concentrator (see Section 4.2.1). They constitute the photosensitive elements of the simulated detector and are implemented either with detailed physical models or as simple, flat disks, which can be seen as an OM's entrance aperture. The latter option was used in the context of this work as it significantly decreases the simulation time for events involving the propagation of large amounts of scintillation photons. Section 5.3 describes the response of an OM disk to a photon hit. The parameters that specify the distribution of the disks with radius R_{disk} inside LENA are depicted on the right side of Figure 5.1; their values are listed Table 5.2.

Table 5.2 – Simulation parameters specifying the OM disk distribution over the caps and the lateral area inside LENA. The right side of Figure 5.1 depicts their meaning.

Parameter Description	Parameter	Value
Total OMs	N_{OMs}	30542
OMs per cap	$N_{\mathrm{OMs,cap}}$	1951
OMs on lateral area	$N_{\mathrm{OMs,lat}}$	26640
OMs per lateral area ring	$N_{\mathrm{OMs,lat,ring}}$	144
Lateral area OM rings	$N_{\mathrm{rings,lat}}$	185
OM rings per cap	$N_{\mathrm{rings,cap}}$	25
OMs in innermost cap ring	$N_{\mathrm{1stRing,cap}}$	6
OM center to inner wall distance	$d_{\mathrm{OM,tank}}$	195 cm
Distance of adjacent lateral area OM rings	$\Delta z_{\mathrm{rings}}$	51.9 cm
Radial distance of adjacent cap OM rings	$\Delta \rho_{\mathrm{rings}}$	55.1 cm
Radius of disk representing OM aperture	R_{disk}	25.5 cm

The simulation includes a total of N_{OMs} OM disks. They are distributed at the inside of the tank and have their centerpoints at a distance $d_{\mathrm{OM,tank}}$ to the walls. Disks at the tank's top or bottom cap are arranged in $N_{\mathrm{rings,cap}}$ concentric rings around a central disk, totaling $N_{\mathrm{OMs,cap}}$ disks per cap. The number of disks N_j that are uniformly distributed over the j^{th} cap ring is calculated according to

$$N_j = j \cdot N_{\mathrm{1stRing,cap}}\,, \quad j \in \{1, \ldots, N_{\mathrm{rings,cap}}\} \tag{5.1}$$

where $N_{\mathrm{1stRring,cap}}$ is a constant defining the number of disks on the first, innermost ring. Any two adjacent rings of a cap have a fixed radial distance $\Delta\rho_{\mathrm{rings}}$. The first disk of any cap ring is located at the same angle φ in cylinder coordinates. At the tank's lateral area, $N_{\mathrm{OMs,lat}}$ OM disks are placed in such a way that their centers are located on $N_{\mathrm{rings,lat}}$ rings in planes parallel to the x-y-plane. The surface normal vectors of the disks point directly towards the detector's symmetry axis. All rings have the same number of $N_{\mathrm{OMs,lat,ring}} = N_{\mathrm{OMs,lat}}/N_{\mathrm{rings,lat}}$ disks. The spacing between two adjacent lateral area OM rings is identical to $\Delta z_{\mathrm{rings}}$. For a symmetric ring distribution, the centerpoint of the lateral area OM ring stack coincides with the origin of the detector coordinate system. Using cylinder coordinates, the angular positions of the disk centers on two adjacent rings are shifted against each other by the half angle difference between two neighboring disks on one ring, $\Delta\varphi = \pi/N_{\mathrm{OMs,lat,ring}}$.

5.2 Optical model

Physical effects related to the production (see Section 3.1) and propagation (see Section 3.2) of scintillation and Cherenkov light in the LENA detector simulation are described by the *optical model*. It consists of a bunch of modules that realize the simulation of optical photon processes. For most of the processes a corresponding module is already included in the `GEANT4` toolkit and utilized by the detector

simulation. Among them are, for example, the Cherenkov process, absorption, and Rayleigh scattering. However, custom implementations of the scintillation process and isotropic scattering are part of the LENA simulation package. As in the case of the simulated detector geometry, some simplifications and approximations are included in the custom parts of the optical model to speed up the simulation of events producing many optical photons.
It has to be noted that the Cherenkov process was disabled for performance reasons in all simulations done for this work. This is justifiable because in reality the fraction of detected Cherenkov photons usually is only a few percent of the detected scintillation photons, resulting from lower production output and increased absorption in the LSc.
General properties of the LSc and the scintillation process are described in Section 5.2.1. A custom implementation of isotropic photon scattering, which is part of the LENA simulation package, is subject of Section 5.2.2.

5.2.1 Liquid scintillator material and scintillation process

The LSc material set as filling of the detector's neutrino target and buffer region not only affects the MC-generated energy loss of a traversing charged particle, but also defines the parameters that are relevant to translate the deposited energy into a luminescence response. Pure LAB ($C_{18}H_{30}$) was used as LSc substance for the studies presented in this work. The simulation's default parameters for the material are listed in Table 5.3. Wavelength-shifting compounds or impurities dissolved in the liquid are not included as simulated materials. However, the effect from adding wavelength shifter to the LSc solvent is taken into account: The decay time components and corresponding weights of the scintillator, which are used with Equation (3.2) to describe the timing p.d.f. of photon emission, correspond to results from a measurement of deoxygenated LAB with an admixture of 2 g/l PPO [216].[3] A realistic value for the light yield of the scintillator mixture is $\sim 10{,}000\,\mathrm{MeV}^{-1}$. However, a smaller value $\mathscr{L}_0 = 2000\,\mathrm{MeV}^{-1}$ is used in the simulation for reasons explained in Section 5.3.

The LENA simulation package contains a custom implementation of the scintillation process. This is due to the fact that the default version delivered with `GEANT4` neither respects quenching effects nor allows to use more than two decay time components to describe the scintillator's timing p.d.f. The customized code for the scintillation process first determines the energy deposition per unit path length, $\mathrm{d}E/\,\mathrm{d}x$, of a charged particle in the LSc material. Based on that value, the mean number of emitted scintillation photons μ_γ is calculated according to Equation (3.1). The actually simulated photon count N_γ is then randomly drawn from a Poisson distribution $\mathcal{P}(\mu_\gamma)$, if $\mu_\gamma \leq 10$, or a normal distribution $\mathcal{N}(\mu_\gamma, \sqrt{\mu_\gamma})$. Simulated photons with a random linear polarization are emitted isotropically from points that are uniformly distributed along the particle's track segment. For each of the emitted photons, the time delay between energy deposition and photon emission is randomly drawn from the p.d.f. described by Equation (3.2), using the scintillator's values for

[3] As mentioned in Section 4.2.1, the scintillator mixture intended for LENA is LAB with admixtures of 3 g/l PPO and 20 mg/l bis-MSB as wavelength-shifter solutes.

Table 5.3 – Properties of LAB ($C_{18}H_{30}$) that is used as LSc in the LENA detector simulation. Optical parameters that normally depend on the wavelength, like the refractive index, the absorption length and the individual scattering lengths, are effectively treated as wavelength-independent in the simulation. Data cited from Ref. [215].

Parameter Description	Parameter	Value
Mass density	ρ_{m}	$0.86\,\mathrm{g\,cm^{-3}}$
Refractive index	n	1.484
Absorption length	l_{A}	20 m
Rayleigh scattering length	l_{ray}	40 m
Isotropic scattering length	l_{iso}	60 m
Light yield (target)	$\mathscr{L}_0$	$2000\,\mathrm{MeV^{-1}}$
Light yield (buffer)	$\mathscr{L}_0'$	$0\,\mathrm{MeV^{-1}}$
Birks constant	kB	$0.15\,\mathrm{mm\,MeV^{-1}}$
1^{st} time component	τ_1	4.6 ns
2^{nd} time component	τ_2	18.0 ns
3^{rd} time component	τ_3	156.0 ns
Weight of 1^{st} time component	ω_1	0.71
Weight of 2^{nd} time component	ω_2	0.22
Weight of 3^{rd} time component	ω_3	0.07
Re-emission time constant	τ_{rem}	1.2 ns

the time constants and weights. The wavelength of the emitted light is restricted to the narrow range from 420 nm to 430 nm, which is close to the emission maximum of the scintillator mixture. However, wavelength-dependent effects are neglected in the simulation to save computation time. This is done by setting the refractive index and the absorption and scattering lengths to constant values. As a result, all optical photons travel with the *phase velocity* $v = c_0/n$ through the medium (see Equation (3.5)).

5.2.2 Isotropic scattering

Another custom module being part of the optical model of the LENA detector simulation describes the isotropic scattering process. In contrast to anisotropic scattering, the differential cross-section $\mathrm{d}\sigma/\,\mathrm{d}\Omega$, where $\mathrm{d}\Omega$ is the solid angle element the incident particle is scattered to, is independent of the scattering angle. As measurements on LAB indicate, the major contribution to isotropic scattering is absorption with subsequent isotropic re-emission [172]. In the simulation, the process is implemented such that the incident optical photon becomes absorbed and a new optical photon is emitted with random direction and linear polarization. The randomized wavelength λ_{out} of the emitted photon λ_{out} is restricted to $\lambda_{\mathrm{in}} < \lambda_{\mathrm{out}} \leq 430\,\mathrm{nm}$. For the time delay Δt between absorption and re-emission a random value is determined from an exponential p.d.f.,

$$\Phi_{\mathrm{rem}}(\Delta t; \tau_{\mathrm{rem}}) = \frac{1}{\tau_{\mathrm{rem}}} e^{-\frac{\Delta t}{\tau_{\mathrm{rem}}}} \ . \tag{5.2}$$

The value of τ_{rem} is given in Table 5.3.

5.3 Optical module and electronics model

As discussed in Section 5.1, the simulations done in the context of this work used flat, circular disks to model the photosensitive detector areas. When an optical photon reaches the disk surface oriented towards the detector's interior, it is checked if the photon is accepted by the light concentrator model to generate a detected hit: First, the photon incident angle θ with respect to the surface normal vector of the disk is determined. Afterwards, the probability $p_{\text{accept}}(\theta)$ that the photon is accepted by the OM's light concentrator is looked-up in tabulated data. The *look-up table* (LUT) for the angle-dependent acceptance function is part of the LENA simulation package and shown in Figure 5.2. It was generated by simulating numerous photon tracks through a geometrical model of a light concentrator [215]. Due to the averaging of the photon acceptance over the concentrator's entrance aperture in the course of the detailed geometry simulation, the resulting LUT data are used for each surface point of an OM disk. Using the probabilities $p_{\text{accept}}(\theta)$ and $1 - p_{\text{accept}}(\theta)$, the MC simulation finally determines if the currently processed photon is accepted by the OM's light concentrator. An unaccepted photon is absorbed and not reflected back into the LSc volume. Although the probability to detect such reflected photons is small due to the dimensions of the detector, they would effectively increase the PE yield by about 4 % [215]. For an accepted photon, which is directly tagged as hit, the simulated arrival time at the disk and the disk's unique identifier are stored persistently for post-processing or immediate analysis. Since every photon passing the light concentrator acceptance creates a hit, this would imply a QE of the PMT photocathode of 100 %. However, as mentioned in Section 5.2.1, a reduced scintillation light yield of only $\mathscr{L}_0 = 2000\,\text{MeV}^{-1}$ is used in the simulation compared to a more realistic value of $\sim$ 10,000 MeV^{-1}. This is done to prevent the time-consuming simulation of a huge fraction of scintillation photons only to discard them for consideration of a PMT cathode's QE. Therefore, this technique to speed-up the simulation actually implies the assignment of a wavelength-independent, uniformly distributed QE of $\eta_{\text{PMT}} = 20\,\%$ to all simulated OMs.

After the simulation, the only post-processing done to the saved, exact photon hit times is a random smearing to simulate the impact of a PMT's TTS ΔT. The unchanged photon hit time t from the simulation is translated to the smeared hit time t' according to

$$t' = t + \delta t\,, \tag{5.3}$$

where δt is randomly drawn from the normal distribution $\mathcal{N}(0, \Delta T)$. The value of ΔT is stated in Table 5.4. Note that the normal distribution is only a rough approximation of the usually asymmetric distribution $\Phi_{\delta T}$ in Section 3.3.1.
No further processing of the photon hit times is done since no proper model for the response of an OM with attached electronics chain existed in the used version of the LENA detector simulation package. Therefore, relevant influences of the light concentrator and the electronics chain on the assignment of time values to individual photon hits are not yet fully respected. In particular, the photon propagation through the light concentrator, the average electron avalanche transit time $\overline{T}$ through the

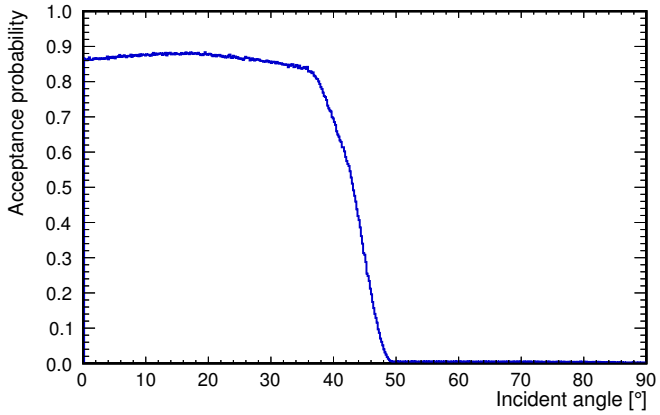

Figure 5.2 – Photon acceptance probability of an OM's light concentrator as a function of the photon incident angle with respect to the surface normal of the concentrator's entrance aperture. The data are part of the LENA detector simulation package. They were generated with a MC simulation including a concentrator geometry model that matches the light concentrator used in BOREXINO [176]. It has 86 % reflectivity and a critical incident angle of $\sim 44°$.

Table 5.4 – PMT parameters in the LENA detector simulation.

Parameter	Value	Comment
Effective QE	20 %	wavelength-independent, uniform
TTS ΔT	1 ns ($\sim$2.4 ns)	standard deviation (FWHM)

PMT and the signal transit time from the PMT anode to the electronic device setting the time stamps for persistent storage are not considered by Equation (5.3).
PMT-related effects, like dark current, pre- and after-pulses, were disabled during the simulations. Moreover, without a simulated digitization of the PMT response, one cannot answer the question if and how well individual photon hits can be identified from a (real) PMT signal waveform at all (see Section 3.3.3). Section 7.1.1 shortly addresses general consequences for the track reconstruction in Chapter 6 that arise from the stated simplifications in the electronics simulation.

Chapter 6

A Novel Track Reconstruction Approach for Liquid Scintillator

A new method for charged particle track reconstruction in unsegmented LSc detectors has been developed by *Björn S. Wonsak* [39]. The new approach is particularly useful for resolving topological features of a muon track that are beyond the reach of currently employed reconstruction techniques. Since the new method functions without fitting a finite set of complex event topology models to the observed photon hit data, its field of application is not bounded to the reconstruction of muon tracks. Due to a limited number of fundamental assumptions, the new reconstruction has the potential to yield useful results for any type of event in LSc. Nevertheless, it is fair to say that for growing topological complexity the algorithm surely needs more computation time and differentiated tuning to produce comparably good results in any case.
In the context of this work, the computational precision was improved at different steps of the reconstruction algorithm with respect to the initial implementation. For example, this was done by incorporating more detailed descriptions of the scintillation light propagation and detection for the considered LSc detector LENA (see Section 4.2). Moreover, the first realization of the algorithm in terms of programming was advanced into a `C++`-based software package. Using *object-oriented design principles*, the reconstruction code became encapsulated behind general interfaces, thus decoupling the algorithm from the actual application context, i.e., the (simulated) detector that provides the (MC) data. This provides a good basis for future development and testing of the new reconstruction technique.

The focus of this chapter is on the description of the novel topological reconstruction method and its current implementation for LENA. First, Section 6.1 covers the motivation for the development of a new (muon) track reconstruction for LSc detectors. Some fundamental ideas on particle tracking in this medium are summarized in Section 6.2. Subsequently, Section 6.3 describes the new reconstruction method in general. After some details on its current implementation (in the context of LENA) in Section 6.4, an outlook on future developments and applications is finally

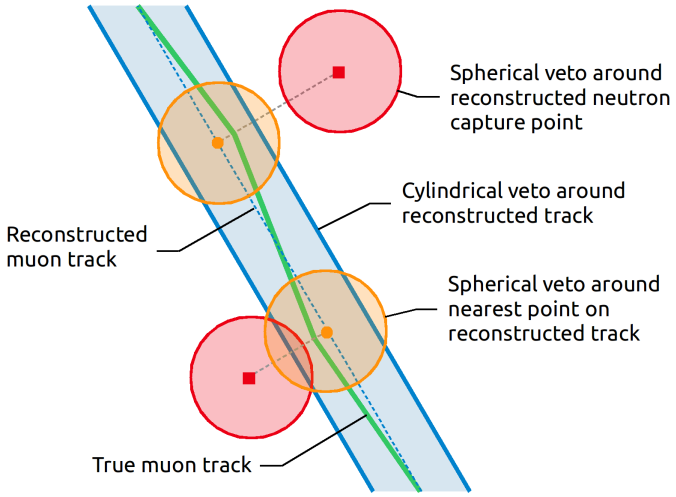

Figure 6.1 – Illustration of the *three-fold coincidence veto* technique. For example, it is used in BOREXINO [30] to reject cosmogenic ^{11}C background produced in the interaction $\mu + {}^{12}C \rightarrow \mu + {}^{11}C + n$. Spherical regions with 1 m radius around the reconstructed neutron capture point (*red*) and the corresponding nearest point (*orange*) on the reconstructed muon track (*dashed blue*) are primarily vetoed. Under certain conditions (e.g., an unreliably reconstructed neutron capture point; see Ref. [30]), a cylindrical volume (*blue*) with 80 cm radius must be vetoed around the reconstructed muon track. Note that the cylinder radius must be chosen such that deviations of the true muon track (*green*) from the reconstructed track are taken into account on average.

given in Section 6.5. Results from the application of the reconstruction technique to MC events from the LENA detector simulation (see Chapter 5) are subject of Chapter 7.

6.1 Motivation

A muon track reconstruction usually is an important part of a strategy to identify and reject cosmogenic background events in LSc detectors (see also Section 4.1.2). Having a precisely reconstructed muon trajectory, one can constrain spatial vetoes to the most likely points of origin for cosmogenic radioisotopes. This minimizes the necessity to veto the full detector for some period of time, which is very inefficient or even impracticable if long-lived radionuclides, e.g., ^{10}C and ^{11}C, must be rejected or the muon rate is high. A technique to avoid a full detector veto is the *three-fold coincidence veto*. It is, for example, employed in BOREXINO to reject cosmogenic ^{11}C background (see Section 4.1.2, Ref. [30]). As illustrated by Figure 6.1, the space vetoed by this method can include a cylindrical volume with 80 cm radius around the reconstructed muon track. Alternatively, the spatial distance between a reconstructed muon track and a delayed LE event can also be used as parameter to build a high-purity sample of radionuclide decay events. Looking at the visible energy spectrum from the decays, an analysis of this sample eventually allows a statistical background subtraction.
In current experiments, the outcome of a dedicated muon track reconstruction is

a straight line. It can be constructed by connecting the entrance point and the exit point determined from the first photon hit times at the photosensors (e.g., see Ref. [37]). However, this only works for *through-going muons*. The fitting of a model for the temporal evolution of the first photon front from a straight track to the observed hit time data (e.g., see Ref. [38]), on the other hand, can also describe *stopping muons*. In either case, muon tracking systems surrounding the central target volume can provide additional information to support or cross-check the muon track finding.

The number of muons simultaneously entering the target volume of a LSc detector with today's dimensions is mostly one. Besides those only going through or stopping in the detector, some muons induce particle cascades. It is known from KamLAND [193] and more recent MC simulations [217] that radioisotope production is strongly correlated with such showers. *Showering muons* can be tagged by looking for a significant energy deposition in addition to the expected energy loss from ionization. Their identification usually results in a full detector veto.
With increasing detector size it becomes more likely that more than one muon enters the LSc volume at the same time. Such *muon bundles* are difficult to reconstruct due to their simultaneous isotropic emission of scintillation light. They likely entail a full detector veto as well.
A concrete example for a large-volume LSc detector especially prone to muon induced background is the one of the future JUNO project (see Section 4.3). Due to the overburden of only $\sim$700 m, a total muon event rate of $\sim 3\,\mathrm{s}^{-1}$ results in a 1 : 1 ratio between IBD signals and the dominant background from cosmogenic, βn-emitting ^{8}He and ^{9}Li. The expected rate of showering muons is $\sim 0.5\,\mathrm{s}^{-1}$ and a muon bundle enters the detector in about 10 % of all cases [42].[1] Due to the high muon rate, a sole use of full detector vetoes would bring the experiment's effective measurement time to zero. For well tracked muons, the current strategy therefore bases on a 1.2 s selective veto in a cylindrical region with 3 m radius around the reconstructed track.[2] Otherwise a full detector veto is applied [42]. Note that the cylinder radius must be chosen such that a deviation of the true muon track from the reconstructed straight track is taken into account. If a muon track, which has an average length of 23 m [42] in JUNO, is reconstructed by connecting entrance point and exit point of the particle, the uncertainty on the true trajectory is largest around the half of the reconstructed track.

Although the novel reconstruction technique presented in this chapter also bases on the assumption of a straight particle track, to some degree it can still correctly resolve deviations from this model. Consequently, it could yield a more precise estimate for a muon trajectory in the LSc volume and would thus allow a more fitting spatial veto for cosmogenic background rejection. More importantly, the new method resolves distinctive features of an event's topology, essentially giving access to the differential energy loss $\mathrm{d}E/\,\mathrm{d}x$. This enables vetoes even more focused on

[1] Similar results were obtained from a detailed MC study in Ref. [217].
[2] The current estimate is that an IBD signal to ^{8}He / ^{9}Li background ratio of 37.5 : 1 can be achieved at the cost of 27.7 % of the signal. This assumes that a muon veto, which bases on good tracking for 99 % of both non-showering and showering muons, preserves 83 % of the signal but only 2.3 % of background from the radioisotopes [42]. A study regarding optimal veto parameters for each science goal is reported in Ref. [218].

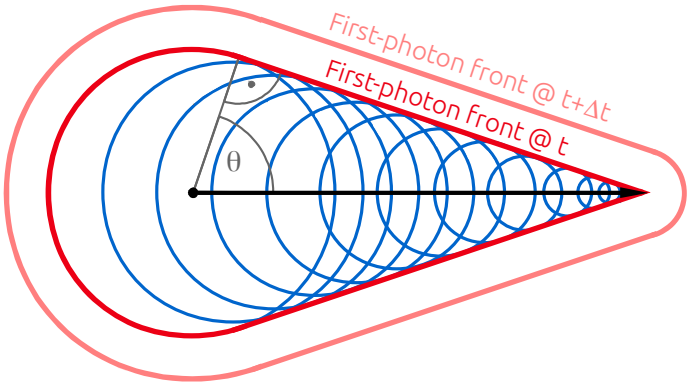

Figure 6.2 – Creation of the first-photon front along a straight track (*black*) in LSc from a charged particle with speed $v = \beta c_0$. Cherenkov light production is not taken into account. Fast, spheric emissions of scintillation light (*blue*) along the particle trajectory superimpose each other and form a cone-like structure, the front with the first photons. After the stop of the particle at time t (*dark red*), the cone tip becomes more and more rounded with further time Δt for photon propagation (*light red*). Similar to the Cherenkov case in Equation (3.3), the angle θ is given by $\cos\theta = 1/[\beta(n(\epsilon) + \epsilon \frac{\mathrm{d}n}{\mathrm{d}\epsilon'}|_\epsilon)]$. This assumes instantaneous emission and follows from the group velocity v_g in Equation (3.5) for the photon of energy ϵ with the fastest propagation in the LSc.

muon-induced particle showers, thereby increasing an experiment's efficiency. Beyond currently tested capabilities, it is expected that the topological reconstruction can also yield valuable results if applied to muon bundle events.

6.2 Fundamentals for track reconstruction in a liquid scintillator detector

In a LSc detector's usual LE range of operation, neutrino interactions lead to essentially *point-like* energy depositions.[3] Since the PE yield is not uniform over the detector, due to geometric and light attenuation effects, a precise determination of the event position and topology is important for a proper reconstruction of the visible energy. A first guess for the location of a point-like event is the *charge barycenter*, which is obtained from the detected *PE distribution* over the photosensors. Likelihood-based fits, which in addition take the observed *photon hit time distribution* into account, allow to refine the result (e.g., see Refs. [50, 51]).
With increasing kinetic energy, the energy deposition of a charged particle in LSc spreads more and more in time and space. This inevitably makes the photon hit time distribution the primary source of information [48]. As illustrated in Figure 6.2, a charged particle mainly produces spheric emissions of scintillation light at each point of its trajectory in LSc. If the particle moves faster than the scintillation photons in the medium, the superimposed light fronts containing the first photons from each point together form a cone-like structure. Although the cone shows similarities with

[3]Note that γ-rays, e.g., from the positron annihilation or neutron capture in an IBD coincidence, can cause a spread of the deposited energy.

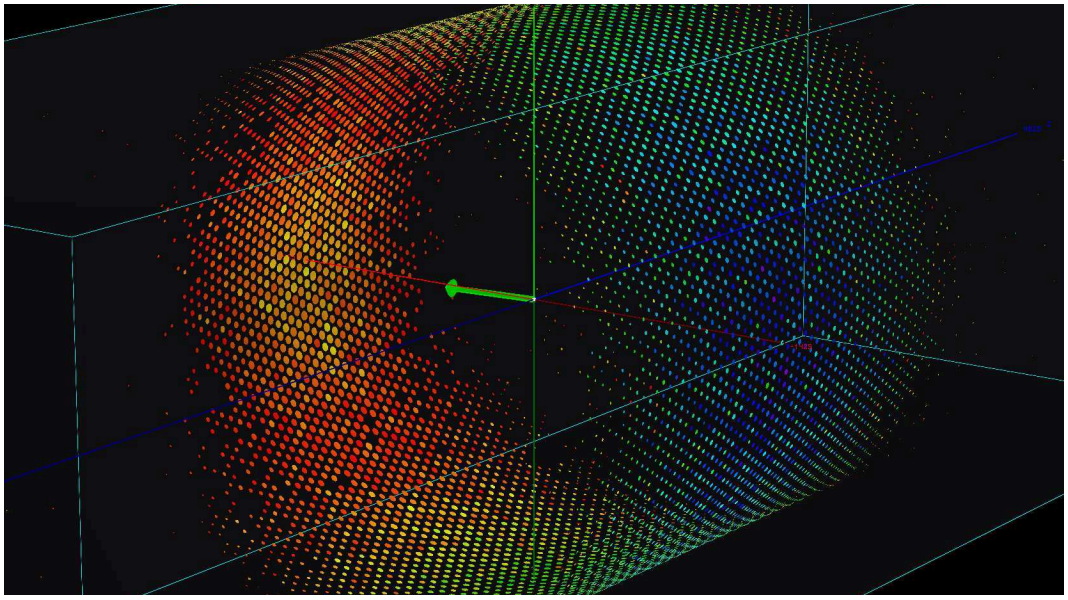

Figure 6.3 – Event display for a simulated muon with 1 GeV initial kinetic energy in LENA. The muon (*green arrow*) traveled from the detector center along the positive x-axis. Colored circles with different areas represent the OMs and their response: A larger circle area indicates a larger number of collected PEs, which is in the range [0, 139]. The color code depicts the arrival time of the first photon between −15 ns (*blue*) and 10 ns (*red*) after a TOF-correction with respect to the reconstructed charge barycenter. OMs with a first hit outside of this time range or without hits are not shown. Figure from Ref. [51].

the Cherenkov cone in Figure 3.1, it has two distinctive features: Isotropic scintillation light is directly emitted into the half-space behind the track and significant amounts of light also propagate in track direction.[4] Given that the shape and population of the *first-photon front* is not deteriorated much due to photon scattering and absorption, the position and orientation of the front should become manifest in the *first-photon hit time pattern* at the photosensors. As an example, this is depicted in Figure 6.3 for a simulated muon in LENA: The shown distribution of the first hit times over the OMs after a TOF-correction with respect to the reconstructed charge barycenter has a cluster in backward direction of the track for the earliest times (*blue*). This is because the TOF-correction with respect to the charge barycenter is in this case larger than the actual TOF of photons from the track's start point. The charge distribution understandably shows a cluster at the OMs closest to the excentric energy deposition. Without high demands on electronics capabilities (see also Section 3.3.3), these features already provide information on the direction of the track.

Although the first-photon front offers a starting point to estimate the orientation and position of an energy deposition, more detailed information can be gained from the ensemble of photons propagating within the expanding cone. They travel behind

[4] In principle, Cherenkov light can also be emitted in track direction if the Cherenkov angle θ_c in Equation (3.3) is zero at the threshold velocity $\beta_t = 1/n(\epsilon)$. Note, however, that in this case the light yield is zero according to Equation (3.4).

the front because of delayed emission from the scintillator (see Section 3.1.1) and/or scattering (see Section 3.2). Clearly, hits from these photons provide deteriorated timing information compared to hits from the first-photon front. Their by far larger number, however, provides access to more detailed features of an energy deposition on a statistical basis. Note that the utilization of these photons puts higher demands on the electronics capabilities. Preferably, it can resolve the hit time of each single photon at a photosensor.
One approach to make use of the information from all photon hits is the fitting of a concrete hypothesis to the spatial and temporal distribution of all photon hits at the photosensors (e.g., see Refs. [50, 51]). However, the study of details in an energy deposition requires complex hypotheses with sufficient amounts of fit parameters. In addition, these parameters need good start values. This already necessitates some prior knowledge on the topology and features of the event at hand. A second, general complication is that a fitting of hypotheses is "blind" to unexpected features.
The method presented in the next section follows a different approach: Using information from all detected photon hits, it aims to reconstruct the *spatial number density distribution of photon emissions* without detailed hypotheses. This allows a direct visualization of the event topology and provides information on the differential energy loss $\mathrm{d}E/\,\mathrm{d}x$. Relevant parameters for succeeding analyses can be extracted with techniques from 3D data processing (see also Chapter 7).

6.3 New reconstruction approach

This section describes the fundamental idea of the new track reconstruction technique for LSc detectors developed by *Björn S. Wonsak* [39]. The goal of the new approach is to reconstruct the *spatial number density distribution of photon emissions* $\Gamma_{\mathrm{em}}(\mathbf{x})$. In its current state, the new method assumes that all photons emitted in the LSc originate from scintillation. However, it is not closed to a future (necessary) extension incorporating the peculiarities of Cherenkov light. It is also assumed that individual hit times can be assigned to all photons even in the case of high photon rates or multi-photon hits (see discussion in Section 3.3.3).
Section 6.3.1 details the first steps towards a reconstruction of $\Gamma_{\mathrm{em}}(\mathbf{x})$ from the information provided by the single photosensors with photon hits. Afterwards, Section 6.3.2 introduces the powerful concept of a *probability mask*, which is used in an iterative procedure to refine the obtained results.

6.3.1 Estimating the spatial number density distribution of photon emissions

For a single photosensor, e.g., a PMT (see Section 3.3.1), the reconstruction bases on a model that establishes a temporal connection between two incidents: i) a charged particle travels through LSc, thereby causing the emission of scintillation and Cherenkov photons, and ii) a photosensor at position $\mathbf{r}_j$ registers a photon hit at time $t_{j,k}$. In the following, the index j refers to the j^{th} of $N^{\mathrm{hit}}_{\mathrm{PMT}}$ hit photonsensors and the index pair (j,k) of $t_{j,k}$ refers to the k^{th} of $N_{\mathrm{hits},j}$ photon hits observed by the j^{th} sensor. To make the temporal link between the incidents, two basic assumptions are made:

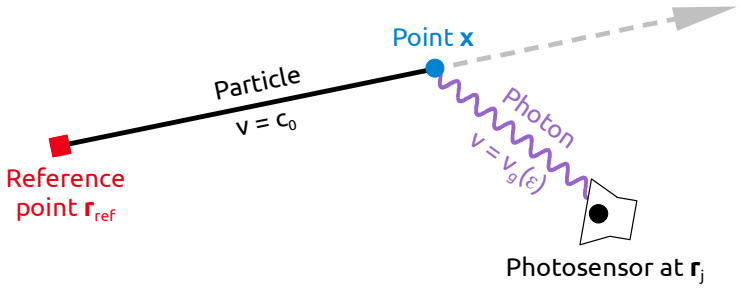

Figure 6.4 – Illustration of the model to calculate $t(\mathbf{x})$ with Equation (6.1). Passing the reference point $\mathbf{r}_{\text{ref}}$ at the reference time t_{ref}, a charged particle travels with the speed of light in vacuum c_0 along a straight track. A photon emitted with energy ϵ at point $\mathbf{x}$ reaches the photosensor at $\mathbf{r}_j$ after it covered the distance $|\mathbf{x} - \mathbf{r}_j|$ with the speed equal to the energy-dependent group velocity $v_g(\epsilon)$.

1. The charged particle travels along a straight track with the speed of light in vacuum c_0.[5]

2. A *reference point* $\mathbf{r}_{\text{ref}}$ on the particle track is known together with the *reference time* t_{ref} when the particle was at $\mathbf{r}_{\text{ref}}$.[6]

For the reconstruction, it is naturally assumed that the two incidents above are causally connected. Given a spatial point $\mathbf{x}$ on the particle track in the LSc volume, the point in time t when a photon with energy ϵ reaches $\mathbf{r}_j$ from $\mathbf{x}$ follows from the model as

$$t(\mathbf{x}) = t_{\text{ref}} \pm \underbrace{\frac{|\mathbf{x} - \mathbf{r}_{\text{ref}}|}{c_0}}_{\text{particle}} + \underbrace{\frac{|\mathbf{r}_j - \mathbf{x}|}{v_g(\epsilon)}}_{\text{photon}} . \tag{6.1}$$

Here $v_g(\epsilon)$ is the speed of the photon, i.e., the energy-dependent group velocity, given by Equation (3.5). A constant term for the average time a signal needs to transit through the sensor is omitted. As one can infer from Figure 6.4, which illustrates the model to calculate $t(\mathbf{x})$ with Equation (6.1), the sign of the time contribution from the particle depends on whether point $\mathbf{x}$ was reached before $(-)$ or after $(+)$ the reference point $\mathbf{r}_{\text{ref}}$. The fundamental idea of the reconstruction approach now is to use Equation (6.1) for a computation of $\mathbf{x}(t_{j,k})$: Given the observed signal at time $t_{j,k}$, what is the origin $\mathbf{x}$ of the photon? Figure 6.5 illustrates, for the two-dimensional case, that there is no unique solution. Instead, one obtains an *isochrone* for each $t_{j,k}$, which corresponds to a surface in three dimensions.

Currently, Equation (6.1) implies that scintillation photons are emitted instantaneously with energy ϵ, propagate unhindered to $\mathbf{r}_j$ and are finally detected with perfect time resolution. In reality, the photon emission is a stochastic process in time with a p.d.f. given by Equation (3.2), and the photosensor has a finite time

[5] The assumption is acceptable for muons without large-angle scattering. If the particle type is known, the speed assumption can be refined by using an *effective speed* from MC simulations, which also takes scattering into account.

[6] For cosmogenic muons, external tracking systems can provide the reference parameters. Some methods described in Ref. [51], especially the *backtracking algorithm*, are candidates to obtain the needed reference parameters in other cases.

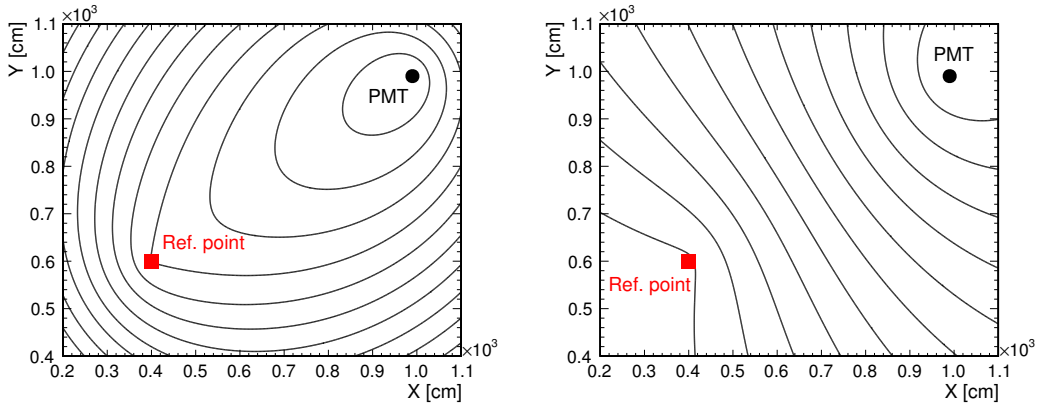

Figure 6.5 – *Isochrones* for different values of $t_{j,k}$ from Equation (6.1) with the plus **(left)** or minus **(right)** sign for the term describing the particle contribution. The photosensor (e.g., a PMT; *black circle*) is located at $(990, 990)$ cm and the reference point (*red square*) was set to $(400, 600)$ cm. For simplicity, the group velocity v_g in Equation (6.1) was replaced by the phase velocity $v = c_0/n$ with the refractive index $n = 1.484$ (see Table 5.3).

resolution (e.g., due to the TTS of a PMT; see Section 3.3.1). Moreover, scintillation light exhibits an energy spectrum characteristic for the LSc, is scattered during its propagation and may hit the photosensor anywhere on the photosensitive area. To take such effects into account, Equation (6.1) is altered to:

$$\hat{t}(\mathbf{x}) = t_{\text{ref}} \pm \underbrace{\frac{|\mathbf{x} - \mathbf{r}_{\text{ref}}|}{c_0}}_{\text{particle}} + \underbrace{t_{\text{ph}}(\mathbf{x}, \mathbf{r}_j)}_{\text{photon}} - t_s \,. \tag{6.2}$$

The quantity $t_{\text{ph}}(\mathbf{x}, \mathbf{r}_j)$ replaces the fixed photon contribution in Equation (6.1). It accounts for the photon's random energy and path from $\mathbf{x}$ to an unknown point on the photosensitive area. Therefore, the corresponding p.d.f. $\Phi_{t_{\text{ph}}}(t; \mathbf{x}, \mathbf{r}_j)$ effectively includes the optical model of the LSc detector (photon emission, propagation and detection; see Chapter 3).
The contribution t_s in Equation (6.2) incorporates the timing uncertainty from the photon emission and the photosensor. An example for the p.d.f. $\Phi_{t_s}(t)$ of this random variable is depicted on the left side of Figure 6.6.
A change from the deterministic value of $t(\mathbf{x})$ to the probabilistic value of $\hat{t}(\mathbf{x})$ also requires a change to the reconstruction procedure: For a given combination of $\mathbf{r}_{\text{ref}}$, $\mathbf{r}_j$ and t_{ref}, the task is to calculate for each point $\mathbf{x}$ in the LSc-filled volume V_{LSc} and each individual photon hit $t_{j,k}$ a spatial probability density $\Phi_{j,k}(\mathbf{x})$ related to the chance that the detected photon originated from that point. The p.d.f. $\Phi_{j,k}(\mathbf{x})$ has to take into account the probability that $t_{\text{ph}}(\mathbf{x}, \mathbf{r}_j)$ and t_s have fitting values to realize $\hat{t}(\mathbf{x}) = t_{j,k}$.
For a calculation of the spatial p.d.f. $\Phi_{j,k}(\mathbf{x})$ based on the time information, which must fulfill the normalization condition

$$\iiint_{V_{\text{LSc}}} \Phi_{j,k}(\mathbf{x}) \, \mathrm{d}x \, \mathrm{d}y \, \mathrm{d}z \stackrel{!}{=} 1 \,, \tag{6.3}$$

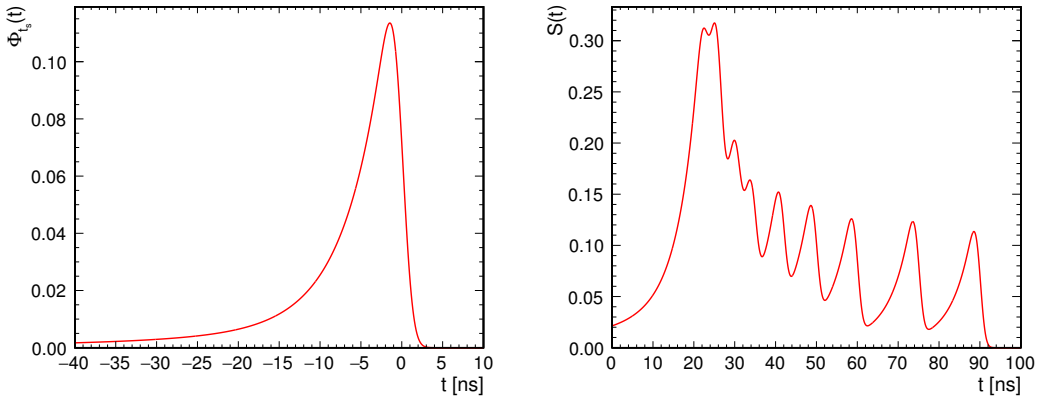

Figure 6.6 – **Left:** The p.d.f. $\Phi_{t_s}(t)$ from the convolution of the timing p.d.f. for the scintillation light emission in Equation (3.2) with a Gaussian p.d.f. for the timing uncertainty of the photosensor. Decay times and weights from Table 5.3 were used for the scintillator's timing p.d.f. The Gaussian resolution function had a standard deviation of 1 ns. Note that the direction of the distribution's tail assumes that t_s is subtracted from the right side of Equation (6.1). **Right:** Example for an *unweighted signal function* $S(t)$ with ten photon hits at 23, 26, 27, 31, 35, 42, 50, 60, 75 and 90 ns. Each signal component has the shape of the p.d.f. $\Phi_{t_s}(t)$ shown on the left.

one constructs a second p.d.f. $\widetilde{\Phi}_{j,k}(t)$ depending on the time t such that $\widetilde{\Phi}_{j,k}(t) = \Phi_{t_s}(t - t_{j,k})$. It calculates the probability density for the case that the random timing uncertainty t_s in (6.2) is responsible for the time difference $\Delta t = t - t_{j,k}$ between any time t and the photon hit time $t_{j,k}$. This allows to compute $\Phi_{j,k}(\mathbf{x})$ as

$$\Phi_{j,k}(\mathbf{x}) = w_{j,k} \int_0^\infty \widetilde{\Phi}_{j,k}\left(\hat{t}(\mathbf{x}; t_{\text{ph}} = t', t_s = 0)\right)\, \Phi_{t_{\text{ph}}}(t'; \mathbf{x}, \mathbf{r}_j)\, \mathrm{d}t' \,. \tag{6.4}$$

The factor $w_{j,k}$ ensures the normalization (6.3) of $\Phi_{j,k}(\mathbf{x})$,

$$w_{j,k} = \left(\iiint_{V_{\text{LSc}}} \int_0^\infty \widetilde{\Phi}_{j,k}\left(\hat{t}(\mathbf{x}; t_{\text{ph}} = t', t_s = 0)\right)\, \Phi_{t_{\text{ph}}}(t'; \mathbf{x}, \mathbf{r}_j)\, \mathrm{d}t' \, \mathrm{d}x \, \mathrm{d}y \, \mathrm{d}z \right)^{-1} . \tag{6.5}$$

One can see on the left side of Figure 6.7, which depicts an example of $\Phi_{j,k}(\mathbf{x})/w_{j,k}$, that the temporal p.d.f. $\widetilde{\Phi}_{j,k}(t)$ leads to a smearing perpendicular to the isochrone previously calculated with Equation (6.1).
Currently, points on the same isochrone of $\Phi_{j,k}(\mathbf{x})$ have the same weight. However, due the solid angle of the photosensor area, the angular acceptance of a potential light concentrator, photon scattering and photon absorption, each point $\mathbf{x}$ has a different probability $P_{\text{det},l}(\mathbf{x})$ that an emitted photon reaches the sensitive area of photosensor l at $\mathbf{r}_l$. To take this fact into account, Equation (6.4) is altered to

$$\Phi^*_{j,k}(\mathbf{x}) = w^*_{j,k} P_{\text{det},j}(\mathbf{x}) \int_0^\infty \widetilde{\Phi}_{j,k}\left(\hat{t}(\mathbf{x}; t_{\text{ph}} = t', t_s = 0)\right)\, \Phi_{t_{\text{ph}}}(t'; \mathbf{x}, \mathbf{r}_j)\, \mathrm{d}t' \tag{6.6}$$

$$= \frac{w^*_{j,k}}{w_{j,k}} P_{\text{det},j}(\mathbf{x}) \Phi_{j,k}(\mathbf{x}) \,. \tag{6.7}$$

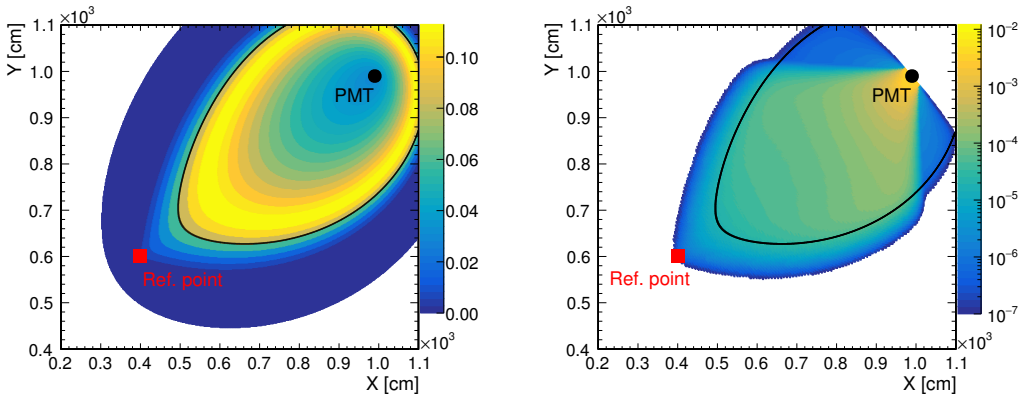

Figure 6.7 – Examples for the two-dimensional (unnormalized) distributions $\Phi_{j,k}(\mathbf{x})/w_{j,k}$ (**left**; from Equation (6.4)) and $\Phi^*_{j,k}(\mathbf{x})/w^*_{j,k}$ (**right**; from Equation (6.6)) with the same configuration of photosensor and reference point as in Figure 6.5. The photon hit time t_0 was set to 33 ns. The time $\hat{t}(\mathbf{x})$ was calculated with Equation (6.2) in both cases, using the plus sign for the particle contribution and approximating the photon contribution t_{ph} as for Figure 6.5. The sharp contour (*black*) followed from Equation (6.1) with $t(\mathbf{x}) = 33$ ns.

Note that $P_{\mathrm{det},j}(\mathbf{x})$ must also be incorporated when the normalization factor $w^*_{j,k}$ is calculated:

$$w^*_{j,k} = \left(\iiint\limits_{V_{\mathrm{LSc}}} P_{\mathrm{det},j}(\mathbf{x}) \int_0^\infty \widetilde{\Phi}_{j,k}\left(\hat{t}(\mathbf{x}; t_{\mathrm{ph}} = t', t_s = 0)\right) \, \Phi_{t_{\mathrm{ph}}}(t'; \mathbf{x}, \mathbf{r}_j) \, \mathrm{d}t' \, \mathrm{d}x \, \mathrm{d}y \, \mathrm{d}z \right)^{-1} . \tag{6.8}$$

The right side of Figure 6.7 shows an example for $\Phi^*_{j,k}(\mathbf{x})/w^*_{j,k}$, where the underlying $\Phi_{j,k}(\mathbf{x})/w_{j,k}$ is from the left side of the figure. As one can see, the distribution $P_{\mathrm{det},j}(\mathbf{x})$ dominates the picture. For example, the photosensor's field of view, which is defined by the assumed angular acceptance of the considered light concentrator (see Figure 5.2), is clearly visible.

Since the p.d.f. $\Phi^*_{j,k}(\mathbf{x})$ can already be interpreted as spatial number density distribution of one detected scintillation photon emission, a reconstruction of the *spatial number density distribution of detected scintillation photon emissions* based on information from photosensor j, $\hat{\Gamma}_{\mathrm{det},j}(\mathbf{x})$, is obtained as the sum over all photon hits:[7]

$$\begin{aligned}
\hat{\Gamma}_{\mathrm{det},j}(\mathbf{x}) &= \sum_{k=1}^{N_{\mathrm{hits},j}} \Phi^*_{j,k}(\mathbf{x}) \\
&= P_{\mathrm{det},j}(\mathbf{x}) \int_0^\infty \left(\sum_{k=1}^{N_{\mathrm{hits},j}} w^*_{j,k} \widetilde{\Phi}_{j,k}\left(\hat{t}(\mathbf{x}; t_{\mathrm{ph}} = t', t_s = 0)\right) \right) \Phi_{t_{\mathrm{ph}}}(t'; \mathbf{x}, \mathbf{r}_j) \, \mathrm{d}t' \\
&= P_{\mathrm{det},j}(\mathbf{x}) \int_0^\infty S^w_j\left(\hat{t}(\mathbf{x}; t_{\mathrm{ph}} = t', t_s = 0)\right) \, \Phi_{t_{\mathrm{ph}}}(t'; \mathbf{x}, \mathbf{r}_j) \, \mathrm{d}t' .
\end{aligned} \tag{6.9}$$

[7] Although $\hat{\Gamma}_{\mathrm{det},j}(\mathbf{x})$ was named *number* density distribution, it has non-integer values.

Here the function $S_j^w(t) = \sum_{k=1}^{N_{\text{hits},j}} w_{j,k}^* \widetilde{\Phi}_{j,k}(t)$ is called *weighted signal function*. An example for an *unweighted signal function* $S_j(t) = \sum_{k=1}^{N_{\text{hits},j}} \widetilde{\Phi}_{j,k}(t)$ with $N_{\text{hits},j} = 10$ photon hits is shown on the right of Figure 6.6.
Note that the normalization of individual photon contributions in Equation (6.6) naturally implicates

$$\iiint\limits_{V_{\text{LSc}}} \hat{\Gamma}_{\text{det},j}(\mathbf{x})\,\mathrm{d}x\,\mathrm{d}y\,\mathrm{d}z \stackrel{!}{=} N_{\text{hits},j}\,. \tag{6.10}$$

To perform the reconstruction, the information from all $N_{\text{PMT}}^{\text{hit}}$ photosensors with photon hits is superimposed:

$$\hat{\Gamma}_{\text{det}}(\mathbf{x}) \equiv \sum_{j=1}^{N_{\text{PMT}}^{\text{hit}}} \hat{\Gamma}_{\text{det},j}(\mathbf{x})\,. \tag{6.11}$$

This finally allows to calculate an estimate for the *spatial number density distribution of all* (i.e., detected and undetected) *scintillation photon emissions* $\hat{\Gamma}_{\text{em}}(\mathbf{x})$ as

$$\hat{\Gamma}_{\text{em}}(\mathbf{x}) \equiv \sum_{j=1}^{N_{\text{PMT}}^{\text{hit}}} \hat{\Gamma}_{\text{em},j}(\mathbf{x}) = \frac{1}{\varepsilon(\mathbf{x})} \sum_{j=1}^{N_{\text{PMT}}^{\text{hit}}} \hat{\Gamma}_{\text{det},j}(\mathbf{x}) = \frac{\hat{\Gamma}_{\text{det}}(\mathbf{x})}{\varepsilon(\mathbf{x})}\,, \tag{6.12}$$

where $\varepsilon(\mathbf{x})$ is the *local detection efficiency* defined as

$$\varepsilon(\mathbf{x}) \equiv \sum_{l=1}^{N_{\text{PMT}}} P_{\text{det},l}(\mathbf{x})\,. \tag{6.13}$$

Note that the sum runs over *all* PMTs.

It has to be pointed out that $\hat{\Gamma}_{\text{em}}(\mathbf{x})$ calculated with (6.12) is not a good estimator for the true $\Gamma_{\text{em}}(\mathbf{x})$, which was mentioned at the beginning of Section 6.3 and represents the actual goal of the reconstruction. Due to the way how $\hat{\Gamma}_{\text{em}}(\mathbf{x})$ is computed, the distribution is largely spread in V_{LSc}. This is different to the true distribution $\Gamma_{\text{em}}(\mathbf{x})$, which of course reflects the event's true topology and position. Consequently, the number of photons one obtains from integrating $\hat{\Gamma}_{\text{em}}(\mathbf{x})$ over V_{LSc} certainly is not the best estimate for the true total number of emitted scintillation photons. To improve on this, the final result of $\hat{\Gamma}_{\text{em}}(\mathbf{x})$ has to be used to extract an estimate for the event topology $\hat{T}$, allowing the creation of a more fitting distribution $\hat{\Gamma}_{\text{em}}^*(\mathbf{x})$. The latter describes the spatial number density distribution of scintillation photon emissions only from points $\mathbf{x} \in \hat{T}$, where $\hat{T} = \{\mathbf{x} \,|\, \mathbf{x} \text{ in } V_{\text{LSc}} \wedge \mathbf{x} \text{ from reconstructed event topology}\}$ contains only points belonging to the reconstructed event topology:

$$\hat{\Gamma}_{\text{em}}^*(\mathbf{x}) \equiv \begin{cases} \frac{1}{\varepsilon(\mathbf{x})} \frac{\hat{\Gamma}_{\text{det}}(\mathbf{x})}{\iiint_{\hat{T}} \hat{\Gamma}_{\text{det}}(\mathbf{x})\,\mathrm{d}x\,\mathrm{d}y\,\mathrm{d}z} \sum\limits_{j=1}^{N_{\text{PMT}}^{\text{hit}}} N_{\text{hits},j}, & \text{if } \mathbf{x} \in \hat{T} \\ 0, & \text{if } \mathbf{x} \notin \hat{T} \end{cases}. \tag{6.14}$$

Without going into details, it has to be explicitly pointed out that the finding of $\hat{T}$ is a highly non-trivial task.

6.3.2 Iterating the procedure with a probability mask

The previously described procedure to reconstruct the spatial number density distribution of scintillation photon emissions $\hat{\Gamma}_{\mathrm{em}}(\mathbf{x})$ or $\hat{\Gamma}^{*}_{\mathrm{em}}(\mathbf{x})$ assumes that all the single photon hits at the individual photosensors constitute fully independent information. This is only partially true. Contrary to the propagation and the detection of a photon, which are independent from other scintillation photons, the production of all the scintillation light fundamentally depends on the temporal evolution of the event topology. To respect this dependence in the reconstruction, a *probability mask* $M(\mathbf{x})$ is included into the calculations of the prior section. The purpose of $M(\mathbf{x})$ is to modify / reweight the reconstructed probability that point $\mathbf{x}$ was the origin of the currently processed photon. Like a *prior* in *Bayesian statistics*, the mask includes *prior knowledge* on an event into a reconstruction pass.
On a large scale, the mask allows to confine the spatial region with the possible origins of the detected photons. On a smaller scale, the mask can emphasize features of the reconstructed event topology, e.g., a locally increased number density of photon emissions as the result of an increased energy deposition from a charged particle shower.
Note that—in the strict sense of probability mask—$M(\mathbf{x})$ by itself has to satisfy the normalization condition

$$\iiint\limits_{V_{\mathrm{LSc}}} M(\mathbf{x})\ \mathrm{d}x\,\mathrm{d}y\,\mathrm{d}z \overset{!}{=} 1\,. \tag{6.15}$$

However, since only relative changes in $M(\mathbf{x})$ are of importance, any deviating normalization will be compensated (see below).

A natural way to obtain a probability mask and to implement it into the reconstruction is to make the whole reconstruction procedure an iterative process. This allows to generate the probability mask for the i^{th} iteration from the result of the $(i-1)^{\mathrm{th}}$ iteration. The simplest possibility to create a probability mask for iteration i is to rescale the calculated distribution $\hat{\Gamma}_{\mathrm{em},i-1}(\mathbf{x})$ from the previous iteration such that Equation (6.15) is fulfilled. However, special care has to be taken that the used probability mask does not promote *self-enhancement effects*: The information contributed by photosensor j in iteration i must not be weighted with a probability mask from the result of iteration $i-1$ already containing the same information. Therefore, the probability mask $M_{i,j}$, which is used to calculate the contribution of the photosensor j in the i^{th} iteration, $\hat{\Gamma}_{\mathrm{em},i,j}(\mathbf{x})$, must be constructed from the result $\widetilde{\Gamma}_{\mathrm{em},i-1,j}(\mathbf{x})$, which does not contain a contribution of photosensor j:

$$\widetilde{\Gamma}_{\mathrm{em},i-1,j}(\mathbf{x}) \equiv \sum_{j',\,j'\neq j}^{N^{\mathrm{hit}}_{\mathrm{PMT}}} \hat{\Gamma}_{\mathrm{em},i-1,j'}(\mathbf{x})\,. \tag{6.16}$$

An alternative mask $M_{i,j}(\mathbf{x})$, which is less prone to the introduction of self-enhancement effects, is a *binary probability mask*. Using a threshold value $\hat{\Gamma}^{\mathrm{min}}_{\mathrm{em,i-1}}$, the mask is defined as

$$M_{i,j}(\mathbf{x}) = \begin{cases} 0, & \text{if } \hat{\Gamma}_{\mathrm{em},i-1}(\mathbf{x}) < \hat{\Gamma}^{\mathrm{min}}_{\mathrm{em},i-1} \\ a, & \text{if } \hat{\Gamma}_{\mathrm{em},i-1}(\mathbf{x}) \geq \hat{\Gamma}^{\mathrm{min}}_{\mathrm{em},i-1} \end{cases}, \tag{6.17}$$

where the constant a follows from Equation (6.15). While the probability mask from the first method is strong in emphasizing distinctive features of the event topology, a binary probability mask less likely introduces false small-scale features into the final distribution $\hat{\Gamma}_{\mathrm{em}}(\mathbf{x})$. Note that one does not necessarily have to use the same probability mask type for all iterations to reconstruct an event. In fact, the iterative procedure, in combination with the probability mask and many options to shape it, give a lot of freedom and power to the reconstruction technique. However, one has to make sure that no bias is artificially introduced into the reconstruction result.
To include a probability mask into the calculations for the i^{th} iteration, the factor $M_{i,j}(\mathbf{x})$ must be multiplied on the right side of Equation (6.6). Moreover, the mask has to be taken into account in the calculation of $w^*_{j,k}$ as a factor under the volume integral in Equation (6.8). This compensates any deviation of the mask's absolute normalization from (6.15). If no prior information can be added to the first reconstruction pass ($i = 0$) with a probability mask $M_{0,j}(\mathbf{x})$ from a different source[8], the factor $M_{0,j}(\mathbf{x})$ simply is an omissible constant. It should be clear from the described procedure to include a probability mask into the reconstruction process that this technique is not equal to a simple, repeated multiplication of a reconstruction result with itself!
The maximum number of useful iterations depends on the number of detected photons and hit sensors. In a practical application, however, the number of iterations required to obtain a usable reconstruction result is surely smaller ($\lesssim 20$)—especially at GeV energies and beyond.
Figure 6.8 shows projections of (intermediate) reconstruction results, which illustrate the capabilities of the reconstruction approach in general and the impact of probability masks in special. One can clearly see that the distribution of the cell content nicely reflects the trajectory of the simulated muon. Moreover, the cell content is correlated with the presence of secondary particles. Even the expected effect of an increased energy loss at the end of the track from the stopping muon is visible. This essentially demonstrates the accessibility of the differential energy loss $\mathrm{d}E/\,\mathrm{d}x$ with the new reconstruction method. If one compares the upper and the middle results, which were later rescaled to probability masks for succeeding iterations, with the final outcome at the bottom, one sees that the use of the probability masks corrected a slight offset in the result from the first reconstruction run and gradually revealed more features of the topology.

6.4 Implementation details

The first realization of the novel approach to reconstruct events in LSc was a `ROOT` script [39]. Within the scope of this work, the initial version of the source code was completely redesigned to obtain a discrete program requiring compilation. It is written in `C++` as a single-thread application for execution on a *central processing unit* (CPU). In addition to the `ROOT` framework, the reconstruction code also makes heavy use of the open-source `BOOST C++` libraries [219]. The software currently comprises about 17,000 physical lines of code and about 23,000 comment lines in

[8] Prior information on the position and topology of an event can be used to prepare a probability mask $M_{0,j}(\mathbf{x})$ for the first reconstruction run. For example, the *backtracking algorithm* presented in Ref. [51] could be used to produce such a probability mask.

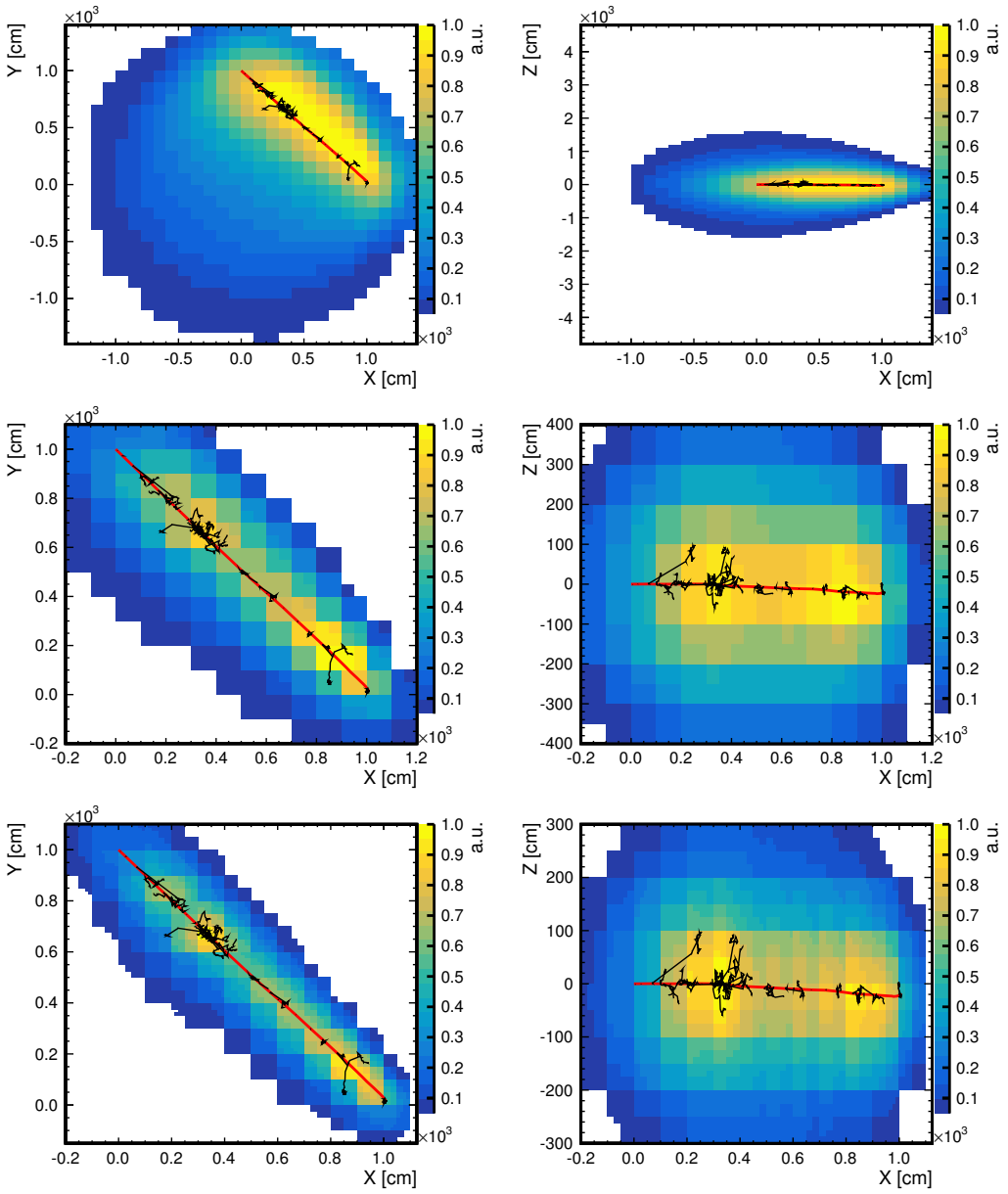

Figure 6.8 – Reconstruction results projected along the z-axis (symmetry axis; *left*) or y-axis (*right*) of the cylindrical LENA detector. The primary particle simulated with the LENA detector simulation (see Chapter 5) was a muon with 3 GeV initial kinetic energy, which started at (0, 1000, 0) cm in the direction (1, −1, 0). Both the projected tracks of the primary particle (*red*) and of secondary particles (*black*) are shown. Due to the projection and for reasons explained in Section 6.4.2, the cell content is given in a.u. and rescaled such that the maximum content is 1. The shown reconstruction outcomes correspond to iteration 0 **(top)**, 8 **(middle)** and 21 **(bottom)**. Note that the axis scales change due to a selection of a *region of interest* (ROI) as explained in Section 6.4.1. Details on the actual reconstruction procedure are given in Section 6.4.4.

`Doxygen` [220] format. They are distributed among four separate libraries and the

main reconstruction program.[9]
As one can infer from the descriptions in the previous section, the new reconstruction method is not exclusive for a particular LSc detector but can in principle be used with any unsegmented large-volume measurement device based on this technology. Therefore, following an *object-oriented approach*, the internal processing of the algorithm relies on general interfaces and base classes. These interfaces and basic building blocks have to be implemented and extended for a specific experiment in order to make the detector characteristics and the experiment's input data structure accessible in the reconstruction program. For example, an abstract base class *EventProvider* defines the method to retrieve an object of the *Event* class used for internal processing. This base class has to be inherited by a concrete class that loads the input data from a data source (e.g., a `ROOT`-file) and transforms them into the internally used *Event* object. The abstract base class *Detector* defines an interface to get geometric parameters of the measurement device and to access individual photosensors represented by the *Pmt* class. Once an *Event* object is loaded into the current realization of the *Detector* interface, the photon hit information for the individual photosensors, which were stored in *PmtData* objects within the *Event* instance, are attached to the corresponding *Pmt* objects. When the reconstruction algorithm iterates over the photosensors, it successively requests these *Pmt* instances by index via the interface of the *Detector* base class. They give access to both the static data (e.g., position and orientation; stored in an object of the *StaticPmt* class) and the dynamic data (stored in the *PmtData* object).
So far, the development of the reconstruction software has been mainly influenced by the needs to analyze MC events from the LENA detector simulation (see Chapter 5). However, with forthcoming implementations and adaptations for MC data from JUNO, a refactoring to extract more generalized interfaces etc. will surely change the existing code structure. Due to this active development, it is refrained from detailing the current layout of the software. However, Section 6.4.1 to Section 6.4.3 deal with some noteworthy issues to realize the reconstruction technique from Section 6.3 and describe solutions implemented in the course of this work. Section 6.4.4 presents a concrete example for a reconstruction procedure that underlies the results in Chapter 7. An outlook on future development plans and other possible areas of application for the reconstruction method are summarized in Section 6.5.

6.4.1 Reconstruction mesh

A decisive limitation for the implementation of the novel reconstruction method from Section 6.3 comes from the fact that the calculations cannot be performed on a continuous domain, i.e., as a continuous function of the spatial point $\mathbf{x}$. Therefore, the LSc-filled volume V_{LSc} of a detector has to be partitioned into cells. At first, this was done by using an instance of the `ROOT` class *TH3D* (three-dimensional histogram) with cubic cells of volume ΔV_{cell} as *reconstruction mesh*. All calculations were then performed with respect to the centerpoints of the mesh cells.[10]

[9] It is intended to decompose the current code into further libraries.
[10] The value calculated at the centerpoint was then taken as constant over the whole cell. Moreover, a binned version of the signal function $S_j(t)$ (Figure 6.6 right) was used to speed up the computations. It based on a binned probability function for t_s, which, for performance reasons, was not obtained

Adaptive mesh refinement To get a first idea on the position of an event inside the LSc volume, the reconstruction iterations likely start with a large ΔV_{cell}, e.g., $1\,\text{m}^3$ for LENA. Once the ROI containing the event is found from the roughly sampled distribution $\hat{\Gamma}_{\text{em}}(\mathbf{x})$ (see Equation (6.12)), it is desirable to exclude the uninteresting regions from the succeeding reconstruction iterations. In the current implementation of the reconstruction, the time contribution $t_{\text{ph}}(\mathbf{x}, \mathbf{r}_j)$ of the photon in Equation (6.2) does not include effects from photon scattering (see also Section 6.4.2). Within this context, it turned out that a confinement of the reconstruction to the volume $V_{\text{ROI}} \leq V_{\text{LSc}}$ of the ROI produces distortions in $\hat{\Gamma}_{\text{em}}(\mathbf{x})$ close to the boundaries of the new volume. The main reason are the contributions of (distant) photosensors with signals mostly from scattered photons. Due to the normalization of $\Phi^*_{j,k}(\mathbf{x})$ in Equation (6.6), every signal—from a scattered or unscattered photon—becomes forced into the volume of interest by replaceing V_{LSc} with V_{ROI} and $\Phi_{j,k}(\mathbf{x})$ with $\Phi^*_{j,k}(\mathbf{x})$ in (6.3). As one can infer from Figure 6.6, the distribution $\Phi_{j,k}(\mathbf{x})$ from Equation (6.4) is essentially uniform for photosensors with signals from scattered photons that have a considerable delay with respect to an unscattered photon. Consequenly, as it follows from Equation (6.7), the distribution $\hat{\Gamma}_{\text{det},j}(\mathbf{x})$ in Equation (6.9) is dominated by $P_{\text{det},j}(\mathbf{x})$, which is maximal at the edge of the reduced reconstruction volume in the direction of the photosensor. The combined contributions from the photosensors with mainly scattered photons finally produce the mentioned distortions at the boundaries of the volume of interest. If the reconstruction is more and more confined to the volume with the highest values of $\hat{\Gamma}_{\text{em}}(\mathbf{x})$, the distortions move closer to the ROI or even overlap with it. It has to be tested if the effect still occurs when photon scattering is properly taken into account for $t_{\text{ph}}(\mathbf{x}, \mathbf{r}_j)$. Additionally, methods for a (statistical) removal of hits from scattered photons are in development [39].

A reconstruction with cubic cells of 1 m edge length is too imprecise. The goal is to go down to 20 or 10 cm length, perhaps even lower. For a large detector like LENA, which already has a target volume of $\sim 5.9 \times 10^4\,\text{m}^3$, the smallest enclosing reconstruction mesh of rectangular shape has a volume of $7.5 \times 10^4\,\text{m}^3$. Besides the effective use of only 78.5 %, a mesh with 20 cm-cells (10 cm-cells) consequently has $\sim 9.4 \times 10^6$ ($\sim 75.3 \times 10^6$) cells. To estimate the total number of computations, the cell count has to be multiplied by the number of hit photosensors, by the number of iterations and by two for the additional calculation of the normalization. This easily yields a too long reconstruction time of a day or more per event.
In order to get rid of the technical limitation to reduce the cell size only for the entire mesh, the common method of *block-structured adaptive mesh refinement* [221, 222] was implemented in the context of this work. This was done with a custom realization of a mesh structure, which replaced the initially used *TH3D* class. As illustrated in Figure 6.9, the reconstruction still runs over the full LSc volume, but the cell size is reduced only in the determined ROI. The use of adaptive mesh refinement significantly reduced the reconstruction time[11] of events while avoiding the mentioned distortions from a confinement of the reconstruction volume.

by a proper bin-wise integration of the template p.d.f. $\Phi_{t_s}(t)$ (Figure 6.6 *left*). Instead, $\Phi_{t_s}(t)$ was sampled at the centers of t_s-bins and the resulting histogram was normalized to one.

[11] Due to a variety of factors (e.g., event energy, position and topology), it is difficult to make a general statement about the improvement. The remaining reconstruction time may still be on the order of hours. However, there is further potential for optimization.

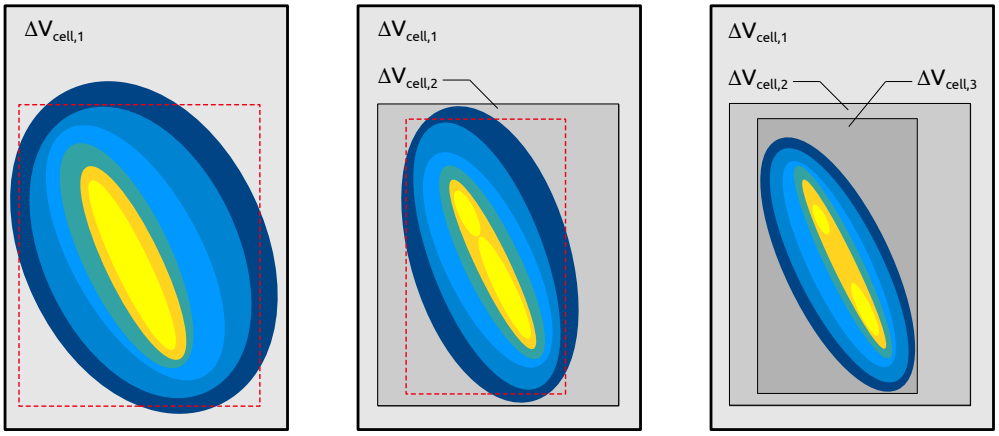

Figure 6.9 – Illustration of the *adaptive mesh refinement approach* implemented for the new reconstruction method. The first reconstruction iterations **(left)** are performed with a mesh cell volume $\Delta V_{\text{cell},1}$ (*light gray*) for the entire LSc volume. If the reconstruction mesh has to be refined, a rectangular-shaped ROI (*red dashed boundary*) is determined in which a cell volume $\Delta V_{\text{cell},2} < \Delta V_{\text{cell},1}$ (*gray*) is set for the succeeding iterations **(middle)**. The steps can be repeated to obtain a new ROI that is refined with cells of volume $\Delta V_{\text{cell},3} < \Delta V_{\text{cell},2}$ (*dark gray*) for future iterations **(right)**. In any case, the reconstruction is always done over the whole LSc volume.

A future development step would be the adaptation of the reconstruction mesh to the geometry of the LSc target, e.g., a cylindrical mesh for LENA. This would prevent the inefficient allocation of memory for unused mesh cells outside of the detector. Moreover, the reconstruction mesh could be prepartitioned into smaller mesh blocks, which are refined on demand. As one can infer from Figure 6.9, the current refinement strategy only helps for events with a not too extensive topology. For through-going, (cosmogenic) muons, on the other hand, there may still be a large volume that is unnecessarily refined with the current approach. The prepartitioning into mesh blocks would support an easy refinement of a more fitting ROI.

Virtual cells A drawback from probing the distribution $\hat{\Gamma}_{\text{det},j}(\mathbf{x})$ at fixed cell positions is that, depending on the size of the cells, the space close to a photosensor may only be covered by a few points. As one can see from the right side of Figure 6.7, this is the region where $\Phi^*_{j,k}(\mathbf{x})$ is most sensitive to $\mathbf{x}$. In general, the precision with which this basic distribution is probed close to the processed photosensor j significantly affects the overall normalization. Moreover, for events close to the edge of the LSc volume, a sufficient sampling of $\hat{\Gamma}_{\text{det},j}(\mathbf{x})$ is critical to avoid distortion effects. To soften the negative effects from a small number of sampling points close to a photosensor, all *real cells* that are below a certain limit for the distance to the edge of V_{LSc} are partitioned into a finite number of *virtual sub-cells*. This is depicted in Figure 6.10. Contrary to a real cell, a virtual cell only defines a position, but has no space in memory to store data. The value of $\hat{\Gamma}_{\text{det},j}(\mathbf{x})$ in a partitioned real cell is computed as the arithmetic mean over the results from the virtual sub-cells. While the virtualization of cells has a small negative effect on the reconstruction time, it

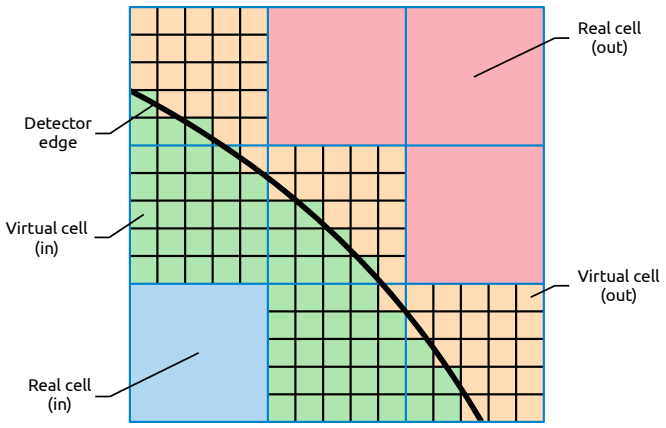

Figure 6.10 – During a reconstruction iteration, real mesh cells (*blue frame*) become partitioned into virtual sub-cells (*black frame*) if their centerpoints have an orthogonal distance to the detector edge (*thick black line*) below a certain value. The cell content of real cells inside the detector (*blue*) is calculated at their centerpoints. Real cells with centerpoints outside of the detector (*red*) are not processed. The content of partitioned real cells is computed as the arithmetic mean of the results calculated at the virtual centerpoints of sub-cells inside the detector (*green*). Virtual sub-cells outside of the detector (*orange*) are not processed.

was found that the technique helps to reduce distortions when an event close to the edge of the LSc volume is reconstructed.

6.4.2 Look-up tables

The distributions $P_{\text{det}}(\mathbf{x})$ and $\Phi_{t_{\text{ph}}}(t;\mathbf{x},\mathbf{r})$ in Equation (6.6) heavily depend on the optical properties of the LSc and the solid angle to reach a sensor's photosensitive area from point $\mathbf{x}$. Their repeated calculation for each photosensor in each iteration would be very time-consuming. Fortunately, the distributions can be precomputed since they only depend on the known position $\mathbf{r}$ of a photosensor and a point $\mathbf{x}$ in the detector of known dimension. Assuming the orientation of a photosensor is described by the unit normal vector $\mathbf{n}$, the precomputed data can be stored in a LUT as a function of the distance $|\mathbf{r}-\mathbf{x}|$ and the angle between $\mathbf{n}$ and $\mathbf{r}-\mathbf{x}$. For $\Phi_{t_{\text{ph}}}(t;\mathbf{x},\mathbf{r})$, the information must be also stored as a function of time.
The number of required LUTs depends on the diversity, distribution and orientations of the photosensors, the symmetry of the detector and the complexity of information used to calculate the LUT data. Assuming equal photosensors, only two LUTs are required for a perfectly symmetric setup, i.e., a spheric detector with sensors that are oriented towards the center:[12] one for $P_{\text{det}}(\mathbf{x})$ and one for $\Phi_{t_{\text{ph}}}(t;\mathbf{x},\mathbf{r})$. If the shape of the LSc volume has a preferred direction, as it is the case for the cylindrical detector LENA, the number of required LUTs depends on how photon scattering is taken into account: If the computations explicitly incorporate the case that a photon

[12] This also assumes that construction parts to not produce *shadowing*, i.e., that photons from certain solid angles and distances are not blocked for some photosensors.

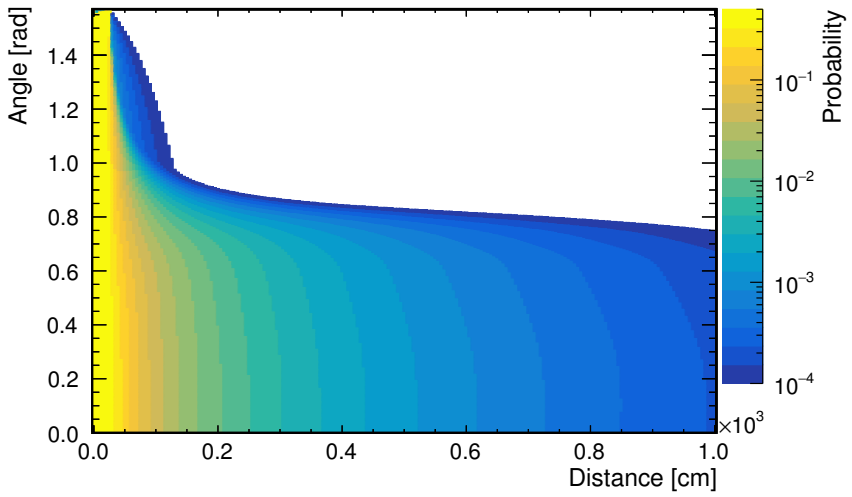

Figure 6.11 – A part of the $P_{\text{det}}(\mathbf{x})$ LUT used for LENA. The original LUT extends up to 1.01×10^4 cm and has $\sim 7.3 \times 10^6$ entries. On the horizontal axis one has the distance $|\mathbf{r} - \mathbf{x}|$ from point $\mathbf{x}$ to the photosensor at position $\mathbf{r}$. The angle between the normal vector of the assumed OM disk (25.5 cm radius) and $\mathbf{r} - \mathbf{x}$ is plotted along the vertical axis. One can clearly see that $P_{\text{det}}(\mathbf{x})$ is strongly affected by the angular acceptance of the light concentrator (see Figure 5.2), which has a critical angle of $\sim 44°$, and the solid angle of the disk area. White colored entries of the LUT have values > 0 but below the shown minimum value.

from $\mathbf{x}$ may reach a point on the photosensitive area of the sensor at $\mathbf{r}$ via one or more intermediate scatter points, these calculations depend on the exact location of the photosensor in the detector. In the worst case, depending on the symmetry of the detector, this requires the production of two LUTs *per sensor*.
The LUTs for the reconstruction of MC events in LENA, which were created in the course of this work, include the crude approximation that all photons scattered on the direct path from $\mathbf{x}$ to a point on the photosensitive area of the sensor are lost. Negative effects from this assumption are expected especially for events close to the photosensors. However, without the consideration of intermediate scatter points for photons, only two LUTs, one for $P_{\text{det}}(\mathbf{x})$ and one for $\Phi_{t_{\text{ph}}}(t; \mathbf{x}, \mathbf{r})$, had to be created. Both of them are adapted to the assumptions made in the LENA detector simulation (see Chapter 5), i.e., the entrance apertures of the OMs are flat disks and the scintillation photons are emitted at a fixed energy. Figure 6.11 shows a part of the $P_{\text{det}}(\mathbf{x})$ LUT created for LENA. A second approximation concerns the LUT for $\Phi_{t_{\text{ph}}}(t; \mathbf{x}, \mathbf{r})$: Instead of tabulating sample points of $\Phi_{t_{\text{ph}}}(t; \mathbf{x}, \mathbf{r})$, only the mean value of this distribution was precalculated and stored in a LUT. This fixed value is then used directly for the calculation of the photon contribution to $\hat{t}(\mathbf{x})$ in Equation (6.2) and thus renders the integration in Equation (6.9) unnecessary.
The precalculation of more detailed LUTs is a time-consuming task. Nevertheless, this task will be inevitable to take into account more complex optical models in the future. Since the current LUTs do not include all details to calculate proper absolute values of $\hat{\Gamma}_{\text{em}}(\mathbf{x})$, the results in Figure 6.8 and Figure 6.12 are presented with a relative scale for the projected cell content. Also the analysis in Chapter 7 bases on a relative scale for $\hat{\Gamma}_{\text{em}}(\mathbf{x})$.

6.4.3 Probability mask

The probability mask $M_{i,j}(\mathbf{x})$ introduced in Section 6.3.2 is a powerful part of the novel approach to reconstruct (muon) tracks in LSc. It essentially represents the link between the input from the individual photosensors. As explained in Section 6.3.2, one way to create a probability mask $M_{i,j}(\mathbf{x})$ for photosensor j in reconstruction iteration i is to rescale the distribution $\widetilde{\Gamma}_{\mathrm{em},i-1,j}(\mathbf{x})$ from Equation (6.16). To prevent self-enhancement effects, this distribution does not contain information from the currently processed photosensor. A technical difficulty regarding the implementation arises from the fact that one three-dimensional mask would have to be stored for each photosensor with photon hits. Therefore, the number of masks may reach some thousands or even tens of thousands in large detectors like JUNO or LENA. Moreover, the growing number of cells in a mask from mesh refinement increases the storage space required per probability mask. For extensive detectors, one easily exceeds the capacity limit of fast accessible memory. A strict recursive calculation of all probability masks from the overall results $\hat{\Gamma}_{\mathrm{em},i-1}(\mathbf{x})$, $\hat{\Gamma}_{\mathrm{em},i-2}(\mathbf{x})$, $\hat{\Gamma}_{\mathrm{em},i-3}(\mathbf{x})$ etc. for each new iteration i saves storage space but takes way too long. However, one could test if it is sufficiently accurate to rescale only $\hat{\Gamma}_{\mathrm{em},i-2}(\mathbf{x})$ in order to approximate $M_{i-1,j}(\mathbf{x})$ for any j. This result could then be used to extract $M_{i,j}(\mathbf{x})$ from $\hat{\Gamma}_{\mathrm{em},i-1}(\mathbf{x})$ with the approximated $M_{i-1,j}(\mathbf{x})$ and a repetition of the reconstruction procedure. Consequently, one would only need to buffer $\hat{\Gamma}_{\mathrm{em},i-1}(\mathbf{x})$ and $\hat{\Gamma}_{\mathrm{em},i-2}(\mathbf{x})$ for the calculation of $\hat{\Gamma}_{\mathrm{em},i}(\mathbf{x})$.
The fast approximation currently used to reduce self-enhancement effects in the probability mask bases on an arbitrary partitioning of the overall photosensor set into two or more subsets, e.g., even- and odd-indexed sensors. The shaping of the probability mask is done by successively switching the photosensor subset for the reconstruction iterations.[13] In the last iteration, all sensors are used to determine the final result of $\hat{\Gamma}_{\mathrm{em}}(\mathbf{x})$.

The reconstruction procedure outlined so far only includes information from photosensors with photon hits. Sensors without photon hits in the processed event can be used to cross-check the computed results for $\hat{\Gamma}_{\mathrm{em},i}(\mathbf{x})$ and allow to shape the probability mask $M_{i+1,j}(\mathbf{x})$ for the next iteration: If $\hat{\Gamma}_{\mathrm{em},i}(\mathbf{x})$ is determined from the contributions of all photosensors with signals, $N_{\mathrm{em},i}(\mathbf{x}) = \hat{\Gamma}_{\mathrm{em},i}(\mathbf{x})\,\Delta V_{\mathrm{cell}}(\mathbf{x})$ estimates the number of photons emitted from the cell with centerpoint $\mathbf{x}$ and volume $\Delta V_{\mathrm{cell}}(\mathbf{x})$. This quantity can be used together with the tabulated data for $P_{\mathrm{det}}(\mathbf{x})$ (see Section 6.4.2) to calculate the expected number of photon hits $\overline{N}_{i,u}(\mathbf{x})$ at photosensor u that did not observe a signal. With the Poisson probability $\mathcal{P}(0;\overline{N}_{i,u}(\mathbf{x}))$, a mask $C(\mathbf{x})$ can be defined as

$$C_i(\mathbf{x}) \equiv \prod_{u}^{N_{\mathrm{PMT}}^{\mathrm{unhit}}} \mathcal{P}(0;\overline{N}_{i,u}(\mathbf{x}))\,, \quad N_{\mathrm{PMT}}^{\mathrm{unhit}} = N_{\mathrm{PMT}} - N_{\mathrm{PMT}}^{\mathrm{hit}}\,, \tag{6.18}$$

which is used for a cell-wise computation of $C_i(\mathbf{x})\widetilde{\Gamma}_{\mathrm{em},i,j}(\mathbf{x})$. A normalization of the product to fulfill Equation (6.15) finally yields $M_{i+1,j}(\mathbf{x})$. The mask $C_i(\mathbf{x})$ effectively

[13] If the number of iterations exceeds the number photosensor subsets, this procedure does not prevent that a sensor sees its own contribution to the probability mask. However, self-enhancement effects become less prominent.

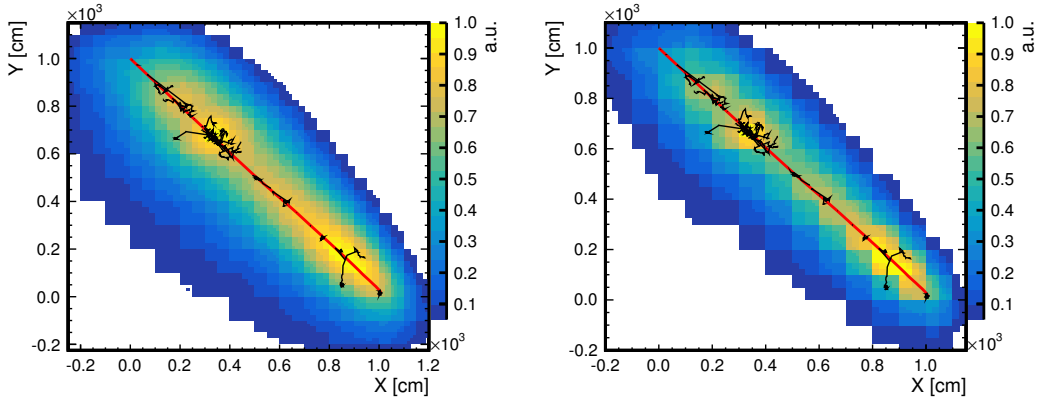

Figure 6.12 – Reconstruction of the muon from Figure 6.8 with (*left*) and without (*right*) the application of the mask $C(\mathbf{x})$ from Equation (6.18). The results correspond to 13 iterations with cubic mesh cells of different edge lengths: $4 \times 100\,\text{cm}$, $4 \times 50\,\text{cm}$, $4 \times 25\,\text{cm}$ and $1 \times 12.5\,\text{cm}$. Each iteration used the information from all hit photosensors to calculate $\hat{\Gamma}_{\text{em},i}(\mathbf{x})$. The scale for the cell content is the same as in Figure 6.8.

smears the total probability mask, as one can see in Figure 6.12, and especially softens distortions that were reconstructed at some distance to the true event. It has to be emphasized that $\hat{\Gamma}_{\text{em},i}(\mathbf{x})$ must be computed from all hit photosensors for a proper calculation of $\overline{N}_{i,u}(\mathbf{x})$. Moreover, the technique should only be applied to shape the probability mask for a next iteration but not to the final result $\hat{\Gamma}_{\text{em}}(\mathbf{x})$ from the last iteration.

6.4.4 Example for a reconstruction procedure

The following gives an overview on the reconstruction procedure underlying the analysis described in Chapter 7. Due to the variety of options for setting up the reconstruction of an event (number of iterations, refinement steps for mesh cell size , etc.), there is nothing like *the reconstruction procedure*. In fact, the different possibilities to configure the processing for speed or precision together with the operations to manipulate the probability masks between two iterations give a lot of flexibility and power to the reconstruction technique. It is one future task to find reasonable default settings for the actual objective, e.g., the reconstruction of cosmogenic muons, but at the same time enable automatic adjustment on per-event-level.

Let $0 \leq i \leq N_i - 1$ be the index of the current iteration, where N_i is the total number of requested iterations per event. Then a reconstruction procedure starting with $i = 0$ can be as follows:

(1) Do reconstruction iteration with hit, even-indexed photosensors; $i = i + 1$. (If $i = 0$, do not use probability mask.)

(2) Create probability mask from intermediate result.

(3) Do reconstruction iteration with hit, odd-indexed photosensors; $i = i + 1$.

(4) Create probability mask from intermediate result.

(5) Refine mesh in ROI if cell size changes for next iteration.

(6) Repeat (1) to (5) as long as $i < N_i - 2$.

(7) Do reconstruction iteration with all hit photosensors; $i = i + 1$.

(8) Smear intermediate result with mask $C(\mathbf{x})$ (see Equation (6.18)).

(9) Create probability mask from smeared, intermediate result.

(10) Refine mesh in ROI if cell size changes for next iteration.

(11) Do final reconstruction iteration with all hit photosensors; $i = i + 1$.

(12) Save / process final result.

The described procedure was used to obtain the projected reconstruction results in Figure 6.8. A total of $N_i = 22$ iterations were performed with cubic mesh cells of different edge lengths: eight iterations with 100 cm, eight iterations with 50 cm, five iterations with 25 cm and one iteration with 12.5 cm. The sector shown by a projection in Figure 6.8 corresponds to the selected ROI at this stage of the reconstruction.

6.5 Outlook

The general task for the future advancement of the reconstruction procedure is to increase its robustness, precision and especially its speed while keeping the program's memory footprint at a reasonable level. A key factor to succeed in this is the consideration of photon scattering, most preferably the statistical removal or even identification of signals from scattered photons. First work in this direction already began [39].
Some ideas to improve on particular (technical) aspects of the reconstruction method's existing implementation were already outlined at different occasions in Section 6.4. In principle, the high parallelizability of the algorithm favors an execution in a parallel computing environment, e.g., on a *graphics processing unit* (GPU). However, it probably is most beneficial to have a fully elaborated algorithm before the required reimplementation for this step is started. Therefore, this point is among the prospects for the future.
More urgent is the inclusion of Cherenkov light into the reconstruction. The method described in Section 6.3 to reconstruct events in LSc can also be adapted to large Cherenkov-based detectors. In fact, the only change is to replace the assumption of isotropic, delayed scintillation light emission with directional, instantaneous Cherenkov photon emission [39].[14] Since the produced light in a LSc detector also includes a fraction of Cherenkov light, the challenge in this hybrid case is a good attribution of the observed photon hits to the two light production mechanisms.[15]

Another important task is to validate the reconstruction results with the true outcomes of MC simulations. This is especially important if one aims for a precise

[14] First tests were already performed in Ref. [223].
[15] If Cherenkov photons are detected well separated in time from scintillation light, a reconstruction under the assumption of pure scintillation light produces a considerable distortion of the result.

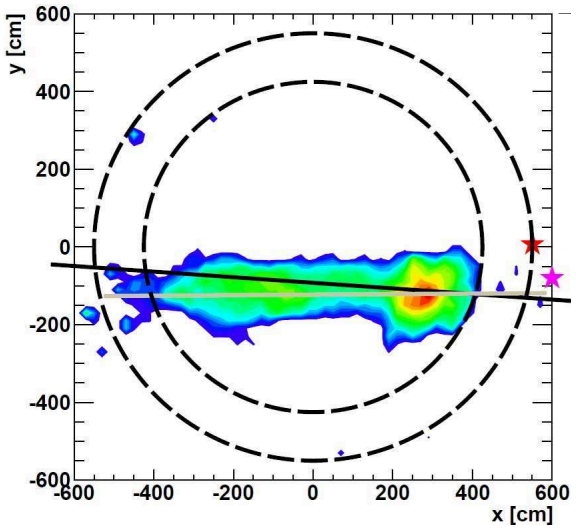

Figure 6.13 – Projection of the outcome from an application of the novel reconstruction technique to a real muon event in BOREXINO. The result, which shows the content of significant cells, is from an early version of the algorithm that used only first photon hits. The inner (outer) dashed circle corresponds to the inner (outer) nylon vessel. A red (magenta) star indicates the position of the first hit PMT (reference point). The solid black (gray) line represents the outcome of the *outer (inner) detector tracking* of BOREXINO (see Ref. [37]). Figure courtesy of *Björn S. Wonsak* [39].

estimate of the differential energy loss $\mathrm{d}E/\,\mathrm{d}x$ from the reconstructed distribution $\hat{\Gamma}^{*}_{\mathrm{em}}(\mathbf{x})$. Because some important features of the optical model (photon scattering) still need to be implemented, this has not yet been done. However, the novel reconstruction technique was applied to a few BOREXINO events from single through-going muons [39]. The tests successfully proofed the feasibility of the concept with real experimental data. Figure 6.13 shows the reconstruction result obtained with an early version of the algorithm. One can see a good agreement between the results from the new method and from the validated standard tracking of BOREXINO. Note that this is despite the limited electronics capabilities of the detector to handle muon events (saturation effects at the PMTs), which allowed to work only with the first photon hit time of each sensor.

So far, the new reconstruction approach for events in LSc was only applied to single muon events (see also Chapter 7). Yet its area of application is not limited to such events. For example, a reconstruction of muon bundles, which is important for JUNO, bases on the use of one reference point and time per muon. An estimation of $\mathrm{d}E/\,\mathrm{d}x$ for each muon will be difficult since it requires the attribution of single photon hits to the individual muons. Nevertheless, one will get some valuable information on the muon trajectories through the detector.
Besides muons, the novel reconstruction technique could also be applied to LE (neutrino interaction) events. A feasibility study to discriminate positron and electron MC events based on their spatial extension is already underway [39]. If one could distinguish these events, completely new and powerful ways to discriminate LE neutrino interactions (e.g., IBD and ES on electrons) and radioactive background would open up.

In the HE domain, the event topologies from neutrino interactions are more complex. Therefore, the reconstruction of individual particle tracks with the new method is challenging, especially in extensive showers. In a beam-based LBNO experiment (see Chapter 8), where the incident direction of the neutrinos is precisely known, the new reconstruction approach can still be useful to search for *missing transversal momentum*, an evidence for a NC background event.

Chapter 7

Results from the New Track Reconstruction Method

After the novel method for charged particle track reconstruction in unsegmented LSc detectors was described in Chapter 6, this chapter presents first results from the application of the new technique to a sample of simulated muon events in LENA. Section 7.1 provides information on the muon sample that was generated with the LENA detector simulation detailed in Chapter 5 and subsequently reconstructed following the procedure outlined in Section 6.4.4. Due to the high expenditure of time for the simulation of events with some GeV or more of energy deposition in the detector—and so far also for their reconstruction—the muon events used for this first analysis only had kinetic energies in the range from 0.1 to 10 GeV.
As explained in the previous chapter, the fundamental outcome of the new reconstruction approach is a 3D mesh describing the reconstructed number density distribution of all (scintillation) photon emissions $\hat{\Gamma}_{\mathrm{em}}(\mathbf{x})$ defined by (6.12). Similar to results from *medical imaging*, e.g., from *tomography*, this basic information in principle allows to apply the full toolkit of 3D data analysis. The objective is to extract high-level information on the reconstructed event, e.g., trajectories of charged particles, which enables the construction of the more refined distribution $\hat{\Gamma}^{*}_{\mathrm{em}}(\mathbf{x})$ defined by (6.14). This essentially paves the way towards the ultimate goal: A reconstruction of the differential energy loss $\mathrm{d}E/\,\mathrm{d}x$.
The analysis performed for this work primarily aimed for a first assessment of the performance of the new reconstruction method. It did not make use of the full potential to retrieve detailed information from the output data. Section 7.2 describes the sequence of analysis steps performed to obtain information on the achievable angular resolution, the potential to identify start and end point of a muon track, and the total number of emitted photons. The results of the analysis are presented in Section 7.3. Finally, a brief outlook on possibilities to improve the current analysis is given in Section 7.4.

7.1 Event sample

This section describes in Section 7.1.1 the simulation of the muon sample in LENA and in Section 7.1.2 its reconstruction with the method detailed in the previous chapter.

7.1.1 Simulation

The simulation of the muon sample was done with the `GEANT4`-based LENA detector simulation described in Chapter 5.[1] Recall that the simulation does not include potential effects from readout-electronics except a Gaussian smearing of the true photon detection times to simulate a timing uncertainty of $\sigma = 1\,\mathrm{ns}$. This uncertainty is already taken into account by the reconstruction method (see Figure 6.6 left). The following parenthesis shortly addresses the likely impact of read-out electronics on the reconstruction.

A smaller (larger) incertitude on a photon detection time essentially means a smaller (larger) temporal smearing of the initially sharp isochrone (see left of Figure 6.7) that comprises the possible photon emission points. Consequently, a better (poorer) time resolution, which also depends on the capabilities of the electronics, yields higher (lower) contrast in displays like Figure 6.8. One probably requires less (more) iterations to obtain results of similar quality. Moreover, the contrast in the reconstruction data is negatively affected by fake signals that are accepted or even introduced by the signal-processing chain. They essentially behave as signals from scattered photons.
If, for any reason, the readout-electronics does not facilitate the identification of individual photon hits, two fallback options exist: One very basic option is to apply the reconstruction scheme (with some minor modifications) only to the first-hit times of each photosensor. Figure 6.13 illustrates—based on real experimental data—that this already provides some information on the position and extension of an event. Another option becomes available if the wave form of each photosensor is recorded. Approximatively treating each wave form sample value as independent, one can convolve the whole wave form with the timing p.d.f. of the scintillator to obtain an unweighted signal function $S(t)$ similar to Figure 6.6, which is the basis for a weighted signal function $S^w(t)$ used in the reconstruction.
Due to changes in the meaning of the normalizations, one has to be especially careful when one interprets the absolute values of the resulting 3D reconstruction data. Although a subsequent determination of $\mathrm{d}E/\,\mathrm{d}x$ is at least difficult, the results are probably still useful to investigate the event topology.

All simulated muons in the sample used for this performance analysis have initial kinetic energies in the range from 0.1 to 10 GeV. The overall sample is composed out of five sub-samples: Three samples individually cover the energy ranges $[0.1, 1]\,\mathrm{GeV}$ (3000 events), $[1, 5]\,\mathrm{GeV}$ (2000 events) and $[5, 10]\,\mathrm{GeV}$ (3580 events). Two sub-samples

[1] The computationally intensive simulations were mainly performed with the *Finnish Grid Infrastructure* (FGI) under supervision of *Kai Loo – University of Jyväskylä, Department of Physics, Finland.* Parts of the simulations were performed by the author of this thesis on the *Batch Infrastruktur Resource am DESY* (BIRD) cluster of *Deutsches Elektronen-Synchrotron* (DESY).

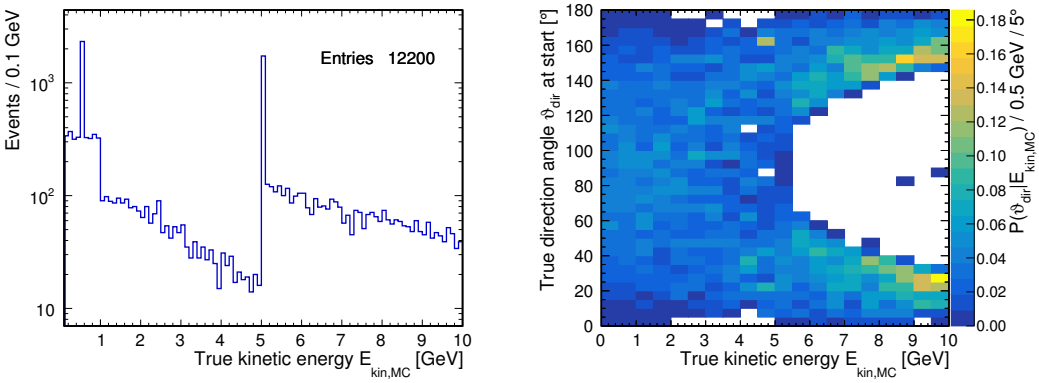

Figure 7.1 – **Left:** True kinetic energy spectrum of the 12,200 simulated muon events used to study the reconstruction performance. The overall event sample is composed of five sub-samples that cover different energy ranges (see text). **Right:** Distribution of the polar angle ϑ_{dir} of the initial muon direction as a function of the kinetic energy $E_{\mathrm{kin,MC}}$ set in the MC simulation. The polar angle is defined with respect to the central axis of LENA. Note that the binned distributions of ϑ_{dir} were renormalized to one for each energy bin.

with high statistics were simulated at fixed kinetic energies, 0.5 GeV (2000 events) and 5 GeV (1620 events). The final energy spectrum of the 12,200 events is shown on the left side of Figure 7.1.
The random start positions of the muons were confined to a cylindrical volume with 50 m height and 24 m diameter around the center of the 96 m high and 28 m wide cylindrical target volume of LENA. Moreover, the event sample only contains events that have the true muon track end point inside a cylinder of 50 m height and 28 m diameter around the center of LENA.[2] This condition especially constrained the directions of muons with higher energies. Due to the long expected track length, they were less likely selected for the final sample if they had their initial momentum direction in a plane essentially perpendicular to the detector's symmetry axis. Consequently, as one can see on the right side of Figure 7.1, the directions of muons with energies near the upper end of the total spectrum cluster around the direction of the central axis of LENA ($\vartheta_{\mathrm{dir}} = 0°, 180°$).

7.1.2 Reconstruction

The reconstruction of the simulated muons with the method explained in Chapter 6 was performed according to the concrete iterative procedure outlined in Section 6.4.4. Both the reference point $\mathbf{r}_{\mathrm{ref}} = (x_{\mathrm{ref}}, y_{\mathrm{ref}}, z_{\mathrm{ref}})$ and the reference time t_{ref} required for the event reconstruction were chosen to be the *true MC parameters* at the muon start point, (t_0, x_0, y_0, z_0), *plus some random shifts*: $t_{\mathrm{ref}} = t_0 + \Delta t$, $x_{\mathrm{ref}} = x_0 + \Delta x$, $y_{\mathrm{ref}} = y_0 + \Delta y$ and $z_{\mathrm{ref}} = z_0 + \Delta z$. The temporal shift Δt was drawn from a normal distribution $\mathcal{N}(0, 1\,\mathrm{ns})$. Each spatial shift Δx, Δy and Δz was independently drawn from a normal distribution $\mathcal{N}(0, 10\,\mathrm{cm})$. The resulting mean radial shift with respect

[2] The sample was primarily adapted for a different reconstruction method (see Ref. [51]). It required that the true muon tracks are fully contained inside the target volume of LENA and that the propagation of the scintillation light is essentially unhindered by the top and bottom detector caps.

to the true start point was ∼16 cm.[3] It is assumed that in a real application, e.g., the reconstruction of cosmogenic muons, the start parameters can be provided to some extent by external measurement devices. Moreover, other reconstruction methods, like the *backtracking-algorithm* described in Ref. [51], can be useful for this task. Since the topological reconstruction can be done both forward and backward in time for any useful reference parameter set (see Equation (6.2)), intermediate reconstruction results can be used to obtain new reference parameters corresponding to the start point of a track. Therefore, the above assumption to have reference parameters close to the true starting point was made for simplicity.

A simulated muon event included both the propagation of the charged particles from the main event as well as a possible muon decay with the emission of the products. Due to the typical time scale of an event in a LSc detector, the decay of a stopped muon (mean life time: ∼2.2 µs [11]) is often tagged separately. For this analysis, muon decays were not separated from the main event. Consequently, scintillation photons from decay products arrived at the PMTs with large delays and essentially had the same (negative) effects on the reconstruction as scattered photons.

To save storage space, and for an easier interfacing with `ROOT`, only the ROI from the total reconstruction mesh was converted to a 3D histogram of type *TH3D* and saved for later analysis. The cuboid region was redetermined based on a new threshold value before each refinement run in the reconstruction procedure. As discussed in Section 6.4.2, the current implementation of the reconstruction method does not yet calculate proper absolute values of $\hat{\Gamma}_{\mathrm{em}}(\mathbf{x})$. Therefore, the threshold had to be chosen based on a relative scale: Weighting with the volumes of the different mesh cells, the weighted mean value $\overline{\hat{\Gamma}}_{\mathrm{em}}$ and the sample standard deviation $\sigma_{\Gamma_{\mathrm{em}}}$ were calculated from all mesh cells inside the LSc-filled volume. The threshold $\hat{\Gamma}_{\mathrm{em,thr}}$ to define the cuboid ROI was then computed according to the arbitrary definition $\hat{\Gamma}_{\mathrm{em,thr}} \equiv \overline{\hat{\Gamma}}_{\mathrm{em}} + 3\sigma_{\Gamma_{\mathrm{em}}}$. If the threshold exceeded the maximum cell content in the mesh, the weighted mean value of the cell content above $\overline{\hat{\Gamma}}_{\mathrm{em}}$ was used instead. Note that the threshold selection has not yet been optimized. In some cases, the current procedure caused the reference point to be outside of the ROI.

7.2 Analysis of 3D reconstruction data

The intermediate outcome from the application of the new reconstruction approach detailed in Section 6.3 is a 3D mesh reflecting the number density distribution of all (scintillation) photon emissions $\hat{\Gamma}_{\mathrm{em}}(\mathbf{x})$. Figure 7.2 depicts a `ROOT`-based event display that has been developed in the course of this work. It shows the 3D distribution of $\hat{\Gamma}_{\mathrm{em}}(\mathbf{x})$ for the simulated muon event underlying Figure 6.8.
For efficiency, the concrete reconstruction procedure outlined in Section 6.4.4 only saves the cuboid ROI likely containing the event. As a consequence, a post-processing of the output is in any case necessary to extract descriptive physics parameters as final reconstruction results, or to obtain the more refined distribution $\hat{\Gamma}^{*}_{\mathrm{em}}(\mathbf{x})$ defined

[3] For example, a start point resolution <7 cm (note the resolution definition) was found in Ref. [51] with a likelihood-based fit method applied to simulated muons with kinetic energies ≤ 1 GeV. The start time resolution was found to be <0.14 ns.

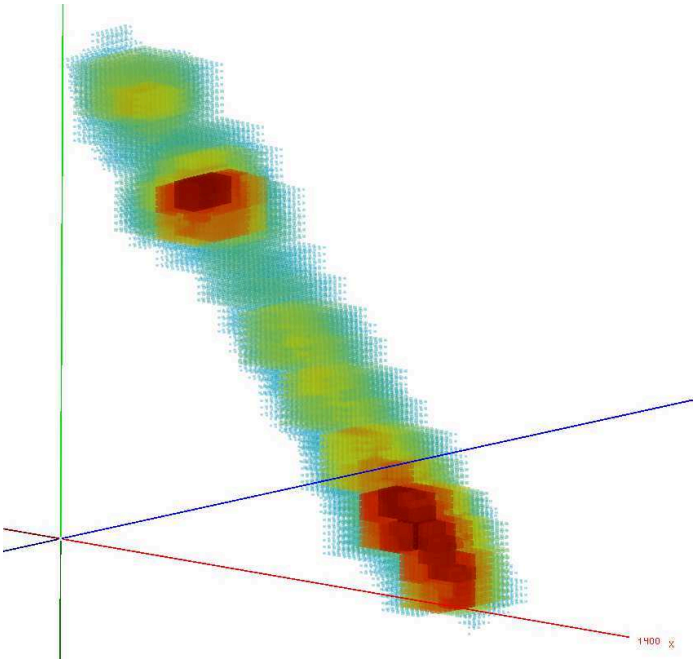

Figure 7.2 – Display for the event underlying Figure 6.8 that shows the 3D distribution of $\hat{\Gamma}_{\mathrm{em}}(\mathbf{x})$ for values $\geq 30\,\%$ of the maximum value. For each cell in the result mesh a box is drawn in the display. The *cell content value* $\hat{\Gamma}_{\mathrm{em}}(\mathbf{x})$ is encoded in the *color* (increasing from blue to red), the *box size* (increasing from small to large) and the *box transparency* (increasing from transparent to opaque). Colored lines represent the x-axis (*red*), the y-axis (*green*) and the z-axis (*blue*) in the LENA detector. The display bases on the *Event Visualization Environment* (EVE) of the `ROOT` framework.

by (6.14).
This section deals with the analysis of the 3D reconstruction data from the sample of stopping muon events simulated in LENA (see Section 7.1). Note that the described steps do not represent the full potential to analyze the output distribution $\hat{\Gamma}_{\mathrm{em}}(\mathbf{x})$. In fact, this task touches complicated fields like *pattern / object recognition* and surely requires more dedicated work once the detailed computation of $\hat{\Gamma}_{\mathrm{em}}(\mathbf{x})$ is fully implemented. However, the procedure described in the following is considered a good starting point to assess the performance of the novel reconstruction method in its current state. Its steps can be summarized as i) selection of the *event region*, ii) binarization of the event region and identification of the *primary blob*, iii) determination of first-guess values for the mean muon direction from an *angle spectrum*, iv) fitting of a 3D line to the primary blob, and v) estimation of the total number of optical photon emissions. The results of this analysis are presented in Section 7.3.

Event region selection The first step was to identify the significant *event region* inside the cuboid ROI of $\hat{\Gamma}_{\mathrm{em}}(\mathbf{x})$. As explained in Section 6.4.2, $\hat{\Gamma}_{\mathrm{em}}(\mathbf{x})$ does not yet have a proper / meaningful absolute normalization due to simplifications in the optical model. Therefore, the event region G was defined based on a relative scale:

$$G \equiv \{\mathbf{x} \,|\, \mathbf{x} \text{ in ROI} \wedge \hat{\Gamma}_{\mathrm{em}}(\mathbf{x}) > a\,\hat{\Gamma}_{\mathrm{em,max}}\}\,. \tag{7.1}$$

The quantity $\hat{\Gamma}_{\mathrm{em,max}}$ is the maximum of $\hat{\Gamma}_{\mathrm{em}}(\mathbf{x})$. Normally, the scaling factor a was chosen to be 2 %. If, however, the reference point $\mathbf{x}_{\mathrm{ref}}$ would have been excluded from G, the threshold was set to be $0.75\,\hat{\Gamma}_{\mathrm{em}}(\mathbf{x}_{\mathrm{ref}})$.

Binarization of event region and "blob"-finding A low threshold value for the definition of G was necessary because for higher thresholds the event region of more and more events would have consisted of disconnected *blobs*[4]. Although this case is expected if a produced γ-ray converts to a shower at some distance to the muon track, it may also be caused by reconstructions with reference parameters that strongly deviated from the true values at the muon start point. The dependence of the reconstruction result quality on the goodness of the reference parameters surely needs further investigation in the future. However, also the low threshold caused the appearance of small blobs remote from the event location due to fluctuations in $\hat{\Gamma}_{\mathrm{em}}(\mathbf{x})$.
In order to facilitate the exclusion of all blobs but the *primary blob* from further processing, which, for this analysis, was defined as the blob containing or being closest to the reference point, a binary version $B(\mathbf{x})$ of the ROI was created with

$$B(\mathbf{x}) \equiv \begin{cases} 1\,, & \text{if } \mathbf{x} \in G \\ 0\,, & \text{if } \mathbf{x} \notin G \end{cases} \quad . \tag{7.2}$$

Subsequently, disconnected blobs in $B(\mathbf{x})$ were tagged to identify the primary blob. Note that blob-finding at increasing binarization thresholds is a fine way to get access to more detailed features of $\hat{\Gamma}_{\mathrm{em}}(\mathbf{x})$, e.g., a shower overlying the energy deposition from a minimum ionizing muon. In the future, this allows to study the correlation of such showers with the production of cosmogenic radioisotopes and, more importantly, gives rise to an efficient veto scheme.

Angle spectrum Having identified the primary blob, the next step was to find the *mean direction* of the muon based on $\hat{\Gamma}_{\mathrm{em}}(\mathbf{x})$ in the blob. To do so, a so-called *angle spectrum* was created: The value $\hat{\Gamma}_{\mathrm{em}}(\mathbf{x}_i)$ was added for each cell with centerpoint $\mathbf{x}_i$ in the primary blob to a 2D histogram as a function of the spherical coordinates φ and θ of the connecting vector $\mathbf{x}_i - \mathbf{x}_{\mathrm{ref}}$. An example for such a spectrum is depicted in Figure 7.3 for the event shown in Figure 6.8. The mean direction of the muon in the LENA coordinate system can be nicely identified and agrees well with the start parameters ($\varphi = 315°, \theta = 90°$) . This procedure to determine the muon direction puts more emphasis on high-weighted cells that have a long lever arm with respect to the fixed point $\mathbf{x}_{\mathrm{ref}}$. Nevertheless, the angle coordinates of the maximum bin were good initial values for the subsequent line fit.[5]

3D line fit For simplicity, this analysis assumed a 3D line as model for a reconstructed muon track. Note that, given a sufficiently precise reconstruction of $\hat{\Gamma}_{\mathrm{em}}(\mathbf{x})$, more complex models can in principle be considered. Using the reference point $\mathbf{x}_{\mathrm{ref}}$

[4] In reference to the usual name in image processing.
[5] The binning of the angle spectrum was calculated based on the mean distance between cells in the current event's primary blob and $\mathbf{x}_{\mathrm{ref}}$.

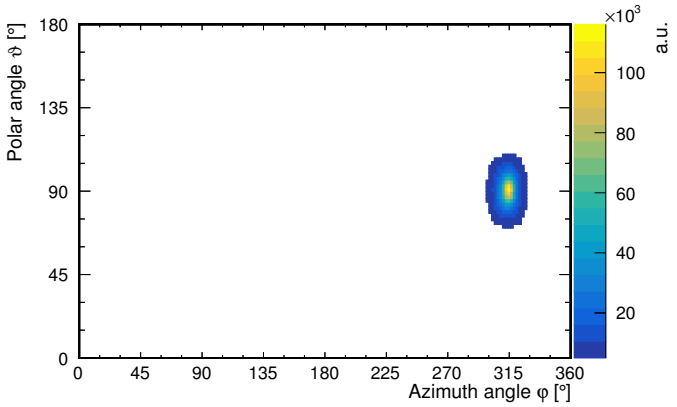

Figure 7.3 – Weighted spectrum of spherical angle coordinates (with respect to the LENA coordinate system) for the connecting vectors $\mathbf{x}_i - \mathbf{x}_{\text{ref}}$ between the reference point $\mathbf{x}_{\text{ref}}$ and the centerpoints $\mathbf{x}_i$ of the cells in the primary blob. The weighting was done with the reconstructed content $\hat{\Gamma}_{\text{em}}(\mathbf{x}_i)$ of the cells. Entries below 5×10^3 a.u. are not shown. The depicted spectrum corresponds to the event underlying Figure 6.8.

and the angle coordinates (φ_m, θ_m) of the maximum bin in the angle spectrum as initial values, a 3D line fit to the distribution $\hat{\Gamma}_{\text{em}}(\mathbf{x})$ inside the primary blob was performed with the minimization package `Minuit` [224] in `ROOT`. The minimized function with five parameters was defined as

$$f(\mathbf{s}, \varphi, \theta) = \ln \sum_i \left(\hat{\Gamma}_{\text{em}}(\mathbf{x}_i)\, d_i(\mathbf{x}_i; \mathbf{s}, \varphi, \theta) \right)^2 , \tag{7.3}$$

where $\mathbf{s}$ is a point on the line and $d_i(\mathbf{x}_i; \mathbf{s}, \varphi, \theta)$ is the orthogonal distance between the line and the centerpoint $\mathbf{x}_i$ of the currently processed cell in the primary blob. Both the logarithm and the squaring were found to improve the minimization speed without much change of the result.

Determination of start point, end point and track length Using the line-like reconstruction of the muon track through the primary blob in $\hat{\Gamma}_{\text{em}}(\mathbf{x})$, the next step of the analysis was the determination of start point and end point of the track. If the reference point $\mathbf{x}_{\text{ref}}$ was inside the primary blob, the reconstructed start point $\hat{\mathbf{x}}_s$ was set to be on the reconstructed line and closest to $\mathbf{x}_{\text{ref}}$. Otherwise $\hat{\mathbf{x}}_s$ was set to be the entrance point of the reconstructed line into the primary blob close to the reference point $\mathbf{x}_{\text{ref}}$. Similarly, the end point estimate $\hat{\mathbf{x}}_e$ was defined as the exit point of the reconstructed line from the primary blob at further distance to $\mathbf{x}_{\text{ref}}$. This allowed to get a track length estimate $\hat{L}$ as

$$\hat{L} \equiv |\hat{\mathbf{x}}_e - \hat{\mathbf{x}}_s| \ . \tag{7.4}$$

Figure 7.4 shows projections of $\hat{\Gamma}_{\text{em}}(\mathbf{x})$ along two different axis of LENA only for the data of the primary blob belonging to the event in Figure 6.8. The two superimposed lines correspond to the direct connections between MC start point and MC end point of the muon (*black*; defines true mean direction) and between the results for $\hat{\mathbf{x}}_s$ and $\hat{\mathbf{x}}_e$ from the line fit (*magenta*). One can see for this event that the line fit result

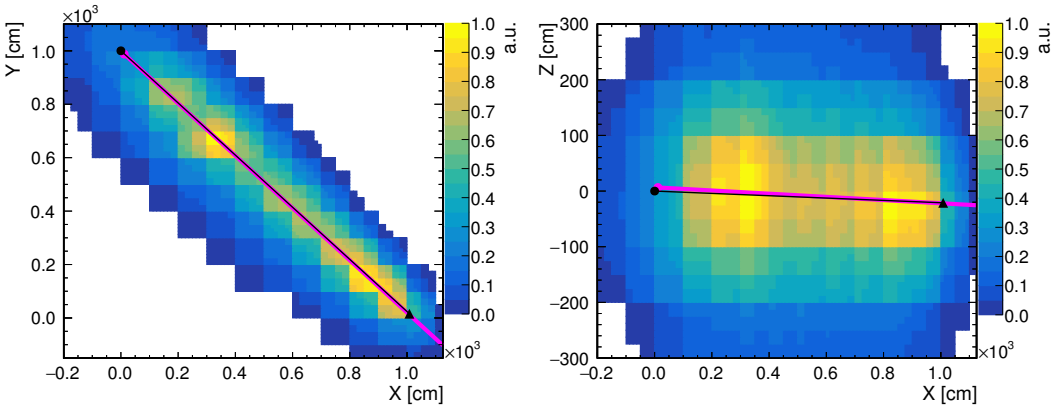

Figure 7.4 – Results for $\hat{\Gamma}_{\mathrm{em}}(\mathbf{x})$ projected along the z-axis **(left)** or y-axis **(right)** of LENA. The data correspond to the primary blob of the event shown in Figure 6.8. Superimposed, *black* lines depict the direct connection between true start (*circle*) and true end (*triangle*) point. The superimposed, *magenta* lines, whose start points are also indicated by *circles*, represent the result from the 3D line fit.

agrees very well with the muon's true mean direction. Since the reference point $\mathbf{x}_{\mathrm{ref}}$ is inside the event's primary blob, $\hat{\mathbf{x}}_s$ was reconstructed close to the true start point, which was the basis for the randomly shifted reference point. However, the fitted line does not properly reconstruct the track's true end point. The reason is that the position of the reconstructed end point $\hat{\mathbf{x}}_e$, which was defined as the exit point of the fitted line from the primary blob, strongly depends on the event region threshold used to define the extension of the primary blob. Therefore, the somewhat arbitrary choice for the global (i.e., event-independent) threshold value introduced a systematic shift of the reconstructed end point with respect to the true end point. The same effect can be observed if the start point has to be reconstructed as the entrance point of the fitted line because the reference point is outside of the primary blob. Consequently, systematic errors for the reconstructed start and end points translate to a systematic error for $\hat{L}$. Its removal on per-event level requires a more sophisticated definition / selection of event regions.
In Figure 7.4 and previously shown projections one an see that lower values of $\hat{\Gamma}_{\mathrm{em}}(\mathbf{x})$ are computed close to the muon start point but along the track. The occurrence of this effect probably depends on the goodness of the reference parameters. However, more detailed studies are required to confirm this.

Estimation of the total number of photon emissions Since the reconstruction result $\hat{\Gamma}_{\mathrm{em}}(\mathbf{x})$ already reflects the number density distribution of all photon emissions, the sum

$$\hat{N}_{\mathrm{em}} = \sum_i \hat{\Gamma}_{\mathrm{em}}(\mathbf{x}_i)\, \Delta V_{\mathrm{cell}}(\mathbf{x}_i) \tag{7.5}$$

was used as estimator for the total number of emitted photons $\hat{N}_{\mathrm{em}}$. Recall, however, that a better reconstruction of $\hat{N}_{\mathrm{em}}$ (and also of $\mathrm{d}E/\,\mathrm{d}x$) can be obtained in the future if the above sum runs over the number density distribution $\hat{\Gamma}^*_{\mathrm{em}}(\mathbf{x})$, which is defined in (6.14) and describes the photon emissions specifically from the event

topology. In principle, the reconstructed line from $\hat{\mathbf{x}}_s$ to $\hat{\mathbf{x}}_e$ could be used as estimate $\hat{T}$ for the event topology in order to construct $\hat{\Gamma}^*_{\mathrm{em}}(\mathbf{x})$. However, due to the currently existing systematic uncertainty in the reconstruction of the muon track length and the improper normalization of the basic result $\hat{\Gamma}_{\mathrm{em}}(\mathbf{x})$, the distribution $\hat{\Gamma}^*_{\mathrm{em}}(\mathbf{x})$ was not computed in the course of this work.

7.3 Results

This section presents the results from the analysis of the 3D reconstruction data described in Section 7.2. The *angular resolution* is topic of Section 7.3.1. Results for the track start and end point resolutions are treated in Section 7.3.2. Subsequently, outcomes for the reconstructed track length are covered in Section 7.3.3. Information on the performance to reconstruct the total number of photon emissions and on the relative energy resolution are finally given in Section 7.3.4.

7.3.1 Angular resolution

The angular resolution of a muon track reconstruction in a LSc detector is important to evaluate the efficiency of a veto strategy for cosmogenic background. More specifically, the precision with which muon directions can be determined affects the size of the region that must be vetoed around a reconstructed track (see also Section 6.1). In order to assess the angular resolution currently achievable with the new reconstruction method, the reconstructed direction $\hat{\mathbf{d}}$ from the line fit to the primary blob (see Section 7.2) is compared to the *mean direction* $\mathbf{d}_{\mathrm{MC}} = (\mathbf{x}_e - \mathbf{x}_s)/|(\mathbf{x}_e - \mathbf{x}_s)|$ of the true muon track from start point $\mathbf{x}_s$ to end point $\mathbf{x}_e$. The *intermediate angle* α is then calculated as

$$\alpha = \arccos\left(\frac{\hat{\mathbf{d}} \cdot \mathbf{d}_{\mathrm{MC}}}{|\hat{\mathbf{d}}|\,|\mathbf{d}_{\mathrm{MC}}|}\right). \tag{7.6}$$

Figure 7.5 shows binned frequency distributions $P(\alpha|E_{\mathrm{kin,MC}})$ as a function of the true kinetic energy $E_{\mathrm{kin,MC}}$. They were created from the reconstruction results of the simulated muon sample in Figure 7.1. While α tends towards zero for energies $> 1\,\mathrm{GeV}$, a large spread of the intermediate angle is visible at lower energies. Even values $> 90°$ (not shown) were found, suggesting that the reconstructed direction must be inverted. Recall, however, that the reconstruction was done with respect to the reference point $\mathbf{r}_{\mathrm{ref}}$. For simplicity, $\mathbf{r}_{\mathrm{ref}}$ was obtained from the true muon start point $\mathbf{x}_s$ by adding a small, random offset $\Delta\mathbf{x}$, and is therefore usually close to $\mathbf{x}_s$. Due to low contrast in the final reconstruction result $\hat{\Gamma}_{\mathrm{em}}(\mathbf{x})$ at lower energies and the finitely small reconstruction mesh cells (12.5 cm edge length), the analyzed event regions below 1 GeV did not exhibit an elongation in track direction. Instead, they had a more compact shape. Since $|\Delta\mathbf{x}|$ can be comparable to the extent of the compact primary blob at these energies, the reconstructed direction inherited the randomness of the spatial reference parameter. Therefore, results in the energy range below 1 GeV are discarded in the following if they depend on the outcome of the line fit. In order to improve the analysis in the low energy range, reconstructions with smaller mesh cells are required in the future. Moreover, the dependence of the reconstruction quality on the goodness of the reference parameters must be studied.

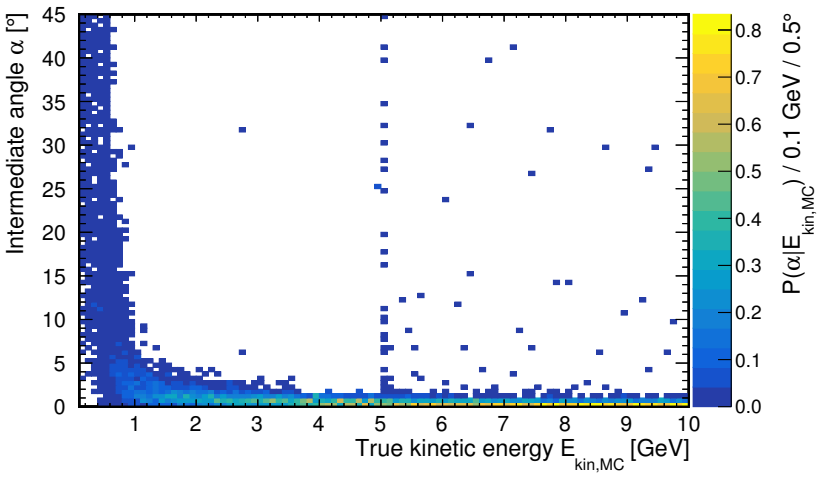

Figure 7.5 – Binned relative frequency distributions $P(\alpha|E_{\mathrm{kin,MC}})$ for the intermediate angle $\alpha < 45°$ between reconstructed and true muon track as a function of the true kinetic energy $E_{\mathrm{kin,MC}}$. The distributions originate from the reconstruction results for the simulated muons in the sample shown in Figure 7.1. More details are visible for $\geq 5\,\mathrm{GeV}$ due to higher statistics in this energy range.

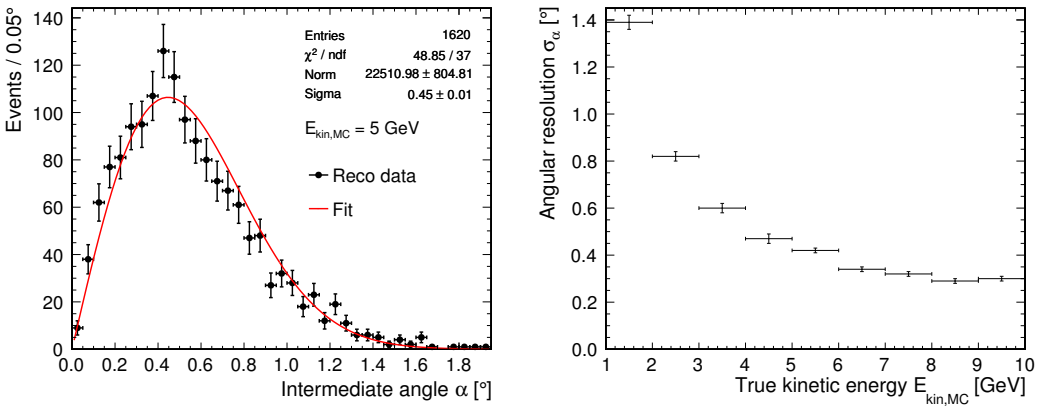

Figure 7.6 – **Left:** Distribution of the intermediate angle α between reconstructed and and true muon track for the high-statistics muon sample with $E_{\mathrm{kin,MC}} = 5\,\mathrm{GeV}$ true kinetic energy. Vertical error bars only indicate statistical errors. A binned likelihood fit to the distribution with function (7.7) was made. At larger angles, there are 52 outliers. **Right:** Angular resolution σ_α as a function of the true kinetic energy $E_{\mathrm{kin,MC}}$ in the range from 1 to 10 GeV. The resolutions were determined by binned likelihood fits of (7.7) to distributions like the one shown on the left side. Vertical error bars indicate errors on σ_α returned from the fits.

The left side of Figure 7.6 shows the distribution of the intermediate angle α for the high-statistics muon sample at 5 GeV. In order to quantify the angular resolution, which was assumed to be independent of the muon track direction,[6] the distribution

[6]Recall that for energies $\gtrsim 6\,\mathrm{GeV}$ the analyzed muon tracks did not have a fully random direction (see Figure 7.1 right).

was fitted with the function

$$F(\alpha) = \sin(\alpha)\, A\, \exp\left(-\frac{\alpha^2}{2\sigma_\alpha^2}\right) . \tag{7.7}$$

The quantity A defines the normalization, $\sin(\alpha)$ accounts for the solid angle dependence and the exponential function describes the resolution function, i.e., a Gaussian function around zero. The fit parameter σ_α is defined to be the measure for the angular resolution. As one can see, the fit is in agreement with the reconstruction data. However, the distribution's tail is not perfectly described by the model; deviations get more distinct at energies $\leq 4\,\mathrm{GeV}$. The origin of the observed kind of tail in the distributions of α, e.g., an actual dependence on the muon track direction in the cylindrical detector, misreconstructions and/or physics processes, has to be investigated in the future.[7]
The right side of Figure 7.6 presents the angular resolution σ_α as a function of the true kinetic energy $E_{\mathrm{kin,MC}}$ of the simulated stopping muons. From 1 to 10 GeV, the angular resolution decreases non-linearly from $(1.39 \pm 0.03)\,^\circ$ to $(0.30 \pm 0.01)\,^\circ$. Some properties of the analyzed distributions of α are listed in Table E.1.
Although a direct comparison is difficult, angular resolution results based on real data from the running experiment Borexino can be used as reference. The analysis of CNGS muons that crossed both OPERA and the LSc-filled inner vessel of Borexino yielded an angular resolution of $(2.44 \pm 0.19)^\circ$ [37]. Considering that the angular resolution obtained with the new reconstruction method probably degrades once more details (e.g., realistic reference parameter finding) are taken into account, the results in this work nevertheless describe a good initial position to be competitive in a fair, future comparison with other methods.

7.3.2 Start and end point resolution

In addition to the angular resolution, the capability to correctly reconstruct the spatial position of the muon track is another important performance measure. Ideally, the spatial resolution is assessed by looking at the distance between the reconstructed, not necessarily straight track and multiple intermediate points of the true MC track. However, for this analysis, only the resolutions of track start point and track end point were studied. Especially the resolution lateral to a track affects the optimal radius of the cylindrical veto region around a reconstructed muon,[8] which is commonly used in strategies to reject background from cosmogenic radionuclides (see also Section 6.1). For stopping muons, also the resolution of the end point parallel to the track is important as it determines the optimal length of the veto region.

Start point Firstly, the start point resolutions in x-, y- and z-direction of the LENA detector were determined: If $\mathbf{u}_s = \mathbf{x}_s - \hat{\mathbf{x}}_s$ is the connecting vector between reconstructed start point $\hat{\mathbf{x}}_s$ and true start point $\mathbf{x}_s$, the distributions of the components $u_{s,x}$, $u_{s,y}$, and $u_{s,z}$ were studied. The left side of Figure 7.7 shows the

[7] The most likely origin of the tail is a dependence of α on the track direction in the cylindrical detector. Therefore, σ_α describes an average angular resolution.
[8] Usually, the optimal radius depends mostly on the distance profile of radionuclide production lateral to a reconstructed track.

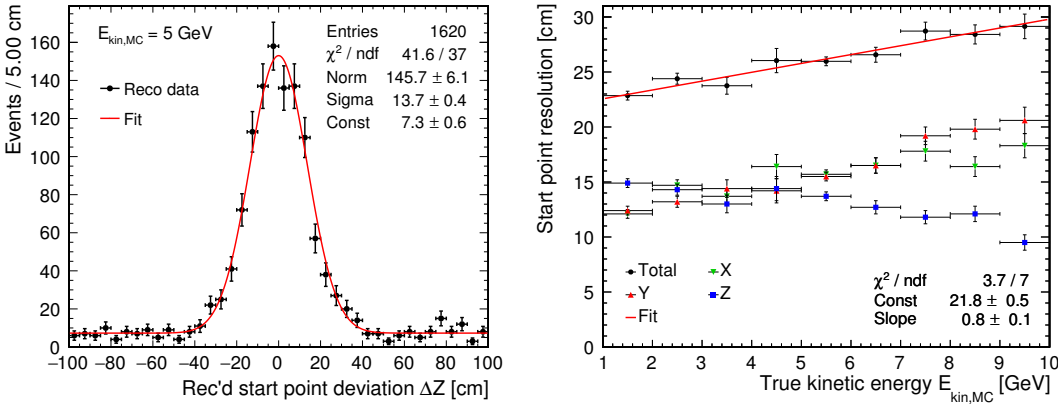

Figure 7.7 – **Left:** Distribution of the deviation $\Delta z \equiv u_{s,z}$ of the reconstructed muon track start point from the true start point in z-direction (detector coordinate system) for the high-statistics muon sample with $E_{\mathrm{kin,MC}} = 5\,\mathrm{GeV}$. Vertical error bars indicate statistical errors only. There are 152 (172) events with smaller (larger) values of Δz outside of the shown range. The distribution was fitted with function (7.8). **Right:** Start point resolutions $\sigma_{s,x}$ (*green tip down triangle*), $\sigma_{s,y}$ (*red tip up triangle*) and $\sigma_{s,z}$ (*blue square*) along the detector coordinates x, y and z as a function of the true kinetic energy $E_{\mathrm{kin,MC}}$ in the range from 1 to 10 GeV. They were obtained from fits of function (7.8) to the distributions of $u_{s,x}$, $u_{s,y}$ and $u_{s,z}$; vertical error bars indicate the errors returned from the fits. The total resolution (*black circle*) was calculated as the square root of the sum of the squared resolutions in the three directions. It was fitted with a linear function. Errors for the total resolution were determined with Gaussian error propagation.

distribution of $u_{s,z}$ belonging to the high-statistics sample at $E_{\mathrm{kin,MC}} = 5\,\mathrm{GeV}$ as an example. While most of the events follow a Gaussian distribution around zero, there are non-Gaussian tails to both sides, which will be explained below. Taking these tails into account as flat contributions in the fit range during the determination of the resolutions, binned likelihood fits with the fit function

$$F(u_{s,c}) = A\,\exp\left(-\frac{u_{s,c}^2}{2\sigma_{s,c}^2}\right) + B\,, \quad c = x,\, y,\, z\,, \tag{7.8}$$

were performed for all components $u_{s,c}$. The right side of Figure 7.7 shows the different resolutions $\sigma_{s,c}$ as a function of the true kinetic energy $E_{\mathrm{kin,MC}}$ in the range from 1 to 10 GeV. Results below 1 GeV, which depend on the highly randomized reconstruction of the track direction, were discarded. Additional information on the distributions of the components $u_{s,x}$, $u_{s,y}$ and $u_{s,z}$ are listed in Table E.2. As one can see on the right side of Figure 7.7, the single resolutions are essentially equal for energies below 6 GeV. Above this energy, which coincides with the point where the muon tracks start to be more and more aligned with the z-axis (symmetry axis) of the detector (see Figure 7.1 right), the uncertainty in z-direction decreases while the uncertainties in x- and y-direction increase. For the essentially up- or downward-going tracks, the x- and y-resolutions tend to reflect the resolution lateral to the reconstructed track, whereas the z-resolution mostly describes the resolution parallel to the track. Therefore, the results for the sample of fully contained muons suggest a dependence of the start point resolution on the track direction (or the

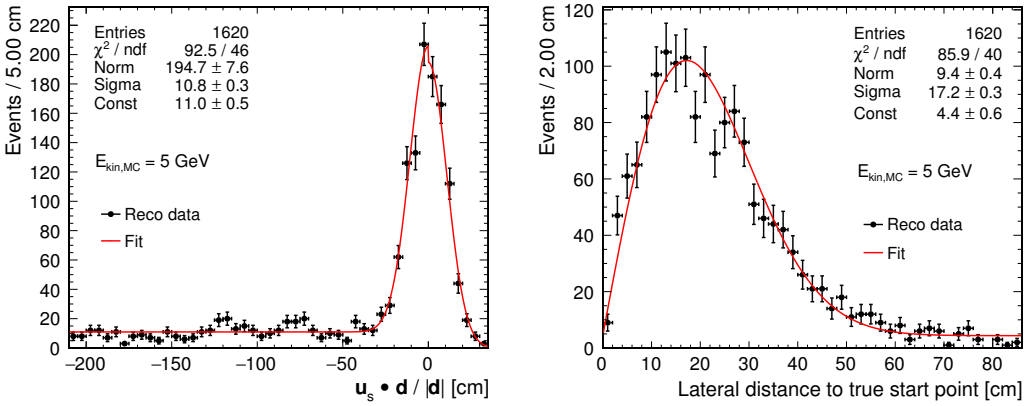

Figure 7.8 – **Left:** Distribution of the projection $u_{s,\mathrm{para}}$ of the connecting vector $\mathbf{u}_s$ onto the reconstructed muon track direction $\hat{\mathbf{d}}/|\hat{\mathbf{d}}|$ for the high-statistics muon sample with $E_{\mathrm{kin,MC}} = 5\,\mathrm{GeV}$. Vertical error bars indicate statistical errors only. There are 103 (4) events with smaller (larger) values of $u_{s,\mathrm{para}}$ outside of the shown range. The distribution was fitted with function (7.11). **Right:** Distribution of the lateral distance $u_{s,\mathrm{lat}}$ between true start point and reconstructed muon track for $E_{\mathrm{kin,MC}} = 5\,\mathrm{GeV}$. Again, the vertical error bars indicate statistical errors only. There are 46 events with larger values of $u_{s,\mathrm{lat}}$ outside of the shown range. The distribution was fitted with function (7.13).

z-position of the start point, i.e., closer or farther to the detector end caps). In principle, such effects can be expected for a LSc volume with cylindrical symmetry. They were not investigated any further in this work because a detailed study surely requires more statistics and sampling points inside the detector.
Figure 7.7 right also depicts the *total start point resolution* $\sigma_{s,\mathrm{tot}}$ as a function of $E_{\mathrm{kin,MC}}$. It was determined as

$$\sigma_{s,\mathrm{tot}} = \sqrt{\sigma_{s,x}^2 + \sigma_{s,y}^2 + \sigma_{s,z}^2} \tag{7.9}$$

based on the resolutions obtained for the three orthogonal directions.[9] A fit with a linear function yielded that the total start point resolution value increases by $(0.8 \pm 0.1)\,\mathrm{cm/GeV}$. Note that the values for $\sigma_{s,\mathrm{tot}}$ are higher than a corresponding resolution of $\sqrt{3} \cdot 10\,\mathrm{cm} \approx 17.3\,\mathrm{cm}$ for the reference point $\mathbf{r}_{\mathrm{ref}}$ from the random shift with respect to the true start point $\mathbf{x}_s$ (see Section 7.1.2).

In order to study the start point resolution $\sigma_{s,\mathrm{para}}$ parallel to the reconstructed track, whose direction $\hat{\mathbf{d}}$ was determined in the line fit, the connecting vector $\mathbf{u}_s$ was projected onto $\hat{\mathbf{d}}/|\hat{\mathbf{d}}|$:

$$u_{s,\mathrm{para}} = \mathbf{u}_s \cdot \frac{\hat{\mathbf{d}}}{|\hat{\mathbf{d}}|}\,. \tag{7.10}$$

The left side of Figure 7.8 shows the distribution of $u_{s,\mathrm{para}}$ for the high-statistics muon sample at $E_{\mathrm{kin,MC}} = 5\,\mathrm{GeV}$. While most of the events follow a Gaussian distribution around $u_{s,\mathrm{para}} = 0$, there is also a long tail towards negative values of $u_{s,\mathrm{para}}$. This

[9] Without the non-Gaussian tails, the total start point resolution $\sigma_{s,\mathrm{tot}}$ would be the *root mean square* (RMS) of the distribution of the distance $|\mathbf{u}_s|$.

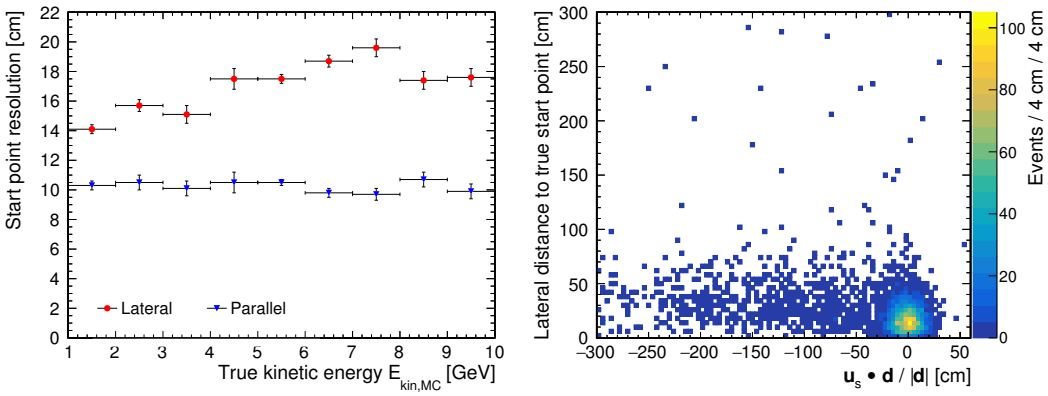

Figure 7.9 – **Left:** Start point resolution lateral (*red circle*) and parallel (*blue triangle*) to the reconstructed track as a function of the true kinetic energy $E_{\mathrm{kin,MC}}$ in the range from 1 to 10 GeV. Vertical error bars indicate errors obtained from fits. **Right:** Lateral distance $u_{s,\mathrm{lat}}$ (defined in Equation (7.12)) to the true start point as a function of the parallel distance $u_{s,\mathrm{para}}$ (defined in Equation (7.10)) to the true start point for the simulated muons with true kinetic energy $E_{\mathrm{kin,MC}}$ in the range from 1 to 10 GeV.

indicates a systematic effect that has the tendency to shift the reconstructed start point $\hat{\mathbf{x}}_s$ down the reconstructed track with respect to the true start point $\mathbf{x}_s$. The most likely origin of this shift is the current approach to determine $\hat{\mathbf{x}}_s$ (see also Section 7.2): If the reference point $\mathbf{r}_{\mathrm{ref}}$ for the reconstruction, which was assumed to be close to the start point of the muon track, is located inside the selected primary blob in the 3D reconstruction output data, $\hat{\mathbf{x}}_s$ is defined to be the point closest to $\mathbf{r}_{\mathrm{ref}}$ on the line from the fit through the primary blob. Since $\mathbf{r}_{\mathrm{ref}}$ was obtained by adding a random offset $\Delta\mathbf{x}$ with Gaussian-distributed components to $\mathbf{x}_s$, the reconstructed start point also inherited from this randomness. However, if $\mathbf{r}_{\mathrm{ref}}$ is outside of the primary blob, $\hat{\mathbf{x}}_s$ is defined to be the intersection of the fitted line with the primary blob. Therefore, $\hat{\mathbf{x}}_s$ is shifted down the reconstructed track by a random[10] distance with respect to $\mathbf{x}_s$. This results in the observed one-sided tail towards negative values in the distribution of $u_{s,\mathrm{para}}$ (see Figure 7.8 left) and also explains the tails to both sides in the distributions of $u_{s,x}$, $u_{s,y}$ and $u_{s,z}$ (e.g., see Figure 7.7 left). In order to increase the robustness of the start point finding on per-event-level, the current method to select the event region / primary blob must be improved.
For a determination of $\sigma_{s,\mathrm{para}}$, the distribution of $u_{s,\mathrm{para}}$ was fitted with the following function:

$$F(u_{s,\mathrm{para}}) = \begin{cases} A \exp\left(-\frac{u_{s,\mathrm{para}}^2}{2\sigma_{s,\mathrm{para}}^2}\right), & \text{if } u_{s,\mathrm{para}} \geq 0 \\ A \exp\left(-\frac{u_{s,\mathrm{para}}^2}{2\sigma_{s,\mathrm{para}}^2}\right) + B, & \text{if } u_{s,\mathrm{para}} < 0 \end{cases} . \tag{7.11}$$

The fit parameter A is the normalization and B roughly approximates the one-sided tail as a constant term. As one can see on the left side of Figure 7.8, the fit describes the Gaussian part of the distribution well, but exhibits deviations in the tail. Figure 7.9 depicts on the left side the resolution $\sigma_{s,\mathrm{para}}$ as a function of $E_{\mathrm{kin,MC}}$. Neglecting the left-sided tail in the distributions of $u_{s,\mathrm{para}}$, the parallel resolution is about 10 cm throughout the analyzed energy range. Due to the projection of $\mathbf{r}_{\mathrm{ref}}$

[10] Recall that the primary blob in the reconstruction data is comprised of small, discrete cells.

onto the fitted line in order to find $\hat{\mathbf{x}}_s$ (see Section 7.2), $u_{s,\text{para}}$ is strongly tied to the random shift $\Delta\mathbf{x}$ of $\mathbf{r}_{\text{ref}}$ with respect to $\mathbf{x}_s$ from the determination of the reference point (see Section 7.1.2). Since the Gaussian standard deviation of each component of $\Delta\mathbf{x}$ was set to 10 cm, the result for $\sigma_{s,\text{para}}$ essentially confirms that the current start point reconstruction works correctly. However, future versions of the analysis must break this dependence of $\hat{\mathbf{x}}_s$ on $\mathbf{r}_{\text{ref}}$.

The start point resolution $\sigma_{s,\text{lat}}$ perpendicular to the reconstructed track gives an idea on the lateral displacement of the latter relative to the true muon track. Amongst other things, this shift affects the optimal radius of a cylindrical veto region for cosmogenic background rejection around the reconstructed track. In order to quantify $\sigma_{s,\text{lat}}$, the distribution of the distance $u_{s,\text{lat}}$, which is calculated as

$$u_{s,\text{lat}} = \frac{|\mathbf{u}_s \times \hat{\mathbf{d}}|}{|\hat{\mathbf{d}}|}\,, \tag{7.12}$$

was studied. This component is not connected to $\mathbf{r}_{\text{ref}}$ as it is the case for $\sigma_{s,\text{para}}$. An example for a distribution of $u_{s,\text{lat}}$ is shown on the right side of Figure 7.8. It was fitted with the function

$$F(u_{s,\text{lat}}) = u_{s,\text{lat}}\, A\, \exp\left(-\frac{u_{s,\text{lat}}^2}{2\sigma_{s,\text{lat}}^2}\right) + B\,. \tag{7.13}$$

Again, the fit parameter A describes the normalization. For simplicity, a constant term given by the fit parameter B was used to roughly approximate a tail to higher values of $u_{s,\text{lat}}$.[11] The the left side of Figure 7.9 shows the results for the lateral start point resolution $\sigma_{s,\text{lat}}$ as a function of $E_{\text{kin,MC}}$. At first view, the outcomes suggest a dependence of the lateral resolution on the energy. However, one has to take into account that the tracks at higher energies become more aligned with the symmetry axis of the cylindrical detector. Therefore, as stated previously, it seems to be that the lateral resolution in fact depends on the direction of the track in the detector. Due to low statistics, this could not be studied any further. Sample mean values and standard deviations of the distributions of $u_{s,\text{para}}$ and $u_{s,\text{lat}}$ analyzed for Figure 7.9 are summarized in Table E.3 and Table E.4, respectively.
The right side of Figure 7.9 shows the 2D distribution of $u_{s,\text{lat}}$ and $u_{s,\text{para}}$ for the analyzed events. The long one-sided tail in $u_{s,\text{para}}$ is clearly visible, but the corresponding events do not necessarily contribute to the tail in $u_{s,\text{lat}}$.

End point In principle, the end point analysis can be performed the same way as the previous start point analysis. One simply has to replace the connecting vector $\mathbf{u}_s$ by the corresponding vector $\mathbf{u}_e = \mathbf{x}_e - \hat{\mathbf{x}}_e$, where $\hat{\mathbf{x}}_e$ and $\mathbf{x}_e$ are the reconstructed and the true track end point, respectively. However, the current analysis procedure for the 3D reconstruction output data (see Section 7.2) introduces a (systematic) displacement in track direction to $\hat{\mathbf{x}}_e$. It is a consequence of the method used to select the event region in the 3D data: As one can see in Figure 7.4, the found primary

[11] A fit including a second Gaussian function with variable mean, standard deviation and normalization to describe the tail of course resulted in better fits, but only yielded minor improvements for the resolution values.

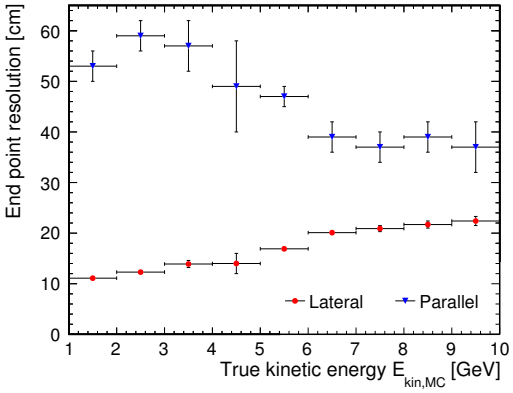

Figure 7.10 – End point resolution lateral (*red circle*) and parallel (*blue triangle*) to the reconstructed track as a function of the true kinetic energy $E_{\mathrm{kin,MC}}$ in the range from 1 to 10 GeV. Vertical error bars indicate parameter errors obtained from fits.

blob reaches beyond the true end point of the track. Since $\hat{\mathbf{x}}_e$ is determined as the intersection point of the fitted, outgoing line with the blob, $\hat{\mathbf{x}}_e$ is systematically shifted in track direction with respect to $\mathbf{x}_e$. It is shown below that the shift mostly depends on the energy of the event. Yet in some cases the shift can be smaller due to the boundaries of the analyzed 3D ROI, which was determined during the reconstruction. Although the energy dependence of the shift in principle allows its statistical removal, the prevention of its occurrence at per-event-level is preferable and requires the development of an improved event region selection approach.

Due to the systematic shift of $\hat{\mathbf{x}}_e$, the distributions of the components $u_{e,x}$, $u_{e,y}$ and $u_{e,z}$ of $\mathbf{u}_e$, which must be studied to get the end point resolutions in x, y and z (detector coordinates), do not exhibit a fittable Gaussian peak around zero. For example, the left side of Figure E.1 depicts the distribution of $u_{e,z}$ for all events in the energy range from 1 to 10 GeV. Instead, the right side of Figure E.1 shows the sample standard deviations of the distributions for the components of $\mathbf{u}_e$ as resolution measures for different ranges of the true kinetic energy $E_{\mathrm{kin,MC}}$. Since the sample standard deviations are heavily affected by tails and outliers, the resulting values are very large. Some properties of the analyzed distributions of $u_{e,y}$ and $u_{e,z}$ of $\mathbf{u}_e$ are listed in Table E.5.
The resolutions parallel and lateral to the reconstructed track were determined based on the distributions of the components $u_{e,\mathrm{para}}$ and $u_{e,\mathrm{lat}}$, which are respectively defined in analogy to (7.10) and (7.12). Since the lateral component $u_{e,\mathrm{lat}}$ featured distributions similar to the one depicted on the right side of Figure 7.9, the lateral resolution was determined with the same fit function (7.13) as in the case of the start point. Data points marked with red circles in Figure 7.10 illustrate the lateral end point resolution as a function of $E_{\mathrm{kin,MC}}$. It is similar in trend and magnitude to the lateral start point resolution.
The distributions of the parallel component $u_{e,\mathrm{para}}$ are heavily affected by the systematic shift of $\hat{\mathbf{x}}_e$. An example for such a distribution is shown on the left side of Figure 7.11 for $E_{\mathrm{kin,MC}} = 5\,\mathrm{GeV}$. One can see that most of the events form a peak at negative values of $u_{e,\mathrm{para}}$, indicating that $\mathbf{x}_e$ for these events lies in the opposite direction of the reconstructed track with respect to $\hat{\mathbf{x}}_e$. The non-Gaussian

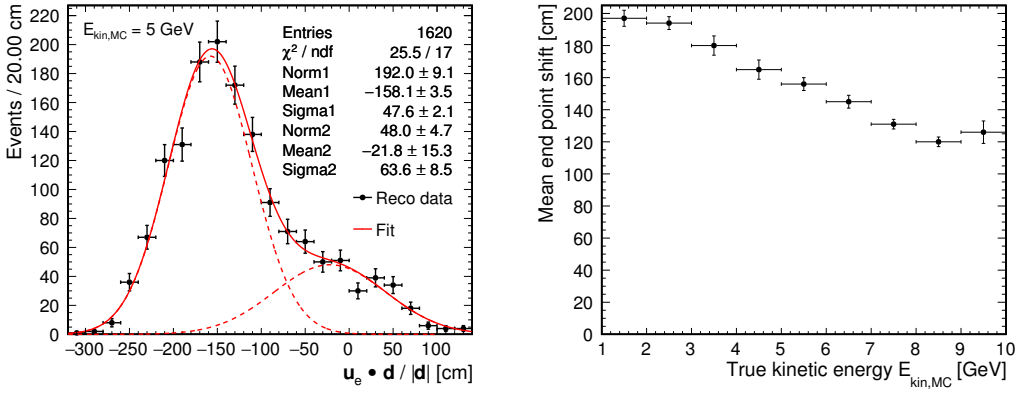

Figure 7.11 – **Left:** Distribution of the projection $u_{e,\text{para}}$ of the connecting vector $\mathbf{u}_e$ onto the reconstructed muon track direction $\hat{\mathbf{d}}/|\hat{\mathbf{d}}|$ for the high-statistics muon sample with $E_{\text{kin,MC}} = 5\,\text{GeV}$. Vertical error bars indicate statistical errors only. There are 13 (80) events with smaller (larger) values of $u_{e,\text{para}}$ outside of the shown range. The distribution was fitted with function (7.14). **Right:** Mean end point shift ($|\mu_{\text{peak}}|$ in Equation (7.14)) as a function of the true kinetic energy $E_{\text{kin,MC}}$ in the range from 1 to 10 GeV. Vertical error bars represent the errors on μ_{peak} obtained from the fits to distributions like the one shown on the left side.

tail to higher values of $u_{e,\text{para}}$ is populated by events where the shift is limited by the boundary of the ROI or a too short primary blob. The latter case can occur due to a breakup of the true event region around the muon track during the analysis (see brief discussion in Section 7.3.3).
With the goal to determine the mean position and width of the peak, the distributions were fitted by the sum of two Gaussian functions:[12]

$$F(u_{e,\text{para}}) = A\,\exp\left(-\frac{(u_{e,\text{para}}-\mu_{\text{peak}})^2}{2\sigma_{\text{peak}}^2}\right) + B\,\exp\left(-\frac{(u_{e,\text{para}}-\mu_{\text{tail}})^2}{2\sigma_{\text{tail}}^2}\right). \quad (7.14)$$

The first term with normalization parameter A describes the peak. It yields both the used measure for the parallel end point resolution, $\sigma_{e,\text{para}} \equiv \sigma_{\text{peak}}$, and the mean shift μ_{peak}. Assuming the (partially technical) issues causing the non-Gaussian tail to higher values of $u_{e,\text{para}}$ (and the mean end point shift) can be fixed in the future, the second term, which describes this tail, is of no further interest in this work. Some properties of the analyzed distributions of $u_{e,\text{para}}$ and $u_{e,\text{lat}}$ are listed in Table E.6 and Table E.7, respectively.
As one can see from the data points marked with blue triangles in Figure 7.10, the values for the parallel end point resolution $\sigma_{e,\text{para}}$ seem to be dominated by the random extent of the primary blob. Figure 7.11 right depicts the change of the mean shift $|\mu_{\text{peak}}|$ as a function of $E_{\text{kin,MC}}$. The decreases of both $\sigma_{e,\text{para}}$ and $|\mu_{\text{peak}}|$ with rising energy can be explained by increasing contrast in the 3D reconstruction data, i.e., the extent of the primary blob is more well-defined and thus less sensitive to the event region selection threshold in (7.1).

In general, the outcomes for the parallel resolutions of start and end point look

[12] The tail to higher values could not be described sufficiently well by a model including the addition of only one parameter similar to (7.11), i.e., a flat component.

promising, but more dedicated effort is required to resolve the outstanding, yet well-understood, issues in the analysis of the reconstruction data, especially concerning the end point reconstruction. The results for the lateral resolutions of start and end point, which seem to depend on the orientation of the track inside the cylindrical LENA detector, already indicate that the lateral position of a mean muon track can be well determined. Taking results from BOREXINO again as reference for the lateral resolution, an analysis of CNGS muons that traversed the inner vessel of the detector yielded that the single Gaussian resolutions in the two orthogonal directions of the plane perpendicular to the track are about 35 cm [37]. Although this measure cannot be compared directly to the one used in this work, the currently determined performance of the new reconstruction method in this particular aspect again seems to be a good initial position for the future development.

7.3.3 Track length

An estimate $\hat{L}$ for the muon track length was defined in (7.4) as the distance between the reconstructed start point $\hat{\mathbf{x}}_s$ and the reconstructed end point $\hat{\mathbf{x}}_e$. Consequently, the precision and accuracy with which the track length can be reconstructed is correlated with the precisions and accuracies for $\hat{\mathbf{x}}_s$ and $\hat{\mathbf{x}}_e$. Although there is currently a tendency to reconstruct both points at systematically shifted positions, the shifts are likely in the same direction (down the track) and therefore partially conserve the track length.
Similar to the reconstructed quantity $\hat{L}$, one can define an *approximated true track length* L_{MC} based on the MC parameters $\mathbf{x}_s$ and $\mathbf{x}_e$:

$$L_{\mathrm{MC}} \equiv |\mathbf{x}_e - \mathbf{x}_s| \ . \tag{7.15}$$

Note that L_{MC} is usually smaller that the true track length due to the neglect of muon scattering. Although L_{MC} often is a good reference to compare $\hat{L}$ to, there is a subtle difference between the quantities: While L_{MC} is a measure for the muon track length, $\hat{L}$ in fact describes the length of the primary blob in the reconstruction data. For example, this becomes important if the muon track is shorter than expected because energy is transfered into the creation of a shower, whose energy deposition in the end "elongates" the primary blob beyond the intended region.[13]

Figure 7.12 shows binned relative frequency distributions $P(\hat{L}|E_{\mathrm{kin,MC}})$ as a function of the true kinetic energy $E_{\mathrm{kin,MC}}$. Events below 1 GeV, which are largely affected by the random determination of a reconstructed track direction (see Section 7.3.1), are not taken into account. As a quantification of the mean trend, the figure also contains the outcomes from linear regressions with the reconstructed data $\hat{L}$ (*solid red line*) and with the MC data L_{MC} (*dashed magenta line*; see Figure E.2). The regression results for the reconstructed data suggest a systematic increase of $\hat{L}$ at lower energies that becomes smaller with rising energy. This is essentially consistent with the findings for the significant energy-dependent shift of the reconstructed end point in Figure 7.11 right. However, the lower slope compared to the MC truth seems to be largely driven by the very short reconstructed track lengths at energies $\geq$3 GeV. From

[13] To reconstruct a better estimate for the muon track length in these cases, a sophisticated object / pattern recognition must be developed and applied to the primary blob.

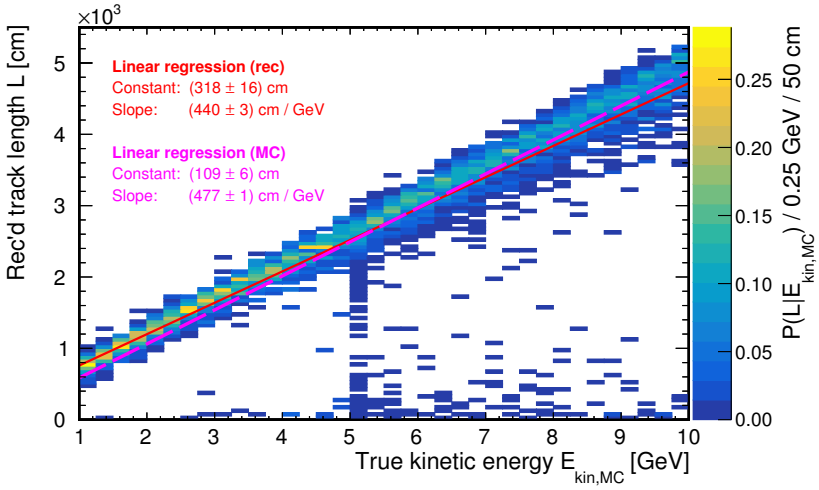

Figure 7.12 – Binned relative frequency distributions $P(\hat{L}|E_{\mathrm{kin,MC}})$ as a function of the true kinetic energy $E_{\mathrm{kin,MC}}$ in the range from 1 to 10 GeV. The distributions were created from the sample of simulated muons shown on the left of Figure 7.1. The *red* line illustrates the result from a linear regression performed with the underlying data. It can be compared to the *dashed magenta* line showing the outcome from a linear regression with the MC truth data L_{MC} (for better comparison the constant was not fixed).

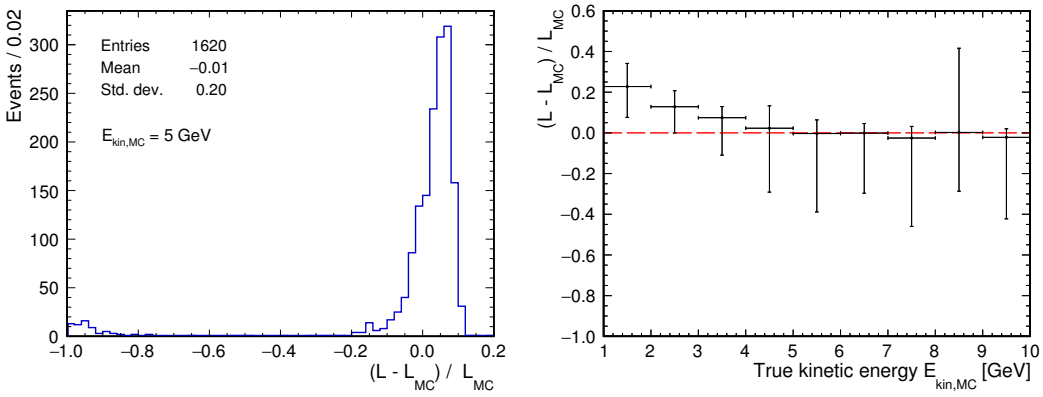

Figure 7.13 – **Left:** Distribution of the normalized track length deviation $(\hat{L} - L_{\mathrm{MC}})/L_{\mathrm{MC}}$ for the high-statistics muon sample at $E_{\mathrm{kin,MC}} = 5$ GeV true kinetic energy. **Right:** Normalized track length deviation as a function of the true kinetic energy $E_{\mathrm{kin,MC}}$ in the range from 1 to 10 GeV. The vertical error bars indicate the left-sided (downwards) and right-sided (upwards) sample standard deviations with respect to the mean value of an asymmetric distribution like the one shown on the left. A *red dashed line* indicates the goal of a zero normalized track length deviation. An event with $L_{\mathrm{MC}} < 50$ cm in the 2–3 GeV bin was excluded from the sample for this figure as it caused a large sample standard deviation in positive direction. The same effect with a smaller scale can be seen in the 8–9 GeV bin. See text for an explanation.

Figure 7.13 it becomes clear that some of these short track lengths are not features of the event sample but merely the results of failed reconstructions. The left side of the figure shows, as an example, the distribution of the *normalized track length deviation*

$(\hat{L} - L_{\mathrm{MC}})/L_{\mathrm{MC}}$ for the high-statistics muon sample at 5 GeV. While the majority of events creates a peak slightly above the goal of $(\hat{L} - L_{\mathrm{MC}})/L_{\mathrm{MC}} = 0$, some events were indeed reconstructed with $\hat{L} \ll L_{\mathrm{MC}}$ and cluster close to $(\hat{L} - L_{\mathrm{MC}})/L_{\mathrm{MC}} = -1$. To characterize such asymmetric distributions as a function of $E_{\mathrm{kin,MC}}$, the left- and right-sided sample standard deviations were determined with respect to the sample mean. The results are shown on the right of Figure 7.13. Events below 1 GeV were discarded due the issues with the reconstruction of the track direction. For $E_{\mathrm{kin,MC}} \geq 3\,\mathrm{GeV}$, the mean values tend towards the goal of a vanishing normalized track length deviation. However, the large sample standard deviations mostly in negative direction indicate that the cluster of events with low $\hat{L}$ at higher energies in Figure 7.12 mainly originates from misreconstructions.
A possible error case is the breakup of the true event region around the muon track into multiple disconnected blobs, either during the reconstruction or during the analysis (see Section 7.2) of the output data. Since only the blob closest to the reference point was tagged as primary blob, a too short track length is determined. Causes for such errors can be bad reference parameters for the reconstruction or a too high threshold for the selection of the event region. The reconstruction of too long track lengths, especially at lower energies, mostly originates from the significant systematic shift of the reconstructed end point in track direction (see Figure 7.4 and Figure 7.11 right). Both cases of deviation again support the future tasks to investigate the dependence of the reconstruction quality on the reference parameters and to improve the event region selection during the analysis.

7.3.4 Total number of photon emissions / energy resolution

The reconstructed total number of emitted scintillation photons per event, $\hat{N}_{\mathrm{em}}$, was obtained by taking the sum (7.5) over the cells of the reconstruction result $\hat{\Gamma}_{\mathrm{em}}(\mathbf{x})$ in the ROI. Figure 7.14 shows binned relative frequency distributions $P(\hat{N}_{\mathrm{em}}|E_{\mathrm{kin,MC}})$ as a function of the true kinetic energy $E_{\mathrm{kin,MC}}$. As one can see, the high-probability regions per energy bin basically depend linearly on $E_{\mathrm{kin,MC}}$. However, the result from a linear regression reveals a too high light yield of $(2.732 \pm 0.003) \times 10^6\,\mathrm{GeV}^{-1}$ compared to the MC truth of $2 \times 10^6\,\mathrm{GeV}^{-1}$ (see Table 5.3). Moreover, the negative value of $(-2.4 \pm 0.1) \times 10^5$ for the constant suggests a loss of photons. Besides errors during the reconstruction, reasons for this result are:

Improper normalization The current implementation of the reconstruction crudely assumes that all scattered photons are lost for detection (see also Section 6.4.2). Therefore, the *local detection efficiency* $\varepsilon(\mathbf{x})$ is always calculated too low in Equation (6.13). A division by $\varepsilon(\mathbf{x})$ in (6.12) consequently yields too high values for $\hat{\Gamma}_{\mathrm{em}}(\mathbf{x})$. This probably is the main cause for the too high reconstructed light yield.

Non-linear behavior of the local detection efficiency As one can infer from Figure 6.11, $\varepsilon(\mathbf{x})$ is not a linear function of $\mathbf{x}$ inside the detector. Assuming that $\hat{\Gamma}_{\mathrm{det}}(\mathbf{x})$ describes a spatial number density distribution of photon emissions that is spread isotropically around the true event topology, some number densities are weighted with a wrong $\varepsilon(\mathbf{x})$ in the calculation of $\hat{\Gamma}_{\mathrm{em}}(\mathbf{x})$ in (6.12). The non-linearity of $\varepsilon(\mathbf{x})$ finally leads to a non-zero bias in the computation of $\hat{N}_{\mathrm{em}}$.

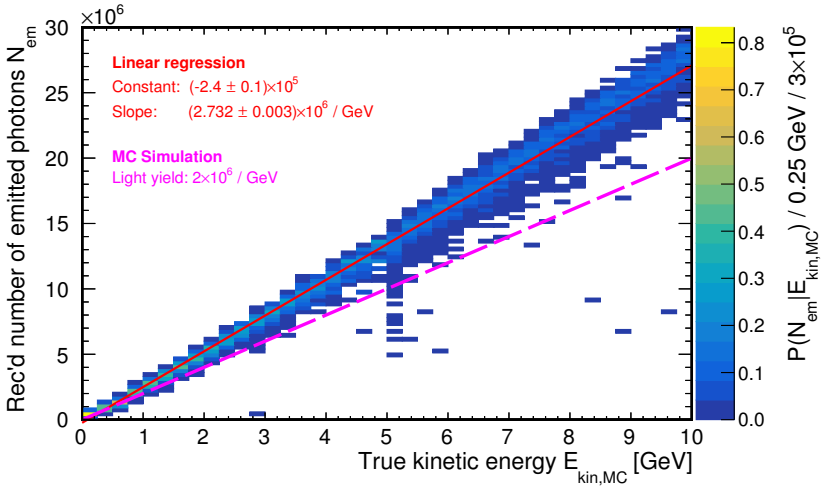

Figure 7.14 – Binned relative frequency distributions $P(\hat{N}_{\mathrm{em}}|E_{\mathrm{kin,MC}})$ as a function of the true kinetic energy $E_{\mathrm{kin,MC}}$. The distributions were created from the sample of simulated muons shown on the left of Figure 7.1. Note that the details at 5 GeV appear as a consequence of the high-statistics sample at this energy. The *red* line illustrates the result from a linear regression performed with the underlying data. It can be compared to the *dashed magenta* line indicating the expected dependence of $\hat{N}_{\mathrm{em}}$ on $E_{\mathrm{kin,MC}}$ as a result of the MC simulation settings (neglects possible muon decays).

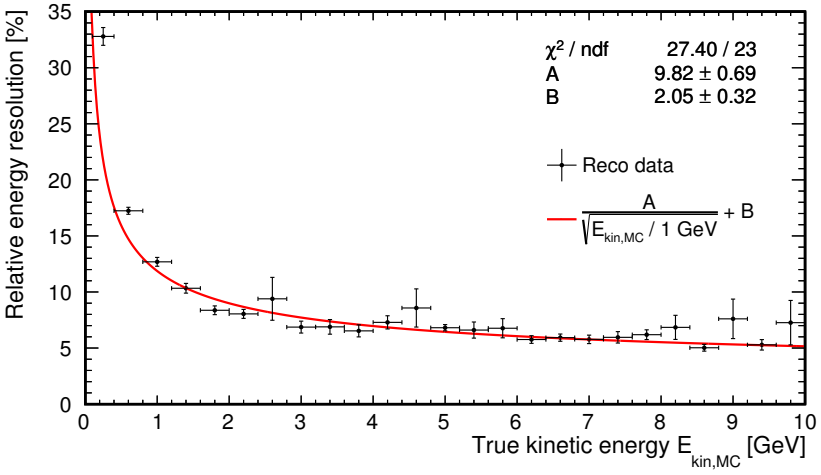

Figure 7.15 – Relative energy resolution from the new reconstruction method as a function of the true kinetic energy of the stopping muons. The resolution was calculated as sample standard deviation over sample mean from the distribution of $\hat{N}_{\mathrm{em}}$ in each energy bin. Gaussian error propagation was used to calculate the uncertainties in the resolution from the errors on the mean and the standard deviation. The latter was estimated from the variance of the unbiased sample variance.

This is the reason why the distribution $\hat{\Gamma}^{*}_{\mathrm{em}}(\mathbf{x})$ from (6.14) should be used to get more precise estimates for $\hat{N}_{\mathrm{em}}$ or $\mathrm{d}E/\,\mathrm{d}x$.

Focus on ROI The computation of $\hat{N}_{\mathrm{em}}$ by taking the sum (7.5) solely over the

ROI discards a non-zero amount of photons distributed in other regions of the detector.

Muon decay Additional photons are created as a result of a muon decay in the detector. Due to their large delay, the detected ones are treated like scattered photons in the reconstruction. Their contribution is spread over the entire LSc volume and largely depends on $P_{\mathrm{det},j}(\mathbf{x})$ in Equation (6.7).

True energy loss Secondary particles, e.g., γ-rays, can leave the LSc-filled volume and do not deposit their entire energy inside the target region. Consequently, the total number of photon emissions is reduced compared to the expectation.

The latter point can also explain the distant outliers in Figure 7.14 at larger energies as well as the tails to lower values of $\hat{N}_{\mathrm{em}}$ for a given energy $E_{\mathrm{kin,MC}}$. It was checked if there is also a visible correlation between the volume integral over the cells traversed by the reconstructed track line (the sum (7.5) runs only over cells from the reconstructed topology $\hat{T}$) and the true kinetic energy. Although the outcome looks promising, it is currently inferior to the results from the total volume integral. This is due to the too imprecise reconstruction of the primary blob, especially of its length.
Taking the non-Gaussian tails to lower values of $\hat{N}_{\mathrm{em}}$ into account, an estimate for the *relative energy resolution* $\sigma_{\hat{E}}/E$ (see also Section 3.4) was calculated from the distribution of $\hat{N}_{\mathrm{em}}$ per energy bin as sample standard deviation over sample mean value. The results for different energy ranges are shown in Figure 7.15. As one can see from the fit, the relative energy resolution for the stopping muons in the kinetic energy range from 0.1 to 10 GeV can be roughly described by

$$\frac{\sigma_{\hat{E}}}{E} \approx \frac{A}{\sqrt{E_{\mathrm{kin,MC}}/1\,\mathrm{GeV}}} + B = \frac{(9.8 \pm 0.7)\%}{\sqrt{E_{\mathrm{kin,MC}}/1\,\mathrm{GeV}}} + (2.0 \pm 0.3)\%\,. \tag{7.16}$$

Note that this result does not make use of the full potential of the new reconstruction approach.

7.4 Outlook

As mentioned before, the analysis procedure described in Section 7.2 does not exploit the full potential to extract valuable information on an event from the reconstructed distribution $\hat{\Gamma}_{\mathrm{em}}(\mathbf{x})$. This section gives a brief overview on some requirements and possibilities to improve and to expand the analysis of the 3D data in the future.
One important task is an improvement of the current event region selection procedure. Especially the results for the mean shift of the reconstructed end point on the right of Figure 7.11 indicate that this basic part of the analysis has strong effects on the outcomes and is a potential source for systematic errors. The possibility to define meaningful absolute threshold values for $\hat{\Gamma}_{\mathrm{em}}(\mathbf{x})$, thanks to a proper normalization, will surely be of help. Nevertheless, the situation remains complicated if one wants to handle events with disconnected event regions from objects with different characteristics, e.g., a spread out energy deposition from a particle shower in addition to a well localized energy deposition along a muon track.
An analysis of the reconstruction result at different threshold values for the event

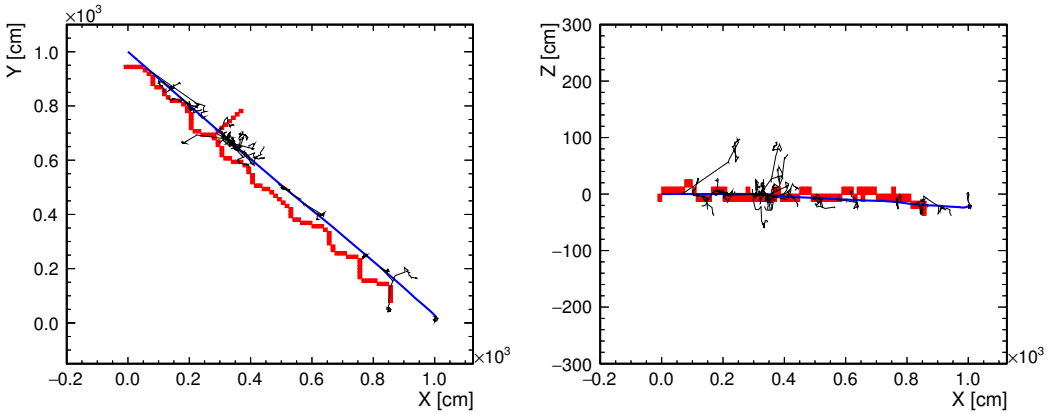

Figure 7.16 – Projection of the *medial line* (*red*) from the event underlying Figure 6.8 along the z-axis **(*left*)** or y-axis **(*right*)** of LENA. The true muon track (*blue*) is depicted together with secondary particle tracks (*black*).

region selection enables the identification and classification of secondary objects essentially overlaying the main object. Consider again the muon track with one or more additional (small) showers as example. As mentioned in Section 7.2, this would open up new ways to study and to efficiently veto cosmogenic radioisotopes in LSc detectors. Moreover, a disentanglement of overlying objects and their individual characterization, e.g., in terms of deposited energy, would give more power to experiments based on HE neutrino interactions in LSc. For example, a better discrimination of neutrino event types based on more detailed information on the event topologies would surely be of help for the LBNO experiment with a multi-GeV neutrino beam to LENA studied in Chapter 8.

Lastly, it has been tried in the context of this work to improve the muon analysis by abandoning the straight-track-assumption in Section 7.2 in favor of a more complex model for the reconstructed event topology $\hat{T}$. The latter is required to build the distribution $\hat{\Gamma}^{*}_{\mathrm{em}}(\mathbf{x})$ according to (6.14), which is an important prerequisite for a good estimate of the differential energy loss $\mathrm{d}E/\,\mathrm{d}x$. Driven by the approximative assumption that the reconstructed distribution $\hat{\Gamma}_{\mathrm{em}}(\mathbf{x})$ follows from the true distribution $\Gamma_{\mathrm{em}}(\mathbf{x})$ by isotropically smearing the true information, it was tested if the *medial line* of the extended primary blob in $\hat{\Gamma}_{\mathrm{em}}(\mathbf{x})$ is a good estimate for $\hat{T}$. The medial line of an object can be defined in 3D Euclidean space as the locus of the centerpoints of fully contained spheres that are tangent to at least two points of the object's surface (see Ref. [225]). It can be used in 3D image processing to simplify the handling of complex objects, e.g., blood vessels in medical images [226]. Figure 7.16 shows, as an example, the medial line cells extracted from the binarized primary blob of the event shown in Figure 6.8. For the extraction, an *iterative thinning algorithm with six sub-iterations* [227] was combined with *iteration-by-iteration smoothing* [228] of the 3D binary image. One can see that the extracted cells produce features that are not present in the true topology and have an offset with respect to the simulated muon track. However, it turned out that the medial line result from the above algorithm is sensitive to the binning of the binarized primary blob and to the configuration of the six sub-iterations. Therefore, combined with the information discarded by the binarization of the primary blob, there is potential to improve the approach.

Chapter 8

An LBNO Experiment with LENA

One of the tasks of the European design study LAGUNA-LBNO was the detailed survey of options for an LBNO experiment from CERN to a site and detector type investigated by LAGUNA (see Appendix C). Primary goals of such an experiment are the determination of the neutrino MO and a measurement of δ_{CP}. Among the different possibilities, the *CERN-to-Pyhäsalmi* (CN2PY) option was intensely discussed [72, 229, 230]. Starting at CERN in *Switzerland / France*, a conventional on-axis neutrino or antineutrino beam to *Pyhäsalmi* in *Finland* would cover a distance of ∼2300 km. Such a long baseline would by far exceed everything that has been realized before in beam-based oscillation experiments. In particular, it would surpass the ∼1300 km baseline that is planned for the *Deep Underground Neutrino Experiment* (DUNE)[1] in the *United States of America*, which has equal research goals. Both LAGUNA-LBNO and DUNE favor a LAr TPC with tens of kilotons of target mass as far-detector, but aimed for different implementations[2] of the technology.
For the European neutrino observatory, LENA was considered as (additional) device for the detection of terrestrial and astrophysical LE neutrinos and antineutrinos. Due to the possible availability of a multi-GeV neutrino beam, it was quite natural to investigate the potential of LENA to contribute measurements regarding leptonic CP-violation and especially of the neutrino MO. However, it must be clearly stated that the broad LE neutrino physics program of LENA at Pyhäsalmi (see Section 4.2.2) would make this detector alone a valuable enrichment for neutrino-related sciences, even in the absence of a neutrino beam.

A way to resolve the neutrino MO by looking at the disappearance of reactor $\overline{\nu}_e$'s was already outlined in the context of JUNO in Section 4.3.2. The method bases on a precise measurement of a fine structure in the oscillated $\overline{\nu}_e$ event energy spectrum. Due to the medium baseline length of some tens of kilometers, the observed neutrino flavor oscillations are essentially free of matter effects.

[1] Formerly *Long-Baseline Neutrino Experiment* (LBNE).
[2] DUNE aims for a single-phase TPC with LAr only. The LAGUNA option, which bases on the *Giant Liquid Argon Charge Imaging Experiment* (GLACIER) design [231], prefers a double-phase TPC containing argon as liquid and vapor.

The approach to determine the neutrino MO and to measure δ_{CP} in a conventional, beam-based LBNO experiment is different. Primary source of information in this case is the appearance of ν_e's ($\overline{\nu}_e$'s) in the beam of mainly ν_μ's ($\overline{\nu}_\mu$'s). Both the effects from the neutrino MO, i.e., the sign of Δm^2_{31}, and a CP-violating value for δ_{CP} become manifest in differences between the appearance probabilities $P_{\mu e}$ and $P_{\bar{\mu}\bar{e}}$. Assuming a constant matter density profile, an approximative analytical expression [232] for $P_{\mu e}$ ($P_{\bar{\mu}\bar{e}}$) as a function of the neutrino energy E and the baseline length L is given by

$$
\begin{aligned}
P_{\mu e} \simeq & \underbrace{\sin^2\theta_{23}\,\sin^2 2\theta_{13}\,\frac{\sin^2\left[(1-\hat{A})\Delta\right]}{(1-\hat{A})^2}}_{C_0} + \underbrace{\alpha^2\,\cos^2\theta_{23}\,\sin^2 2\theta_{12}\frac{\sin^2(\hat{A}\Delta)}{\hat{A}^2}}_{C_1} \\
& \underbrace{\mp\,\alpha\,\sin 2\theta_{13}\,\cos\theta_{13}\,\sin 2\theta_{12}\,\sin 2\theta_{23}\,\sin(\Delta)\,\frac{\sin(\hat{A}\Delta)}{\hat{A}}\,\frac{\sin\left[(1-\hat{A})\Delta\right]}{(1-\hat{A})}}_{C_-}\,\sin\delta_{\mathrm{CP}} \\
& \underbrace{+\,\alpha\,\sin 2\theta_{13}\,\cos\theta_{13}\,\sin 2\theta_{12}\,\sin 2\theta_{23}\,\cos(\Delta)\,\frac{\sin(\hat{A}\Delta)}{\hat{A}}\,\frac{\sin\left[(1-\hat{A})\Delta\right]}{(1-\hat{A})}}_{C_+}\,\cos\delta_{\mathrm{CP}}\,,
\end{aligned}
\tag{8.1}
$$

with

$$
\Delta \equiv \frac{\Delta m^2_{31} L}{4E}\,, \quad \hat{A} \equiv \frac{A}{\Delta m^2_{31}}\,, \quad A = \pm 2\sqrt{2}\,G_F\,n_e\,E\,.
$$

The approximation is up to the second order in the small quantities $\alpha \equiv \Delta m^2_{21}/\Delta m^2_{31}$ and θ_{13}. The upper (lower) sign of the matter potential A and the term C_- corresponds to neutrinos (antineutrinos). Term C_0 is most sensitive to matter effects. Therefore, it can be used to determine the sign of Δm^2_{31}. CP-violation is introduced through the term C_- if $\delta_{\mathrm{CP}} \neq 0,\, \pi$. This is due to its different contributions to $P_{\mu e}$ and $P_{\bar{\mu}\bar{e}}$. Despite its dependence on $\cos\delta_{\mathrm{CP}}$, the term C_+ is CP-conserving as its contribution is equal for neutrinos and antineutrinos.

This chapter deals with the performance of LENA in the LBNO experiment from CERN to Pyhäsalmi. It is mainly focused on the neutrino MO discovery potential and only briefly covers the sensitivity to leptonic CP-violation. The underlying oscillation study assumed the *standard three-flavor paradigm*. It was performed with the `C`-based *General Long Baseline Experiment Simulator* (`GLoBES`) package [233,234]. Earlier results of this study were included into the final, unpublished LAGUNA-LBNO documents.
Section 8.1 details the experimental setup that was assumed in the oscillation analysis. The description of an *"average experiment"*, which is fundamental to the calculations of `GLoBES`, is subject of Section 8.2. Both the analysis procedure in connection with `GLoBES` and the statistical framework for this study are summarized in Section 8.3. Finally, the obtained results for the sensitivities to the neutrino MO and leptonic CP-violation are presented in Section 8.4 and Section 8.5, respectively.

8.1 Experimental setup

A complete description of an experimental setup in the context of a `GLoBES`-based oscillation analysis includes information on the neutrino / antineutrino source, a set of oscillation parameter values for the simulated flavor oscillation along the baseline and a parameterization of the detector. Section 8.1.1 details the assumptions for the performance parameters and neutrino energy spectra of the CN2PY beam. The presumed "true" oscillation parameters and a model for the baseline's mass density profile are subject of Section 8.1.2 and Section 8.1.3, respectively. Aspects that are relevant to describe LENA in `GLoBES` are treated in Section 8.1.4.

8.1.1 Neutrino / antineutrino source

The neutrino / antineutrino source for the considered LBNO experiment with LENA from CERN to Pyhäsalmi is a conventional on-axis ν_μ / $\overline{\nu}_\mu$ WBB (see Section 2.6), which was already studied in Refs. [72, 229, 230]. In its lowest configuration level, the beam is produced with 400 GeV protons from an upgraded version of the CERN SPS accelerator, providing a nominal beam power of ∼750 kW. This is almost 50 % more compared to the CNGS beam (see Table 2.2). A possible upgrade could be a new *high-power proton synchrotron* (HP-PS) that reaches a nominal beam power of 2 MW with 50 GeV protons.
The neutrino beam setups assumed in this work are described by the parameters listed in Table 8.1. It was further presumed that the beam facility would run almost exclusively for the CN2PY beam, delivering the full 1.4×10^{20} (2.9×10^{21}) POT per year. A total number of 1.4×10^{21} POT at 400 GeV was considered for the *default setup*, equating to 10 (3.75) years of running with the SPS (HP-PS) beam option. The distribution of the total runtime between neutrino (PHF) and antineutrino (NHF) mode was defined to be 50 %–50 %.

The flux spectra describing the energy distributions of the neutrinos and antineutrinos in PHF and NHF mode are shown in Figure 8.1. They were used for the SPS as well as the HP-PS beam, neglecting the question if matching flux spectrum shapes

Table 8.1 – List of SPS and HP-PS neutrino beam parameters. The stated proton energies E_{beam}, beam intensities I_{beam} in *protons per pulse* and cycle times, i.e., the time between proton pulses, result in the stated estimates for the beam powers P_{beam}. As in Ref. [229], the given ranges of POT per year assume 200 days effective runtime at 80 % global accelerator efficiency and a factor ϵ_{share} between 60 % and 85 % due to proton beam sharing with other facilities. Data for E_{beam}, I_{beam} and cycle times are cited from Ref. [229].

Parameter	SPS beam	HP-PS beam
E_{beam} [GeV]	400	50
I_{beam} [ppp]	7×10^{13}	2.5×10^{14}
Cycle time [s]	6	1
P_{beam} [MW]	0.748	2
POT / year [10^{21}]	0.10–0.14	2.1–2.9

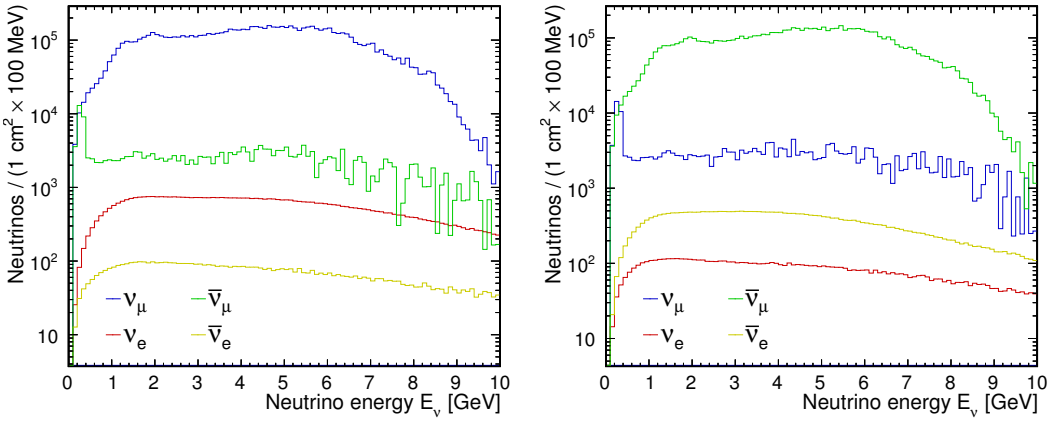

Figure 8.1 – Unoscillated neutrino and antineutrino flux spectra at 2288 km distance from the beam source in PHF **(left)** and NHF **(right)** mode. The normalizations correspond to 0.375×10^{21} (3×10^{21}) POT at 400 GeV (50 GeV) proton energy. Data from Ref. [236].

from 50 GeV and 400 GeV proton beams could be obtained at all. The employed spectra resulted from simulations [235, 236] of a WBB that is produced with 50 GeV protons and was optimized for maximal sensitivity to $\sin^2 2\theta_{13}$.[3] Since the provided spectra contain only data up to 10 GeV in neutrino energy, the number of NC and ν_τ / $\overline{\nu}_\tau$ CC events from the HE tails migrating into the energy range of interest (see Section 8.2.3) was slightly underestimated. In order to model the SPS beam, the original POT normalization of the spectra was divided by eight. It is stated in Ref. [72] that the neutrino yield below 10 GeV neutrino energy scales well with the incident power. Therefore, the assumption that one 400 GeV proton equals eight 50 GeV protons is justified.

8.1.2 Neutrino flavor oscillation parameters

The neutrino propagation from the beam source at CERN to the detector location in Pyhäsalmi depends on the mass density distribution along the baseline (see Section 8.1.3) and the neutrino flavor oscillation parameters in vacuum. Based on this parameterization, `GLoBES` automatically calculates the effective mixing angles and mass-squared differences in matter. The *true oscillation parameters*, i.e., the parameters that are assumed to be realized in Nature, are given by the *central values* in Table 8.2. Since δ_{CP} is unknown, its true value was varied in the interval $[0°, 360°]$ during the analysis. Moreover, Table 8.2 lists conservative 1σ uncertainties for some of the parameters. These *input errors* represent the assumed external information on the oscillation parameters, e.g., from other experiments. Therefore, an input error together with its central value functions as *prior* during the analysis (see Section 8.3.2).

[3] New spectra, which were optimized for maximal sensitivity of GLACIER to the neutrino MO and leptonic CP-violation, emerged from studies in the context of LAGUNA-LBNO (see Refs. [229, 230]). The improved beam spectra have increased fluxes at the first and second oscillation maxima, but also exhibit stronger HE tails beyond the energy region of interest.

Table 8.2 – Neutrino oscillation parameters used in the sensitivity study. The central values are the assumed true values, i.e., the parameters that are realized in Nature. In addition, the central values together with the absolute / relative 1σ errors represent external information on the oscillation parameters, e.g., from other measurements. Parameters without errors were kept fixed during the parameter fitting. The true value of δ_{CP} varied during the study; as a fit parameter it was left completely free. In general, the central values base on the global analysis results presented in Table 1.2. However, the central value of θ_{23} was set to be the mean value of the two hierarchy-dependent solutions in Table 1.2. All errors were chosen conservatively. In the case of θ_{23} it covered the solutions in both octants.

Parameter	Central value	Abs. error	Rel. error
θ_{12} [°]	33.48	—	—
θ_{13} [°]	8.5	±0.43	±5 %
θ_{23} [°]	45.9	±4.59	±10 %
Δm^2_{21} [$10^{-5}\,\mathrm{eV}^2$]	7.5	—	—
Δm^2_{31} [$10^{-3}\,\mathrm{eV}^2$] (NO)	2.457	±0.123	±5 %
Δm^2_{31} [$10^{-3}\,\mathrm{eV}^2$] (IO)	-2.374	±0.119	±5 %
δ_{CP} [°]	varied	∞	∞

Based on the parameters in Table 8.2, the appearance probabilities $P_{\mu e}$ and $P_{\bar{\mu}\bar{e}}$ for the CN2PY baseline are illustrated in Figure 8.2. They are shown as a function of the true neutrino (antineutrino) energy for both neutrino MO possibilities. For true NO, one can clearly see that $P_{\mu e}$ at the maximum around 3–4 GeV is larger than the corresponding $P_{\bar{\mu}\bar{e}}$ for any value of δ_{CP}; the opposite holds for true IO. The large separation of the probability bands is the result of the long CN2PY baseline and reflects the power to discriminate the MO possibilities. Leptonic CP-violation is measured if the probabilities $P_{\mu e}$ and $P_{\bar{\mu}\bar{e}}$ are found in the colored bands in Figure 8.2, but are different from the curves for $\delta_{\mathrm{CP}} = 0°$ (*solid lines*) and $\delta_{\mathrm{CP}} = 180°$ (*dashed lines*). Figure 8.3 shows the survival probabilities $P_{\mu\mu}$ and $P_{\bar{\mu}\bar{\mu}}$, which are essentially independent of the MO and less dependent on δ_{CP} than the appearance probabilities.

8.1.3 Baseline

The baseline for the LBNO experiment from CERN in *Switzerland / France* to the Pyhäsalmi mine in *Finland* is 2288 km long. A model for the mass density distribution along the CN2PY baseline was built from information in Ref. [237]: As one can see on the left of Figure 8.4, the total baseline length was divided in ten, not equally long steps. Each step corresponded to a constant matter density with a value between 2.5 and 3.37 g/cm^3. The average matter density was ∼3.23 g/cm^3. For comparison, the average from the *Preliminary Reference Earth Model* (PREM) [238, 239], which is integrated into `GLoBES`, is ∼3.22 g/cm^3 for a 2288 km long step. The right side of Figure 8.4 shows a comparison between the appearance probabilities $P_{\mu e}$ for the used CN2PY density profile model and different constant matter densities. One can see that the actually used model had a slightly increased appearance probability around

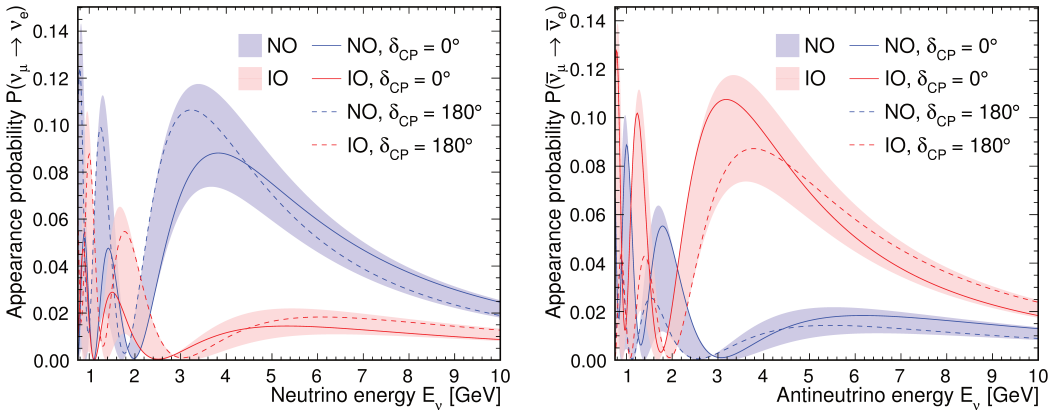

Figure 8.2 – Appearance probabilities $P_{\mu e}$ **(left)** and $P_{\bar{\mu}\bar{e}}$ **(right)** for the 2288 km long CN2PY baseline as a function of the neutrino (antineutrino) energy. The widths of the probability bands for true NO (*blue*) or true IO (*red*) indicate the variance due to the true value of δ_{CP} from $[0°, 360°)$. The oscillation parameters are from Table 8.2.

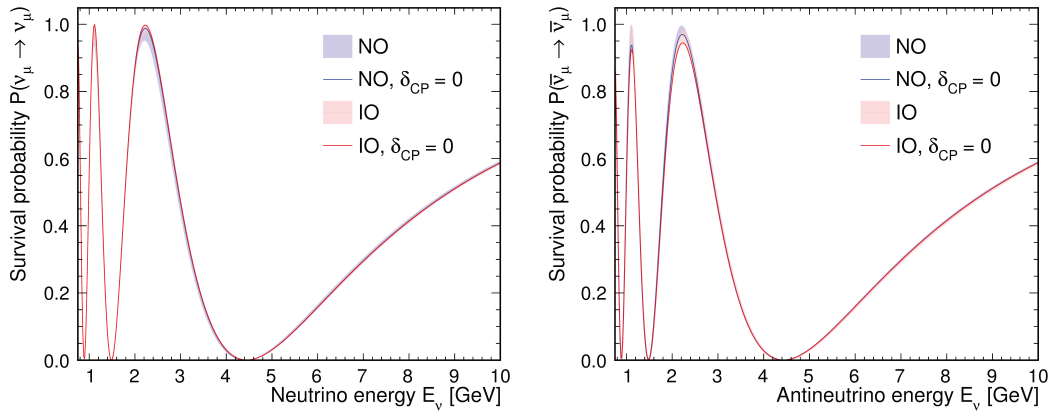

Figure 8.3 – Same as Figure 8.2 but for the survival probabilities $P_{\mu\mu}$ **(left)** and $P_{\bar{\mu}\bar{\mu}}$ **(right)**.

the first oscillation maximum. A global 1σ scaling uncertainty of 4 % was assumed for the mass density in the analysis with `GLoBES`. Compared to the average model uncertainty of ∼2 % from the eight density steps with errors on the left of Figure 8.4, this was conservative and took into account the unknown uncertainties for the two longest steps of the model.

8.1.4 Detector

In the context of this study, the LENA detector was modeled in terms of three relevant aspects: Firstly, the flavor-dependent CC and NC *cross-sections* for neutrinos and antineutrinos together with the number of available *interaction targets* were decisive for estimating the event counts of the different signals and backgrounds. Secondly, in view of the calorimetric energy measurement approach of LSc detectors, efficiencies for selecting *fully-contained events* needed to be considered. Thirdly, the *event energy*

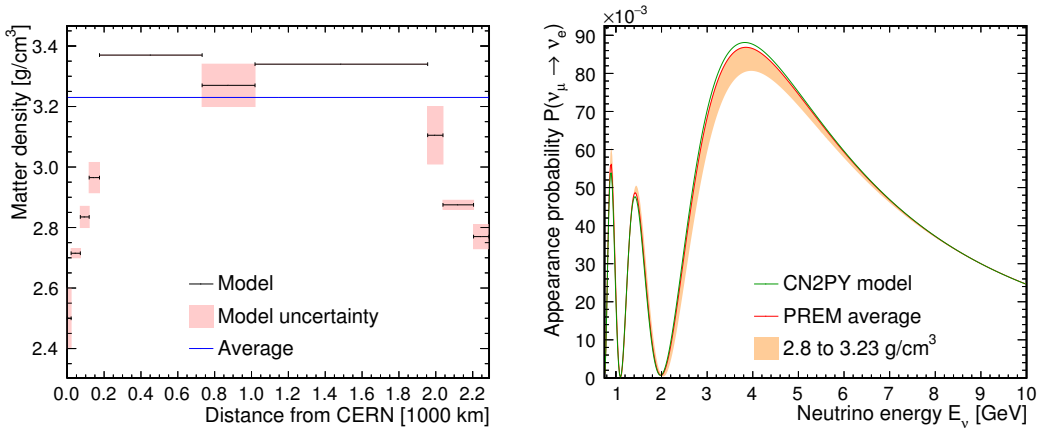

Figure 8.4 – **Left:** Model for the matter density profile of the 2288 km long CN2PY baseline (*black*) that was used in GLoBES. The model data are from Ref. [237]. If the data provided a range of density values for one step, the mean value was used. The upper and lower values of density ranges are shown as model uncertainies (*light red*), but did not go into the study. The average matter density (*blue*) of $\sim$3.23 g/cm^3 is also shown. **Right:** Appearance probability $P_{\mu e}$ in the case of true NO and $\delta_{\mathrm{CP}} = 0°$ for different mass density profiles. The oscillation parameters are from Table 8.2. The CN2PY model (*green*) with ten density steps is compared with constant density distributions in the range from 2.8 to 3.23 g/cm^3 (*orange band*). The average value of 3.22 g/cm^3 from the PREM is highlighted (*red*).

reconstruction was modeled with *energy migration matrices*, which described the translation of the true neutrino energy to the reconstructed energy used in the final analysis.

Interaction targets and cross-sections The primary targets for the interactions of the multi-GeV neutrinos and antineutrinos from the beam are the nuclei, nucleons and quarks of the carbon and hydrogen atoms constituting the LSc. It was assumed that the LSc of LENA is pure LAB made of molecules with 18 ^{12}C and 30 ^{1}H atoms. This totals 246 nucleons per molecule. For practical reasons, a neutrino / antineutrino interaction target was redefined within the scope of this study to be a whole LAB molecule. Considering only interactions with the designated target material, the 50 kt LAB of LENA correspond to $\sim 1.25 \times 10^{32}$ single molecular targets. This assumes a molecular weight of 241 g/mol [40].

The GENIE[4] event generator framework with default settings was used to determine the cross-sections for neutrinos and antineutrinos. This was done despite discrepancies between current MC neutrino event generators and up-to-date cross-section measurements (see Section 1.2.2). However, the obtained results are considered to be sufficiently accurate in the view of the overall precision of this GLoBES sensitivity study. Flavor- and energy-dependent CC and NC cross-sections for interactions on ^{12}C and ^{1}H were calculated in the energy range from 0.1 to 10 GeV. The outcomes were weighted and combined to form the total effective cross-section for $C_{18}H_{30}$.

[4]Version 2.6.6

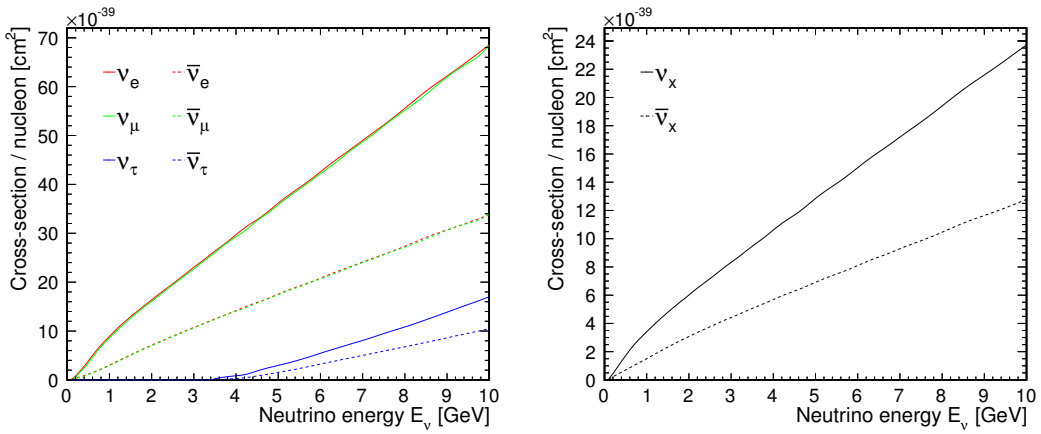

Figure 8.5 – Effective, energy-dependent CC **(left)** and NC **(right)** cross-sections per nucleon for neutrino ν_x (*solid*) and antineutrino $\overline{\nu}_x$ (*dashed*) interactions on $C_{18}H_{30}$ as computed with `GENIE`. The CC cross-sections are for the flavors $x = e$ (*red*), μ (*green*) and τ (*blue*).

Figure 8.5 shows the corresponding effective CC and NC cross-sections per nucleon.

Event containment and event energy reconstruction A precisely reconstructed and flavor-resolved energy spectrum of neutrino and antineutrino interaction events is an important prerequisite for a flavor oscillation analysis with maximum significance. Since a LSc detector measures the neutrino energy E_ν from the energy depositions of charged interaction products, this requires a rejection of event topologies that do not have the deposited energy fully contained inside the active target volume. Such *semi-contained events*, where energy escapes detection in the form of charged and neutral particles, distort the reconstructed energy spectrum. Note that this naturally makes a NC interaction semi-contained, due to the outgoing neutrino. In principle, the same is true for events where neutrinos or antineutrinos can be produced in charged lepton decays , e.g., in ν_τ / $\overline{\nu}_\tau$ and ν_μ / $\overline{\nu}_\mu$ CC interactions. However, the containment status of a neutrino interaction can only be determined from the energy depositions of charged particles. Therefore, the above-mentioned cases may still be identified as fully-contained events if no hints for *missing energy / momentum* were found.[5]

In the `GLoBES` analysis, the loss of statistics from using only events that were accepted as fully contained was implemented with so-called *pre-smearing efficiencies*. They were applied to the neutrino and antineutrino event spectra as a function of the true neutrino energy E_ν, i.e., before the spectra were smeared to obtain the spectra in terms of the reconstructed energy $\hat{E}_{\text{rec}}$. The *energy-dependent containment efficiencies* are shown in Figure 8.6. They were determined in an ancillary study (see Appendix D) with the MC truth information of 5×10^6 simulated neutrino events per interaction type: The cylindrical target volume of LENA was divided into an

[5] An advanced version of the reconstruction from Chapter 6 could provide information to the algorithm that determines an event's containment status.

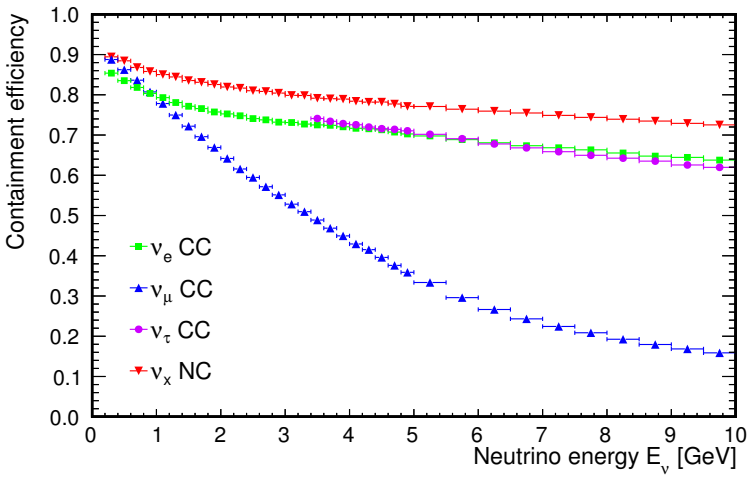

Figure 8.6 – Fractions of ν_e CC (*green square*), ν_μ CC (*blue triangle with tip up*), ν_τ CC (*violet circle*) and NC (*red triangle with tip down*) events that were selected as fully contained as a function of the true neutrino energy E_ν. The binning of E_ν is roughly adjusted to the energy resolution of LENA. Details on the determination of the *containment efficiencies* can be found in Appendix D.1.

inner FV and a surrounding, 50 cm thick *decision region*. An event was rejected as semi-contained if its estimated energy loss to the LSc in the decision region exceeded 75 MeV or 2 % of the energy loss in the FV. In a strict sense, these decision criteria do not aim for an exclusive selection of fully-contained events. The reason is outlined in Appendix D.1.
As expected, the fraction of ν_μ CC events that is selected as fully contained strongly decreases with rising E_ν. This is a result of the almost linearly growing muon track length. NC events always have higher containment efficiencies than ν_e CC interactions because only a fraction of E_ν is available to produce extensive topologies of charged particle tracks and showers.
The consideration of energy-dependent selection efficiencies for fully-contained neutrino events in this study is new compared to former studies for LENA (e.g., see Ref. [240]). Nevertheless, the aspect of event containment and its now discussed connection with the neutrino energy reconstruction needs more investigation once the required reconstruction algorithms are available.

The energy information entering the oscillation analysis is not the true neutrino energy E_ν. Instead, it is a value $\hat{E}_{\mathrm{rec}}$, which is the sum of the *total visible energy estimate* $\hat{E}_{\mathrm{vis}}$ and an estimate for the invisible energy leakage $\hat{E}_{\mathrm{inv}}$ (see also Section 3.4). However, without a (partial) recovery of missing energy, e.g., for semi-contained events, $\hat{E}_{\mathrm{rec}} \equiv \hat{E}_{\mathrm{vis}}$ holds. The visible energy estimate for an event bases on the actual observables, i.e., the PE distribution at the PMTs. Due to the spatial dependence of the PE yield from an energy deposition, the accurate determination of $\hat{E}_{\mathrm{vis}}$ requires knowledge on the event position and topology. Uncertainties from the reconstruction and random fluctuations in the PE yield limit the resolution of the *true visible energy* E_{vis}. In the analysis, both an energy leakage and a limited energy resolution had to be respected when E_ν was translated to $\hat{E}_{\mathrm{rec}}$. This was done with tabulated probability

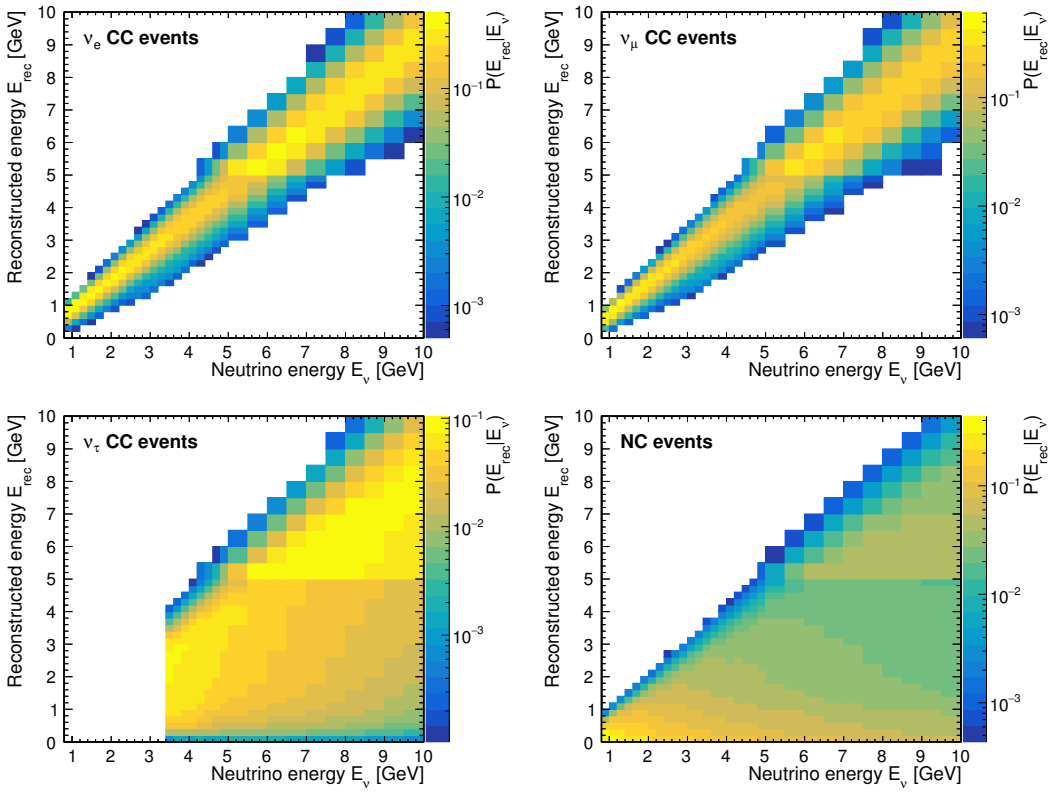

Figure 8.7 – Energy migration matrices for ν_e CC **(top left)**, ν_μ CC **(top right)**, ν_τ CC **(bottom left)** and NC **(bottom right)** events in LENA. Only events that were selected as fully contained were used during the matrix generation. No recovery of missing energy was assumed. A relative Gaussian energy resolution of 7 % is included in the matrices. Note the change of binning from 200 MeV bins to 500 MeV bins at 5 GeV. Details on the matrix computation can be found in Appendix D.2.

distributions $P(\hat{E}_{\text{rec}}|E_\nu)$ as functions of E_ν, so-called *energy migration matrices*. Figure 8.7 shows matrices that were used for both neutrinos and antineutrinos. They were generated from results of the above-mentioned study to obtain the containment efficiencies (for details see Appendix D.2). The matrices contain only the information from events that were selected as fully contained and do not take a recovery of missing energy into account. Recalling $\hat{E}_{\text{rec}} \equiv \hat{E}_{\text{vis}}$, a *relative Gaussian energy resolution* of $\sigma_{\hat{E}_{\text{rec}}}/E_{\text{vis}} = 7\,\%$ was included during the matrix generation.[6]
The ν_τ CC and NC matrices exhibit strong migration to a wide range of lower $\hat{E}_{\text{rec}}$ values for a given E_ν. This is due to significant amounts of energy that are carried away by one or more outgoing neutrinos.

[6] Using the assumption of a point-like event at the reconstructed charge barycenter for a simple energy reconstruction algorithm, a relative energy resolution of 9 % was found in Ref. [51] for multi-GeV ν_e CC events in LENA. However, the non-Gaussian resolution was dominated by outliers; the Gaussian contribution was 5.6 % [241].

8.2 An average experiment

As detailed in Section 8.3, a neutrino flavor oscillation analysis with `GLoBES` is done by comparing a simulated experimental outcome from a set of "true" oscillation parameters with the data expected from hypothetic sets of parameters. In reality, the detection of neutrino interactions is a stochastic process; the resulting event count spectra are subject to random fluctuations. `GLoBES`, however, does not employ MC techniques to simulate the observed data. Instead, ensembles of MC-generated event count distributions for the considered signal and background channels are replaced by a single, deterministically calculated representation without statistical fluctuations—the *Asimov data set* [242]. Therefore, `GLoBES` consequently returns the same result for the same input. Assuming the input data are average values for the beam fluxes, cross-sections, etc., the calculated event spectra can be seen as the outcome of an *average experiment*.
The previous section described the basic input to calculate event count distributions in `GLoBES`. This section deals with the construction of Asimov data sets for the final analysis in Section 8.3. *Signal* and *background channels* that are relevant in this sensitivity study are described in Section 8.2.1. Subsequently, Section 8.2.2 summarizes the default values assumed for the *signal and background event selection efficiencies*, which are essential to build specific Asimov data sets for different oscillation searches. Examples for such data sets are provided in Section 8.2.3, together with raw event rates as performance measures.

8.2.1 Signal and backgrounds

As shown by Figure 8.2 and Figure 8.3, the information on the true neutrino MO and leptonic CP-violation is primarily contained in the oscillatory transition $\nu_\mu \to \nu_e$ ($\overline{\nu}_\mu \to \overline{\nu}_e$) of the main flux component of the conventional ν_μ ($\overline{\nu}_\mu$) beam. In addition to this ν_e ($\overline{\nu}_e$) *appearance search*, the investigation of ν_μ ($\overline{\nu}_\mu$) *disappearance* allows to constrain the atmospheric oscillation parameters during the final fit. The following details the considered signal and background channels in both flavor oscillation cases. Note that only beam-related backgrounds are taken into account. Since the neutrinos and antineutrinos from the beam come in short pulses, a well-defined arrival time window means an effective reduction of uncorrelated background, e.g., from atmospheric neutrinos. Moreover, the incident direction of the beam neutrinos is precisely known. This allows a rejection of events from neutrinos with strongly deviating directions of incident.

$\boldsymbol{\nu_e}$ / $\boldsymbol{\bar{\nu}_e}$ appearance search The signature of a ν_e ($\overline{\nu}_e$) CC interaction is mainly defined by the electromagnetic particle shower initiated from the outgoing primary e^- (e^+). Therefore, the searched-for event signature in the appearance signal channel $\nu_\mu \to \nu_e$ ($\overline{\nu}_\mu \to \overline{\nu}_e$) is referred to as *e-like*. However, an e-like event character is not unique to the appeared ν_e ($\overline{\nu}_e$). Other types of events produce the same or very similar signatures, making them background for the ν_e ($\overline{\nu}_e$) appearance search. The considered background contributions were

- intrinsic beam contamination ($\nu_e \to \nu_e$, $\overline{\nu}_e \to \overline{\nu}_e$),

- ν and $\overline{\nu}$ NC events that mimic an e-like signature, e.g., with π^0-production,
- events from $\overline{\nu}_\mu \to \overline{\nu}_e$ ($\nu_\mu \to \nu_e$) transitions in PHF (NHF) beam mode,
- misidentified $\mu^\mp$ from ν_μ / $\overline{\nu}_\mu$ CC interactions or the muonic decays of $\tau^\mp$ from ν_τ / $\overline{\nu}_\tau$ CC interactions,
- ν_τ and $\overline{\nu}_\tau$ CC interactions where a produced $\tau^\mp$ decays into an $e^\mp$ or hadrons.

It has to be emphasized that LENA cannot distinguish a final-state lepton from the corresponding antilepton. This is especially important for the items one and three.

ν_μ / $\bar{\nu}_\mu$ disappearance search The outgoing primary μ^- (μ^+) with its elongated track dominates the event signature of a ν_μ ($\overline{\nu}_\mu$) CC interaction. Such *μ-like* events are of interest in the studies of the disappearance channels $\nu_\mu \to \nu_\mu$ in PHF mode and $\overline{\nu}_\mu \to \overline{\nu}_\mu$ in NHF mode. Considered background types showing the characteristic features of a μ-like event were

- ν and $\overline{\nu}$ NC events that mimic a μ-like signature,
- CC events from the surviving contamination of the beam with $\overline{\nu}_\mu$ (ν_μ) in PHF (NHF) mode,
- ν_τ and $\overline{\nu}_\tau$ CC interactions where a produced $\tau^\mp$ decays into a $\mu^\mp$ or hadrons.

A background contribution from misidentified ν_e / $\overline{\nu}_e$ CC interactions was neglected.

ν_τ / $\bar{\nu}_\tau$ CC background The backgrounds in the appearance and disappearance studies included contributions from the decays of taus. These charged leptons originate from CC interactions of ν_τ's / $\overline{\nu}_\tau$'s that appeared in $\nu_\mu \to \overline{\nu}_\tau$ and $\overline{\nu}_\mu \to \overline{\nu}_\tau$ flavor transitions. The corresponding appearance probabilities for the CN2PY baseline are shown in Figure 8.8 as a function of the neutrino (antineutrino) energy. A tau has three major decay branches: the *electronic decay*

$$\tau^- \to e^- + \overline{\nu}_e + \nu_\tau\,, \quad \tau^+ \to e^+ + \nu_e + \overline{\nu}_\tau\,, \quad \text{BR} : \sim 17.8\,\%\,, \tag{8.2}$$

the *muonic decay*

$$\tau^- \to \mu^- + \overline{\nu}_\mu + \nu_\tau\,, \quad \tau^+ \to \mu^+ + \nu_\mu + \overline{\nu}_\tau\,, \quad \text{BR} : \sim 17.4\,\%\,, \tag{8.3}$$

and the *hadronic decay*

$$\tau^- \to \nu_\tau + \text{hadrons}\,, \quad \tau^+ \to \overline{\nu}_\tau + \text{hadrons}\,, \quad \text{BR} : \sim 64.8\,\%\,. \tag{8.4}$$

All BRs are from Ref. [11]. For this study it was assumed that

- all electronic decays produce e-like signatures,
- all muonic decays produce μ-like signatures,
- all hadronic decays produce NC-like signatures.

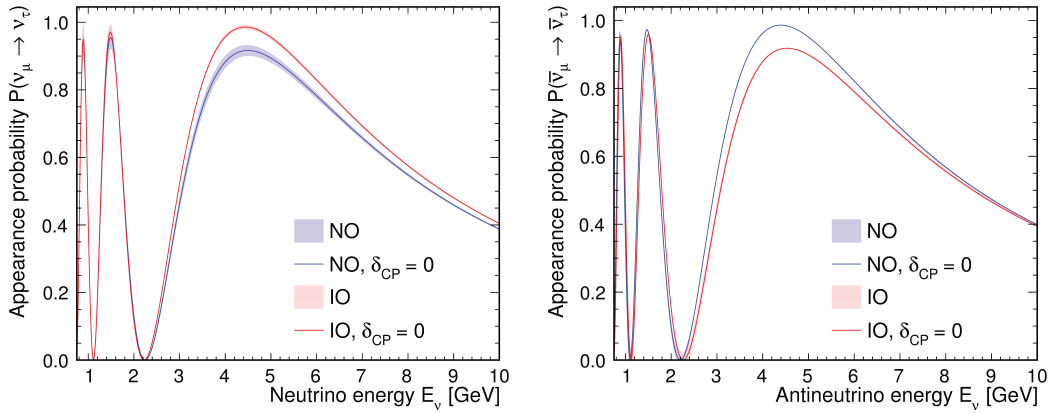

Figure 8.8 – Same as Figure 8.2 but for the appearance probabilities $P_{\mu\tau}$ **(left)** and $P_{\bar{\mu}\bar{\tau}}$ **(right)**.

In general, NC-like signatures may be correctly rejected as background or falsely selected as e-like or μ-like signal. The corresponding selection efficiencies for signals and backgrounds are discussed next.

8.2.2 Signal and background selection efficiencies

Event selection efficiencies define the composition of the specific Asimov data sets in terms of the different signal and background channels. They reflect the goal to maximize the signal to background ratio by sorting out background events, usually at the cost of some wrongly rejected signal events. In this work, a selection efficiency ϵ was defined as the fraction of events in a signal or background channel that entered the oscillation analysis. The selection efficiencies were assumed to be *global*, i.e., independent of the reconstructed event energy. Note that they were applied in addition to the containment efficiencies.
A determination of the selection efficiencies normally includes extensive tuning and testing of dedicated algorithms with MC-based event samples. The potential to discriminate different event categories at multi-GeV neutrino energies has not yet been elaborated for a LSc detector though. Using reliable values for the different signal and background selection efficiencies in this study was difficult under these circumstances. Therefore, the following defaults for the ν_e / $\overline{\nu}_e$ appearance and ν_μ / $\overline{\nu}_\mu$ disappearance searches basically have been (educated) assumptions. Some of them were varied in this study to demonstrate their impact on the experiment's performance. Future event reconstruction algorithms, especially the approach presented in Chapter 6, will surely be of help to discriminate different event types.

ν_e / $\bar{\nu}_e$ appearance search The default selection efficiencies that were assumed for the ν_e ($\overline{\nu}_e$) appearance search discussed in Section 8.2.1 are summarized in Table 8.3. They essentially reflect the goal to minimize NC background, which probably is the most difficult task. Both ν_e / $\overline{\nu}_e$ CC and NC interactions mainly produce event topologies that are characteristic for particle showers. First investigations were done to discriminate these showers based on features of the overall pulse shape observed

Table 8.3 – Default values for the global signal and background selection efficiencies of the ν_e ($\overline{\nu}_e$) appearance search.

Selection efficiency	Parameter	Value
ν_e / $\overline{\nu}_e$ CC events	$\epsilon^{\text{app}}_{\text{eCC}}$	0.27
NC-like events	$\epsilon^{\text{app}}_{\text{NC}}$	0.11
μ-like events	$\epsilon^{\text{app}}_{\mu}$	0.01

Table 8.4 – Input for the ν_e appearance search rule in `GLoBES`. The different signal and background sources were discussed in Section 8.2.1; corresponding selection efficiencies ϵ^{app} are from Table 8.3. The constant factors for the background from tau decays are the BRs of the decay modes (see Section 8.2.1). One obtains the $\overline{\nu}_e$ appearance search rule by interchanging neutrinos and antineutrinos.

Type	Source	Sel. efficiency	Value
Signal	$\nu_\mu \to \nu_e$	$\epsilon^{\text{app}}_{\text{eCC}}$	0.27
Background	Beam contamination	$\epsilon^{\text{app}}_{\text{eCC}}$	0.27
	$\overline{\nu}_\mu \to \overline{\nu}_e$	$\epsilon^{\text{app}}_{\text{eCC}}$	0.27
	ν / $\overline{\nu}$ NC	$\epsilon^{\text{app}}_{\text{NC}}$	0.11
	Hadronic τ decays	$0.648 \times \epsilon^{\text{app}}_{\text{NC}}$	0.07
	Electronic τ decays	$0.178 \times \epsilon^{\text{app}}_{\text{eCC}}$	0.05
	Misid. μ-like events	$\epsilon^{\text{app}}_{\mu}$	0.01

by the LSc detector. The results obtained from a *multivariate analysis* with *boosted decision trees* (see Ref. [243] for details on the method) supported the assumptions for $\epsilon^{\text{app}}_{\text{eCC}}$ and $\epsilon^{\text{app}}_{\text{NC}}$. If detailed topological reconstruction possibilities become available, new chances to distinguish NC background from signal events open up: Given that the momentum direction of the incoming beam neutrinos is precisely known, thanks to the long CN2PY baseline, evidence for *missing transversal momentum* from outgoing neutrinos could provide additional power to identify NC and ν_τ / $\overline{\nu}_\tau$ CC events. A discrimination of shower-like event topologies and elongated muon tracks from ν_μ / $\overline{\nu}_\mu$ CC interactions or $\tau^{\mp}$ decays should be comparatively easy and improves with increasing energy.[7] The detection of a muon decay is another discriminating feature. However, muons of lower energy are also produced from the decays of charged pions, which can emerge from hadronic showers in deep-inelastic ν_e / $\overline{\nu}_e$ CC events too. This reduces the discrimination power of this feature. Nevertheless, the assumed selection efficiencies for the signal and backgrounds in the appearance search likely reflect conservative lower limits for LENA. This seems especially true in the light of the development of new reconstruction techniques.

In `GLoBES`, the signal and background contributions to build a specific Asimov data set define a so-called *rule*. Table 8.4 summarizes the input for the ν_e appearance search rule.

[7] Ref. [50] reports that the observed overall pulse shape from lepton tracks in LSc already has power to distinguish electrons and muons below 1 GeV. The power increases with rising energy.

Table 8.5 – Default values for the global signal and background selection efficiencies of the ν_μ ($\overline{\nu}_\mu$) appearance search.

Selection efficiency	Parameter	Value
ν_μ / $\overline{\nu}_\mu$ CC events	$\epsilon_{\mu\mathrm{CC}}^{\mathrm{disa}}$	0.90
NC-like events	$\epsilon_{\mathrm{NC}}^{\mathrm{disa}}$	0.10

Table 8.6 – Input for the ν_μ disappearance search rule in `GLoBES`. The different signal and background sources were discussed in Section 8.2.1; corresponding selection efficiencies ϵ^{disa} are from Table 8.5. The constant factors for the background from tau decays are the BRs of the decay modes (see Section 8.2.1). One obtains the $\overline{\nu}_\mu$ disappearance search rule by interchanging neutrinos and antineutrinos.

Type	Source	Sel. efficiency	Value
Signal	$\nu_\mu \to \nu_\mu$	$\epsilon_{\mu\mathrm{CC}}^{\mathrm{disa}}$	0.90
Background	$\overline{\nu}_\mu \to \overline{\nu}_\mu$	$\epsilon_{\mu\mathrm{CC}}^{\mathrm{disa}}$	0.90
	ν / $\overline{\nu}$ NC	$\epsilon_{\mathrm{NC}}^{\mathrm{disa}}$	0.10
	Hadronic τ decays	$0.648 \times \epsilon_{\mathrm{NC}}^{\mathrm{disa}}$	0.06
	Muonic τ decays	$0.174 \times \epsilon_{\mu\mathrm{CC}}^{\mathrm{disa}}$	0.16

ν_μ / $\bar{\nu}_\mu$ disappearance search Table 8.5 summarizes the default values for the selection efficiencies that were assumed for the signal and the backgrounds in the ν_μ ($\overline{\nu}_\mu$) disappearance search. Both the actual disappearance signal and considered backgrounds were previously discussed in Section 8.2.1. The final input for the ν_μ disappearance search rule in `GLoBES` is listed in Table 8.6.

8.2.3 Event counts and event energy spectra

Table 8.7 lists raw event counts for the LBNO experiment from CERN to the 50 kt LSc detector LENA at Pyhäsalmi after one year, i.e., for 50 kt a exposure. They essentially document how the total number of events in various channels were calculated[8] from the input described in Section 8.1. Furthermore, they suggest the fundamental potential of the experiment. Since the SPS and HP-PS beam options use the same neutrino / antineutrino flux spectra, the event counts for the HP-PS option are simply obtained by multiplying the counts for the SPS option with the factor 2 MW/0.75 MW $\sim$ 2.67.
Event energy spectra of specific Asimov data sets for the ν_e ($\overline{\nu}_e$) appearance and ν_μ ($\overline{\nu}_\mu$) disappearance searches in PHF (NHF) mode with true NO and $\delta_{\mathrm{CP}} = 0°$ are shown as examples in Figure 8.9 and Figure 8.10, respectively. As expected for this oscillation case, the neutrino running has a strong excess of ν_e appearance events over the background (Figure 8.9 *left*). The antineutrino running for $\overline{\nu}_e$ appearance (Figure 8.9 *right*), on the other hand, shows no excess but instead has larger background from the wrong $\nu_\mu \to \nu_e$ appearance. Moreover, one can clearly see that the appearance search benefits from the migration of NC background to

[8] Since `GLoBES` works with Asimov data sets, the obtained values originally were non-integer numbers.

Table 8.7 – Raw, average event counts, i.e., without applied efficiency factors, for the CN2PY LBNO experiment with LENA and the SPS or the HP-PS neutrino / antineutrino beam option. The average event counts were computed with `GLoBES` and non-integer values were rounded to nearest integers. All stated values correspond to an exposure of 50 kt a and are given as functions of the neutrino MO and the beam mode. The underlying oscillation parameters are from Table 8.2, assuming $\delta_{\mathrm{CP}} = 0°$ unless otherwise specified. While the upper part of the table lists (un-)oscillated event counts for CC interactions of the original beam flux components as well as NC interactions, the lower part shows the number of CC events from $\nu_\mu \to \nu_e$ ($\overline{\nu}_\mu \to \overline{\nu}_e$) appearance for different values of δ_{CP}.

		SPS beam 400 GeV, 750 kW 1.4×10^{20} POT/a 50 kt a		**HP-PS beam** 50 GeV, 2 MW 2.9×10^{21} POT/a 50 kt a	
		PHF	NHF	PHF	NHF
ν_μ ($\overline{\nu}_\mu$) unosc. CC		3076 (35)	91 (1302)	8203 (94)	243 (3474)
ν_e ($\overline{\nu}_e$) unosc. CC		20 (1)	3 (6)	54 (3)	8 (15)
ν_μ ($\overline{\nu}_\mu$) osc.	NO	742 (10)	27 (299)	1978 (26)	72 (797)
CC	IO	744 (10)	27 (295)	1984 (26)	72 (788)
ν_e ($\overline{\nu}_e$) osc.	NO	18 (1)	3 (6)	48 (3)	8 (15)
CC	IO	20 (1)	3 (5)	52 (3)	8 (14)
$\nu_\mu(\overline{\nu}_\mu) \to \nu_\tau(\overline{\nu}_\tau)$	NO	206 (3)	7 (111)	550 (8)	17 (297)
CC	IO	219 (3)	7 (107)	583 (8)	18 (286)
NC		1128	557	3008	1485
$\nu_\mu(\overline{\nu}_\mu) \to \nu_e(\overline{\nu}_e)$ CC					
$\delta_{\mathrm{CP}} = -\pi/2$	NO	223 (0)	6 (12)	594 (1)	16 (32)
	IO	60 (2)	2 (65)	161 (4)	5 (172)
$\delta_{\mathrm{CP}} = 0$	NO	185 (1)	5 (21)	493 (2)	13 (57)
	IO	38 (2)	1 (80)	101 (5)	3 (213)
$\delta_{\mathrm{CP}} = \pi/2$	NO	153 (1)	4 (25)	409 (2)	11 (66)
	IO	28 (2)	1 (93)	76 (6)	2 (247)

lower reconstructed energies, away from the energy range of interest.

8.3 Analysis procedure and statistical framework

In general, the goal of a neutrino flavor oscillation analysis is to find the set of oscillation parameters $\hat{\boldsymbol{\theta}}$ that best describes (fits) the experimental data as an estimator for the true set of parameters $\boldsymbol{\theta}_{\mathrm{true}}$ "chosen by Nature". Assuming an analysis for data $\mathbf{n} = \{n(\hat{E}_{\mathrm{rec},0}), n(\hat{E}_{\mathrm{rec},1}), n(\hat{E}_{\mathrm{rec},2}), \ldots, n(\hat{E}_{\mathrm{rec},k-1})\}$ in k bins of reconstructed energy $\hat{E}_{\mathrm{rec}}$, this can be done by successively testing the *goodness-*

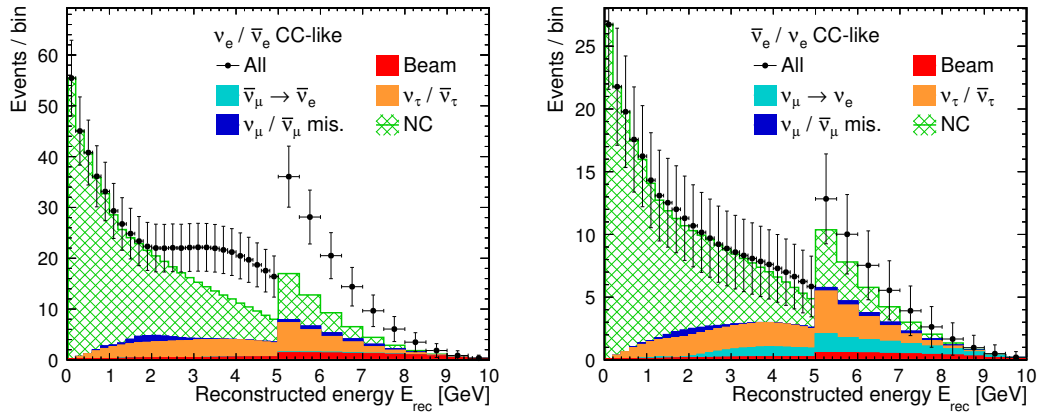

Figure 8.9 – Event energy spectra of specific Asimov data sets for the ν_e appearance search in PHF mode **(left)** and for the $\overline{\nu}_e$ appearance search in NHF mode **(right)**. They are given as a function of the reconstructed event energy $\hat{E}_{\text{rec}}$, i.e., after the application of the energy migration matrices. Moreover, they take the event containment and selection efficiencies into account. In each case, an exposure of 250 kt a (∼94 kt a) with the SPS (HP-PS) beam option was assumed. The underlying NO oscillation parameters are from Table 8.2 with $\delta_{\text{CP}} = 0°$. Vertical bars at the points showing the counts of all e-like events indicate the statistical errors. They are, however, not taken into account in the `GLoBES` analysis. Note that the bin size changes from 200 MeV to 500 MeV at $\hat{E}_{\text{rec}} = 500$ MeV.

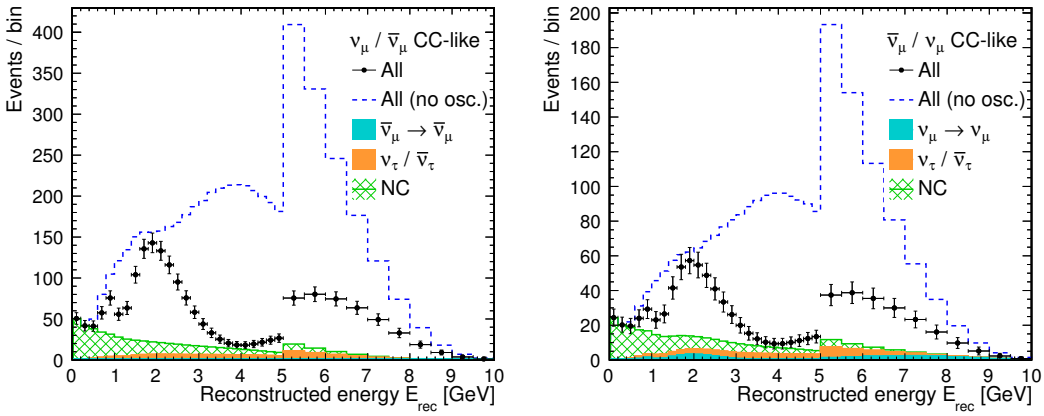

Figure 8.10 – Same as Figure 8.9 but for the ν_μ disappearance search in PHF mode **(left)** and the $\overline{\nu}_\mu$ disappearance search in NHF mode **(right)**.

of-fit between the observed experimental outcome $\mathbf{n}_{\text{true}}(\boldsymbol{\theta}_{\text{true}})$ and data $\mathbf{n}_{\text{test}}(\boldsymbol{\theta}_{\text{test}})$ expected from different but well-defined sets of oscillation parameters $\boldsymbol{\theta}_{\text{test}}$. A particular type of quantitative measure for the goodness-of-fit is the *likelihood ratio* $\lambda(\boldsymbol{\theta}_{\text{test}})$ (see Ref. [11] for details). It is defined in such a way that a smaller value of the *negative logarithmic likelihood ratio* $-2 \ln \lambda(\boldsymbol{\theta}_{\text{test}})$ indicates a better agreement between $\mathbf{n}_{\text{true}}(\boldsymbol{\theta}_{\text{true}})$ and $\mathbf{n}_{\text{test}}(\boldsymbol{\theta}_{\text{test}})$. In the given case, the hypothesized data $\mathbf{n}_{\text{test}}(\boldsymbol{\theta}_{\text{test}})$ were used to test the assumption of a particular neutrino MO or CP-conservation ($\delta_{\text{CP}} = 0, 180°$). The outcome from the goodness-of-fit tests for different MO assumptions allowed to calculate a *test statistic* T, whose statistical

Table 8.8 – Defaults for the central values and relative 1σ uncertainties of the systematic parameters in the *default model* for systematic uncertainties without correlations.

Name	Parameter	Central value	Rel. error
Signal normalization	f_{sig}	1	$\pm 5\,\%$
Background normalization	f_{bkg}	1	$\pm 10\,\%$

interpretation finally defined a measure for the MO sensitivity. Similarly, a test statistic S was calculated from the goodness-of-fit test for leptonic CP-conservation to define a measure for the sensitivity to CP-violation.

Section 8.3.1 details two different models that were used to include systematic uncertainties in the oscillation parameter fitting. The construction of the test statistics T and S, as well as the χ^2-function minimized in the `GLoBES` analysis, are treated in Section 8.3.2. The reported measures for the neutrino MO and leptonic CP-violation sensitivities, which followed from the statistical interpretations of T and S, are subject of Section 8.3.3.

8.3.1 Systematic uncertainties

Systematic uncertainties originate from imprecisely known cross-sections, beam fluxes, number of target particles, etc. They were taken into account as to *bin-to-bin-correlated errors* in the energy spectra $\mathbf{n}(\boldsymbol{\theta})$. Therefore, they only affected the absolute normalization of the spectra but not their shape. Two models for the systematic uncertainties were considered and are described in the following.

Default model without correlations The systematic uncertainties in the *default model* were uncorrelated between all the ν_e and $\overline{\nu}_e$ appearance searches as well as the ν_μ and $\overline{\nu}_\mu$ disappearance searches, i.e., between the single rules. Following the standard implementation in `GLoBES`, different systematic normalization errors were assumed for the signal channel and for the combined backgrounds. Consequently, the total number of systematic parameters for the total of four appearance and disappearance rules was eight. The default values for the set of systematic parameters $\boldsymbol{f}$ are documented in Table 8.8, where the actual systematic 1σ uncertainties are stated in the last column.
In the context of this model, the number of events in a bin was given by

$$n_x(\hat{E}_{\text{rec}};\boldsymbol{\theta},\boldsymbol{f}) = f_{\text{sig}}\, n_{x,\text{sig}}(\hat{E}_{\text{rec}};\boldsymbol{\theta}) + f_{\text{bkg}}\, n_{x,\text{bkg}}(\hat{E}_{\text{rec}};\boldsymbol{\theta})\,, \tag{8.5}$$

where x either denotes e-like (n_e) or μ-like (n_μ) events. The quantity $n_{x,\text{sig}}$ ($n_{x,\text{bkg}}$) refers to the corresponding number of signal (background) events that were selected and accepted as fully contained. For the observed data $\mathbf{n}_{\text{true}}(\boldsymbol{\theta}_{\text{true}})$, the systematic parameters usually take the central value.

Alternative model with full correlations To test the impact of correlations between different systematic parameters, a second model for systematic uncertainties—the *alternative model*—was defined and could be used instead of the default model.

Table 8.9 – Defaults for the central values and relative 1σ uncertainties of the systematic parameters in the *alternative model* for systematic uncertainties with full correlations.

Name	Parameter	Central value	Rel. error
Signal normalization	f_{sig}	1	$\pm 5\,\%$
ν_e / $\overline{\nu}_e$ contamination normalization	f_{ν_e}	1	$\pm 5\,\%$
ν_τ / $\overline{\nu}_\tau$ normalization	f_{ν_τ}	1	$\pm 50\,\%$
NC and ν_μ / $\overline{\nu}_\mu$ CC normalization	f_{NC}	1	$\pm 10\,\%$

Representing an extreme scenario, the model described the case where the systematic parameters are fully correlated between the different appearance and disappearance rules. It adopted the assumptions made for CN2PY with GLACIER in Ref. [229] and required a user-defined implementation of systematics in `GLoBES` (see Ref. [234]). The set $\boldsymbol{f}$ of systematic parameters in the alternative model included one parameter for the signal and three parameters for different background components described in Section 8.2.1. The model's parameter values are summarized in Table 8.9.
In the alternative model for systematic uncertainties, the equivalent to Equation (8.5) for the number of e-like events n_e was calculated as

$$\begin{aligned} n_e(\hat{E}_{\text{rec}};\boldsymbol{\theta},\boldsymbol{f}) = f_{\text{sig}}\, n_{e,\text{sig}}(\hat{E}_{\text{rec}};\boldsymbol{\theta}) + f_{\nu_e}\, n_{e,\nu_e}(\hat{E}_{\text{rec}};\boldsymbol{\theta}) \\ + f_{\nu_\tau}\, n_{e,\nu_\tau}(\hat{E}_{\text{rec}};\boldsymbol{\theta}) + f_{\text{NC}}\, n_{e,\text{NC}}(\hat{E}_{\text{rec}};\boldsymbol{\theta})\,. \end{aligned} \tag{8.6}$$

The quantities $n_{e,\text{sig}}$, n_{e,ν_τ} and $n_{e,\text{NC}}$ describe the number of events in the signal channel, background events produced from ν_τ / $\overline{\nu}_\tau$ CC interactions and background introduced from NC and ν_μ / $\overline{\nu}_\mu$ CC events, respectively. Both the CC background events from the intrinsic contamination of the beam with ν_e / $\overline{\nu}_e$ and from the "wrong oscillation" ($\overline{\nu}_\mu \to \overline{\nu}_e$ in PHF mode and vice versa) are summed up in n_{e,ν_e}.
Similar to Equation (8.6), the number of μ-like events n_μ was calculated as

$$\begin{aligned} n_\mu(\hat{E}_{\text{rec}};\boldsymbol{\theta},\boldsymbol{f}) = f_{\text{sig}} \left(n_{\mu,\text{sig}}(\hat{E}_{\text{rec}};\boldsymbol{\theta}) + n_{\mu,\nu_\mu}(\hat{E}_{\text{rec}};\boldsymbol{\theta}) \right) \\ + f_{\nu_\tau}\, n_{\mu,\nu_\tau}(\hat{E}_{\text{rec}};\boldsymbol{\theta}) + f_{\text{NC}}\, n_{\mu,\text{NC}}(\hat{E}_{\text{rec}};\boldsymbol{\theta})\,. \end{aligned} \tag{8.7}$$

Here n_{μ,ν_μ} accounts for CC background events from the "wrong survival" ($\overline{\nu}_\mu \to \overline{\nu}_\mu$ in PHF mode and vice versa), which, for simplicity, were assumed to scale with f_{sig} too.
To be fair, it remains to be tested if the systematic uncertainties at the levels stated in Table 8.8 and Table 8.9 can be realized at all (see also the discussion in Ref. [164]). They certainly require the use of a dedicated near-detector.

8.3.2 Neutrino flavor oscillation analysis with `GLoBES`

For assessing the sensitivity to the neutrino MO, the test statistic T was defined as

$$T = \min_{\boldsymbol{\theta}_{\text{test}} \in \text{IO}} \chi^2(\boldsymbol{\theta}_{\text{test}}) - \min_{\boldsymbol{\theta}_{\text{test}} \in \text{NO}} \chi^2(\boldsymbol{\theta}_{\text{test}}) \equiv \chi^2_{\text{IO}} - \chi^2_{\text{NO}}\,, \tag{8.8}$$

in accordance with Ref. [69]. To minimize the χ^2-function, the nonfixed oscillation parameters (see Table 8.2) in $\boldsymbol{\theta}_{\text{test}}$ were varied. However, they were confined to a

particular neutrino MO to represent the tested hypothesis. The statistic S for testing CP-conservation was defined as in Ref. [70]:

$$S = \min_{\delta_{\mathrm{CP}}=0°,\,180°} \chi^2(\boldsymbol{\theta}_{\mathrm{test}}) - \min_{\mathrm{global}} \chi^2(\boldsymbol{\theta}_{\mathrm{test}})\,. \tag{8.9}$$

For the first term on the right side of Equation (8.9), the minimum was found with respect to the CP-conserving values 0° and 180° for δ_{CP} in $\boldsymbol{\theta}_{\mathrm{test}}$. In the global minimization of the second term, the phase was left free. The θ_{23} *octant degeneracy* was taken into account in both the MO and the leptonic CP-violation analyses. However, since the central value of θ_{23} (see Table 8.2) was close to 45°, it only had a small effect.

The χ^2-function minimized by `GLoBES` during the oscillation parameter fitting was

$$\chi^2(\boldsymbol{\theta}_{\mathrm{test}}) = \chi^2_{\mathrm{appear}}(\boldsymbol{\theta}_{\mathrm{test}}) + \chi^2_{\mathrm{disa}}(\boldsymbol{\theta}_{\mathrm{test}}) + \chi^2_{\mathrm{sys}}(\boldsymbol{\theta}_{\mathrm{test}})\,. \tag{8.10}$$

It contains contributions from the ν_e and $\overline{\nu}_e$ appearance searches (χ^2_{appear}), from the ν_μ and $\overline{\nu}_\mu$ disappearance searches (χ^2_{disa}) and from constraining the oscillation and systematic parameters (χ^2_{sys}). The term χ^2_{appear} followed from the Poissonian negative logarithmic likelihood (see Ref. [11]) as

$$\begin{aligned}
\chi^2_{\mathrm{appear}}(\boldsymbol{\theta}_{\mathrm{test}}) &\equiv -2\,\ln\lambda(\boldsymbol{\theta}_{\mathrm{test}}) \\
&= 2\sum_{+/-}\sum_{\hat{E}_{\mathrm{rec}}} n_e(\hat{E}_{\mathrm{rec}};\boldsymbol{\theta}_{\mathrm{test}},\boldsymbol{f}_{\mathrm{test}}) - n_e(\hat{E}_{\mathrm{rec}};\boldsymbol{\theta}_{\mathrm{true}},\boldsymbol{f}_{\mathrm{true}}) \\
&\quad + n_e(\hat{E}_{\mathrm{rec}};\boldsymbol{\theta}_{\mathrm{true}},\boldsymbol{f}_{\mathrm{true}})\ln\frac{n_e(\hat{E}_{\mathrm{rec}};\boldsymbol{\theta}_{\mathrm{true}},\boldsymbol{f}_{\mathrm{true}})}{n_e(\hat{E}_{\mathrm{rec}};\boldsymbol{\theta}_{\mathrm{test}},\boldsymbol{f}_{\mathrm{test}})}\,.
\end{aligned} \tag{8.11}$$

While the first sum runs over the results from the PHF (+) and the NHF (−) beam mode, the second sum runs over all $\hat{E}_{\mathrm{rec}}$-bins from the analysis energy window. The latter was set to be the interval $[1\,\mathrm{GeV}, 9\,\mathrm{GeV}]$. Oscillation parameters $\boldsymbol{\theta}$ and systematic parameters $\boldsymbol{f}$ with the subscript *true* denote the values "chosen by Nature" and were used to generate the specific Asimov data sets. The total number of e-like events n_e in a $\hat{E}_{\mathrm{rec}}$-bin was determined with Equation (8.5) or Equation (8.6), depending on the model for the systematic parameters. Similar to χ^2_{appear}, the term χ^2_{disa} in Equation (8.10) for the disappearance searches was calculated by replacing n_e in Equation (8.11) with the number of μ-like events n_μ. Again, n_μ depends on the model for the systematic parameters and was given by Equation (8.5) or Equation (8.7). Finally, the term χ^2_{sys} in Equation (8.10) combined the external constraints on the oscillation parameters (see Table 8.2) and the global mass density scaling (see Section 8.1.3) with the effects from the systematic parameters f_j (see Section 8.3.1). Using the so-called *pull method* [244] to take into account the systematic errors, `GLoBES` calculated χ^2_{sys} by summing Gaussian penalties:

$$\chi^2_{\mathrm{sys}} = \sum_i \frac{(\theta_{0,i}-\theta_i)^2}{\sigma^2_{\theta_i}} + \sum_j \frac{(1-f_j)^2}{\sigma^2_{f_j}}\,. \tag{8.12}$$

The parameter $\theta_{0,i}$ (θ_i) denotes the *prior* (test) value of the i^{th} oscillation parameter; σ_{θ_i} is the corresponding prior uncertainty. In this analysis, four priors (only three

oscillation parameters and the global mass density scaling had errors) and, depending on the model, four or eight systematic parameters contributed to χ^2_{sys}. The minimization of χ^2 in Equation (8.10) was done with respect to all nonfixed oscillation parameters, the global mass density scaling and all systematic parameters.

8.3.3 Statistical interpretation

After the outcome of an average experiment was calculated (see Section 8.2) and analyzed (see Section 8.3.2) with `GLoBES`, the analysis result required a statistical interpretation to determine its significance. Based on Refs. [69, 70], the following summarizes how the sensitivity to the neutrino MO and leptonic CP-violation was quantified for the LBNO experiment with LENA.

Confidence level and power of a binary hypothesis test The sensitivity to the neutrino MO was assessed in the *frequentist approach* by testing the validity of a *null hypothesis* H_0 against an *alternative hypothesis* H_1. In this case, the two possible, mutually exclusive hypotheses are H_{NO} and H_{IO}. The test requires a *criterion* to define when the current null hypothesis is accepted or rejected. Such a criterion is usually realized by defining a *critical region* for the p.d.f. $\Phi(T|H_0)$ of the test statistic T if H_0 is true. The test statistic is a stochastic variable that depends on the experimental outcome. For the MO study it was defined as in Equation (8.8), resulting in different p.d.f.s for the two possible hypotheses. If T is within the critical region of H_0, the null hypothesis is accepted. Otherwise it is rejected. The probability that one falsely rejects the true hypothesis H_0 ("type I" error), because T was found outside of the critical region, is commonly denoted by $\alpha \equiv P(T > T_c^\alpha|H_0)$. Consequently, one defines the CL as the probability $1-\alpha$ that the null hypothesis is accepted as true. For a one-sided hypothesis test, the following holds:

$$\text{CL} \equiv 1-\alpha = 1 - P(T > T_c^\alpha|H_0) = 1 - \int_{T_c^\alpha}^{\infty} \Phi(T|H_0)\, \mathrm{d}T\,. \tag{8.13}$$

This also defines the *critical value* T_c^α belonging to α, i.e., H_0 is rejected if $T > T_c^\alpha$. One also has to take into account the probability β that H_0 is falsely accepted although H_1 is true ("type II" error), $\beta \equiv P(T < T_c^\alpha|H_1)$. The corresponding *power* p of a binary hypothesis test, i.e., the probability that a wrong hypothesis is correctly rejected, is defined as

$$p \equiv 1-\beta = 1 - P(T < T_c^\alpha|H_1) = 1 - \int_{-\infty}^{T_c^\alpha} \Phi(T|H_1)\, \mathrm{d}T\,. \tag{8.14}$$

In order to calculate α and β, one needs to know the p.d.f.s of T for H_0 and H_1.

The concept is similar when CP-conservation is tested with the statistic S from Equation (8.9). In this case, the null and alternative hypotheses are given by leptonic CP-conservation and CP-violation, respectively.

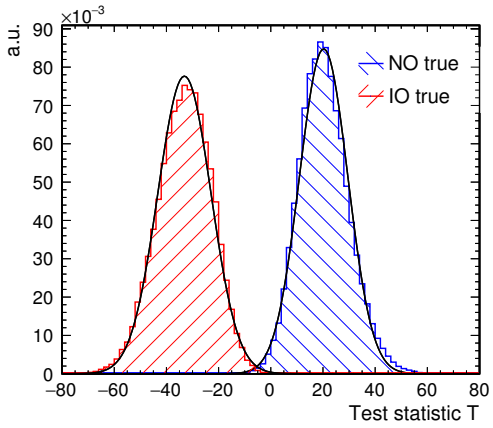

Figure 8.11 – Distributions of the test statistic T from 5×10^4 MC simulations per true MO, NO (*blue*) or IO (*red*). The distributions correspond to $\delta_{\mathrm{CP}} = 90°$ and the default experimental setup. A total of 1.4×10^{21} POT at 400 GeV with equal sharing between PHF and NHF mode was assumed. The black curves show the fits with Gaussian functions.

Probability density functions of the test statistic T As derived in Refs. [69, 245], the p.d.f. of the test statistic T in Equation (8.8) for the neutrino MO can be approximated by a normal distribution with mean T_0 and width $\sigma = 2\sqrt{T_0}$:

$$\Phi(T|\mathrm{MO}) \simeq \mathcal{N}(\pm T_0^{\mathrm{MO}}, 2\sqrt{T_0^{\mathrm{MO}}}) \,, \tag{8.15}$$

where the true MO is either NO (+) or IO (−). This approximation is valid in case a *simple hypothesis* is tested, i.e., T_0 does not depend on free parameters. One example where simple hypothesis testing applies with good accuracy is the neutrino MO determination with JUNO [69] (see Section 4.3.2). However, in an LBNO experiment with a neutrino beam, the mean value T_0 is especially dependent on the unknown phase δ_{CP} (see Equation (8.1)). Therefore, the quantification of the MO sensitivity is a case of *composite hypothesis testing*; both T_0 and $\Phi(T|\mathrm{MO})$ become functions of the free oscillation parameters $\boldsymbol{\vartheta}$. As an example, Figure 8.11 shows the distributions $\Phi(T|\mathrm{MO}, \delta_{\mathrm{CP}} = 90°)$ for both MO cases as obtained from MC simulations for the default experimental setup. One can see that the sampled p.d.f.s agree well with the fitted Gaussian functions.
The MC sampling in Figure 8.11 was done as follows: `GLoBES` calculated the reconstructed event energy spectra of the Asimov data sets. In each bin of the spectra, the event count was then replaced by a random number drawn from a Poissonian p.d.f. having the Asimov event count as mean value. Additionally, overall normalization factors for the spectra were randomly drawn from Gaussian distributions with mean and standard deviation being equal to the systematic parameters in Table 8.8. This compensated an excessive amount of degrees of freedom due to the fit parameters from systematic normalization errors (see Equation (8.5) and Equation (8.12)) [246]. Finally, the test statistic T in Equation (8.8) was calculated with `GLoBES`. The procedure was repeated multiple times for both NO and IO as true MO.
A comparison between Gaussian widths σ_T obtained from fitting sampled p.d.f.s of T and the expected widths from the Gaussian approximation in Equation (8.15) is shown on the left of Figure 8.12 for different combinations of the true MO and

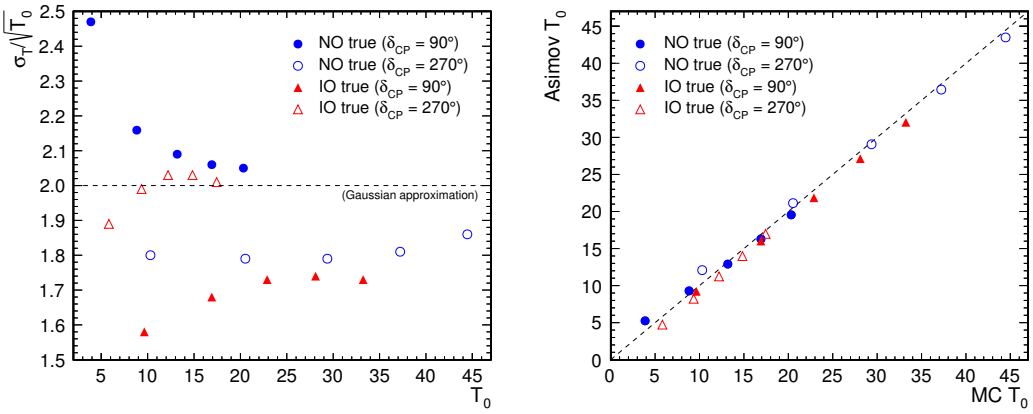

Figure 8.12 – **Left:** Comparison of the widths of p.d.f.s for the test statistic T with the theoretical expectations from the Gaussian approximation in Equation (8.15) as a function of T_0. The quantities T_0 and σ_T were determined with Gaussian fits to p.d.f.s of T from 5×10^4 MC simulations per combination of true MO and value of δ_{CP}. They are the mean value and standard deviation of the Gaussian function. The five data points per combination correspond to the default setup with a total of (from left to right) 2.8×10^{20}, 5.6×10^{20}, 8.4×10^{20}, 1.12×10^{21} and 1.4×10^{21} POT at 400 GeV and equal sharing between PHF and NHF mode. From the Gaussian approximation one expects that the ratio $\sigma_T/\sqrt{T_0}$ equals two. **Right:** Comparison of T_0 from the fitted, MC-generated p.d.f.s for T with the "Asimov T_0" calculated by `GLoBES` with the Asimov data sets. The data points are the same as on the left side. As indicated by the dashed line, the values should be identical.

δ_{CP}. The values of δ_{CP} correspond to the expected minima and maxima of the MO sensitivity. As one can see, the widths obtained from the MC simulations deviate from the values expected by the Gaussian approximation. However, for the right-most point of each data set, which always corresponds to the number of POT used in the final analysis, the deviation is in any case $< 14\,\%$. Moreover, the strongly deviating widths are smaller than the expectation, making the Gaussian approximation a conservative assumption. The right side of Figure 8.12 illustrates that T_0 from the MC simulations agrees well with the corresponding value obtained from a `GLoBES` calculation with the Asimov data sets. Therefore, the Gaussian approximation was used in the following of the MO sensitivity study.

Probability density functions of the test statistic S As discussed by the authors of Ref. [70], it is often assumed that the test statistic S to study the sensitivity to leptonic CP-violation has a *χ^2-distribution with one degree of freedom*. However, they found that S is close to being χ^2-distributed only if the experiment has a good sensitivity to δ_{CP}. For experiments with poor sensitivity, they obtained values of S that were lower than expected from a χ^2-distribution.
To probe the p.d.f. $\Phi(S)$ for the default setup of the investigated experiment, the same MC-based sampling method as in the case of T for the MO was used. Figure 8.13 shows the outcomes under the null hypothesis, i.e, $\delta_{\mathrm{CP}} = 0°, 180°$, for both MO possibilities. One can clearly see that the values of S from the MC sampling are shifted in both MO cases to lower values compared to the expectation from a χ^2-

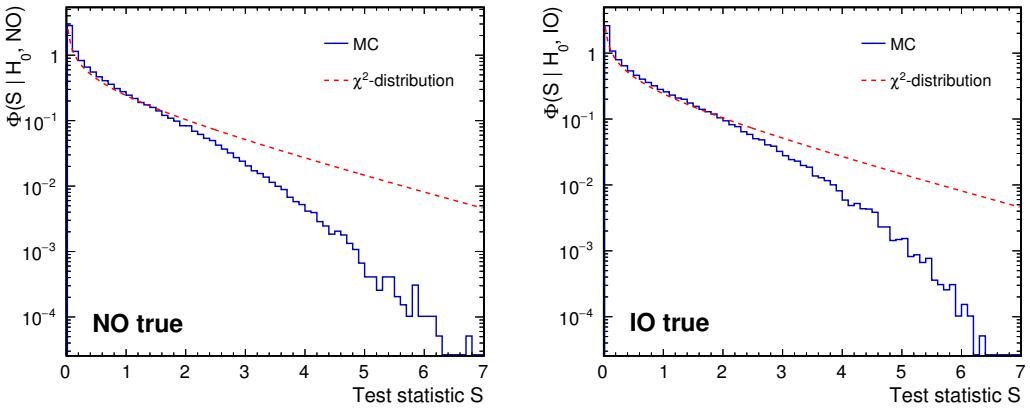

Figure 8.13 – Sampling of the p.d.f.s $\Phi(S|H_0, \text{NO})$ **(left)** and $\Phi(S|H_0, \text{IO})$ **(right)** under the null hypothesis H_0 ($\delta_{\text{CP}} = 0°, 180°$) with 1×10^5 MC simulations per neutrino MO and CP-conserving value of δ_{CP} (*solid blue line*). All MC simulations were performed with the default setup of the experiment. The p.d.f. of the χ^2-distribution with one degree of freedom (*dashed red line*) is also shown.

distribution with one degree of freedom. The construction of a sensitivity measure for leptonic CP-violation from $\Phi(S)$ is outlined further below.

Neutrino mass ordering: Standard, median and crossing sensitivity The following assumes a test for NO, i.e., $H_0 = H_{\text{NO}}$, but the procedure is formally similar for IO. For the NO test at a defined confidence level one needs to find a critical value T_c^α with the probability $P(T < T_c^\alpha) = \alpha$ (see also Figure 8.11). In composite hypothesis testing, the tested hierarchy shall be rejected at CL $1 - \alpha$ for all values of the free oscillation parameters $\boldsymbol{\vartheta}$. This requires a conservative value for T_c^α. If one uses the Gaussian approximation in Equation (8.15), one can calculate an analytic expression for α in Equation (8.13) and finally obtains a connection between α, T_c^α and T_0^{NO} [69]:

$$(T_c^\alpha)_{\text{min}} = \min_{\boldsymbol{\vartheta} \in \text{NO}} \left[T_0^{\text{NO}}(\boldsymbol{\vartheta}) - \sqrt{8 T_0^{\text{NO}}(\boldsymbol{\vartheta})}\ \text{erfc}^{-1}(2\alpha) \right] . \tag{8.16}$$

Here $\text{erfc}(x)$ denotes the *complementary error function*, $\text{erfc}(x) \equiv 1 - \text{erf}(x)$. The minimum in Equation (8.16) is usually found at $\delta_{\text{CP}} = 90°$ ($\delta_{\text{CP}} = 270°$) for NO (IO). For β in Equation (8.14) one finds the following connection to $(T_c^\alpha)_{\text{min}}$ and T_0^{IO} with the Gaussian approximation [69]:

$$\beta(\boldsymbol{\vartheta}) = \frac{1}{2}\,\text{erfc}\left[\frac{T_0^{\text{IO}}(\boldsymbol{\vartheta}) + (T_c^\alpha)_{\text{min}}}{\sqrt{8 T_0^{\text{IO}}(\boldsymbol{\vartheta})}} \right] . \tag{8.17}$$

A sensitivity measure commonly used in the literature is the *standard sensitivity*: It assumes that T_0 (sometimes referred to as "$\overline{\Delta\chi^2}$") follows a χ^2-distribution with one degree of freedom. Considering the quantiles of the distribution, the CL in terms of Gaussian standard deviations at which a given neutrino MO can be identified is then calculated as $\sqrt{T_0}$. Note, however, that T_0 is not a statistic since it does not depend

on random data. Therefore, assigning a distribution to it is not well defined [69].
The sensitivity measure mostly reported in the following is the *median sensitivity*: It corresponds to the CL $(1-\alpha)$ for which the probability to reject the false neutrino MO hypothesis is 50 %, i.e., $\alpha(\beta = 0.5)$. A useful expression to estimate the median sensitivity for composite hypotheses in the Gaussian approximation, which was derived and confirmed with MC simulations in Ref. [69], follows from Equation (8.16) and Equation (8.17) as

$$\alpha(\boldsymbol{\vartheta}) \approx \frac{1}{2}\,\mathrm{erfc}\sqrt{\frac{T_0^{\mathrm{IO}}(\boldsymbol{\vartheta})}{2}} \quad \text{(median sensitivity)}\,. \tag{8.18}$$

Depending on the values of $(T_c^{\alpha})^{\mathrm{NO}}_{\mathrm{min}}$ and $(T_c^{\alpha})^{\mathrm{IO}}_{\mathrm{min}}$, it can happen that one, both or no MO hypotheses are rejected at the CL $(1-\alpha)$. The case where exactly one hypothesis can be rejected is defined by $(T_c^{\alpha})^{\mathrm{NO}}_{\mathrm{min}} = (T_c^{\alpha})^{\mathrm{IO}}_{\mathrm{min}}$ (or $\alpha = \beta$). In Ref. [69], the sensitivity corresponding to this point is called *crossing sensitivity* and the formula for its calculation is provided as

$$\alpha = \frac{1}{2}\,\mathrm{erfc}\left(\frac{1}{\sqrt{8}}\,\frac{\hat{T}_0^{\mathrm{NO}} + \hat{T}_0^{\mathrm{IO}}}{\sqrt{\hat{T}_0^{\mathrm{NO}}} + \sqrt{\hat{T}_0^{\mathrm{IO}}}}\right) \quad \text{(crossing sensitivity)}\,. \tag{8.19}$$

Here $\hat{T}_0^{\mathrm{NO}}$ and $\hat{T}_0^{\mathrm{IO}}$ refer to the minima of $T_0^{\mathrm{NO}}(\boldsymbol{\vartheta})$ and $T_0^{\mathrm{IO}}(\boldsymbol{\vartheta})$ with respect to the free oscillation parameters $\boldsymbol{\vartheta}$.
One commonly converts the probability α into a corresponding number of Gaussian standard deviations $n\sigma$. The following adopts the convention in neutrino physics to use a double-sided Gaussian test for this conversion [69]:

$$\alpha(n) = \mathrm{erfc}\left(\frac{n}{\sqrt{2}}\right) \quad \Leftrightarrow \quad n = \sqrt{2}\,\mathrm{erfc}^{-1}(\alpha)\,. \tag{8.20}$$

For instance, a hypothesis is rejected at a CL $(1-\alpha)$ of 68.27 %, 95.45 %, 99.73 % if the test outcome is more then 1σ, 2σ, 3σ away from the mean, respectively.

Leptonic CP-Violation: Standard and median sensitivity If S_0 is the average result for the test statistic S in Equation (8.9) from the Asimov data set, the *standard sensitivity* is commonly reported as $\sqrt{S_0}$ (see discussion in Ref. [70]). As in the previously treated case of the neutrino MO, this assumes a χ^2-distribution with one degree of freedom. In Ref. [70] it was found that for experiments with good sensitivity to δ_{CP} the standard sensitivity is very similar to the *median sensitivity*. However, for the default experimental setup of CN2PY with LENA, the MC sampling of the p.d.f. of S assuming CP-conservation revealed a strong deviation from the p.d.f. of the χ^2-distribution (see Figure 8.13). Therefore, the standard method probably does not give a good description of the experiment's sensitivity.
The median sensitivity to leptonic CP-violation is defined as the CL at which the probability to correctly reject CP-conservation is 50 % [70]. Its finding is conceptually similar to the neutrino MO case: The p.d.f. of S under the null hypothesis H_0 of CP-conservation, $\Phi(S|H_0)$, allows to define a critical value S_c^{α} such that the probability $P(S > S_c^{\alpha})$ is equal to α. Consequently, the null hypothesis is rejected at the CL $(1-\alpha)$ if $S > S_c^{\alpha}$. For the median sensitivity, the critical value S_c^{α} is set to the

median of the p.d.f. of S under the alternative hypothesis H_1 assuming CP-violation, $\Phi(S|H_1)$. Since $\Phi(S|H_1)$ depends on the true δ_{CP}, the median sensitivity to leptonic CP-violation of the default setup is reported in Section 8.5 as a function of the true phase value.

8.4 Results: Sensitivity to the neutrino mass ordering

This section presents the results of the study regarding the sensitivity of LENA to the neutrino MO in the CN2PY LBNO experiment. Primary measure for the sensitivity is the *median sensitivity* [69], which was introduced in Section 8.3.3 and assumed the *Gaussian approximation* in Equation (8.15) for the p.d.f. of the test statistic T in Equation (8.8). It is the CL $(1-\alpha)$ for which the probability to reject the false neutrino MO is 50 %, i.e., $\alpha(\beta = 0.5)$.[9] The results are shown for the cases where the NO is realized in Nature (i.e., *a test for IO*) and where the IO is true (i.e., *a test for NO*).
First, Section 8.4.1 describes the results for the *default setup* detailed in Sections 8.1 and 8.2. Single changes to the default setup and their effects on the experiment's sensitivity are explored subsequently. In particular, Section 8.4.2 discusses the consequences from changes to the true values of some oscillation parameters. The dependence of the results on the energy resolution is topic of Section 8.4.3. Finally, the impacts of the event selection efficiencies, systematic uncertainties and the containment efficiencies are subject of Section 8.4.4, Section 8.4.5 and Section 8.4.6, respectively.

8.4.1 Performance of the default setup

The default setup assumed a total number of 1.4×10^{21} POT at 400 GeV with equal sharing between PHF and NHF beam mode. This corresponds to an exposure of about 500 kt a (187.5 kt a) with the SPS (HP-PS) beam option (see Section 8.1.1). Figure 8.14 shows T_0, the modulus of the mean value of the test statistic T in the Gaussian approximation, as a function of the true value of δ_{CP} for both MO possibilities. The results followed from testing the NO and IO hypotheses with the Asimov data sets. As one can see, the values of T_0 for true IO are lower than the values for true NO. This is a result of the smaller antineutrino cross-sections and a slightly lower total beam flux in NHF mode, which lead to a less significant number of $\overline{\nu}_e$ signal events for true IO compared to the ν_e appearance event counts for true NO.
Using the approximation in Equation (8.18), the T_0 values were converted to a number of Gaussian standard deviations from a double-sided test with Equation (8.20) to estimate the median sensitivity. This is displayed by the solid lines in Figure 8.15. One can see a clear dependence of the sensitivity on δ_{CP}, as already implied by Figure 8.2. Note that the sensitivity in the case of true NO is minimal (maximal) if δ_{CP} equals 90° (270°), whereas the opposite holds if IO is true. Moreover, for a given MO case, the sensitivity is always equal for the CP-conserving values 0° and 180°. Both features follow from the CP-violating term C_- in Equation (8.1)

[9] Of course, one wants a higher probability in a real application.

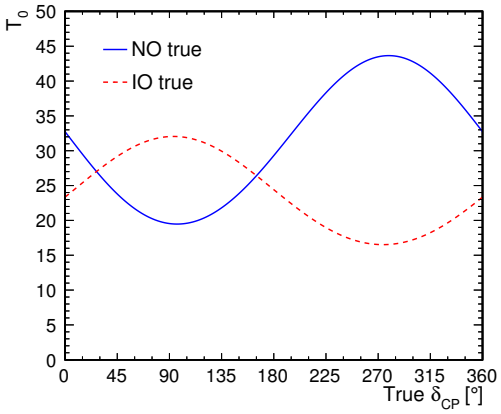

Figure 8.14 – GLoBES results for T_0, the modulus of the mean value of the test statistic T in Gaussian approximation, as a function of the true value for δ_{CP}. They were obtained by testing the IO hypothesis for true NO (*solid blue*) and the NO hypothesis for true IO (*dashed red*) with the Asimov data sets from the default setup.

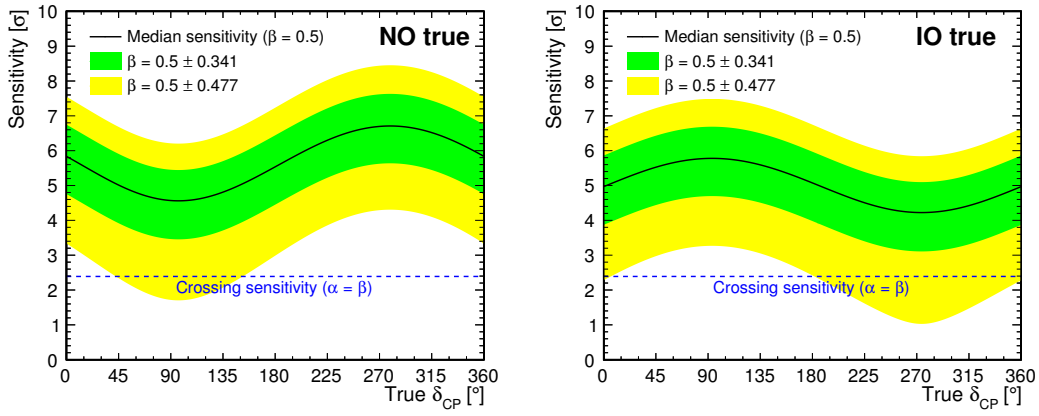

Figure 8.15 – Median sensitivity (*solid black line*), i.e., with the condition $\beta = 0.5$ for the type II error in Equation (8.17), in the cases of true NO **(left)** and true IO **(right)** as a function of the true value for δ_{CP}. The results are for the default setup and were obtained by converting Figure 8.14 with Equation (8.18) and Equation (8.20). The colored bands were obtained with the conditions $\beta = 0.5 \pm 0.6827/2$ and $\beta = 0.5 \pm 0.9545/2$ for the rate of the type II error. They show the range of sigmas around the mean value with which the tested MO can be rejected in 68.27 % (*green*) and 95.45 % (*yellow*) of the experiments, respectively. The crossing sensitivity (dashed blue line) was determined with Equation (8.19) and shows the CL at which exactly one MO hypothesis can be rejected.

through its different signs for neutrinos and antineutrinos in combination with the $\sin\delta_{\mathrm{CP}}$-dependence. The green and yellow bands in Figure 8.15 followed from the conditions $\beta = 0.5 \pm 0.6827/2$ and $\beta = 0.5 \pm 0.9545/2$ for the rate of the type II error in Equation (8.17). They indicate the range of sigmas around the mean value with which the tested MO can be rejected in 68.27 % (1σ range) and 95.45 % (2σ range) of the experiments, respectively [69].
The crossing sensitivity (dashed blue lines) was determined to be $\sim 2.4\sigma$. It is the

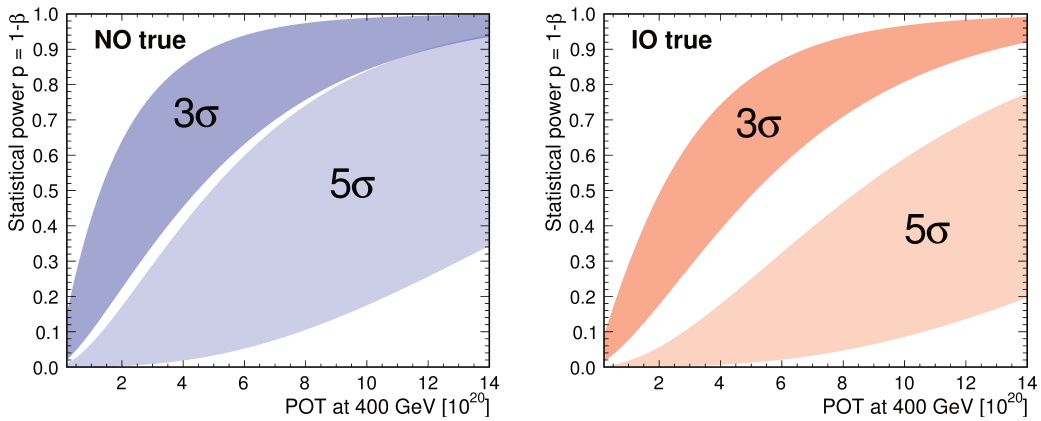

Figure 8.16 – Statistical power $p = 1-\beta$ corresponding to the test of the IO hypothesis **(left)** or the NO hypothesis **(right)** at 3σ (5σ) CL as a function of the number of POT at 400 GeV with the default setup. The widths of the bands indicate the impact from the true value of δ_{CP}.

CL at which exactly one MO hypothesis can be rejected ($\alpha = \beta$).
In particle physics, one often uses the threshold value of 3σ (5σ) for the statistical significance to express that there is "evidence" for (a "discovery" of) a particular effect in the observed data. Therefore, Figure 8.16 shows the statistical power $p = 1 - \beta$ of the MO hypothesis test, i.e., the probability for correctly rejecting the false MO hypothesis, as a function of the number of POT for both the 3σ and 5σ CLs.[10] The widths of the bands reflect the dependence on the true value of δ_{CP}. As one can see from the left side of the figure for maximum POT, the IO hypothesis can be correctly rejected with $> 93.5\,\%$ probability at 3σ CL and with a probability between $34.4\,\%$ and $94.0\,\%$ at 5σ CL. The right side of Figure 8.16 shows that a correct rejection of the NO hypothesis at 3σ CL is possible in 92.0–99.1 % of all experiments with maximum POT, whereas the probability to correctly reject the same hypothesis at 5σ CL is between $19.7\,\%$ and $77.6\,\%$.

Compared to a 20 kt GLACIER-type LAr detector, which has always been seen as the designated far-detector for the CN2PY beam, the considered default setup of LENA would require a longer runtime of the LBNO experiment to determine the neutrino MO with similar statistical significance. Using the SPS-driven beam, GLACIER would guarantee a 3σ (5σ) measurement after about 1.4 (2.9) years, corresponding to 2×10^{20} POT (4×10^{20} POT) [229]. The main reason for the weaker performance of LENA, despite the larger target mass, are the worse background rejection efficiencies, whose influence is subject of Section 8.4.4. For the recently started NOνA (off-axis) experiment [67, 247] with 810 km baseline length the expected median sensitivity to the neutrino MO is $\lesssim 3\sigma$ [69]. This assumes the scheduled runtime of six years with a 700 kW beam. Assuming the same runtime, the median sensitivity of the reactor experiment JUNO is projected to be $\sim 3\sigma$ (without external information), independent of δ_{CP} (see Section 4.3 and Refs. [42, 69]). Sensitivity estimates for other experiments, including DUNE (dubbed LBNE) and those studying atmospheric

[10] The Gaussian approximation for the test statistic T was used despite the deviations found on the left of Figure 8.12 for lower numbers of POT.

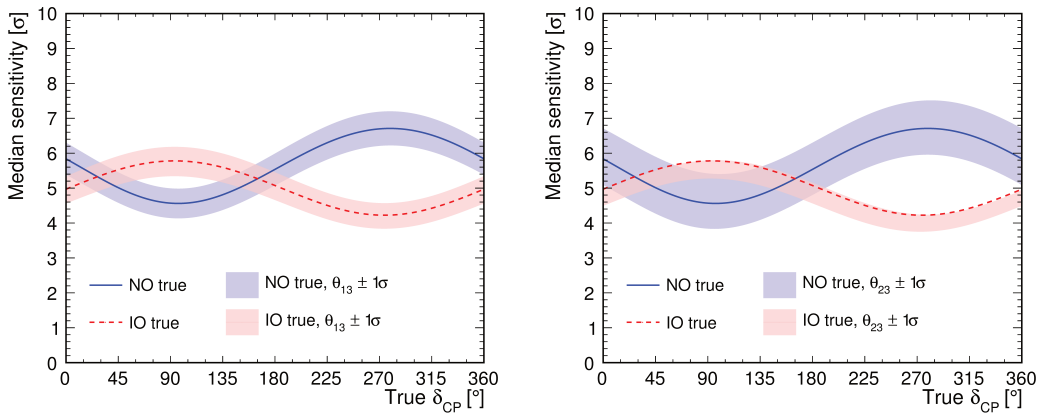

Figure 8.17 – Effects on the median sensitivity from changing the central value of θ_{13} **(left)** or θ_{23} **(right)** in Table 8.2 by $\pm 1\sigma$. The results corresponding to the default setup with true NO (*blue solid line*) or true IO (*red dashed line*) are also shown.

neutrinos, can be found in Ref. [69].

8.4.2 Effects of the true oscillation parameters

To illustrate the effect of the assumptions for the true oscillation parameters θ_{13} and θ_{23} in Table 8.2 on the result for the default setup, the central values of these parameters were varied by $\pm 1\sigma$. The relative errors were kept fixed. On the left of Figure 8.17 one sees the impact on the median sensitivity from changing the true θ_{13} by $\pm 0.43°$. For both MO possibilities, the changes with respect to the outcomes for the default setup are only about $\pm 0.4\sigma$. Note, however, that the considered 1σ range for θ_{13} is quite conservative in the view of current global fits (see Table 1.2) and the precision of the latest Daya Bay measurement reported in Ref. [248].
The right side of Figure 8.17 shows the effect from changing the true θ_{23} by $\pm 4.6°$. With the larger deviation of θ_{23} from 45°, the impact of the θ_{23} octant degeneracy grew. This mostly affected the case with true IO and is the main reason for the difference between the median sensitivity bands from the parameter variation.[11] Due to the sizable θ_{23} change and the $\sin^2\theta_{23}$-dependence of the term C_0 in Equation (8.1), which is most sensitive to the neutrino MO, the $\sim 1.5\sigma$ width of the NO median sensitivity band is comprehensible.

8.4.3 Effects of the energy resolution

In order to test the sensitivity of the result for the default setup to the assumed energy resolution (see Section 8.1.4), the relative energy uncertainty, which entered the energy migration matrices via the Gaussian energy resolution function, was varied between 5 % and 30 %. The bin sizes in reconstructed energy remained unchanged. As one can see in Figure 8.18, there is no visible difference between the 5 % case and the default value of 7 %. For the very pessimistic assumption of 30 % relative

[11] It was checked that without the θ_{23} octant degeneracy the median sensitivity band for true IO has a shape similar to the one of the band for the true NO case.

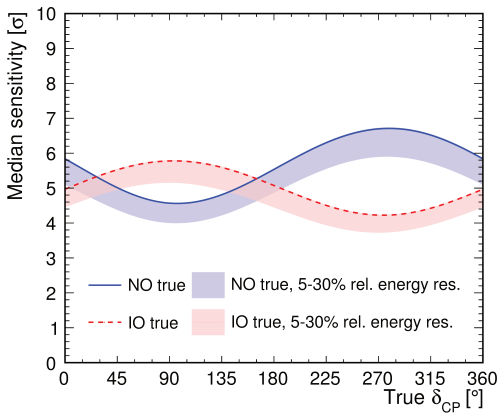

Figure 8.18 – Effect on the median sensitivity from varying the relative energy resolution in the energy migration matrices between 5 % and 30 %. The results corresponding to the default setup (7 %) with true NO (*blue solid line*) or true IO (*red dashed line*) are also shown.

energy resolution, the loss in median sensitivity is about 0.6σ. Note, however, that the nonconsideration of shape uncertainties in the default model for systematic errors (see Section 8.3.1) implies that the translation of the neutrino energies to the reconstructed energies is perfectly understood. A possibly correlated change of shape uncertainty with the increase of the relative energy uncertainty was not taken into account. Nevertheless, the outcome demonstrates that for the given binning of the reconstructed energy the different neutrino MOs lead to robust, distinguishing features in the event spectra for the CN2PY baseline.

8.4.4 Effects of the event selection efficiencies

As mentioned in Section 8.2.2, the selection efficiencies for signal and background events are one of the major unknowns for assessing the MO sensitivity of LENA at multi-GeV neutrino energies. To explore the dependency of the median sensitivity on the efficiency parameters $\epsilon^{\text{app}}_{\text{eCC}}$ and $\epsilon^{\text{app}}_{\text{NC}}$ of the ν_e and $\overline{\nu}_e$ appearance searches (see Table 8.3), a step-wise scan through a part of the parameter space was performed. Figure 8.19 shows the minimum (*left*) and maximum (*right*) median sensitivity as a function of the parameters for true NO. The matrix for true IO looks similar, but the maximum displayed value of the minimum (maximum) median sensitivity is $\sim 12\sigma$ ($\sim 16\sigma$). In a real experiment, optimized event selection algorithms likely yield $\epsilon^{\text{app}}_{\text{eCC}} \gtrsim \epsilon^{\text{app}}_{\text{NC}}$. Two particular cases shall be explicitly highlighted:
The matrices in Figure 8.19 suggest that it is better not to aim for a rejection of NC-like background ($\epsilon^{\text{app}}_{\text{eCC}}$, $\epsilon^{\text{app}}_{\text{NC}} = 90\,\%$)[12] than to use the default strategy with $\epsilon^{\text{app}}_{\text{eCC}} = 27\,\%$ and $\epsilon^{\text{app}}_{\text{NC}} = 11\,\%$. Events are only categorized as e-like or μ-like in this case. The probability to correctly reject the IO (NO) hypothesis with these new efficiency values is $> 98.9\,\%$ ($> 98.7\,\%$) at 3σ CL and 68.2–99.6 % (44.9–94.0 %) at 5σ CL, depending on the true value of δ_{CP}.

[12] Remember, 10 % of the NC-like events that were selected as fully contained were assumed to be background to the ν_μ and $\overline{\nu}_\mu$ disappearance searches (see Table 8.6).

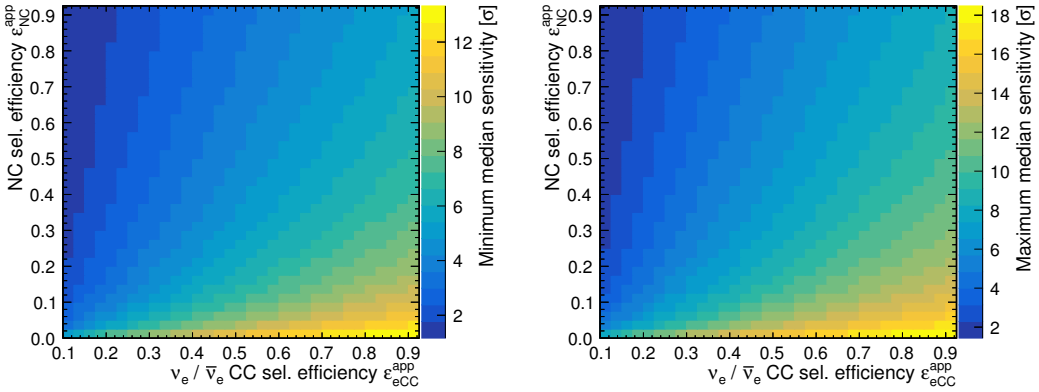

Figure 8.19 – Minimum **(left)** and maximum **(right)** median sensitivity for true NO as a function of the ν_e / $\overline{\nu}_e$ CC event selection efficiency $\epsilon_{\mathrm{eCC}}^{\mathrm{app}}$ and the NC event selection efficiency $\epsilon_{\mathrm{NC}}^{\mathrm{app}}$ in the ν_e and $\overline{\nu}_e$ appearance searches (see Table 8.3).

Considering the progress in event reconstruction for LSc detectors (see Chapter 6, Ref. [51]), there probably is room for improvement concerning the global event selection efficiencies and a rejection of NC background. Assuming a scenario with $\epsilon_{\mathrm{eCC}}^{\mathrm{app}} = 50\,\%$ and $\epsilon_{\mathrm{NC}}^{\mathrm{app}} = 10\,\%$, almost a doubling in signal selection, the probability to correctly reject a MO hypothesis at 3σ is essentially 100 %. At 5σ, the correct rejection of the IO hypothesis is possible in $> 97.6\,\%$ of the experiments, whereas it is $> 94.5\,\%$ for the NO hypothesis.
An increase of misidentified muon background to the ν_e and $\overline{\nu}_e$ appearance searches ($\epsilon_{\mu}^{\mathrm{app}}$) from 1 % to 5 % (10 %) resulted in a $\sim 0.2\sigma$ ($\sim 0.5\sigma$) loss in median sensitivity for all values of δ_{CP}.

8.4.5 Effects of the systematic uncertainties

The model for systematic uncertainties in the default setup only accounts for errors in the absolute normalization of signal and background events (see Table 8.8). Since the corresponding systematic parameters were assumed to be fully uncorrelated between the four different appearance and disappearance searches, a total of eight fit parameters was contributed by the model. On the left side of Figure 8.20 one sees the small $\sim 0.4\sigma$ decrease in median sensitivity from a doubling of the four systematic background normalization uncertainties to 20 %. The deteriorating effect from a doubling of the four systematic signal normalization uncertainties to 10 % is even smaller. This indicates that the specific MO feature in the reconstructed event spectrum cannot be reproduced by global variations of the signal and background normalizations in the event spectrum expected for the wrong MO.
An alternative model for systematic uncertainties is explained Section 8.3.1. It assumed normalization errors for the signal and three particular background contributions (see Table 8.9), which were fully correlated between the different appearance and disappearance searches. As expected from the reduction of the systematic fit parameters to four, the right side of Figure 8.20 shows a considerable increase in median sensitivity by 1–1.5σ with respect to the default setup. A rejection of the IO (NO) hypothesis at 3σ CL would then be possible with $> 99\,\%$ ($> 98.9\,\%$)

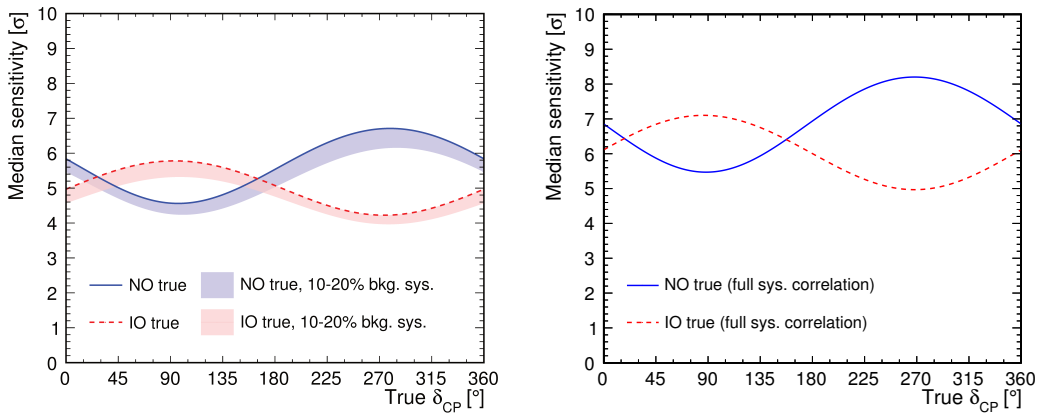

Figure 8.20 – **Left:** Effect on the δ_{CP}-dependent median sensitivity from varying the systematic background normalization error between 10 % and 20 % in the default model for systematic uncertainties. The results for the default setup with true NO (*sold blue line*) or true IO (*dashed red line*) are also shown. **Right:** Median sensitivity as a function of the true δ_{CP} for the alternative systematic uncertainty model with full correlations (see Table 8.9).

probability. At 5σ CL, the IO (NO) hypothesis could be rejected in 67.7–99.5 % (49.7–96.6 %) of all experiments. The results from this rather extreme case of fully correlated systematic uncertainties demonstrate that there is potential to improve the experiment's MO sensitivity by exploiting these correlations.

8.4.6 Effects of the event containment efficiencies

As detailed in Section 8.1.4 and Appendix D, energy-dependent containment efficiencies were considered in the description of the LSc detector LENA. This was done to take into account a loss of statistics due to events that were rejected as semi-contained. Effects from events that were falsely accepted as fully contained were propagated to the energy migration matrices. The assumed algorithm to select fully-contained events based on three parameters: the thickness of a decision region surrounding a central FV and the absolute and relative amount of energy maximally allowed to be deposited in the decision region.
As shown in Figure 8.21, the effects on the median sensitivity from three cases with different acceptance conditions for fully-contained events were studied. Note that the different cases not only include a change of the event containment efficiencies but also the setting of corresponding energy migration matrices. The long-dashed blue line just below the solid black line for the default setup shows the case where absolutely no energy deposition was allowed in the 50 cm thick decision region. This strict condition reduces the unseen loss of energy via particles that leave the detector's target region. However, it also means a higher loss of statistics. The visible net effect is a decrease in median sensitivity by $\sim 0.4\sigma$. An even more restrictive case is illustrated by the green dot-dashed line. It shows the outcome for the same strict condition applied to a 100 cm thick decision region. Again, the loss of statistics outweighs the superior information from the more precisely reconstructed neutrino energy spectrum. The net decrease in median sensitivity is $\sim 0.6\sigma$ with respect to the default setup. Finally,

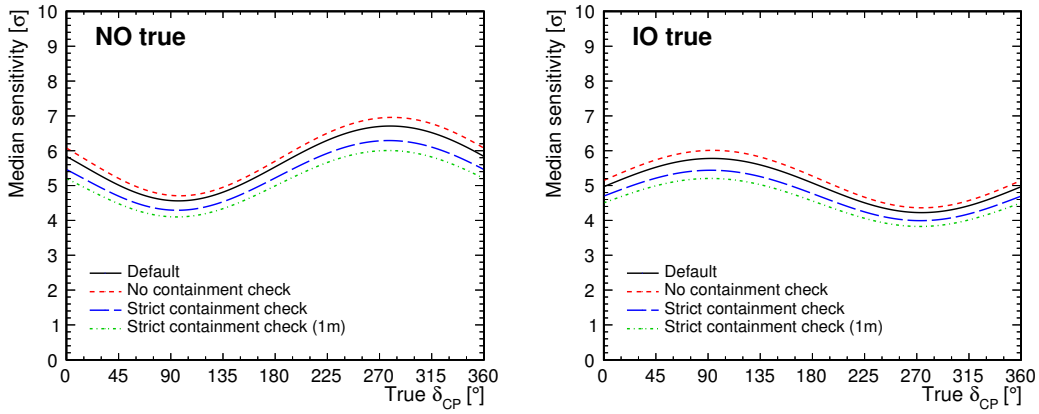

Figure 8.21 – Effects on the δ_{CP}-dependent median sensitivity from varied event containment efficiencies. They correspond to different scenarios for the selection of fully-contained events in the case of true NO **(left)** or true IO **(right)**. The algorithm to reject semi-contained events in the default setup (*solid black line*) is explained in Section 8.1.4. Aiming for the exclusive selection of fully-contained events, the strict containment check (*long-dashed blue line*) required that no energy was deposited in a 50 cm thick decision region around a central FV in the designated neutrino target of LENA. In an even stricter case (*dot-dashed green line*), the thickness of the decision region was increased to 100 cm. Finally, no containment check (*short-dashed red line*) was done at all. Note that not only the containment efficiencies but also the energy migration matrices were changed for each scenario.

the short-dashed red line represents the case where no containment check was done at all. The corresponding energy migration matrices are shown in Figure D.5. At first glance it is surprising (but consistent with the other cases) that the effect from increased statistics outbalances the much worsened energy information, yielding a $\sim 0.25\sigma$ increase in median sensitivity. Recall, however, that the nonconsideration of systematic uncertainties for the shape of the event spectrum means that the energy migration is assumed to be known perfectly. This assumption is probably overstressed in the given case. Moreover, without a containment check, there is no handle to discriminate neutrino interactions that occur outside of the target region but inject charged particles into the active volume.[13]. Therefore, it remains to be tested if the result is still valid once proper, *uncorrelated bin-to-bin errors* are taken into account for the reconstructed event spectrum. The same essentially holds for the other two cases as well since the positive effect from a larger certainty on the reconstructed neutrino energy spectrum is not yet fully included.

8.5 Results: Sensitivity to leptonic CP-violation

The sensitivity to leptonic CP-violation of the experiment's default setup was studied with the Asimov data sets as well as with MC simulations. Figure 8.22 shows the results from testing the hypothesis of CP-conservation with the Asimov / MC data as a function of the true value of δ_{CP}. Since it is assumed that the true MO is known (from an external measurement), the results are shown separately for the

[13]Such events were not yet incorporated into the analysis.

two MO cases. Both the standard sensitivity from the Asimov data sets and the median sensitivity from the MC simulations indicate a peak sensitivity of $\sim 1.1\sigma$ at the maximally CP-violating values of δ_{CP}. Close to the CP-conserving values $\delta_{\mathrm{CP}} = 0°$, 180°, however, the different sensitivity measures show discrepancies. As explained in Ref. [70], the MC results close to these values do not go to zero because any fluctuations around the Asimov data sets only increase the values of the test statistic S in Equation (8.9). Instead, as expected, the median sensitivity at the minima is close to 0.67σ, which corresponds to a CL of 50 %.
The green and yellow bands indicate the range of sigmas with which CP-conservation can be rejected in 68.27 % (1σ range) and 95.45 % (2σ range) of the experiments, respectively [70]. Due to the large dispersion of the bands, which suggests that for maximal CP-violation a rejection of CP-conservation could be possible even at about 3σ CL, a prediction of the experiment's sensitivity is difficult. Given the assumed runtime of ten years with the SPS beam option in Figure 8.22, the CN2PY experiment with the default assumptions for LENA is probably not a competitor for other proposed projects searching for leptonic CP-violation (e.g. see Refs. [70, 73, 230]).[14] Therefore, the potential to discover leptonic CP-violation with LENA was not explored in depth. However, it might be interesting to do so as soon as more reliable information on the potential to discriminate different neutrino interaction types at multi-GeV energies in LSc are available. For example, the standard sensitivity from the Asimov data set increased to a peak value of about 1.6σ with the event selection efficiencies $\epsilon_{\mathrm{eCC}}^{\mathrm{app}} = 50\,\%$ and $\epsilon_{\mathrm{NC}}^{\mathrm{app}} = 10\,\%$; a scenario that was also investigated in the context of the neutrino MO sensitivity in Section 8.4.4.

[14] In fact, the median sensitivity and dispersion of the 1σ and 2σ bands are similar to estimates for NOνA in Ref. [70]. Note, moreover, that no statement was made about the precision with which δ_{CP} could be measured.

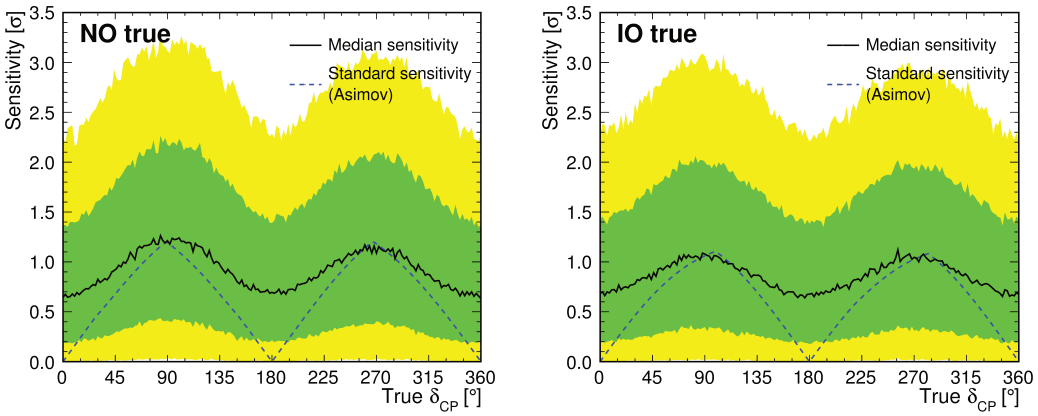

Figure 8.22 – Estimates for the median sensitivity (*solid black line*) and the standard sensitivity (*dashed blue line*) to leptonic CP-violation of the default experimental setup in the case of true NO **(left)** or true IO **(right)** as functions of the true value of δ_{CP}. The standard sensitivity was calculated as $\sqrt{S_0}$, where S_0 is the value of the test statistic S (see Equation (8.9)) from the Asimov data sets. For the median sensitivity, 1×10^5 MC simulations per true neutrino MO and CP-conserving value of δ_{CP} were performed to obtain the sampled p.d.f.s of S shown in Figure 8.13. In order get the medians of the p.d.f.s under the alternative hypotheses for particular values of δ_{CP}, 2×10^3 MC simulations per true neutrino MO and true value of δ_{CP} were made. The colored bands show the range of sigmas around the mean value with which CP-conservation can be rejected in 68.27 % (*green*) and 95.45 % (*yellow*) of the experiments, respectively.

Summary and Conclusion

Neutrino research is a vivid field of physics. Aspects of interest are the elementary particle character of the light neutral leptons and their use as messengers from terrestrial and astrophysical sources. Especially the quantum-mechanical phenomenon of neutrino flavor oscillations is in the focus of comprehensive exploration. Unsegmented neutrino detectors based on LSc have made important contributions to the above (interdisciplinary) fields. Despite their focus on LE neutrino and antineutrino measurements, a reconstruction of multi-GeV events in LSc is nevertheless an essential asset for existing and future experiments:
For the MO analysis of JUNO, the efficient suppression of cosmogenic background is important. This requires detailed reconstructions of different types of muon event topologies in the LSc volume.
For LENA, a reconstruction of neutrino interactions in an LBNO experiment with a multi-GeV neutrino beam would bring a meaningful extension of the project's research program.

In the first part of this thesis I explore the use of a novel reconstruction approach that reconstructs the spatial number density distribution of optical photon emissions from a HE event in LSc. Within the scope of this work, I have implemented the method first proposed by Björn Wonsak as a `C++`-based software package and advanced it in terms of speed and precision. To test the performance of the algorithm, I applied it to fully-contained muons in the kinetic energy range from 1 to 10 GeV that were simulated in LENA. Moreover, I have developed a set of basic analyses for the reconstruction results, e.g., a line fit through the 3D output data. This has yielded first quantitative performance measures (as a function of the muon energy):
For the simulated muons I have found that the angular resolution improves non-linearly from $\sim$1.4° to $\sim$0.3° with rising energy. Resolutions $\lesssim$ 22 cm have been determined for the start point in x, y and z direction of the LENA detector, resulting in combined 3D resolutions <30 cm. The start point resolutions lateral to the reconstructed track have been determined to be $\lesssim$ 25 cm. I have found similar results also for the end point, indicating that the lateral position of the whole muon track is well reconstructed. This is important to define efficient, localized cosmogenic background vetoes in the future. However, systematic effects in the analysis of the reconstruction results complicated the determination of the start and especially the end point resolutions parallel to the reconstructed track. Neglecting long tails from these effects in the analyzed distance distributions, I have obtained parallel resolutions <65 cm for the end point. Due to the assumptions made for the reconstruction, my results for the parallel start point resolutions being <12 cm

confirm that the start point reconstruction works correctly. The reconstructed end point is also affected by a significant shift down the track, which decreases from ∼200 cm to ∼120 cm with rising energy in the above-stated range. These systematic effects are well understood and while their removal is an important task for the future application of the reconstruction method, the above results already demonstrate that the novel reconstruction approach is more than competitive with respect to other, commonly used methods.
Another outcome from my performance assessment comprises a first estimate for the achievable relative energy resolution: For muons with energy E in the range from 0.1 to 10 GeV, it approximately follows the function $10\,\%/\sqrt{E/1\,\mathrm{GeV}} + 2\,\%$. This can probably be improved with more detailed reconstructions of the event topologies. Visual inspections of reconstruction results indicate that features like small particle showers are resolvable, supporting the ability to define cosmogenic background vetoes that are focused on such particular regions.
Besides further effort to explore and to provide the full potential, the novel reconstruction needs to improve on speed, robustness and precision in the future. Especially the consideration of Cherenkov light and a more detailed handling of scattered photons are important. Since the new method is in principle not restricted to muon events, further advancements could also include its application to HE neutrino interaction events.

The second part of this work is a study regarding the neutrino MO and leptonic CP-violation discovery potential of LENA in the CN2PY LBNO experiment with a multi-GeV neutrino WBB from CERN to the ∼2300 km distant *Pyhäsalmi mine* in central *Finland*. I used both MC techniques and Asimov data sets created with the `GLoBES` framework to assess the experiment's sensitivity. The final statistical interpretation of the outcomes for commonly employed test statistics I performed in consideration of the latest findings on this subject.
At the beginning, I have developed a conservative default setup of the hypothetical LBNO experiment with the 50 kt LSc detector LENA. Besides neutrino cross-sections from computations with `GENIE`, the description of the detector includes energy migration matrices and, for the first time, energy-dependent event containment efficiencies. I have produced both the matrices and the containment efficiencies in an ancillary study for all CC and NC neutrino interactions. Taking into account the calorimetric energy measurement approach of the 50 kt LSc detector, the containment efficiencies reflect the goal to exclude semi-contained events from the oscillation analysis. Effects from erroneous containment identification and a Gaussian energy resolution of 7 % are incorporated into the matrices. A critical point were the event selection efficiencies for multi-GeV neutrino interactions in a LSc detector, since they are not yet well elaborated. Therefore, I have used conservative values in the default setup under the assumption that NC events need to be discriminated from ν_e / $\overline{\nu}_e$ CC interactions. Background induced by ν_τ / $\overline{\nu}_\tau$ CC events has been taken into account.
Two different models for the consideration of systematic uncertainties have been used: The default model comprises bin-to-bin correlated normalization errors, which are fully uncorrelated between the signals and backgrounds of the different ν_e ($\overline{\nu}_e$) appearance and ν_μ ($\overline{\nu}_\mu$) disappearance searches. An alternative model includes bin-to-bin correlated normalization errors for the signal and three different background contributions that are fully correlated between the appearance and disappearance

searches.
I have assumed a total of 1.4×10^{21} POT at 400 GeV with equal sharing between neutrino and antineutrino mode for the CN2PY experiment with LENA, corresponding to ~ 10 (~ 3.75) years of running with the considered SPS (HP-PS) on-axis beam. Concerning the neutrino MO discovery potential, I have found that the IO (NO) hypothesis can be rejected at true NO (IO) with a median sensitivity of 4.6–6.7σ (4.2–5.8σ), depending on the true value of δ_{CP}. The crossing sensitivity with which exactly one MO can be excluded has been determined to be $\sim 2.4\sigma$. Moreover, I have found a probability of $> 93.5\,\%$ (92.0–99.1 %) for a correct rejection of the IO (NO) hypothesis at 3σ CL, again depending on δ_{CP}. The same hypothesis can be correctly rejected at 5σ CL in 34.4–94.0 % (19.7–77.6 %) of all cases.
I have also tested how the results change with single modifications of the true mixing angles θ_{13} and θ_{23}, the energy resolution, the event selection efficiencies and the systematic uncertainty model. Most of the changes only have effects $< 1\sigma$ on the median sensitivity to the neutrino MO. However, the event selection efficiencies have a lot of potential to improve the experiment's performance. Even an event selection strategy without the discrimination of e-like and NC-like events has come up as a viable option for the MO measurement. This is due to the energy migration of NC events and the strong MO signature in the event spectrum from the matter-driven ν_e / $\overline{\nu}_e$ appearance in the ν_μ / $\overline{\nu}_\mu$ beam. It essentially demonstrates the power of the LBNO experiment with the $\sim$2300 km long baseline. The exploitation of systematic error correlations between different oscillation searches as included in the alternative systematics model increases the median sensitivity by 1-1.5σ. Lastly, the impact of different scenarios for the rejection of semi-contained events and corresponding energy migration matrices has been studied. I have found that the resulting changes to the total statistics outweigh the related effects from a different energy smearing. In particular, the outcomes suggest that the sensitivity to the MO is better without the rejection of semi-contained events. However, with the sole consideration of normalization errors in the systematic uncertainty models, it remains to be tested if this result is still valid once proper shape uncertainties for the event spectra are taken into account.
The sensitivity to leptonic CP-violation of the assumed default setup for the experiment has been studied only briefly. Both the standard sensitivity from the computations with Asimov data sets and the median sensitivity from MC simulations have peak values of $\sim 1.1\sigma$ at the maximally CP-violating values $\delta_{\mathrm{CP}} = 90°, 180°$, independent of the neutrino MO. However, due to statistical fluctuations, the wide range of sigmas with which the hypothesis of CP-conservation can be excluded in 95.45 % of the experiments around the mean value makes it hard to estimate the experiment's sensitivity.

Without elaborated efficiencies for discriminating neutrino interaction types in LSc at multi-GeV energies, it remains difficult to make accurate predictions for the performance of LENA in the CN2PY experiment. However, this study shows that, with respect to the neutrino MO sensitivity, a neurino beam from CERN would meaningfully extend the HE neutrino program of the LENA project at Pyhäsalmi. The limited sensitivity to leptonic CP-violation certainly does not justify the building of a beam only for the large LSc-based apparatus. Nevertheless, in combination with a dedicated far-detector, LENA would excel in the LE neutrino physics measurements

and, at the same time, could contribute a significant result for the neutrino MO. The event reconstruction algorithm elaborated in the first part of this thesis forms an important corner stone in the further assessment of experimental sensitivities and the final realization of such an LBNO experiment.

Appendix A

Neutrino–Carbon Reactions

As generally described in Section 1.2.1, LE neutrinos and antineutrinos can be detected through neutrino–nucleus interactions. In the context of LSc-based neutrino detectors, the neutral leptons can undergo CC and NC reactions with the ^{12}C of the organic scintillator compound. Possible detection reactions along with their thresholds are summarized in Table A.1. Due to the high energy thresholds and low cross sections, these channels are primarily beneficial for the detection of core-collapse SN neutrinos with higher energy (see Section 2.2).
The CC reactions allow to exploit a delayed coincidence to tag an event: A e^- / e^+ is created together with an unstable isotope through the capture of a ν_e / $\overline{\nu}_e$ on a ^{12}C nucleus. The prompt e^- / e^+ emission signal is followed 10 ms / 20 ms later by the β^+ / β^- decay of the produced ^{12}N / ^{12}B. A discrimination of ν_e and $\overline{\nu}_e$ on event-by-event basis is nevertheless experimentally challenging due to similar endpoints and half-lives of the $\beta^\pm$ decays.
The inelastic NC interaction of a neutrino or antineutrino with ^{12}C leaves behind an excited carbon nucleus. With the event signature from the mono-energetic 15.11 MeV disexcitation γ ray one can only count the number of interactions above the reaction's energy threshold. Neither spectral nor flavor information becomes available for the interacting neutrino or antineutrino.

Due to 1.1 % natural abundance of ^{13}C, two more detection reactions are available in organic LSc. Corresponding information is listed in Table A.1. With the respective energy thresholds of 2.22 MeV and 3.68 MeV, the ν_e CC reaction and the inelastic NC scattering offer interesting possibilities for neutrino detection despite the lower number of target nuclei. This is especially true in the case of the delayed coincidence signal from the CC reaction, which can be applied for the detection of solar ^{8}B and SN ν_e [250].

Table A.1 – Summary of CC and NC detection reactions for ν_ℓ and $\overline{\nu}_\ell$, $\ell = e$, μ, τ, on ^{12}C and ^{13}C with their respective energy thresholds. $\langle E_{^8\mathrm{B}} \rangle$ means the average energy of the solar ^{8}B neutrino spectrum. Values cited from [191, 249–251].

Reaction	Current	Threshold [MeV]	Cross-section [$10^{-44}\,\mathrm{cm}^2$]
$\nu_e + {}^{12}\mathrm{C} \to {}^{12}\mathrm{N} + e^-$ ${}^{12}\mathrm{N} \to {}^{12}\mathrm{C} + \nu_e + e^+$, $\tau_{1/2} = 11.0\,\mathrm{ms}$	CC	17.34	28.7 @ 20 MeV
$\overline{\nu}_e + {}^{12}\mathrm{C} \to {}^{12}\mathrm{B} + e^+$ ${}^{12}\mathrm{B} \to {}^{12}\mathrm{C} + \overline{\nu}_e + e^-$, $\tau_{1/2} = 20.2\,\mathrm{ms}$	CC	14.39	71.1 @ 20 MeV
$\nu_\ell + {}^{12}\mathrm{C} \to \nu_\ell + {}^{12}\mathrm{C}^*$ $\overline{\nu}_\ell + {}^{12}\mathrm{C} \to \overline{\nu}_\ell + {}^{12}\mathrm{C}^*$ ${}^{12}\mathrm{C}^* \to {}^{12}\mathrm{C} + \gamma$	NC NC	15.11	30.2 27.9 @ 20 MeV
$\nu_e + {}^{13}\mathrm{C} \to {}^{13}\mathrm{N} + e^-$ ${}^{13}\mathrm{N} \to {}^{13}\mathrm{C} + \nu_e + e^+$, $\tau_{1/2} = 597.6\,\mathrm{s}$	CC	2.22	85.7 @ $\langle E_{^8\mathrm{B}} \rangle$
$\nu_\ell + {}^{13}\mathrm{C} \to \nu_\ell + {}^{13}\mathrm{C}^*$ ${}^{13}\mathrm{C}^* \to {}^{13}\mathrm{C} + \gamma$	NC	3.68	11.5 @ $\langle E_{^8\mathrm{B}} \rangle$

Appendix B

Luminescence of Organic Scintillator

The phenomenon of luminescence from an organic scintillator fundamentally bases on the electronic structure of carbon and its property to form conjugated and aromatic organic molecules [166]: In its ground state, the electronic configuration of the C atom (Z = 6) is $1s^2 2s^2 2p^2$. To establish a maximum of four single bindings one electron from the 2s state must be excited to a 2p state. The *hybridization* of four (sp^3-hybridization), three (sp^2-hybridization) or two (sp-hybridization) of the onefold occupied states enables four, three or two *covalent σ-bonds* with other atoms, respectively. The associated electrons are called σ-electrons. Electrons not included in a hybrid state form additional bindings with a neighbor atom that is already bound to the C atom by one σ-bond. These additional bindings through electrons in the p-orbital, so-called *π-bonds*, create a double or triple bond between the C atom and its neighbor, commonly another C atom. In the case of conjugated and aromatic organic molecules, the π-electrons in the π-bonds are not associated with a single atom but considered *delocalized*. One example for an aromatic molecule that is often found in an organic scintillator compound is *benzene*. As indicated by the simplified benzene structure shown in Figure B.1, the delocalized π-electrons form ring-shaped orbitals above and below the nodal plane of cyclic σ-bonds between six C atoms. It is the transition of such a delocalized π-electron from an excited state to the ground state that causes luminescence.

Following Ref. [166], a schematic representation of the π-electron states in an organic scintillator molecule is shown in Figure B.2. The π-electron states with total spin 0 (*singlet states*) are denoted by S_0, S_1, $S_2, \ldots$ up to the π-electron ionization energy I_π. Each state is associated with an excitation energy of 0, E_1, $E_2, \ldots$ with respect to the ground state S_0. The spacing between the energy levels is around 1 eV to 4 eV. Vibrational states of the molecule give fine structure with a spacing of ~ 0.16 eV to the electronic states. These sub-levels are denoted by S_{00}, S_{01}, $S_{02}, \ldots$, S_{10}, $S_{11}, \ldots$ etc. With sufficient absorbed energy a π-electron is excited from the ground state S_0 to any state S_{ij} with $i > 0$ or even ionized. However, a fast radiative disexcitation causing *fluorescence* normally occurs only for the transition from S_{10} to any S_{0j}. Since radiative decays from S_i with $i > 1$ to the ground state S_0 are not observed, the

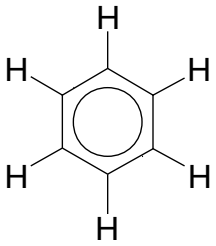

Figure B.1 – Structure of the *benzene* molecule. The straight lines indicate the covalent σ-bonds between the H atoms and the six C atoms located at the intersections of the lines. Indicated by the circle, six delocalized π-electrons form the π-molecular orbital outside of the common nodal plane.

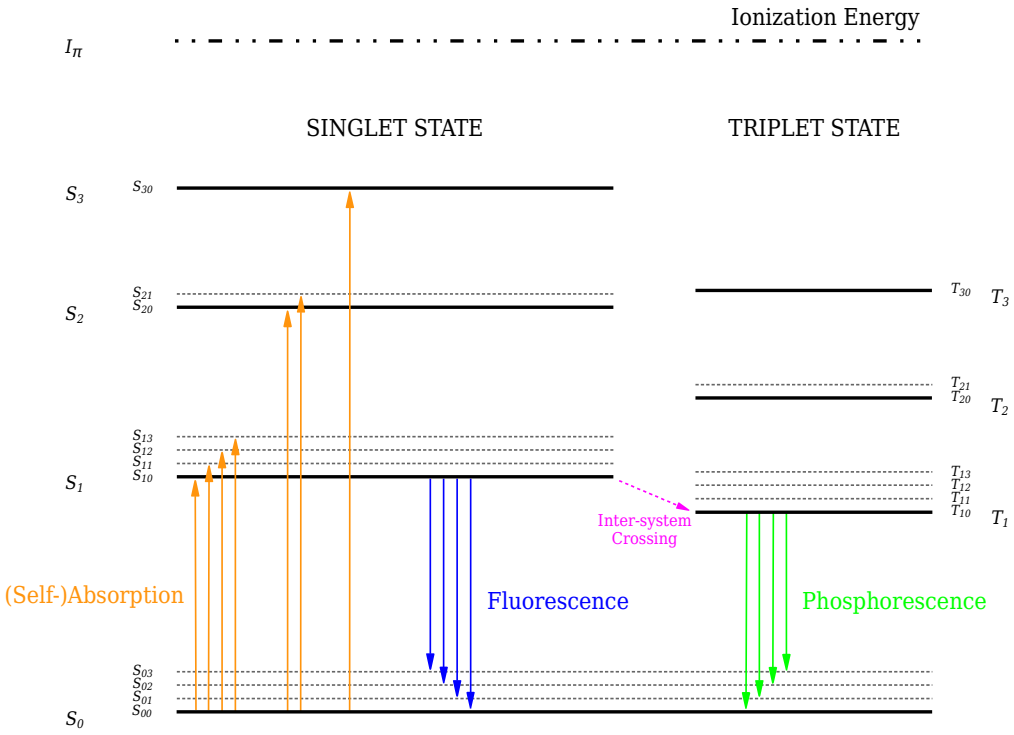

Figure B.2 – Scheme of π-electron states in an organic scintillator molecule. S_0 marks the ground state. The energy levels of excited singlet and triplet states are denoted by S_i and T_i, $i = 1, 2, 3, \ldots$, respectively. Vibrational sub-levels of a state are identified by a second index j, $j = 0, 1, 2, \ldots$, in S_{ij} and T_{ij}. I_π denotes the ionization energy of the π-electron. Scheme adapted from [166].

prior transitions from S_{ij} with $i \geq 1$ to S_{10} must take place via fast, non-radiative, internal conversion processes between excited states or via thermal degradation of energy in the vibrational sub-levels. Similar processes exist for the transition $S_1 \rightarrow S_0$ as well. In all cases they mean a significant dissipation of excitation energy to undetectable forms.
Besides the singlet states, a sequence of excited states with total spin 1 (*triplet states*)

T_1, T_2, T_3, ... exists for the π-electron. They are at energy levels that are lower than their corresponding singlet states and also have a fine structure. The direct radiative transition from the long-lived triplet state T_1 to any S_{0j} is called *phosphorescence*. A similar process known as *delayed fluorescence* includes the absorption of thermal activation energy for the transition from T_1 to S_1 and the subsequent fluorescence process for the disexcitation to any S_{0j}. Since the direct excitation through absorption from S_0 to an excited triplet state is spin-forbidden, the triplet state T_1 is populated by the non-radiative transition of a fraction of π-electrons from S_1 to T_1, a process called *inter-system crossing*.

Due to significant overlap of the emission and absorption spectra of a single-component scintillator (unitary system), re-absorption of the emitted scintillation photons occurs frequently. This results in a series of lossy scintillation photon re-emissions and absorptions, which deteriorate the energy and time information on the primary luminescence process. In order to suppress this behavior, one (binary system) or two (ternary system) organic, wavelength-shifting components are usually added to the scintillator solvent with a concentration of up to a few grams per liter. These *wavelength-shifter* solutes, which are attuned to the primary solvent in terms of compound and concentration, gain excitation energy from the primary scintillator through radiative and non-radiative energy transfer processes. When the wavelength-shifter molecules disexcite by radiative decays, photons are emitted isotropically in a wavelength region where the solvent is transparent. Details on photon wavelength-shifting based on energy transfers between the components of binary and ternary systems can be found in Ref. [166].

Appendix C

The European Design Studies LAGUNA and LAGUNA-LBNO

The European neutrino physics community realized the need for a multipurpose large-volume neutrino observatory of the next generation. Therefore, first ideas on the detector designs were brought up for discussion [197]:

- The *Megaton Mass Physics* (MEMPHYS) project [252,253] bases on the proven water Cherenkov technology and comprises 2–3 tank modules with a total fiducial mass on the order of 500 kt. Besides the detection of LE neutrinos, e.g., from the Sun or a core-collapse SN, the search for proton decay and a measurement of the CP-violating phase δ_{CP} with a beam of neutrinos at a few hundred MeV are part of its research program.
- GLACIER [231] uses LAr in a TPC to detect charged particles. It is considered to scale an improved version of the technology that was in principle pioneered by the detector of the *Imaging Cosmic and Rare Underground Signals* (ICARUS) project [254] to 100 kt.[1] The objectives of GLACIER include the measurement of LE neutrinos, proton decay search and a determination of the neutrino MO and δ_{CP} with a multi-GeV neutrino beam.
- The LENA project (see Section 4.2) envisages the upscaling of the well established LSc technology to a 50 kt detector. Primary goals are the detection of LE neutrinos and antineutrinos from different types of sources and the search for proton decay. The potential to determine the neutrino MO and to measure leptonic CP-violation with multi-GeV neutrinos / antineutrinos from a beam is subject of Chapter 8.

A complete design, construction and operation of such a next-generation neutrino observatory is an endeavor and financial strain probably too large for a single country and its participating research community. Therefore, the first steps of such an

[1] ICARUS used a single-phase LAr TPC whereas GLACIER aims to use a two-phase TPC including argon both as liquid and vapor.

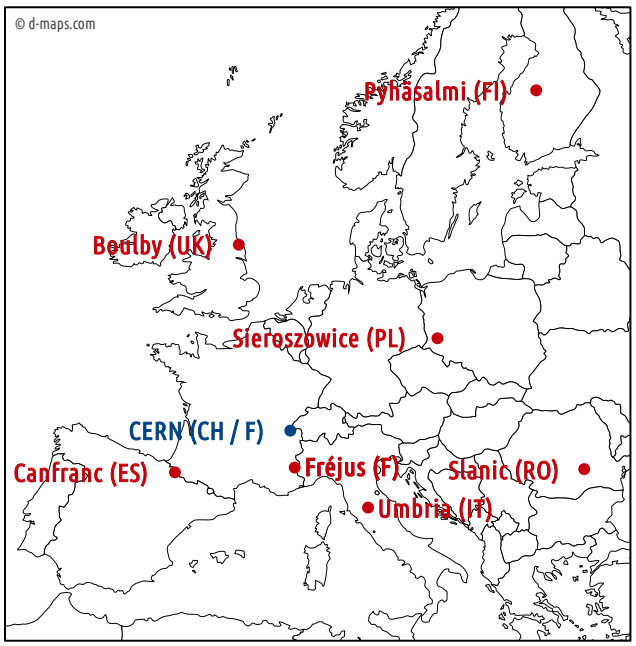

Figure C.1 – Potential detector sites (*red*) in Europe that were investigated by LAGUNA. The location of CERN (*blue*) is also marked. Image adapted from Ref. [255].

effort—a careful assessment of all possible options and the development of conceptual designs for all aspects and components of the project—were concentrated in two consecutive design studies at European level. Due to the development and scientific evaluation in a common framework, considerable progress has been made on the idea of LENA and the other benefiting projects.

C.1 LAGUNA

The LAGUNA design study was a pan-European project funded[2] by the 7^{th} *Framework Programme for Research and Technological Development* of the *European Union*. Its goal was to elaborate concepts for a multipurpose next-generation neutrino observatory in Europe with a target mass in the range from 50 kt to 500 kt [44, 45]. During the study from July 2008 to June 2011 with 21 beneficiaries, a consortium of scientific[3] and industrial partners[4] focused on the survey of potential underground laboratory sites and their excavation. The locations of the sites investigated by LAGUNA are shown in Figure C.1. Additional information is given in Table C.1. Moreover, the sensitivity of each considered detector option was studied with respect to the detection of LE neutrinos, e.g., from the Sun or a core-collapse SN, and the search for proton decay.

[2] Grant Agreement No. 212343
[3] Academic institutions from Denmark, Finland, France, Germany, Poland, Spain, Switzerland and United Kingdom.
[4] Specialized in civil and mechanical engineering and rock mechanics.

Table C.1 – Sites investigated in the context of the LAGUNA design study. The given distances from CERN and the energies of the respective first $\nu_\mu \to \nu_e$ oscillation maximum are important parameters to optimize a possible LBNO experiment with a LAGUNA detector. Data cited from Ref. [44].

Location	Type	Envisaged depth [mw.e.]	Distance from CERN [km]	Energy 1st osc. max. [GeV]
Fréjus *(F)*	Road tunnel	$\simeq 4800$	130	0.26
Canfranc *(ES)*	Road tunnel	$\simeq 2100$	630	1.27
Umbria *(IT)*	Green field	$\simeq 1500$	665	1.34
Sieroszowice *(PL)*	Mine	$\simeq 2400$	950	1.92
Boulby *(UK)*	Mine	$\simeq 2800$	1050	2.12
Slanic *(RO)*	Salt mine	$\simeq 600$	1570	3.18
Pyhäsalmi *(FI)*	Mine	up to $\simeq 4000$	2300	4.65

C.2 LAGUNA-LBNO

The follow-up design study of LAGUNA, LAGUNA-LBNO, was carried out from September 2011 to August 2014 and also received funding[5] from the 7^{th} *Framework Programme* [46, 47]. Based on the results of the precursor study, more precise excavation plans for the caverns of the different detector options and connected underground laboratories were developed. Furthermore, the construction plans for the different detectors were refined.
The key aspect of LAGUNA-LBNO was to outline potential LBNO experiments for determining the neutrino MO and for measuring δ_{CP} with a LAGUNA-type detector and a neutrino beam from CERN. Two scenarios were considered:

CN2PY: A neutrino beam from CERN to Pyhäsalmi comprises the longest baseline for an LBNO experiment among all possible LAGUNA sites. Due to the long distance a neutrino beam would cover in Earth's crust, the large matter effects on the $\nu_\mu \to \nu_e$ or $\overline{\nu}_\mu \to \overline{\nu}_e$ oscillations would allow an easy determination of the neutrino MO. More important, the same oscillation channel would allow to observe a possible non-zero value for δ_{CP} and thus enables a discovery of CP-violation in the lepton sector. As can be seen from Table C.1, the neutrino energy to reach the first oscillation maximum at the CN2PY baseline is about 4.6 GeV. A neutrino WBB tuned for this baseline would probably have the upper edge of its energy spectrum at even higher energy. Therefore, the preferred detector option for measuring the resulting HE neutrino interactions likely is a LAr-TPC like GLACIER [72, 229, 230]. The power of such an experiment could even be more enhanced by aiming a second neutrino beam from the 1160 km distant *Institute for High Energy Physics* accelerator complex in Protvino (Russia) to the detector at Pyhäsalmi [256].
In order to complement the sensitivity to LE neutrino and antineutrino detection, the LSc detector LENA was considered as second measurement apparatus

[5] Grant Agreement No. 284518

of the underground neutrino observatory. Due to this, the sensitivity of LENA to the neutrino MO and leptonic CP-violation in an LBNO experiment with the CN2PY beam was assessed in the context of LAGUNA-LBNO. Parts of this work are presented in Chapter 8.

CN2FR: With a baseline of 130 km, the *CERN-to-Fréjus* (CN2FR) option has the shortest distance from CERN. This would allow to measure δ_{CP} through ν_e / $\overline{\nu}_e$ appearance in a conventional ν_μ / $\overline{\nu}_\mu$ WBB almost without interfering matter effects. Due to the position of the first oscillation maximum at around 0.26 GeV (see Table C.1), the water Cherenkov option MEMPHYS with its ∼500 kt target mass is—similar to the T2K experiment—considered a suitable device to perform measurements in this energy range.

The joint effort of LAGUNA-LBNO culminated in the elaboration of a set of deliverables to the European Union. They document the outcomes of the design study and also include a part of the work presented in Chapter 8. Unfortunately, the pursuit of a new large-volume neutrino observatory in Europe ceased after the end of LAGUNA-LBNO. The attention mostly turned towards the forthcoming large-scale experiments DUNE in the *United States of America* and JUNO in *China* (see Section 4.3).

Appendix D

Multi-GeV Neutrino Beam Events in LENA

Chapter 8 presents a study regarding the neutrino MO and leptonic CP-violation discovery potential of LENA in the CN2PY LBNO experiment with a multi-GeV neutrino WBB beam. One essential input to the `GLoBES`-based sensitivity study is a model to translate the oscillated neutrino energy spectrum to the spectrum of reconstructed event energies. The following deals with two important components of this model, which were created in ancillary studies in the context of this work: An estimate for the *energy-dependent selection efficiencies of fully-contained events in LENA* is subject of Section D.1. The actual conversion from the *true neutrino energy* to the *reconstructed event energy*, which includes the detector's energy resolution capability and is influenced by the selection of fully-contained events, is topic of Section D.2.

D.1 Event containment

In a LSc detector like LENA, the primary information on the energy of an observed neutrino comes from the calorimetric measurement of the total energy deposit, i.e., from the estimate for the *reconstructed visible energy*. However, this estimate is inaccurate in the case of a NC interaction as the neutrino deposits only a fraction of its energy. Moreover, a part of the energy deposit can escape detection. For example, a conversion of energy to undetectable forms, e.g., heat, or the leakage of energy out of the active LSc region through (neutral) particles add to this *missing energy*. Similarly, a neutrino interaction outside of the designated neutrino target can inject some of its charted products into the active region. Although missing energy might be partially recovered at the cost of large systematic uncertainties, the selection of fully-contained events is a key factor to obtain an accurately reconstructed neutrino energy spectrum.
The primary criterion to decide if an event can be tagged as fully-contained naturally bases on the event's reconstructed position and topology inside the LSc volume. This provides another motivation for further development of the reconstruction approach discussed in Chapter 6. Note that the decision regarding an event's containment

status can only base on the reconstructed energy depositions from charged particles. Therefore, an event that was accepted as fully-contained may still include undetected particles that transported significant amounts of energy out of the active detector region. Such an error corrupts the reconstructed neutrino energy spectrum. On the other hand, the error that a fully-contained event is falsely tagged as semi-contained prevents a "good event" from entering the subsequent analyses. For maximum performance of the experiment, it is important to balance these errors. This usually requires dedicated studies with extensive MC simulations.

For LENA, there is not yet an elaborated framework to reconstruct multi-GeV events in the LSc volume. This circumstance makes it difficult obtain reliable containment efficiencies for the `GLoBES`-analysis in Chapter 8. Therefore, the MC truth information of large event samples had to be used to approximate the work of an algorithm dedicated to the rejection of semi-contained events. With a view to a real scenario, a simple rejection rule was qualitatively defined as follows: *Reject an event as semi-contained if*

1. *a relatively large energy deposition is reconstructed close to the edge of the designated target volume, or*

2. *a reconstructed energy deposition close to the edge of the designated target volume exceeds a certain limit.*

This rule was applied to simulated NC and CC interactions of any neutrino flavor with hydrogen and carbon. Five million events per category were simulated with `GENIE`[1]. The neutrino energies were drawn from an almost flat spectrum in the energy range from 0.1 to 10 GeV. All simulations took into account that the CN2PY neutrino beam at the Pyhäsalmi site would come from the lower hemisphere and has an angle of $\sim$79.6° [72] with respect to the symmetry axis of LENA. The evolution of the final state during the propagation through the detector was computed with the LENA detector simulation from Chapter 5.[2] To obtain the MC truths for the different topologies, all events were started at the center of the detector and the simulation of scintillation light was disabled. It was made sure that all events were fully contained by artificially increasing the dimensions of the detector's LSc volume. The information stored for each simulated particle track included the kinetic energy at the particle's origin, its start point and its end point.
Before the analysis of an event, its whole topology was shifted to a random vertex position. All vertices were uniformly distributed over the 96 m high and 28 m wide cylindrical target volume of LENA.[3] For a later application of the above-mentioned rule, the target volume was divided into two subregions: A FV was defined by an inner cylinder with 95 m height and 27 m width. The total reconstructed energy deposition in this region is denoted by E_{fid}. Filling the gap between the FV and the buffer region of LENA, a cylindrical shell with 50 cm thickness at all sides defined the *decision region*. Reconstructed energy depositions in this region are denoted by E_{dec}. Any deposited energy outside of the target volume adds to E_{out}. During the analysis, an event's total energy loss E to the LSc was calculated as $E = \sum_i E_i$,

[1] Version 2.6.6
[2] Decays of tau leptons were processed by `GEANT4`.
[3] Events injecting charged particles into the designated neutrino target from outside are neglected.

where E_i is the energy loss of the i^{th} charged particle track. Energy transfers to other particles and the release of rest mass energy in particle decays were taken into account when E_i was calculated from the MC truth data. Neglecting quenching effects, the summed energy loss $E_{\text{fid}} + E_{\text{dec}}$ of an event was used as estimate for the total amount of reconstructed energy,

$$\hat{E}_{\text{rec}} \equiv E_{\text{fid}} + E_{\text{dec}} \,. \tag{D.1}$$

Further assuming a constant energy loss rate along a straight particle track, the distribution of E over the FV, the decision region and the outer region was determined for each event: $E = E_{\text{fid}} + E_{\text{dec}} + E_{\text{out}}$. This finally allowed to apply the above-stated rule to reject semi-contained events in terms of the following set of conditions:

$$E_{\text{fid}} > 0 \tag{D.2}$$

$$E_{\text{dec}} \leq A \tag{D.3}$$

$$E_{\text{dec}}/E_{\text{fid}} \leq B \tag{D.4}$$

Based on the energy depositions from the charged particle tracks, an event was accepted as fully contained only if it fulfilled all the conditions. If an event failed at one or more conditions, it was rejected as semi-contained. Note that the charged particle tracks of an event are fully contained in the literal sense only if $E_{\text{out}} = 0$. This is hardly testable in a real application. Moreover, according to the most strict definition of full containment, an event must deposit all of E_ν inside the detector's active region. Due to the outgoing neutrino that carries away some energy, this naturally defines a NC event as semi-contained (in principle, the same holds for all events with outgoing neutrinos from charged lepton decays). However, without a dedicated search for missing energy, the charged particle tracks in a NC event could still cause its acceptance as fully contained by the selection conditions above.
Condition D.2 requires that an event has deposited energy in the FV. The second condition rejects events that have a too high total energy deposition in the decision region, i.e., close to the edge of the designated neutrino target volume. Note that in a real case one probably looks for significant peaks in the local density of deposited energy instead of the accumulated energy E_{dec}. This, however, would require input from a topological reconstruction like the one from Chapter 6. Condition D.4 enforces that the major part of the deposited energy is inside the FV. It aims to reject edge events that fulfill the conditions D.2 and D.3 but likely have a large E_{out}.
In the strict sense of "aiming for a selection of fully-contained events", the parameters A and B must be zero. However, non-zero parameter values allow to accept some more of those events as fully contained where, compared to the truly deposited amount, only a small fraction of energy escapes detection, e.g., through LE γ-rays. Looking at the γ-rays that were produced in the detector simulations of the neutrino interactions, Figure D.1 depicts the γ-ray distribution as a function of the start energy and the distance between the start and end points in the simulated LSc. On the one hand, one can clearly see that the majority of γ-rays only has energies $<$10 MeV, which can be invisibly transported over several meters. On the other hand, there are also γ-rays that carry more significant amounts of energy over equally long ranges, potentially introducing a large error to the reconstructed energy with respect to the true amount of deposited energy.

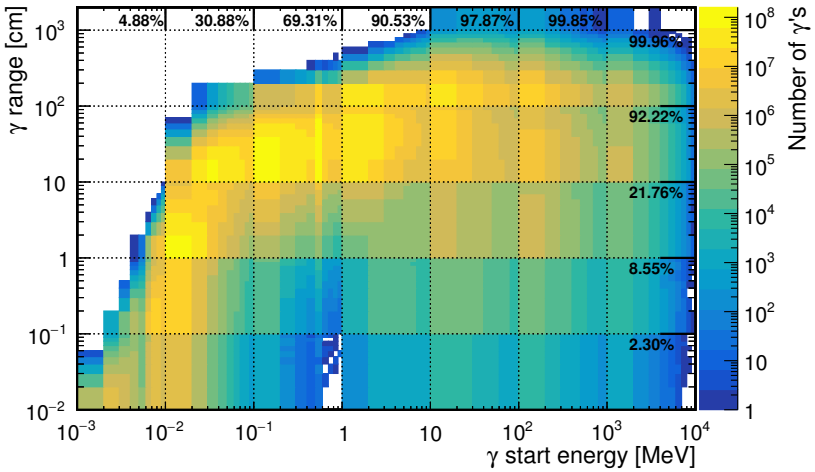

Figure D.1 – Distribution of $\sim 5.5 \times 10^9$ γ-rays as a function of their start energy and the distance between their start and end points. The γ-rays were produced during the detector simulation of 2×10^7 neutrino interactions in the energy range from 0.1 to 10 GeV. The percentages at the upper and right axis indicate the fractions of γ-rays in the distribution up to this point along the corresponding axis.

Table D.1 – Default values of the parameters A and B in the conditions D.3 and D.4 for the `GLoBES` study in Chapter 8.

Parameter	Value
A	75 MeV
B	2 %

In principle, the size of the decision region and the values of the parameters A and B can be tuned to optimize the amount of accepted events together with the rates of the two above-mentioned misidentification cases and their impacts. The figure of merit for the optimization depends on the actual science goal.
Given the approximative nature of this study, the baseline parameters for the `GLoBES`-analysis in Chapter 8 without dedicated optimization are summarized in Table D.1. The containment efficiencies, i.e., *the fractions of events that were selected as fully contained*, are shown in Figure 8.6 as a function of the true neutrino energy E_ν. Figure D.2 depicts them together with the results for A, $B = 0$ as well as with the case where $E_{\text{out}} = 0$ is required. For a given interaction type in Figure D.2, the differences between the efficiencies for the default parameter set and the ideal case $E_{\text{out}} = 0$ are due to misidentifications. The probability for falsely accepting a true semi-contained event, $P(\text{acc} \,|\, \text{semi})$, is shown in Figure D.3 as a function of E_ν. It also shows the probability $P(\text{rej} \,|\, \text{full})$ for the error case that a true fully-contained event is rejected. Recall that an event's true containment status in the current context is defined with respect to the containment of all charged particle tracks. The sum $P(\text{error}) = P(\text{acc} \,|\, \text{semi}) + P(\text{rej} \,|\, \text{full})$ is the probability that the containment algorithm makes an erroneous decision. As one can see, it is $\lesssim 12\,\%$ throughout the considered range of E_ν. The most notable difference in the behavior of the

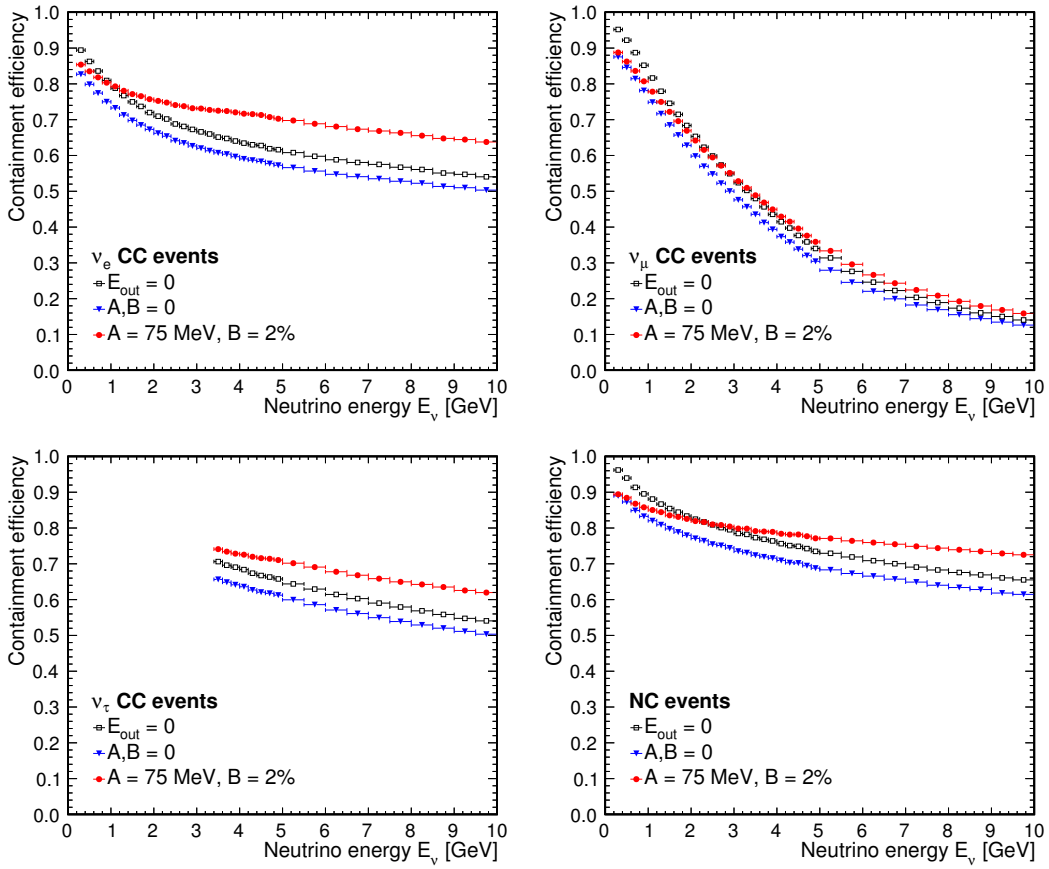

Figure D.2 – Containment efficiencies for ν_e CC **(top left)**, ν_μ CC **(top right)**, ν_τ CC **(bottom left)** and NC **(bottom right)** MC events (5×10^6 per type) as a function of the true neutrino energy E_ν. The efficiency values base on the parameter set in Table D.1 (*red circle*), on the case A, $B = 0$ in the conditions D.3 and D.4 (*blue triangle*) and on the exclusive acceptance of true fully-contained events ($E_{\text{out}} = 0$, *black square*). The binning of E_ν is roughly adjusted to the energy resolution of LENA.

error probabilities is between ν_e and ν_μ CC events. While $P(\text{acc}\,|\,\text{semi})$ increases for ν_e CC events with rising E_ν, it decreases for ν_μ CC events. The main reason is the larger and faster rising number of produced γ-rays in the simulated ν_e CC events. On average, $\sim$500 γ-rays were simulated in a single ν_e CC event, which is three times more than the number of produced γ-rays in a ν_μ CC event. The higher number of γ-rays in the end leads to a higher probability that energy invisibly crosses the decision region and adds to the energy leakage E_{out}. At the same time, the track lengths for muons from ν_μ CC interactions almost linearly grow with rising E_ν. Once their track length are similar to the diameter of the FV, it gets more and more unlikely that a semi-contained event is not correctly identified. This leads to a decrease in $P(\text{acc}\,|\,\text{semi})$. Figure D.4 shows the distribution of E_{out} as a function of E_ν for events that were accepted as fully contained with the parameters in Table D.1. Although the lost amounts of energy range up to several GeV, $\geq 75\,\%$ of the events in the considered E_ν range lose $\leq 100\,\text{MeV}$, which is approximately the mean value of E_{out}.

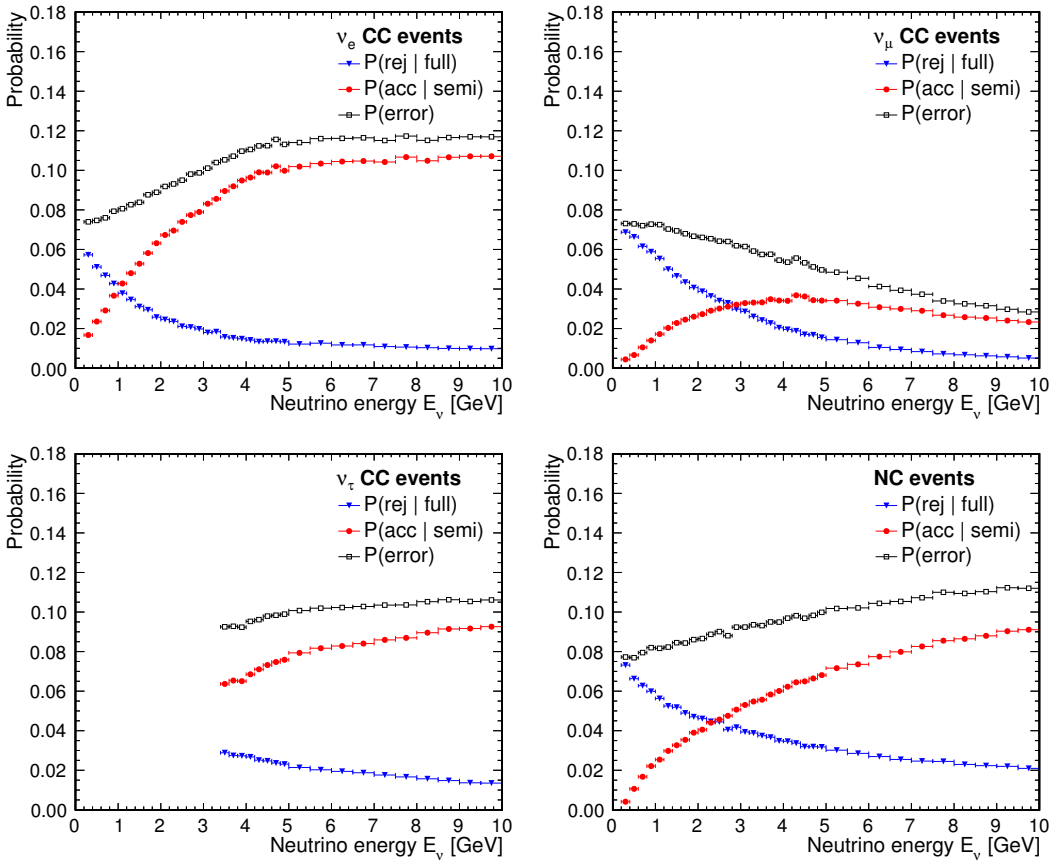

Figure D.3 – Probabilities of erroneous containment identifications for ν_e CC **(top left)**, ν_μ CC **(top right)**, ν_τ CC **(bottom left)** and NC **(bottom right)** MC events (5×10^6 per type) as a function of the true neutrino energy E_ν. The values base on the parameter set in Table D.1. $P(\text{rej}\,|\,\text{full})$ (*blue triangle*) is the probability that a true fully-contained event is rejected. The probability for falsely accepting a true semi-contained event is denoted by $P(\text{acc}\,|\,\text{semi})$ (*red circle*). By summing both probabilities, one obtains $P(\text{error})$ (*black square*), the total probability that the algorithm makes a wrong decision. The binning of E_ν is roughly adjusted to the energy resolution of LENA.

D.2 Event energy reconstruction

In the context of a calorimetric energy measurement with a LSc detector, the amount of visible energy is deduced from the amount of observed PEs. This conversion requires a good knowledge on the properties of the LSc, e.g., the spatial dependence of the PE yield, and the photosensors. Nevertheless, random fluctuations in the light propagation and detection as well as imprecisions from the event reconstruction yield an uncertainty for the reconstructed energy with respect to the true amount of deposited energy. As a result, the translation from the true neutrino energy E_ν to the reconstructed energy $\hat{E}_{\text{rec}}$ includes the effects from both the previously discussed event containment and a limited energy resolution.

The `GLoBES` framework, which is used for the study in Chapter 8, incorporates the translation from E_ν to $\hat{E}_{\text{rec}}$ with so-called *energy migration matrices* $\mathcal{M}^t_{i,j}$. For a given

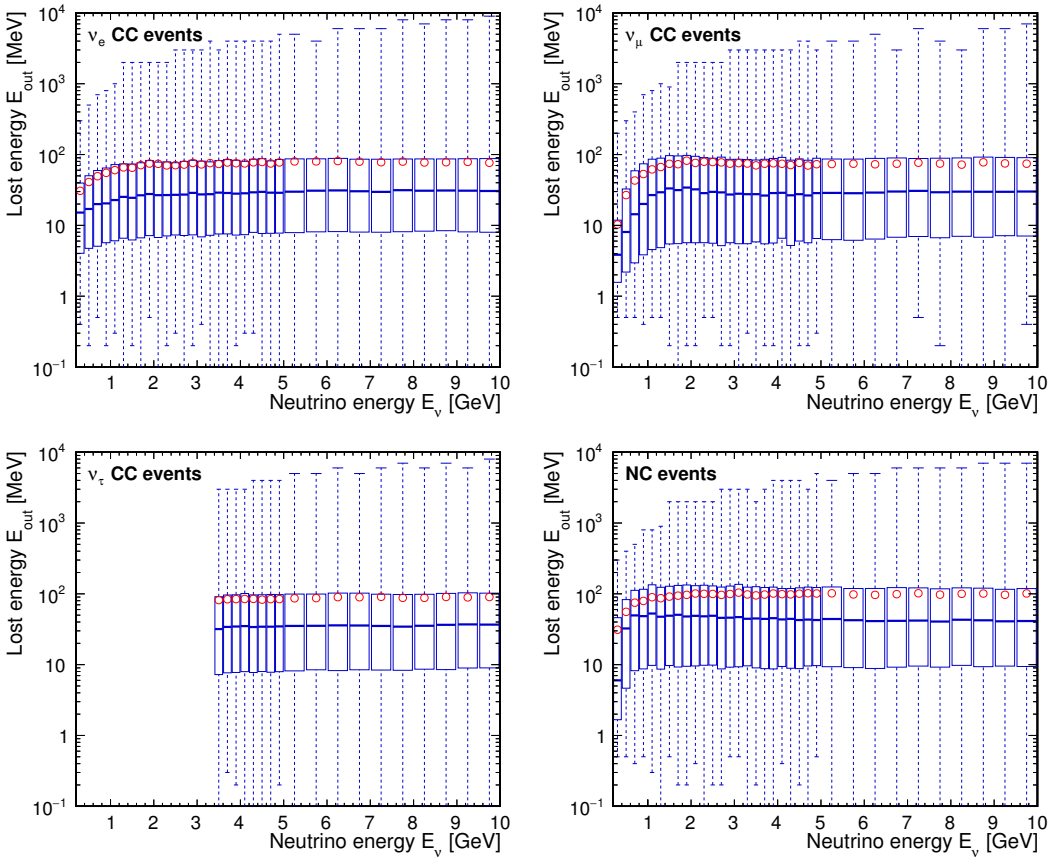

Figure D.4 – Lost energy E_{out} from ν_e CC **(top left)**, ν_μ CC **(top right)**, ν_τ CC **(bottom left)** and NC **(bottom right)** MC events (5×10^6 per type) as a function of the true neutrino energy E_ν. The values base on the parameter set in Table D.1. E_{out} is the sum of energy depositions from charged particle track segments outside of the active target region of LENA. The vertical dashed lines indicate the ranges of E_{out} values. Thick, horizontal lines mark the median values in the single E_ν-bins. Red circles highlight the mean values of E_{out}. The boxes contain 50 % of the E_{out} values in such a way that 25 % of the values are below the lower bound (25 %-quantile) and 75 % of the values are below the upper bound (75 %-quantile). The binning of E_ν is roughly adjusted to the energy resolution of LENA.

neutrino interaction type t, the column index j runs over the true neutrino energy bins $E_{\nu,j}$; the row index i covers the sample points of the distribution $P(\hat{E}_{\text{rec}}|E_{\nu,j})$. Since a neutrino in a given bin $E_{\nu,j}$ must be *smeared* to anywhere in $\hat{E}_{\text{rec}}(E_{\nu,j})$ space, the normalization condition for $\mathcal{M}^t_{i,j}$ is

$$\sum_i \mathcal{M}^t_{i,j} = 1 \quad \forall j \,. \tag{D.5}$$

Energy migration matrices were created from simulated NC and CC events of all neutrino flavors that were accepted as as fully contained in the course of the analysis detailed in Section D.1. For this purpose, the reconstructed energy value $\hat{E}_{\text{rec}}$ from Equation (D.1), which does not take a finite energy resolution into account, was

redefined as

$$\hat{E}_{\mathrm{rec}} = \hat{E}^{*}_{\mathrm{rec}} + X\,, \quad X \text{ from } \mathcal{N}(0, a \times \hat{E}^{*}_{\mathrm{rec}})\,, \quad a > 0\,. \tag{D.6}$$

The quantity $\hat{E}^{*}_{\mathrm{rec}}$ equals the right side of Equation (D.1). It is randomly shifted by a value X that is drawn from a normal distribution around zero and with a standard deviation of $a \times \hat{E}^{*}_{\mathrm{rec}}$. The parameter a represents the *relative energy resolution*. Migration matrices obtained with the default value of $a = 7\,\%$ are shown in Figure 8.7. They are very similar to results in Ref. [51], which were created with full MC simulations and subsequent energy reconstructions[4]. Compared to these outcomes, the matrices created with Equation (D.6) do not account for energy quenching and (systematic) effects from reconstruction. Furthermore, they only account for the detector's energy resolution capability in a statistical way with a simple Gaussian model. However, they include the right proportions of effects from energy leakage in falsely accepted semi-contained events. Therefore, the matrices created in this study are used for the `GLoBES`-analysis in Chapter 8 together with the containment efficiencies from Section D.1. For comparison, Figure D.5 shows a set of migration matrices including a finite energy resolution but no algorithmic selection of fully-contained events. A significant chance of a strong migration to lower reconstructed energy for a given E_ν is now visible for all neutrino event types.

[4]The energy estimate assumes a point-like event at the position of the event's reconstructed charge barycenter.

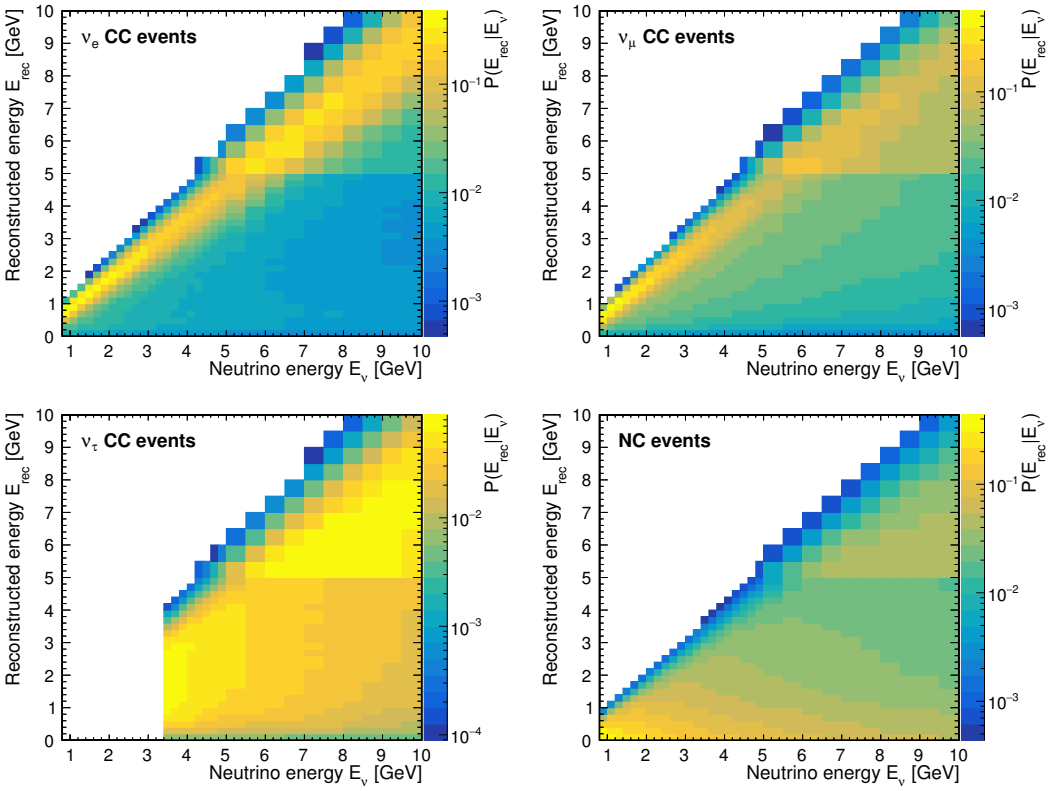

Figure D.5 – Same as Figure 8.7, but without the selection of fully-contained events with the algorithm from Section D.1.

Appendix E

Additional Plots and Tables

The following presents additional plots and tables for Chapter 7 about the results from the performance evaluation of the novel track reconstruction method.

Angular resolution

Table E.1 – Properties of the distributions of the intermediate angle α analyzed to obtain the results for the angular resolutions σ_α on the right side of Figure 7.6. For each energy bin E in the figure, the underlying number of events N, the sample mean value $\overline{\alpha}$ and the sample standard deviation $S_{\alpha,0}$ with respect to $\overline{\alpha} = 0$ are given.

E [GeV]	N	$\overline{\alpha}$ [°]	$S_{\alpha,0}$ [°]
1–2	868	1.72	2.11
2–3	603	1.07	1.79
3–4	320	0.78	0.94
4–5	209	1.71	8.78
5–6	2675	1.64	8.79
6–7	816	1.11	6.32
7–8	610	0.95	5.20
8–9	561	1.16	7.48
9–10	438	1.04	6.21

Start point resolution

Table E.2 – Properties of the distributions of the components $u_{s,x}$, $u_{s,y}$ and $u_{s,z}$ analyzed to obtain the results for the start point resolutions $\sigma_{s,x}$, $\sigma_{s,y}$ and $\sigma_{s,z}$ on the right side of Figure 7.7. For each energy bin E and component $u_{s,c}$, the sample mean value $\overline{u}_{s,c}$ and the sample standard deviation $S_{s,c}$ are given. The numbers of events in the energy bins are the same as listed in Table E.1.

E [GeV]	$\overline{u}_{s,x}$ [cm]	$S_{s,x}$ [cm]	$\overline{u}_{s,y}$ [cm]	$S_{s,y}$ [cm]	$\overline{u}_{s,z}$ [cm]	$S_{s,z}$ [cm]
1–2	−0.2	13.0	0.2	13.0	0.4	14.8
2–3	0.4	18.0	−1.0	17.3	−0.5	19.4
3–4	−1.8	28.7	1.7	31.8	−0.3	39.0
4–5	1.3	44.6	−2.3	43.0	−0.7	75.8
5–6	1.2	62.5	1.0	59.2	−4.4	110.4
6–7	3.0	42.5	−0.5	53.6	−0.9	132.0
7–8	3.8	71.6	0.3	59.6	10.9	178.8
8–9	−1.1	41.0	−3.3	52.9	−1.2	162.5
9–10	2.3	56.9	2.2	46.4	10.0	140.5

Table E.3 – Properties of the distributions of the component $u_{s,\text{para}}$ analyzed to obtain the results for the parallel start point resolution $\sigma_{s,\text{para}}$ on the left side of Figure 7.9. For each energy bin E, the sample mean value $\overline{u}_{s,\text{para}}$ and the left- (right-) sided standard deviation $S_{s,\text{para},-}$ ($S_{s,\text{para},+}$) with respect to $\overline{u}_{s,\text{para}}$ are given. The numbers of events in the energy bins are the same as listed in Table E.1.

E [GeV]	$\overline{u}_{s,\text{para}}$ [cm]	$S_{s,\text{para},-}$ [cm]	$S_{s,\text{para},+}$ [cm]
1–2	−0.8	13.0	10.3
2–3	−5.2	32.1	12.3
3–4	−17.7	99.5	20.3
4–5	−37.0	157.6	38.1
5–6	−50.9	218.0	50.8
6–7	−63.6	198.1	62.7
7–8	−80.7	307.7	76.2
8–9	−73.2	262.6	70.0
9–10	−81.0	200.8	76.3

Table E.4 – Properties of the distributions of the component $u_{s,\mathrm{lat}}$ analyzed to obtain the results for the lateral start point resolution $\sigma_{s,\mathrm{lat}}$ on the left side of Figure 7.9. For each energy bin E, the sample mean value $\overline{u}_{s,\mathrm{lat}}$ and the standard deviation $S_{s,\mathrm{lat},0}$ with respect to $\overline{u}_{s,\mathrm{lat}} = 0$ are given. The numbers of events in the energy bins are the same as listed in Table E.1.

E [GeV]	$\overline{u}_{s,\mathrm{lat}}$ [cm]	$S_{s,\mathrm{lat},0}$ [cm]
1–2	17.6	20.6
2–3	19.1	22.4
3–4	22.1	26.9
4–5	25.1	38.6
5–6	28.4	50.4
6–7	28.2	57.8
7–8	29.6	51.3
8–9	28.3	45.9
9–10	26.7	37.6

End point resolution

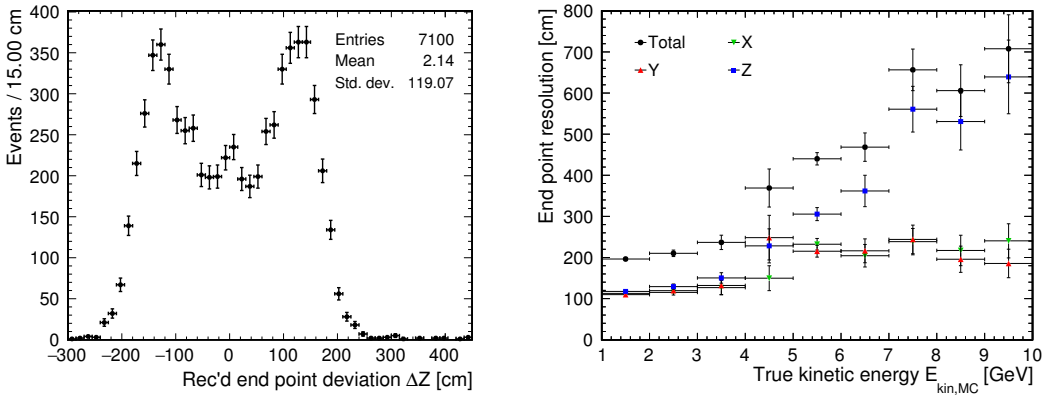

Figure E.1 – **Left:** Distribution of the deviation $\Delta z \equiv u_{e,z}$ of the reconstructed muon track end point from the true end point in z-direction (detector coordinate system) for events with $E_{\mathrm{kin,MC}}$ in the range from 1 to 10 GeV. The left (right) peak originates from the systematic end point shifts for muon tracks at higher energies that go mostly downward (upward) in the detector, essentially parallel to the z-axis. Vertical error bars indicate statistical errors only. There are 92 (100) events with smaller (larger) values of Δz outside of the shown range. **Right:** End point resolutions $S_{e,x}$ (*green tip down triangle*), $S_{e,y}$ (*red tip up triangle*) and $S_{e,z}$ (*blue square*) along the detector coordinates x, y and z as a function of the true kinetic energy $E_{\mathrm{kin,MC}}$ in the range from 1 to 10 GeV. They were obtained as sample standard deviations from the distributions of $u_{e,x}$, $u_{e,y}$ and $u_{e,z}$; vertical error bars were calculated as the square root of the variance of the unbiased sample variance. The total resolution (*black circles*) was calculated as the square root of the sum of the squared resolutions in the three directions. Errors for the total resolution were determined with Gaussian error propagation. Note that the resolution measure shown in this plot is different to the one shown in the corresponding plot on the right side of Figure 7.7 for the start point!

Table E.5 – Properties of the distributions of the components $u_{e,x}$, $u_{e,y}$ and $u_{e,z}$ analyzed to obtain the results for the end resolutions $S_{e,x}$, $S_{e,y}$ and $S_{e,z}$ on the right side of Figure E.1. For each energy bin E and component $u_{e,c}$, the sample mean value $\overline{u}_{e,c}$ and the sample standard deviation $S_{e,c}$ are given. The numbers of events in the energy bins are the same as listed in Table E.1.

E [GeV]	$\overline{u}_{e,x}$ [cm]	$S_{e,x}$ [cm]	$\overline{u}_{e,y}$ [cm]	$S_{e,y}$ [cm]	$\overline{u}_{e,z}$ [cm]	$S_{e,z}$ [cm]
1–2	3.8	112.8	−1.8	109.7	2.2	117.5
2–3	−7.0	115.1	0.8	119.4	−8.6	129.2
3–4	−6.6	126.7	−7.9	132.0	−0.7	150.3
4–5	0.1	149.7	15.1	248.3	1.5	228.3
5–6	−1.4	232.3	−8.0	215.3	−9.4	305.6
6–7	−9.8	204.3	4.5	216.3	−3.2	361.9
7–8	−7.5	238.6	−12.3	244.0	20.7	560.8
8–9	−8.4	217.1	−5.7	195.8	−36.4	530.7
9–10	−24.9	240.5	−8.1	185.5	−28.8	639.2

Table E.6 – Properties of the distributions of the component $u_{e,\text{para}}$ analyzed to obtain the results for the parallel end point resolution $\sigma_{e,\text{para}}$ in Figure 7.10. For each energy bin E, the sample mean value $\overline{u}_{e,\text{para}}$ and the left- (right-) sided standard deviation $S_{e,\text{para},-}$ ($S_{e,\text{para},+}$) with respect to $\overline{u}_{e,\text{para}}$ are given. Moreover, the values of the parameter μ_{peak} from the fit function (7.14) are listed, which describes the position of the peak in the distribution. The numbers of events in the energy bins are the same as listed in Table E.1.

E [GeV]	μ_{peak} [cm]	$\overline{u}_{e,\text{para}}$ [cm]	$S_{e,\text{para},-}$ [cm]	$S_{e,\text{para},+}$ [cm]
1–2	-197 ± 5	−172.4	65.7	121.3
2–3	-194 ± 4	−166.6	82.1	171.9
3–4	-180 ± 6	−146.7	79.8	289.6
4–5	-165 ± 6	−97.8	98.8	467.4
5–6	-156 ± 4	−63.4	107.9	722.3
6–7	-145 ± 4	−72.7	86.5	903.8
7–8	-131 ± 3	5.6	137.6	2218.0
8–9	-120 ± 3	−48.5	92.1	1420.0
9–10	-126 ± 7	−11.2	110.0	2573.4

Table E.7 – Descriptive statistics for the distributions of the component $u_{e,\mathrm{lat}}$ analyzed to obtain the results for the lateral end point resolution $\sigma_{e,\mathrm{lat}}$ in Figure 7.10. For each energy bin E, the sample mean value $\overline{u}_{e,\mathrm{lat}}$ and the standard deviation $S_{e,\mathrm{lat},0}$ with respect to $\overline{u}_{e,\mathrm{lat}} = 0$ are given. The numbers of events in the energy bins are the same as listed in Table E.1.

E [GeV]	$\overline{u}_{e,\mathrm{lat}}$ [cm]	$S_{e,\mathrm{lat},0}$ [cm]
1–2	15.3	18.4
2–3	17.9	22.0
3–4	19.6	23.5
4–5	50.4	230.0
5–6	55.5	254.3
6–7	54.8	267.9
7–8	54.9	258.0
8–9	71.3	391.6
9–10	72.2	377.3

Track length

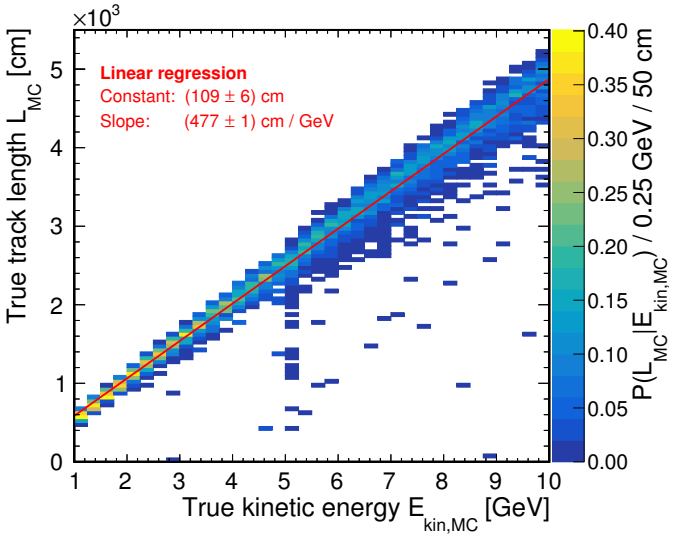

Figure E.2 – Binned relative frequency distributions $P(L_{\mathrm{MC}}|E_{\mathrm{kin,MC}})$ as a function of the true kinetic energy $E_{\mathrm{kin,MC}}$ in the range from 1 to 10 GeV. The distributions were created from the MC truths of the simulated muons shown on the left of Figure 7.1. The *red* line illustrates the result from a linear regression performed with the underlying data.

List of Abbreviations and Acronyms

$0\nu\beta\beta$	neutrinoless double-beta
ADC	analog-to-digital converter
a.u.	arbitrary units
BIRD	Batch Infrastruktur Resource am DESY – Batch infrastructure resource at DESY
bis-MSB	1,4-Bis(2-methylstyryl)benzene
BooNE	Booster Neutrino Experiment
BR	branching ratio
CC	charged current
CERN	Conseil Européen pour la Recherche Nucléaire – European Organization for Nuclear Research
CL	confidence level
CN2FR	CERN-to-Fréjus
CN2PY	CERN-to-Pyhäsalmi
CNGS	CERN Neutrinos to Gran Sasso
CPU	central processing unit
DAQ	data acquisition system
DESY	Deutsches Elektronen-Synchrotron – German electron synchrotron
DONUT	Direct Observation of NU Tau
DSNB	diffuse supernova neutrino background
DUNE	Deep Underground Neutrino Experiment
EC	electron capture
ES	elastic scattering

EVE	Event Visualization Environment
FGI	Finnish Grid Infrastructure
FNAL	Fermi National Accelerator Laboratory
FV	fiducial volume
FWHM	full width at half maximum
GALLEX	Gallium Experiment
GERDA	Germanium Detector Array
GLACIER	Giant Liquid Argon Charge Imaging Experiment
GLoBES	General Long Baseline Experiment Simulator
GPU	graphics processing unit
GUT	Grand Unified Theory
HE	high-energy
HP-PS	high-power proton synchrotron
IBD	inverse beta decay
ICARUS	Imaging Cosmic and Rare Underground Signals
IO	inverted ordering
J-PARC	Japan Proton Accelerator Research Complex
JUNO	Jiangmen Underground Neutrino Observatory
Kamiokande	Kamioka Nucleon Decay Experiment
KamLAND	Kamioka Liquid Scintillator Antineutrino Detector
KATRIN	Karlsruhe Tritium Neutrino Experiment
LAB	linear alkylbenzene
LAGUNA	Large Apparatus for Grand Unification and Neutrino Astrophysics
LAr	liquid argon
LBNE	Long-Baseline Neutrino Experiment
LBNO	long-baseline neutrino oscillation
LE	low-energy
LENA	Low Energy Neutrino Astronomy
LH	left-handed
LIGO	Laser Interferometer Gravitational-Wave Observatory
LNGS	Laboratori Nazionali del Gran Sasso

LSc	liquid scintillator
LSM	Laboratoire Souterrain de Modane
LUT	look-up table
MC	Monte Carlo
MCP	micro-channel plate
MEMPHYS	Megaton Mass Physics
MINERνA	Main Injector Experiment for ν-A
MINOS	Main Injector Neutrino Oscillation Search
MO	mass ordering
MSW	Mikheyev–Smirnov–Wolfenstein
NBB	narrow band beam
NC	neutral current
NHF	negative horn focusing
NO	normal ordering
NOνA	NuMI Off-axis ν_e Appearance
NuMI	Neutrinos at the Main Injector
OM	optical module
OPERA	Oscillation Project with Emulsion-Tracking Apparatus
p.d.f.	probability density function
PE	photoelectron
PHF	positive horn focusing
PMNS	Pontecorvo–Maki–Nakagawa–Sakata
PMT	photomultiplier tube
POT	protons on target
PPO	2,5-diphenyloxazole
PXE	phenyl-o-xylylethane
QE	quantum efficiency
QEL	quasi-elastic
PREM	Preliminary Reference Earth Model
RENO	Reactor Experiment for Neutrino Oscillation
RH	right-handed
RMS	root mean square

ROI	region of interest
SAGE	Soviet–American Gallium Experiment
SciBooNE	SciBar BooNE
SHiP	Search for Hidden Particles
SK	Super-Kamiokande
SM	Standard Model
SN	supernova
SNEWS	SuperNova Early Warning System
SNO	Sudbury Neutrino Observatory
SOX	Short distance neutrino oscillations with Borexino
SPS	Super Proton Synchrotron
SSM	Standard Solar Model
T2K	Tokai-to-Kamioka
TOF	time of flight
TPC	time projection chamber
TTS	transit time spread
WBB	wide band beam
w.e.	water-equivalent

Bibliography

[1] U. Lindenberg, *Mein Hermann Hesse* (Suhrkamp Verlag GmbH, 2008).

[2] J. Chadwick, *The intensity distribution in the magnetic spectrum of beta particles from radium (B + C)*, Verh. Phys. Gesell. **16**, 383 (1914).

[3] W. Pauli, *Dear radioactive ladies and gentlemen*, Phys. Today **31N9**, 27 (1978).

[4] F. Hoyle, *Concluding Remarks*, Proceedings of the Royal Society of London A: Mathematical, Physical and Engineering Sciences **301**, 171 (1967).

[5] F. Reines and C. Cowan, *Detection of the free neutrino*, Phys.Rev. **92**, 830 (1953).

[6] C. Cowan, F. Reines, F. Harrison, H. Kruse and A. McGuire, *Detection of the free neutrino: A Confirmation*, Science **124**, 103 (1956).

[7] F. Reines and C. Cowan, *The Reines-Cowan experiments: Detecting the Poltergeist*, Los Alamos Sci. **25**, 4 (1997).

[8] Nobel Foundation / Nobel Media AB, The Official Web Site of the Nobel Prize, `http://www.nobelprize.org/`, 2015, Accessed November 18, 2015.

[9] G. Danby *et al.*, *Observation of High-Energy Neutrino Reactions and the Existence of Two Kinds of Neutrinos*, Phys.Rev.Lett. **9**, 36 (1962).

[10] DONUT, K. Kodama *et al.*, *Observation of tau neutrino interactions*, Phys. Lett. **B504**, 218 (2001), [hep-ex/0012035].

[11] Particle Data Group, K. A. Olive *et al.*, *Review of Particle Physics (RPP)*, Chin.Phys. **C38**, 090001 (2014).

[12] S. Alekhin *et al.*, *A facility to Search for Hidden Particles at the CERN SPS: the SHiP physics case*, hep-ph/1504.04855.

[13] J. N. Bahcall and R. Davis, *Solar Neutrinos - a Scientific Puzzle*, Science **191**, 264 (1976).

[14] B. Cleveland *et al.*, *Measurement of the solar electron neutrino flux with the Homestake chlorine detector*, Astrophys.J. **496**, 505 (1998).

[15] J. N. Bahcall, *Solar models: An Historical overview*, AAPPS Bull. **12N4**, 12 (2002), [astro-ph/0209080].

[16] J. N. Bahcall, A. M. Serenelli and S. Basu, *New solar opacities, abundances, helioseismology, and neutrino fluxes*, Astrophys.J. **621**, L85 (2005), [astro-ph/0412440].

[17] Kamiokande-II, K. Hirata *et al.*, *Observation of B-8 Solar Neutrinos in the Kamiokande-II Detector*, Phys.Rev.Lett. **63**, 16 (1989).

[18] B. Pontecorvo, *Neutrino Experiments and the Problem of Conservation of Leptonic Charge*, Sov.Phys.JETP **26**, 984 (1968).

[19] SNO, J. Boger *et al.*, *The Sudbury neutrino observatory*, Nucl.Instrum.Meth. **A449**, 172 (2000), [nucl-ex/9910016].

[20] SNO, Q. Ahmad *et al.*, *Measurement of the rate of $\nu_e + d \to p + p + e^-$ interactions produced by ^8B solar neutrinos at the Sudbury Neutrino Observatory*, Phys.Rev.Lett. **87**, 071301 (2001), [nucl-ex/0106015].

[21] SNO, Q. Ahmad *et al.*, *Direct evidence for neutrino flavor transformation from neutral current interactions in the Sudbury Neutrino Observatory*, Phys.Rev.Lett. **89**, 011301 (2002), [nucl-ex/0204008].

[22] Super-Kamiokande Collaboration, Y. Fukuda *et al.*, *The Super-Kamiokande detector*, Nucl.Instrum.Meth. **A501**, 418 (2003).

[23] Super-Kamiokande, Y. Fukuda *et al.*, *Evidence for oscillation of atmospheric neutrinos*, Phys.Rev.Lett. **81**, 1562 (1998), [hep-ex/9807003].

[24] OPERA, M. Guler *et al.*, *OPERA: An appearance experiment to search for $\nu_\mu \leftrightarrow \nu_\tau$ oscillations in the CNGS beam. Experimental proposal*, (2000).

[25] OPERA, N. Agafonova *et al.*, *Discovery of τ Neutrino Appearance in the CNGS Neutrino Beam with the OPERA Experiment*, Phys. Rev. Lett. **115**, 121802 (2015), [hep-ex/1507.01417].

[26] X. Qian and P. Vogel, *Neutrino Mass Hierarchy*, Prog. Part. Nucl. Phys. **83**, 1 (2015), [hep-ex/1505.01891].

[27] Planck, P. A. R. Ade *et al.*, *Planck 2015 results. XIII. Cosmological parameters*, astro-ph.CO/1502.01589.

[28] G. C. Branco, R. G. Felipe and F. R. Joaquim, *Leptonic CP Violation*, Rev. Mod. Phys. **84**, 515 (2012), [hep-ph/1111.5332].

[29] P. Alivisatos *et al.*, *KamLAND: A Liquid scintillator anti-neutrino detector at the Kamioka site*, (1998).

[30] Borexino Collaboration, G. Bellini *et al.*, *Final results of Borexino Phase-I on low energy solar neutrino spectroscopy*, Phys.Rev. **D89**, 112007 (2014), [hep-ex/1308.0443].

[31] BOREXINO Collaboration, G. Bellini *et al.*, *Neutrinos from the primary proton–proton fusion process in the Sun*, Nature **512**, 383 (2014).

[32] KamLAND, A. Gando *et al.*, *Reactor On-Off Antineutrino Measurement with KamLAND*, Phys.Rev. **D88**, 033001 (2013), [hep-ex/1303.4667].

[33] Borexino, M. Agostini *et al.*, *Spectroscopy of geoneutrinos from 2056 days of Borexino data*, Phys. Rev. **D92**, 031101 (2015), [hep-ex/1506.04610].

[34] Double Chooz, F. Ardellier *et al.*, *Double Chooz: A Search for the neutrino mixing angle theta(13)*, hep-ex/0606025.

[35] Daya Bay, X. Guo *et al.*, *A Precision measurement of the neutrino mixing angle θ_{13} using reactor antineutrinos at Daya-Bay*, hep-ex/0701029.

[36] RENO, J. Ahn *et al.*, *RENO: An Experiment for Neutrino Oscillation Parameter θ_{13} Using Reactor Neutrinos at Yonggwang*, hep-ex/1003.1391.

[37] Borexino, G. Bellini *et al.*, *Muon and Cosmogenic Neutron Detection in Borexino*, JINST **6**, P05005 (2011), [physics.ins-det/1101.3101].

[38] Double Chooz, Y. Abe *et al.*, *Precision Muon Reconstruction in Double Chooz*, Nucl. Instrum. Meth. **A764**, 330 (2014), [physics.ins-det/1405.6227].

[39] B. S. Wonsak, Institut für Experimentalphysik, Universität Hamburg, Private communication, 2013–2015.

[40] LENA Collaboration, M. Wurm *et al.*, *The next-generation liquid-scintillator neutrino observatory LENA*, Astropart.Phys. **35**, 685 (2012), [astro-ph.IM/1104.5620].

[41] S.-B. Kim, *New results from RENO and prospects with RENO-50*, Nucl. Part. Phys. Proc. **265-266**, 93 (2015), [hep-ex/1412.2199].

[42] JUNO, F. An *et al.*, *Neutrino Physics with JUNO*, J. Phys. **G43**, 030401 (2016), [physics.ins-det/1507.05613].

[43] JUNO, Z. Djurcic *et al.*, *JUNO Conceptual Design Report*, physics.ins-det/1508.07166.

[44] LAGUNA Collaboration, A. Rubbia, *The LAGUNA design study: Towards giant liquid based underground detectors for neutrino physics and astrophysics and proton decay searches*, Acta Phys.Polon. **B41**, 1727 (2010).

[45] Laguna Collaboration, T. Patzak, *Laguna: Future megaton detectors in europe*, J.Phys.Conf.Ser. **309**, 012022 (2011).

[46] LAGUNA-LBNO Collaboration, T. Patzak, *LAGUNA and LAGUNA-LBNO: Future megaton neutrino detectors in Europe*, Nucl.Instrum.Meth. **A695**, 184 (2012).

[47] A. Rubbia, *LAGUNA-LBNO: Design of an underground neutrino observatory coupled to long baseline neutrino beams from CERN*, J.Phys.Conf.Ser. **408**, 012006 (2013).

[48] J. G. Learned, *High Energy Neutrino Physics with Liquid Scintillation Detectors*, hep-ex/0902.4009.

[49] J. Peltoniemi, *Liquid scintillator as tracking detector for high-energy events*, physics.ins-det/0909.4974.

[50] D. Hellgartner, *Lepton track reconstruction in LENA and attenuation length measurements in liquid scintillators*, Diploma thesis, Munich, Tech. U., 2011.

[51] D. Hellgartner, *Advanced Event Reconstruction in LENA and Precision Attenuation-Length Measurements in Liquid Scintillators*, Dissertation, Munich, Tech. U., Munich, 2015.

[52] P. Schmüser, *Feynman-Graphen und Eichtheorien für Experimentalphysiker* (Springer, 1995).

[53] S. King, *Neutrino mass models*, Rept.Prog.Phys. **67**, 107 (2004), [hep-ph/0310204].

[54] B. Pontecorvo, *Mesonium and anti-mesonium*, Sov.Phys.JETP **6**, 429 (1957).

[55] B. Pontecorvo, *Inverse beta processes and nonconservation of lepton charge*, Sov.Phys.JETP **7**, 172 (1958).

[56] S. M. Bilenky and B. Pontecorvo, *Quark-Lepton Analogy and Neutrino Oscillations*, Phys.Lett. **B61**, 248 (1976).

[57] Super-Kamiokande, S. Fukuda *et al.*, *Solar B-8 and hep neutrino measurements from 1258 days of Super-Kamiokande data*, Phys.Rev.Lett. **86**, 5651 (2001), [hep-ex/0103032].

[58] S. Bilenky, *Introduction to the Physics of Massive and Mixed Neutrinos (Lecture Notes in Physics)* (Springer, 2010).

[59] L. Wolfenstein, *Neutrino Oscillations in Matter*, Phys.Rev. **D17**, 2369 (1978).

[60] S. Mikheev and A. Y. Smirnov, *Resonance Amplification of Oscillations in Matter and Spectroscopy of Solar Neutrinos*, Sov.J.Nucl.Phys. **42**, 913 (1985).

[61] E. K. Akhmedov, *Parametric resonance in neutrino oscillations in matter*, Pramana **54**, 47 (2000), [hep-ph/9907435].

[62] Z. Maki, M. Nakagawa and S. Sakata, *Remarks on the unified model of elementary particles*, Prog.Theor.Phys. **28**, 870 (1962).

[63] T2K Collaboration, K. Abe *et al.*, *The T2K Experiment*, Nucl.Instrum.Meth. **A659**, 106 (2011), [physics.ins-det/1106.1238].

[64] MINOS, P. Adamson *et al.*, *A Study of Muon Neutrino Disappearance Using the Fermilab Main Injector Neutrino Beam*, Phys.Rev. **D77**, 072002 (2008), [hep-ex/0711.0769].

[65] M. Gonzalez-Garcia, M. Maltoni and T. Schwetz, *Updated fit to three neutrino mixing: status of leptonic CP violation*, JHEP **1411**, 052 (2014), [hep-ph/1409.5439].

[66] D. Forero, M. Tortola and J. Valle, *Neutrino oscillations refitted*, Phys.Rev. **D90**, 093006 (2014), [hep-ph/1405.7540].

[67] NOvA Collaboration, D. Ayres *et al.*, *NOvA: Proposal to build a 30 kiloton off-axis detector to study $\nu_\mu \to \nu_e$ oscillations in the NuMI beamline*, hep-ex/0503053.

[68] S. K. Agarwalla, S. Prakash and S. U. Sankar, *Resolving the octant of θ_{23} with T2K and NOvA*, JHEP **1307**, 131 (2013), [hep-ph/1301.2574].

[69] M. Blennow, P. Coloma, P. Huber and T. Schwetz, *Quantifying the sensitivity of oscillation experiments to the neutrino mass ordering*, JHEP **1403**, 028 (2014), [hep-ph/1311.1822].

[70] M. Blennow, P. Coloma and E. Fernandez-Martinez, *Reassessing the sensitivity to leptonic CP violation*, JHEP **1503**, 005 (2015), [hep-ph/1407.3274].

[71] K. Deepthi, C. Soumya and R. Mohanta, *Revisiting the sensitivity studies for leptonic CP-violation and mass hierarchy with T2K, NOvA and LBNE experiments*, New J.Phys. **17**, 023035 (2015), [hep-ph/1409.2343].

[72] A. Stahl *et al.*, *Expression of Interest for a very long baseline neutrino oscillation experiment (LBNO)*, (2012).

[73] LBNE, C. Adams *et al.*, *The Long-Baseline Neutrino Experiment: Exploring Fundamental Symmetries of the Universe*, hep-ex/1307.7335.

[74] Hyper-Kamiokande Working Group, K. Abe *et al.*, *A Long Baseline Neutrino Oscillation Experiment Using J-PARC Neutrino Beam and Hyper-Kamiokande*, physics.ins-det/1412.4673.

[75] ESSnuSB, E. Baussan *et al.*, *A very intense neutrino super beam experiment for leptonic CP violation discovery based on the European spallation source linac*, Nucl.Phys. **B885**, 127 (2014), [hep-ex/1309.7022].

[76] ICAL, S. Ahmed *et al.*, *Physics Potential of the ICAL detector at the India-based Neutrino Observatory (INO)*, physics.ins-det/1505.07380.

[77] KM3NeT, U. F. Katz, *The ORCA Option for KM3NeT*, PoS (2014), [astro-ph.IM/1402.1022].

[78] IceCube PINGU, M. Aartsen *et al.*, *Letter of Intent: The Precision IceCube Next Generation Upgrade (PINGU)*, physics.ins-det/1401.2046.

[79] S. Razzaque and A. Y. Smirnov, *Super-PINGU for measurement of the leptonic CP-phase with atmospheric neutrinos*, hep-ph/1406.1407.

[80] K. Scholberg, *Supernova Neutrino Detection*, Ann.Rev.Nucl.Part.Sci. **62**, 81 (2012), [astro-ph.IM/1205.6003].

[81] J. Formaggio and G. Zeller, *From eV to EeV: Neutrino Cross Sections Across Energy Scales*, Rev.Mod.Phys. **84**, 1307 (2012), [hep-ex/1305.7513].

[82] J. F. Beacom, W. M. Farr and P. Vogel, *Detection of supernova neutrinos by neutrino proton elastic scattering*, Phys.Rev. **D66**, 033001 (2002), [hep-ph/0205220].

[83] K. Zuber, *Neutrino Physics, Second Edition (Series in High Energy Physics, Cosmology and Gravitation)* (CRC Press, 2011).

[84] P. Vogel and J. F. Beacom, *Angular distribution of neutron inverse beta decay, $\overline{\nu}_e + p \to e^+ + n$*, Phys.Rev. **D60**, 053003 (1999), [hep-ph/9903554].

[85] S.-B. Kim, T. Lasserre and Y. Wang, *Reactor neutrinos*, Adv.High Energy Phys. **2013**, 453816 (2013).

[86] D. Casper, *The Nuance neutrino physics simulation, and the future*, Nucl.Phys.Proc.Suppl. **112**, 161 (2002), [hep-ph/0208030].

[87] J. Hewett *et al.*, *Fundamental Physics at the Intensity Frontier*, hep-ex/1205.2671.

[88] DONuT, K. Kodama *et al.*, *Final tau-neutrino results from the DONuT experiment*, Phys.Rev. **D78**, 052002 (2008), [hep-ex/0711.0728].

[89] MINERvA, L. Aliaga *et al.*, *Design, Calibration, and Performance of the MINERvA Detector*, Nucl.Instrum.Meth. **A743**, 130 (2014), [physics.ins-det/1305.5199].

[90] MINERvA, G. Fiorentini *et al.*, *Measurmenet of Muon Neutrino Quasielastic Scattering on a Hydrocarbon Target at* $E_\nu \sim 3.5$ *GeV*, Phys.Rev.Lett. **111**, 022502 (2013), [hep-ex/1305.2243].

[91] MINERvA, L. Fields *et al.*, *Measurement of Muon Antineutrino Quasielastic Scattering on a Hydrocarbon Target at* $E_\nu \sim 3.5$ *GeV*, Phys.Rev.Lett. **111**, 022501 (2013), [hep-ex/1305.2234].

[92] MINERvA, A. Higuera *et al.*, *Measurement of Coherent Production of* $\pi^\pm$ *in Neutrino and Antineutrino Beams on Carbon from* E_ν *of* 1.5 *to* 20 *GeV*, Phys.Rev.Lett. **113**, 261802 (2014), [hep-ex/1409.3835].

[93] MINERvA, B. Tice *et al.*, *Measurement of Ratios of* ν_μ *Charged-Current Cross Sections on C, Fe, and Pb to CH at Neutrino Energies 2-20 GeV*, Phys.Rev.Lett. **112**, 231801 (2014), [hep-ex/1403.2103].

[94] C. Andreopoulos *et al.*, *The GENIE Neutrino Monte Carlo Generator*, Nucl.Instrum.Meth. **A614**, 87 (2010), [hep-ph/0905.2517].

[95] C. Andreopoulos *et al.*, GENIE Neutrino Monte Carlo Generator - Homepage, `http://www.genie-mc.org/`.

[96] C. Weinheimer and K. Zuber, *Neutrino Masses*, Annalen Phys. **525**, 565 (2013), [hep-ex/1307.3518].

[97] S. Dell'Oro, S. Marcocci and F. Vissani, *New expectations and uncertainties on neutrinoless double beta decay*, Phys.Rev. **D90**, 033005 (2014), [hep-ph/1404.2616].

[98] H. Klapdor-Kleingrothaus, I. Krivosheina, A. Dietz and O. Chkvorets, *Search for neutrinoless double beta decay with enriched Ge-76 in Gran Sasso 1990-2003*, Phys.Lett. **B586**, 198 (2004), [hep-ph/0404088].

[99] H. Klapdor-Kleingrothaus and I. Krivosheina, *The evidence for the observation of 0nu beta beta decay: The identification of 0nu beta beta events from the full spectra*, Mod.Phys.Lett. **A21**, 1547 (2006).

[100] GERDA, M. Agostini *et al.*, *Results on Neutrinoless Double-β Decay of ^{76}Ge from Phase I of the GERDA Experiment*, Phys.Rev.Lett. **111**, 122503 (2013), [nucl-ex/1307.4720].

[101] N. Palanque-Delabrouille *et al.*, *Neutrino masses and cosmology with Lyman-alpha forest power spectrum*, JCAP **1511**, 011 (2015), [astro-ph.CO/1506.05976].

[102] C. Kraus *et al.*, *Final results from phase II of the Mainz neutrino mass search in tritium beta decay*, Eur.Phys.J. **C40**, 447 (2005), [hep-ex/0412056].

[103] Troitsk, V. Aseev *et al.*, *An upper limit on electron antineutrino mass from Troitsk experiment*, Phys.Rev. **D84**, 112003 (2011), [hep-ex/1108.5034].

[104] KATRIN, J. Angrik *et al.*, *KATRIN design report 2004*, (2005).

[105] J. M. Conrad, W. C. Louis and M. H. Shaevitz, *The LSND and MiniBooNE Oscillation Searches at High Δm^2*, Ann.Rev.Nucl.Part.Sci. **63**, 45 (2013), [hep-ex/1306.6494].

[106] C. Giunti and M. Laveder, *Statistical Significance of the Gallium Anomaly*, Phys. Rev. **C83**, 065504 (2011), [hep-ph/1006.3244].

[107] T. Mueller *et al.*, *Improved Predictions of Reactor Antineutrino Spectra*, Phys.Rev. **C83**, 054615 (2011), [hep-ex/1101.2663].

[108] P. Huber, *On the determination of anti-neutrino spectra from nuclear reactors*, Phys.Rev. **C84**, 024617 (2011), [hep-ph/1106.0687], [Erratum: Phys.Rev. C vol. 85].

[109] G. Mention *et al.*, *The Reactor Antineutrino Anomaly*, Phys.Rev. **D83**, 073006 (2011), [hep-ex/1101.2755].

[110] Borexino, G. Bellini *et al.*, *SOX: Short distance neutrino Oscillations with BoreXino*, JHEP **1308**, 038 (2013), [physics.ins-det/1304.7721].

[111] C. Spiering, *Towards High-Energy Neutrino Astronomy. A Historical Review*, Eur.Phys.J. **H37**, 515 (2012), [astro-ph.IM/1207.4952].

[112] IceCube, M. Aartsen *et al.*, *Atmospheric and astrophysical neutrinos above 1 TeV interacting in IceCube*, Phys.Rev. **D91**, 022001 (2015), [astro-ph.HE/1410.1749].

[113] IceCube, M. Aartsen *et al.*, *Evidence for High-Energy Extraterrestrial Neutrinos at the IceCube Detector*, Science **342**, 1242856 (2013), [astro-ph.HE/1311.5238].

[114] D. R. Williams, NASA Sun Fact Sheet, `http://nssdc.gsfc.nasa.gov/planetary/factsheet/sunfact.html`, 2013, Accessed March 14, 2015.

[115] R. Mitalas and K. R. Sills, *On the photon diffusion time scale for the sun*, Astrophys.J. **401**, 759 (1992).

[116] J. N. Bahcall, M. Gonzalez-Garcia and C. Pena-Garay, *Does the sun shine by pp or CNO fusion reactions?*, Phys.Rev.Lett. **90**, 131301 (2003), [astro-ph/0212331].

[117] M. Salaris and S. Cassisi, *Evolution of Stars and Stellar Populations* (Wiley, 2006).

[118] H. A. Bethe, *Energy Production in Stars*, Phys. Rev. **55**, 434 (1939).

[119] Borexino Collaboration, G. Bellini *et al.*, *First evidence of pep solar neutrinos by direct detection in Borexino*, Phys.Rev.Lett. **108**, 051302 (2012), [hep-ex/1110.3230].

[120] M. Asplund, N. Grevesse, A. J. Sauval and P. Scott, *The chemical composition of the Sun*, Ann.Rev.Astron.Astrophys. **47**, 481 (2009), [astro-ph.SR/0909.0948].

[121] J. Bahcall, Homepage of John Bahcall - Solar Neutrino Viewgraphs, `http://www.sns.ias.edu/~jnb/SNviewgraphs/snviewgraphs.html`, 2005, Accessed March 14, 2015.

[122] N. Grevesse and A. J. Sauval, *Standard Solar Composition*, Space Sci.Rev. **85**, 161 (1998).

[123] A. Serenelli, S. Basu, J. W. Ferguson and M. Asplund, *New Solar Composition: The Problem With Solar Models Revisited*, Astrophys.J. **705**, L123 (2009), [astro-ph.SR/0909.2668].

[124] A. M. Serenelli, W. Haxton and C. Pena-Garay, *Solar models with accretion. I. Application to the solar abundance problem*, Astrophys.J. **743**, 24 (2011), [astro-ph.SR/1104.1639].

[125] H.-T. Janka, K. Langanke, A. Marek, G. Martinez-Pinedo and B. Mueller, *Theory of Core-Collapse Supernovae*, Phys.Rept. **442**, 38 (2007), [astro-ph/0612072].

[126] S. Woosley and T. Janka, *The physics of core-collapse supernovae*, Nature Phys. **1**, 147 (2005), [astro-ph/0601261].

[127] H.-T. Janka *et al.*, *Core-Collapse Supernovae: Reflections and Directions*, PTEP **2012**, 01A309 (2012), [astro-ph.SR/1211.1378].

[128] S. Horiuchi, J. F. Beacom and E. Dwek, *The Diffuse Supernova Neutrino Background is detectable in Super-Kamiokande*, Phys.Rev. **D79**, 083013 (2009), [astro-ph/0812.3157].

[129] Virgo, LIGO Scientific, B. P. Abbott *et al.*, *Observation of Gravitational Waves from a Binary Black Hole Merger*, Phys. Rev. Lett. **116**, 061102 (2016), [1602.03837].

[130] G. G. Raffelt, *Supernova neutrino observations: What can we learn?*, Nucl.Phys.Proc.Suppl. **221**, 218 (2011), [astro-ph/0701677].

[131] T. Foglizzo *et al.*, *The explosion mechanism of core-collapse supernovae: progress in supernova theory and experiments*, Publ.Astron.Soc.Austral. **32**, 9 (2015), [astro-ph.HE/1501.01334].

[132] W. D. Arnett, J. N. Bahcall, R. P. Kirshner and S. E. Woosley, *Supernova 1987A*, Ann.Rev.Astron.Astrophys. **27**, 629 (1989).

[133] T. Fischer, S. Whitehouse, A. Mezzacappa, F.-K. Thielemann and M. Liebendorfer, *Protoneutron star evolution and the neutrino driven wind in general relativistic neutrino radiation hydrodynamics simulations*, Astron.Astrophys. **517**, A80 (2010), [astro-ph.HE/0908.1871].

[134] P. Antonioli *et al.*, *SNEWS: The Supernova Early Warning System*, New J.Phys. **6**, 114 (2004), [astro-ph/0406214].

[135] SNEWS: SuperNova Early Warning System - Homepage at Brookhaven National Laboratory, `http://snews.bnl.gov`, Accessed April 30, 2015.

[136] J. F. Beacom, *The Diffuse Supernova Neutrino Background*, Ann.Rev.Nucl.Part.Sci. **60**, 439 (2010), [astro-ph.HE/1004.3311].

[137] Super-Kamiokande, K. Bays *et al.*, *Supernova Relic Neutrino Search at Super-Kamiokande*, Phys.Rev. **D85**, 052007 (2012), [hep-ex/1111.5031].

[138] Super-Kamiokande, H. Zhang *et al.*, *Supernova Relic Neutrino Search with Neutron Tagging at Super-Kamiokande-IV*, Astropart.Phys. **60**, 41 (2014), [hep-ex/1311.3738].

[139] KamLAND, A. Gando *et al.*, *A study of extraterrestrial antineutrino sources with the KamLAND detector*, Astrophys.J. **745**, 193 (2012), [astro-ph.HE/1105.3516].

[140] G. Bellini, A. Ianni, L. Ludhova, F. Mantovani and W. McDonough, *Geo-neutrinos*, Prog.Part.Nucl.Phys. **73**, 1 (2013), [physics.geo-ph/1310.3732].

[141] C. Jaupart, S. Labrosse and J. C. Mareschal*Treatise on Geophysics* Vol. 7, 2 ed. (Elsevier B.V., 2007), chap. 7.06: Temperatures, Heat and Energy in the Mantle of the Earth, pp. 253–303.

[142] J. H. Davies and D. R. Davies, *Earth's surface heat flux*, Solid Earth **1**, 5 (2010).

[143] J. Herndon, *Substructure of the inner core of the Earth*, Proceedings of the National Academy of Sciences of the United States of America **93**, 646 (1996).

[144] T. Araki *et al.*, *Experimental investigation of geologically produced antineutrinos with KamLAND*, Nature **436**, 499 (2005).

[145] Borexino, G. Bellini *et al.*, *Observation of Geo-Neutrinos*, Phys.Lett. **B687**, 299 (2010), [hep-ex/1003.0284].

[146] Borexino Collaboration, G. Bellini *et al.*, *Measurement of geo-neutrinos from 1353 days of Borexino*, Phys.Lett. **B722**, 295 (2013), [hep-ex/1303.2571].

[147] P. Vogel, L. Wen and C. Zhang, *Neutrino Oscillation Studies with Reactors*, Nature.Commun. **6**.

[148] S.-F. Ge, K. Hagiwara, N. Okamura and Y. Takaesu, *Determination of mass hierarchy with medium baseline reactor neutrino experiments*, JHEP **05**, 131 (2013), [hep-ph/1210.8141].

[149] A. Hayes, J. Friar, G. Garvey, G. Jungman and G. Jonkmans, *Systematic Uncertainties in the Analysis of the Reactor Neutrino Anomaly*, Phys.Rev.Lett. **112**, 202501 (2014), [nucl-th/1309.4146].

[150] Daya Bay, D. V. Naumov, *Recent results from Daya Bay experiment*, EPJ Web Conf. **95**, 04043 (2015), [hep-ex/1412.7806].

[151] Double Chooz, J. I. Crespo-Anadon, Double Chooz: Latest results, in *Neutrino Oscillation Workshop (NOW 2014) Conca Specchiulla, Otranto, Lecce, Italy, September 7-14, 2014*, 2014, [hep-ex/1412.3698].

[152] RENO, S.-H. Seo, *New Results from RENO and The 5 MeV Excess*, AIP Conf. Proc. **1666**, 080002 (2015), [hep-ex/1410.7987].

[153] L. Zhan, Y. Wang, J. Cao and L. Wen, *Determination of the Neutrino Mass Hierarchy at an Intermediate Baseline*, Phys. Rev. **D78**, 111103 (2008), [hep-ex/0807.3203].

[154] M. Sajjad Athar, M. Honda, T. Kajita, K. Kasahara and S. Midorikawa, *Atmospheric neutrino flux at INO, South Pole and Pyhasalmi*, Phys.Lett. **B718**, 1375 (2013), [hep-ph/1210.5154].

[155] W. Winter, *Neutrino tomography: Learning about the earth's interior using the propagation of neutrinos*, Earth Moon Planets **99**, 285 (2006), [physics/0602049].

[156] J. Alonso *et al.*, *Expression of Interest for a Novel Search for CP Violation in the Neutrino Sector: DAEdALUS*, physics.ins-det/1006.0260.

[157] C. Aberle *et al.*, *Whitepaper on the DAEdALUS Program*, physics.acc-ph/1307.2949.

[158] P. Zucchelli, *A novel concept for a $\overline{\nu}_e$ / ν_e neutrino factory: The beta beam*, Phys.Lett. **B532**, 166 (2002).

[159] Neutrino Factory and Muon Collider, C. H. Albright *et al.*, *The neutrino factory and beta beam experiments and development*, physics/0411123.

[160] S. Geer, *Neutrino beams from muon storage rings: Characteristics and physics potential*, Phys.Rev. **D57**, 6989 (1998), [hep-ph/9712290].

[161] S. E. Kopp, *Accelerator-based neutrino beams*, Phys.Rept. **439**, 101 (2007), [physics/0609129].

[162] NOvA, D. S. Ayres *et al.*, *The NOvA Technical Design Report*, (2007).

[163] T2K, K. Abe *et al.*, *T2K neutrino flux prediction*, Phys.Rev. **D87**, 012001 (2013), [hep-ex/1211.0469].

[164] P. Coloma, P. Huber, J. Kopp and W. Winter, *Systematic uncertainties in long-baseline neutrino oscillations for large θ_{13}*, Phys.Rev. **D87**, 033004 (2013), [hep-ph/1209.5973].

[165] W. R. Leo, *Techniques for Nuclear and Particle Physics Experiments: A How-to Approach* (Springer, 1992).

[166] J. B. Birks, *The Theory and Practice of Scintillation Counting: International Series of Monographs in Electronics and Instrumentation (Volume 27)* (Pergamon, 1964).

[167] G. Ranucci, A. Goretti and P. Lombardi, *Pulse-shape discrimination of liquid scintillators*, Nucl.Instrum.Meth. **A412**, 374 (1998).

[168] J. Jackson, *Klassische Elektrodynamik* (Walter de Gruyter, Berlin New York, 2006).

[169] S. G. Warren, *Optical constants of ice from the ultraviolet to the microwave*, Appl. Opt. **23**, 1206 (1984).

[170] G. M. Hale and M. R. Querry, *Optical Constants of Water in the 200-nm to 200-μm Wavelength Region*, Appl. Opt. **12**, 555 (1973).

[171] M. Antonello *et al.*, *Detection of Cherenkov light emission in liquid argon*, Nucl.Instrum.Meth. **A516**, 348 (2004).

[172] M. Wurm *et al.*, *Optical Scattering Lengths in Large Liquid-Scintillator Neutrino Detectors*, Rev.Sci.Instrum. **81**, 053301 (2010), [physics.ins-det/1004.0811].

[173] M. Yeh *et al.*, *A new water-based liquid scintillator and potential applications*, Nucl.Instrum.Meth. **A660**, 51 (2011).

[174] Hamamatsu Photonics K.K., *Photomultiplier Tubes - Basics and Applications*, Manual, ed. 3a.

[175] B. Lubsandorzhiev, P. Pokhil, R. Vasiljev and A. Wright, *Studies of prepulses and late pulses in the 8" electron tubes series of photomultipliers*, Nucl.Instrum.Meth. **A442**, 452 (2000).

[176] L. Oberauer, C. Grieb, F. von Feilitzsch and I. Manno, *Light concentrators for Borexino and CTF*, Nucl.Instrum.Meth. **A530**, 453 (2004), [physics/0310076].

[177] M. Akashi-Ronquest *et al.*, *Improving Photoelectron Counting and Particle Identification in Scintillation Detectors with Bayesian Techniques*, Astropart.Phys. **65**, 40 (2014), [physics.ins-det/1408.1914].

[178] Borexino Collaboration, H. Back *et al.*, *Borexino calibrations: Hardware, Methods, and Results*, JINST **7**, P10018 (2012), [physics.ins-det/1207.4816].

[179] A. Balantekin *et al.*, *Neutrino mass hierarchy determination and other physics potential of medium-baseline reactor neutrino oscillation experiments*, hep-ex/1307.7419.

[180] L. Zhan, Y. Wang, J. Cao and L. Wen, *Experimental Requirements to Determine the Neutrino Mass Hierarchy Using Reactor Neutrinos*, Phys.Rev. **D79**, 073007 (2009), [hep-ex/0901.2976].

[181] F. Reines and C. Cowan, *A Proposed experiment to detect the free neutrino*, Phys.Rev. **90**, 492 (1953).

[182] C. Cowan, F. Reines, F. Harrison, E. Anderson and F. Hayes, *Large liquid scintillation detectors*, Phys.Rev. **90**, 493 (1953).

[183] B. Dasgupta and J. F. Beacom, *Reconstruction of supernova ν_μ, ν_τ, anti-ν_μ, and anti-ν_τ neutrino spectra at scintillator detectors*, Phys.Rev. **D83**, 113006 (2011), [hep-ph/1103.2768].

[184] Borexino, G. Bellini *et al.*, *Cosmogenic Backgrounds in Borexino at 3800 m water-equivalent depth*, JCAP **1308**, 049 (2013), [physics.ins-det/1304.7381].

[185] C. Aberle *et al.*, *Large scale Gd-beta-diketonate based organic liquid scintillator production for antineutrino detection*, JINST **7**, P06008 (2012), [physics.ins-det/1112.5941].

[186] Daya Bay Collaboration, F. An *et al.*, *A side-by-side comparison of Daya Bay antineutrino detectors*, Nucl.Instrum.Meth. **A685**, 78 (2012), [physics.ins-det/1202.6181].

[187] RENO collaboration, J. Ahn *et al.*, *Observation of Reactor Electron Antineutrino Disappearance in the RENO Experiment*, Phys.Rev.Lett. **108**, 191802 (2012), [hep-ex/1204.0626].

[188] Daya Bay Collaboration, F. An *et al.*, *Improved Measurement of Electron Antineutrino Disappearance at Daya Bay*, Chin.Phys. **C37**, 011001 (2013), [hep-ex/1210.6327].

[189] CHOOZ, M. Apollonio *et al.*, *Determination of neutrino incoming direction in the CHOOZ experiment and supernova explosion location by scintillator detectors*, Phys.Rev. **D61**, 012001 (2000), [hep-ex/9906011].

[190] J. Zhao *et al.*, *$^{13}C(\alpha,n)^{16}O$ background in a liquid scintillator based neutrino experiment*, Chin. Phys. **C38**, 116201 (2014), [physics.ins-det/1312.6347].

[191] National Nuclear Data Center - Brookhaven National Laboratory - , `http://www.nndc.bnl.gov/chart/`, Evaluated Nuclear Structure Data File from January 5, 2015; Accessed January 20, 2015.

[192] G. Zuzel, Low-background techniques applied in the BOREXINO experiment, Workshop talk - Low Radioactivity Techniques 2015 at Seatle, USA, `https://www.npl.washington.edu/indico/getFile.py/access?contribId=46&sessionId=11&resId=0&materialId=slides&confId=5`, 2015.

[193] KamLAND Collaboration, S. Abe *et al.*, *Production of Radioactive Isotopes through Cosmic Muon Spallation in KamLAND*, Phys.Rev. **C81**, 025807 (2010), [hep-ex/0907.0066].

[194] D. Tilley *et al.*, *Energy levels of light nuclei*, Nuclear Physics A **745**, 155 (2004).

[195] Borexino Collaboration, G. Bellini *et al.*, *Cosmic-muon flux and annual modulation in Borexino at 3800 m water-equivalent depth*, JCAP **1205**, 015 (2012), [hep-ex/1202.6403].

[196] Double Chooz Collaboration, Y. Abe *et al.*, *Improved measurements of the neutrino mixing angle θ_{13} with the Double Chooz detector*, JHEP **1410**, 86 (2014), [hep-ex/1406.7763].

[197] D. Autiero *et al.*, *Large underground, liquid based detectors for astro-particle physics in Europe: Scientific case and prospects*, JCAP **0711**, 011 (2007), [hep-ph/0705.0116].

[198] M. Wurm, Status of LENA R&D, Conference talk - NNN 2014 at APC Paris, `http://indico.in2p3.fr/event/10162/session/9/contribution/30/material/slides/0.pdf`, 2014.

[199] W. Trzaska *et al.*, *LAGUNA in Pyhaesalmi*, Acta Phys.Polon. **B41**, 1779 (2010).

[200] L. Mosca, *Frejus site for the LAGUNA projects*, Acta Phys.Polon. **B41**, 1773 (2010).

[201] R. Möllenberg *et al.*, *Detecting the Upturn of the Solar ^8B Neutrino Spectrum with LENA*, Phys.Lett. **B737**, 251 (2014), [physics.ins-det/1408.0623].

[202] R. Möllenberg *et al.*, *Detecting the Diffuse Supernova Neutrino Background with LENA*, Phys.Rev. **D91**, 032005 (2015), [astro-ph.IM/1409.2240].

[203] Super-Kamiokande, K. Abe *et al.*, *Search for proton decay via $p \to \nu K^+$ using 260 kiloton $\cdot$ year data of Super-Kamiokande*, Phys.Rev. **D90**, 072005 (2014), [hep-ex/1408.1195].

[204] S. Choubey, S. T. Petcov and M. Piai, *Precision neutrino oscillation physics with an intermediate baseline reactor neutrino experiment*, Phys. Rev. **D68**, 113006 (2003), [hep-ph/0306017].

[205] J. Learned, S. T. Dye, S. Pakvasa and R. C. Svoboda, *Determination of neutrino mass hierarchy and theta(13) with a remote detector of reactor antineutrinos*, Phys. Rev. **D78**, 071302 (2008), [hep-ex/0612022].

[206] X. Qian *et al.*, *Mass Hierarchy Resolution in Reactor Anti-neutrino Experiments: Parameter Degeneracies and Detector Energy Response*, Phys. Rev. **D87**, 033005 (2013), [physics.ins-det/1208.1551].

[207] Y.-F. Li, J. Cao, Y. Wang and L. Zhan, *Unambiguous Determination of the Neutrino Mass Hierarchy Using Reactor Neutrinos*, Phys.Rev. **D88**, 013008 (2013), [hep-ex/1303.6733].

[208] X. B. Ma, W. L. Zhong, L. Z. Wang, Y. X. Chen and J. Cao, *Improved calculation of the energy release in neutron-induced fission*, Phys. Rev. **C88**, 014605 (2013), [nucl-ex/1212.6625].

[209] S. K. Agarwalla, S. Prakash and W. Wang, *High-precision measurement of atmospheric mass-squared splitting with T2K and NOvA*, hep-ph/1312.1477.

[210] GEANT4, S. Agostinelli *et al.*, *GEANT4: A Simulation toolkit*, Nucl.Instrum.Meth. **A506**, 250 (2003).

[211] J. Allison *et al.*, *Geant4 developments and applications*, IEEE Trans.Nucl.Sci. **53**, 270 (2006).

[212] R. Brun and F. Rademakers, *ROOT: An object oriented data analysis framework*, Nucl.Instrum.Meth. **A389**, 81 (1997).

[213] T. M. Undagoitia, *Measurement of light emission in organic liquid scintillators and studies towards the search for proton decay in the future large-scale detector LENA*, PhD thesis, Munich, Tech. U., 2008.

[214] J. M. Winter, *Phenomenology of Supernova Neutrinos, Spatial Event Reconstruction, and Scintillation Light Yield Measurements for the Liquid-Scintillator Detector LENA*, Diploma thesis, Munich, Tech. U., 2007.

[215] R. Möllenberg, *Monte Carlo Study of Solar ^8B Neutrinos and the Diffuse Supernova Neutrino Background in LENA*, PhD thesis, Munich, Tech. U., 2013.

[216] H. O'Keeffe, E. O'Sullivan and M. Chen, *Scintillation decay time and pulse shape discrimination in oxygenated and deoxygenated solutions of linear alkylbenzene for the SNO+ experiment*, Nucl.Instrum.Meth. **A640**, 119 (2011), [physics.ins-det/1102.0797].

[217] M. Grassi, J. Evslin, E. Ciuffoli and X. Zhang, *Showering Cosmogenic Muons in A Large Liquid Scintillator*, JHEP **09**, 049 (2014), [physics.ins-det/1401.7796].

[218] M. Grassi, J. Evslin, E. Ciuffoli and X. Zhang, *Vetoing Cosmogenic Muons in A Large Liquid Scintillator*, JHEP **10**, 032 (2015), [physics.ins-det/1505.05609].

[219] BOOST C++ libraries, `http://www.boost.org/`, Used libraries: *Accumulators* (E. Niebler), *Assert* (P. Dimov), *Bind* (P. Dimov), *Foreach* (E. Niebler), *Function* (D. Gregor), *Program Options* (V. Prus), *Smart Ptr* (G. Colvin, B. Dawes, P. Dimov, D. Adler, G. Fernandes), *Test* (G. Rozental), *Tuple* (J. Järvi).

[220] D. van Heesch, Doxygen, `http://www.doxygen.org/`.

[221] M. J. Berger and J. Oliger, *Adaptive Mesh Refinement for Hyperbolic Partial Differential Equations*, J. Comput. Phys. **53**, 484 (1984).

[222] M. J. Berger and P. Colella, *Local Adaptive Mesh Refinement for Shock Hydrodynamics*, J. Comput. Phys. **82**, 64 (1989).

[223] D. J. Meyhöfer, *Studium zur Spurrekonstruktion in großen Wasser-Cherenkov-Detektoren*, Bachelor thesis, Universität Hamburg, 2014.

[224] F. James and M. Roos, *Minuit: A System for Function Minimization and Analysis of the Parameter Errors and Correlations*, Comput. Phys. Commun. **10**, 343 (1975).

[225] K. Siddiqi and S. Pizer, *Medial Representations: Mathematics, Algorithms and Applications (Computational Imaging and Vision)* (Springer, 2010).

[226] K. Palàgyi and A. Kuba, A thinning algorithm to extract medial lines from 3D medical images, in *Information Processing in Medical Imaging*, edited by J. Duncan and G. Gindi, , Lecture Notes in Computer Science Vol. 1230, pp. 411–416, Springer Berlin Heidelberg, 1997.

[227] K. Palàgyi and A. Kuba, *A 3D 6-subiteration thinning algorithm for extracting medial lines*, Pattern Recognition Letters **19**, 613 (1998).

[228] G. Németh, P. Kardos and K. Palágyi, *Thinning combined with iteration-by-iteration smoothing for 3D binary images*, Graphical Models **73**, 335 (2011), Computational Modeling in Imaging Sciences.

[229] LAGUNA-LBNO Collaboration, S. Agarwalla *et al.*, *The mass-hierarchy and CP-violation discovery reach of the LBNO long-baseline neutrino experiment*, JHEP **1405**, 094 (2014), [hep-ph/1312.6520].

[230] LAGUNA-LBNO Collaboration, S. Agarwalla *et al.*, *Optimised sensitivity to leptonic CP violation from spectral information: the LBNO case at 2300 km baseline*, hep-ph/1412.0593.

[231] A. Rubbia, *Underground Neutrino Detectors for Particle and Astroparticle Science: The Giant Liquid Argon Charge Imaging ExpeRiment (GLACIER)*, J.Phys.Conf.Ser. **171**, 012020 (2009), [hep-ph/0908.1286].

[232] M. Freund, P. Huber and M. Lindner, *Systematic exploration of the neutrino factory parameter space including errors and correlations*, Nucl. Phys. **B615**, 331 (2001), [hep-ph/0105071].

[233] P. Huber, M. Lindner and W. Winter, *Simulation of long-baseline neutrino oscillation experiments with GLoBES (General Long Baseline Experiment Simulator)*, Comput. Phys. Commun. **167**, 195 (2005), [hep-ph/0407333].

[234] P. Huber, J. Kopp, M. Lindner, M. Rolinec and W. Winter, *New features in the simulation of neutrino oscillation experiments with GLoBES 3.0: General Long Baseline Experiment Simulator*, Comput. Phys. Commun. **177**, 432 (2007), [hep-ph/0701187].

[235] A. Longhin, *Optimization of neutrino beams for underground sites in Europe*, physics.ins-det/1206.4294.

[236] A. Longhin, Neutrino fluxes for the LAGUNA sites, `http://irfu.cea.fr/en/Phocea/Pisp/index.php?id=72`.

[237] E. Kozlovskaya, J. Peltoniemi and J. Sarkamo, *The density distribution in the Earth along the CERN-Pyhasalmi baseline and its effect on neutrino oscillations*, hep-ph/0305042.

[238] A. Dziewonski and D. Anderson, *Preliminary reference earth model*, Phys.Earth Planet.Interiors **25**, 297 (1981).

[239] F. Stacey, *Physics of the earth*, 2 ed. (Wiley, 1977).

[240] P. Coloma, T. Li and S. Pascoli, *A Comparative Study of Long-Baseline Superbeams within LAGUNA for large θ_{13}*, hep-ph/1206.4038.

[241] D. Hellgartner, Munich, Tech. U., Private communication, 2015.

[242] G. Cowan, K. Cranmer, E. Gross and O. Vitells, *Asymptotic formulae for likelihood-based tests of new physics*, Eur. Phys. J. **C71**, 1554 (2011), [physics.data-an/1007.1727], [Erratum: Eur. Phys. J. C73, 2501 (2013)].

[243] A. Hocker *et al.*, *TMVA - Toolkit for Multivariate Data Analysis*, PoS **ACAT**, 040 (2007), [physics/0703039].

[244] G. L. Fogli, E. Lisi, A. Marrone, D. Montanino and A. Palazzo, *Getting the most from the statistical analysis of solar neutrino oscillations*, Phys. Rev. **D66**, 053010 (2002), [hep-ph/0206162].

[245] X. Qian *et al.*, *Statistical Evaluation of Experimental Determinations of Neutrino Mass Hierarchy*, Phys. Rev. **D86**, 113011 (2012), [hep-ph/1210.3651].

[246] P. Ballett, Institute for Particle Physics Phenomenology, University of Durham, Private communication, 2014.

[247] NOvA, R. B. Patterson, *The NOvA Experiment: Status and Outlook*, hep-ex/1209.0716, [Nucl. Phys. Proc. Suppl.235-236,151(2013)].

[248] Daya Bay, L. Zhan, *Recent Results from Daya Bay*, hep-ex/1506.01149.

[249] M. Fukugita, Y. Kohyama and K. Kubodera, *Neutrino reaction cross sections on* ^{12}C *target*, Physics Letters B **212**, 139 (1988).

[250] A. Ianni, D. Montanino and F. Villante, *How to observe B-8 solar neutrinos in liquid scintillator detectors*, Phys.Lett. **B627**, 38 (2005), [physics/0506171].

[251] L. Cadonati, F. Calaprice and M. Chen, *Supernova neutrino detection in borexino*, Astropart.Phys. **16**, 361 (2002), [hep-ph/0012082].

[252] A. de Bellefon *et al.*, *MEMPHYS: A Large scale water Cerenkov detector at Frejus*, hep-ex/0607026.

[253] J. Borne *et al.*, *The MEMPHYS project*, Nucl.Instrum.Meth. **A639**, 287 (2011).

[254] ICARUS Collaboration, S. Amerio *et al.*, *Design, construction and tests of the ICARUS T600 detector*, Nucl.Instrum.Meth. **A527**, 329 (2004).

[255] D. Dalet, d-maps.com, `http://d-maps.com/carte.php?num_car=2233&lang=en`, Accessed February 12, 2015.

[256] LAGUNA-LBNO Collaboration, S. Agarwalla *et al.*, *The LBNO long-baseline oscillation sensitivities with two conventional neutrino beams at different baselines*, hep-ph/1412.0804.

Danksagung / Acknowledgement

Diese Arbeit hätte nicht ohne die Unterstützung, den Rat und den Zuspruch seitens einiger Personen erstellt werden können, denen ich an dieser Stelle unbedingt danken möchte.
Im Allgemeinen bedanke ich mich bei (ehemaligen) Kollegen aus der *Forschungsgruppe Neutrinophysik* der *Universität Hamburg*, Prof. Dr. *Caren Hagner*, Prof. Dr. *Walter Schmidt-Parzefall*, Prof. Dr. *Michael Wurm*, Dr. *Daniel Bick*, Dr. *Joachim Ebert*, Dr. *Torben Ferber*, Dr. *Christoph Göllnitz*, Dr. *Nadine Heidrich*, Dr. *Jan Lenkeit*, Dr. *Christian Oldorf*, Dr. *Jan H.K. Timm*, Dr. *Björn S. Wonsak*, *Bosse Bein*, *Ruth Biermann*, *Stefan Bieschke*, *Volker Braunert*, *Benjamin Büttner*, *Annika Hollnagel*, *Markus Kaiser*, *Michel Meyer*, *Mikko Meyer*, *David Meyhöfer*, *Philipp Neuhäußer*, *Hans-Jürgen Ohmacht*, *Henning Rebber*, *David Schwickert*, *Lisa Steppat*, und *Laura Vanhoefer*, für interessante Meetings, unterhaltsame Gespräche beim Mittagessen in der Kantine oder um den Grill, spaßige Weihnachtsfeiern und Betriebsausflüge, spannende Spiele am Kickertisch, gemeinsame Besuche der DPG-Frühjahrstagung und manch andere tolle Momente mehr.

I thankfully recieved funding for parts of my work from the LAGUNA-LBNO design study (Grant Agreement No. 284518) in the context of the 7^{th} *Framework Programme for Research and Technological Development* of the *European Union*. Den Verantwortlichen des BIRD-Clusters am DESY danke ich dafür, dass ich die große Rechenpower im Rahmen meiner Arbeit nutzen konnte.

Einigen Menschen möchte ich an dieser Stelle meinen besonderen Dank ausdrücken:
Für die Möglichkeit zur Durchführung meiner Promotion in ihrer Arbeitsgruppe bedanke ich mich bei Frau Prof. Dr. *Caren Hagner*. Ihre ansteckende Begeisterung für Neutrinophysik und die von ihr gegebene Möglichkeit zur freien Entfaltung bei der Bearbeitung meines Themas waren für mich eine wichtige Motivation.
Bei Herrn Prof. Dr. *Michael Wurm*, der mir sowohl fachlich als auch menschlich ein Vorbild ist, bedanke ich mich allerherzlichst für eine angenehme und geduldige Betreuung, sowie für die hilfreichen Kommentare zu dieser Arbeit. Sein stetiges Interesse an meinen Arbeitsthemen, auch nach seinem Weggang aus der Arbeitsgruppe, war mir immer ein wichtiger Ansporn.
Ebenso ein Vorbild ist mir Herr Dr. *Björn S. Wonsak*, bei dem ich mich sehr für die Möglichkeit zur Erweiterung meiner Arbeit um das Mitwirken an seinem Rekonstruktionsansatz, sowie für wichtige Kommentare zu großen Teilen dieser Niederschrift

bedanke. Durch seine ansteckende Euphorie und seinen schier endlosen Optimismus war mir die inspirierende Zusammenarbeit bei der Weiterentwicklung seiner Idee immer eine große Freude.
Für eine entspannte Atmosphäre im gemeinsamen Büro und für konstruktive Hinweise zu dieser Arbeit gilt mein besonderer Dank Herrn Dr. *Daniel Bick*. Die Unterhaltungen mit ihm über Familie, Filme und Flugzeuge waren mir immer eine willkommene Zerstreuung.
Bei Herrn Dr. *Joachim Ebert* bedanke ich mich für seinen Einsatz und seine Hilfe bei Vertrags- und Verwaltungsangelegenheiten.
Mein Dank geht außerdem an *Annika Hollnagel*, die neben angenehmen Plauderein fern von Arbeitsthemen auch meine Späße ertragen hat / musste.
Ich danke Herrn *Hans-Jürgen („Hajo") Ohmacht* für nette Gespräche und die allmorgendliche Kontrolle meiner Handtemperatur beim begrüßenden Händedruck.

Neben Herrn Prof. Dr. *Michael Wurm* und Herrn Dr. *Björn S. Wonsak* danke ich auch den weiteren Mitarbeitern der LENA-Arbeitsgruppe für eine freundliche und produktive Zusammenarbeit:
Für hilfreiche Kommentare zu meinen Arbeitsthemen und die Zurverfügungstellung von Erfahrungen bezüglich LENA und zugehöriger Software sowie Material aus seiner Arbeit gilt mein Dank Herrn Dr. *Dominikus A. Hellgartner* von der *TU München*. Sein Einsatz und seine Arbeiten zur Teilchenspurrekonstruktion in Flüssigszintillator waren mir stets eine große Motivation.
Teile dieser Arbeit wären nicht möglich gewesen ohne die Betreuung der LENA-Detektorsimulation durch Herrn Dr. *Randolph Möllenberg* von der *TU München*. Dafür, sowie für schnelle Hilfestellungen bei der Benutzung der Software, bedanke ich mich sehr.
I want to warmly thank *Kai Loo* from the *University of Jyväskylä* for the time-consuming execution and supervision of event simulation and reconstruction runs on the FGI. Without his commitment and his access to the computation power, the application of the new reconstruction approach to a large sample of events in a short time would not have been possible.
For his strong and enduring enthusiasm regarding LENA, which was a great motivation for me, I want to thank Dr. *Wladyslaw H. Trzaska* from the *University of Jyväskylä*.

Des Weiteren möchte ich an dieser Stelle mir wichtigen Menschen danken, die mich in meinem Leben abseits der Arbeit begleiten:
Bei meiner besten Freundin *Nele M. Märcker* bedanke ich mich für ihre langjährige, treue Freundschaft. Sie ist mir stets ein sicherer Hafen bei rauer See.
Meinem guten Freund und „Leidensgenossen"*Jens S. Kienitz* danke ich für lustige Tanzabende und eine unvergessliche Wanderung entlang des *Hadrian's Wall*.

Abschließend gilt mein allerherzlichster Dank meiner ganzen Familie. Vor allem danke ich meiner Mama *Elke* und meinem Papa *Wilfried* sowie meinem Schwesterherz *Ann-Kathrin* dafür, dass sie immer für mich da sind und mir mit Rat und Tat in allen Lebenslagen zur Seite stehen - DANKE!